Seasonal and interannual variability in Saturn's stratosphere

A thesis submitted for the degree of *Doctor of Philosophy*

James Andrew Sinclair

Lady Margaret Hall

Michaelmas Term 2013

Atmospheric, Oceanic & Planetary Physics

Department of Physics

University of Oxford

Abstract

The stratosphere of Saturn is highly variable. With an axial tilt of 26.7°, Saturn experiences seasons like Earth and is currently approaching northern summer solstice in 2017. In addition to general seasonal change, previous studies have highlighted that Saturn's stratosphere is host to a range of dynamical phenomena. These processes have an observable effect on the vertical temperature profile and stratospheric concentrations of acetylene (C_2H_2) and ethane (C_2H_6), which may be determined or *retrieved* from thermal infrared observations of Saturn. This thesis presents an analysis of observations of Saturn acquired by Voyager's IRIS (Infrared Interferometer Spectrometer, 180 - 2500 cm^{-1}, Hanel et al. [1980]) instrument in 1980, Cassini's CIRS (Composite Infrared Spectrometer, 10 - 1400 cm^{-1}, Flasar et al. [2004]) instrument from 2005 to 2012 and the Celeste spectrometer (400 - 2000 cm^{-1}, Moran et al. [2007]) on NASA's IRTF (Infrared Telescope Facility) in 2012 in order to track seasonal and interannual changes in Saturn's stratosphere.

The concentrations of C_2H_2 and C_2H_6 were seen to decrease at 15°S and increase at 25°N from 2005 to 2009/2010. These changes at 15°S and 25°N respectively indicate upward and downward branches associated with cross-equatorial *seasonally-reversing Hadley circulation* that has been predicted by a general circulation model [Friedson and Moses, 2012]. Strong cooling of up to 17 K at high-southern latitudes from 2005 to 2010 suggests an autumnal weakening of a vortex that appears to form at the pole of the summer hemisphere [Fletcher et al., 2008]. The emergence of a similar northern polar vortex as northern summer solstice approaches was yet to be observed in 2012. Interannual differences in the equatorial temperature structure between 1980 and 2009/2010 suggest Saturn's semiannual oscillation (or SSAO, Fouchet et al. [2008]; Orton et al. [2008]) has been captured in a different phase from one *year* to the next. This is puzzling since the oscillation would be expected to have undergone two cycles assuming its period is half a Saturn year (14.7 years). This contrast is suggestive that the period of the SSAO is more quasi-semiannual.

Acknowledgements

It's hard to believe that several years of conferences, Hawaii trips and many pints of Rev at the Gardener's Arms has finally produced a Thesis that needs an Acknowledgements page.

Firstly, a big thank you to the STFC (Science & Technology Facilities Council) for funding this DPhil and making several years of very interesting work possible.

I am immensely grateful to my supervisor, Pat Irwin, for all his guidance and patience over the last few years. I would also like to thank other members of the Planetary group - Leigh, Jane, Cecile, Dane, Jo, Neil, Simon, Peter - for all their help and suggestions during my time here. My project has also been greatly helped by colleagues across the Pond, and the English channel. Thank you to: Brigette Hesman for kindly introducing me to ground-based observing and giving me the chance to go to Hawaii (twice!), Nico Gorius for his improvements to the calibration of CIRS observations, Tommy Greathouse for his enthusiasm of my work, Jim Friedson for generously providing me unpublished model results, Julie Moses for very helpful feedback on my work and Sandrine Guerlet for sharing her results for comparison.

There are too many people to thank for making AOPP a great place to work but those that stand out: Pat and Simon for offering me a postdoctoral position after my thesis submission and easing my transition into real life, Sarah for looking after all the graduate students, Jane and Cecile ("There was no mess!") for being great office mates in my first year and an effective cure of my imposter syndrome when I arrived, the organisers of the Coffee club who have enabled my coffee addiction but ultimately ensured I submitted my thesis and everyone else for all those coffee breaks and pub lunches.

Lady Margaret Hall has been a great place to call home and I've made many good friends through the MCR. LMH also introduced me to rowing, which has become a big hobby in these last few years. Many thanks to Goose, Ken, SJ, NataLAD, BenB, BenW, Beth and all the other men and women of LMHBC and the Oxford Academicals Rowing Club for lots of specific rowing chat, my fitness and a very needed distraction while I was writing this thesis.

Finally, lots of love to my Mum and sisters, Caroline and Lizzie, for being a constant source of support and not making too much fun of me for being a Physics geek.

Contents

Chapter 1

Introduction

1.1 The early solar system

The formation of our solar system began with the collapse of an interstellar gas cloud possible triggered by a shockwave from a nearby supernova (e.g., Herbst and Assousa [1977]). While the centre of the nebula became optically thick such that temperatures rose producing the protostar which would later become the Sun, the remaining material (hydrogen, helium and 'dust') flattened into a rotating disc of material known as a circumstellar disc. The planets of our solar system were then formed from this disc by two accepted but contrasting theories.

The *core accretion model* or CAM is described in several phases [Pollack et al., 1996] but is initiated by the growth of cm-sized dust grains through aggregation and coagulation to km-sized objects known as *planetesimals*. At this point, these objects have achieved sufficient mass such that further growth is achieved via collisions due to gravitational attraction, eventually producing larger objects called *planetary embryos*. The masses of these embryos were predicted to increase with distance from the protosun since the outer, slower-rotating regions of the disc represent more favourable conditions for attraction and growth while the inner, turbulent regions of the disc hinder the formation of larger objects. In addition, planetary embryos that formed beyond the water ice condensation line or *snow line* [Lecar et al., 2006] were more abundant in ices and refractory elements which are denser and thus higher in mass. Eventually, these embryos grew large enough in mass to begin accreting gas from the surrounding disc to form their atmospheres. Embryos in the outer solar system, in particular those that eventually became Jupiter and Saturn, are thought to

have reached this stage sooner and accreted the most gas. Less massive embryos in the inner solar system, which eventually formed the terrestrial planets, however accreted very little gas. When nuclear fusion was initiated in the core of the Protosun and the Sun was born, all remaining gas and dust was removed from the disc by radiation pressure leaving the Solar System we observe today. These stages summarise the CAM, which is under constant revision but nicely explains the contrast in planet size and mass between the inner and outer solar system. The alternative *gravitational instability* model or GIM predicts the formation of gas giant planets by gravitational collapse directly from the circumstellar disc [Boss, 1997]. This formation theory more readily explains the existence of *hot Jupiter* exoplanets such as HD209458b and HD189733b [Charbonneau et al., 2000; Hébrard and Lecavelier Des Etangs, 2006], which orbit their parent star considerably closer than the snow line at orbital separations closer than 0.1 AU. However, this theory cannot account for the formation of terrestrial-sized planets.

1.2 Saturn and its atmosphere

Table 1.1 compares the physical properties of our own planet, Earth, with Saturn. Saturn is almost 10 times larger and over 100 times more massive than Earth. This sheer contrast in size and mass is explained readily by the CAM, with Saturn's formation in the outer solar system where the slowly-rotating disc and the abundance of ices/refractory elements favoured the growth of larger planetary bodies.

There are further contrasts in the physical properties of Earth and Saturn. While Earth spins on its own axis approximately every 24 hours, Saturn rotates over two times faster. With such a fast rotation on such a large planet, equatorial latitudes bulge out centrifugally giving Saturn a significantly larger oblateness than Earth. This oblate shape has given rise to two latitude systems. Planetocentric latitude (as used on Earth) is the angle subtended

Parameters	Earth	Saturn	Saturn/Earth ratio
Mass (kg)	5.97×10^{24}	5.68×10^{26}	95.16
Equatorial Radius (km)	6378	60268	9.45
Polar Radius (km)	6356	54362	6.5
Oblateness	0.0034	0.0979	28.8
Volume (km^3)	1.08×10^{12}	8.2713×10^{14}	763.6
Mean density ($g\ cm^{-3}$)	5.53	0.7	0.13
Sidereal Day (hours)	23.9345	10.65	0.45
Semi-major axis at perihelion (km)	1.47×10^8	1.35×10^9	9.04
Orbital eccentricity	0.0167	0.054	3.23
Sidereal orbital period (years)	1	29.42	29.42
Axial tilt	23.4°	26.7°	1.1
Five most abundant atmospheric constituents	N_2(78%), O_2(21%), Ar (1%), CO_2(<0.1%), Ne(<0.1%)	H_2 (96%), He(3%), CH_4(0.4%), NH_3(<0.1%), HD(<0.1%)	-

Table 1.1: A comparison of the physical properties of Earth and Saturn. The chemical compositions quoted are approximate and altitudinal averages - more detailed models of Earth and Saturn's atmospheric composition are presented in Appendix B and Chapter 3 respectively.

at the centre of the planet by a point on the planet's meridian with respect to the equatorial plane. Planetographic latitude is instead the angle subtended by the equatorial plane and the gravity vector of a point on the planet's meridian. At low-to-mid latitudes where there is a significant bulge, this gravity vector does not point towards the centre of the planet as it would if the planet was spherical. In this thesis, all latitudes quoted are planetographic. With Saturn's larger semi-major axis, the time taken to complete one orbit around the Sun or *year* is 29.4 times longer than for Earth. During this time, Saturn's distance from the Sun varies by up to 0.9 AU (where 1 AU is the mean distance between the Earth and

the Sun) due to the eccentricity of its orbit. As we will see in Section 1.4.1, this orbital eccentricity affects the climate of Saturn. However, one similarity that can be drawn of the physical properties of Earth and Saturn is their axial tilt. The orbital and rotational axes of both planets are not parallel but at an angle of greater than 23° and so both planets experience *seasons*. Only, a season on Saturn is longer than 6 (Earth) years in contrast to seasons of only a few months in length on Earth due to the former's 29.4 year orbital period.

Th contrasts in atmospheric composition of Earth and Saturn can be explained by their different evolutions. H_2 and He initially accreted from the circumstellar disc by the planetary embryo that became Earth have since been lost as they escaped Earth's gravity. Instead, the atmosphere observed today is considered a *secondary* atmosphere where molecular nitrogen (N_2) and molecular oxygen (O_2) and other atmospheric constituents have been produced by outgassing from the planet's interior or transported from the outer solar system by comets/asteroids. Saturn has however been able to retain hydrogen and helium due to its considerably larger mass and these two gases form the bulk (∼99%) of Saturn's atmosphere observed today. The constituents which form the remaining 1% of Saturn's atmosphere are described as *trace species* and are of greater interest in this work. In particular, methane (CH_4) and other hydrocarbons such as acetylene (C_2H_2) and ethane (C_2H_6) are used as sensors of stratospheric structure and motion in this work. A more detailed model of Saturn's atmospheric composition is provided in Section 3.1.4 later in this thesis.

1.3 The stratosphere of Saturn

Observations of limb brightening of CH_4 emission at 7 μm on Saturn first indicated the presence of a temperature inversion in its atmosphere [Gillett and Forrest, 1974]. A sim-

ilar limb brightening at approximately 12 μm was later determined to be C_2H_6 emission [Tokunaga et al., 1975] and likewise suggested the presence of this molecule above a temperature inversion. Such a temperature inversion gives rise to a highly stratified region of atmosphere known as the stratosphere.

1.3.1 Photochemistry

Our own planet has a stratosphere. From the Earth's surface to a temperature minimum ranging or *tropopause* at an altitude of approximately 15 km, the atmospheric temperature decreases with height at a rate (depending on the water vapour content of the atmosphere) ranging from 5 K/km to 10 K/km [Andrews, 2000]. The subsequent rise in temperature with height is a result of heating produced by photochemical reactions of oxygen-bearing compounds such as O_2 and ozone (O_3) with ultraviolet light from the Sun. On Saturn, the presence of CH_4 is the main cause of the temperature inversion. Photolysis of this molecule by solar ultraviolet light initiates a complex photochemistry, as shown below.

$$CH_4 + h\nu \rightarrow CH_3 + H$$

Here, hν represents an ultraviolet photon from the Sun. Methyl and other by-products of ultraviolet photolysis recombine to produce numerous higher-order hydrocarbons. This is exemplified below in the catalysed production of ethane (C_2H_6) and acetylene (C_2H_2) though there are of course a significant number of alternative pathways in the production of these species.

$$2CH_3 + M \rightarrow C_2H_6 + M$$

$$C_2H_6 + C_2H \rightarrow C_2H_2 + C_2H_5$$

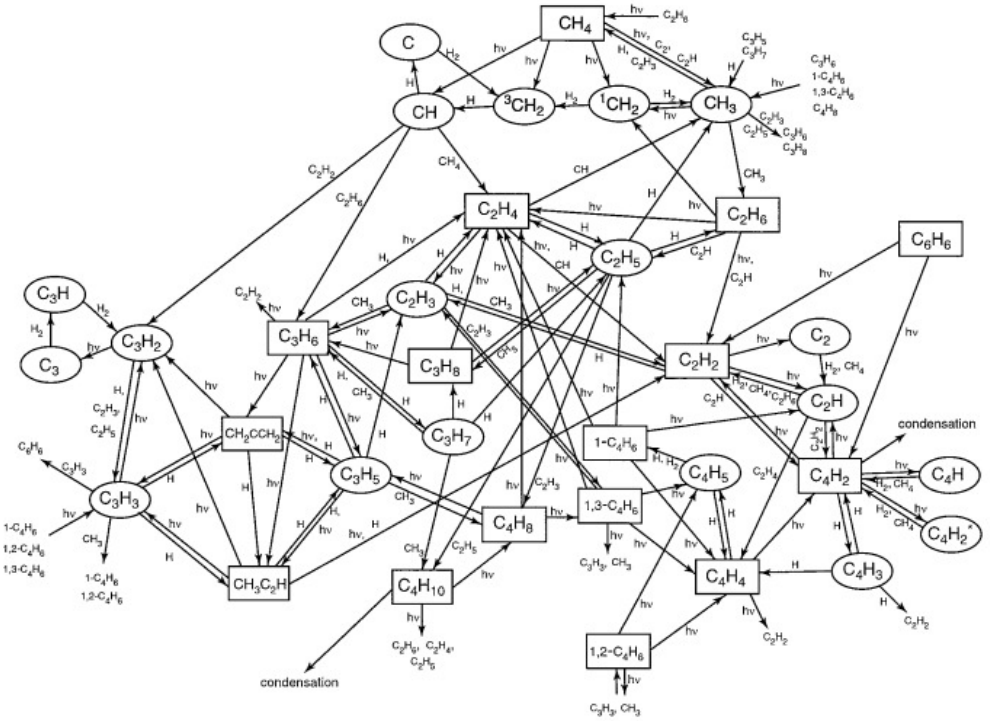

Figure 1.1: The chemical and photochemical reaction schemes for hydrocarbons (up to C_6 compounds) using in a photochemical model (Figure 3 of Moses et al. [2000]). 'hν' signifies an ultraviolet photon. Radical species are outlined as ovals while neutral compounds are outlined as rectangles.

Here, M is a catalyst molecule. Given the sheer number of molecules that can form from recombination of photochemical radicals, which themselves can be photolysed, the photochemistry of Saturn's stratosphere is highly complex. Figure 1.1 shows the reaction scheme used in a photochemical model of Saturn's stratosphere [Moses et al., 2000]. The photochemistry produces an extensive range of higher-order hydrocarbons, even aromatic hydrocarbons like benzene. However, ethane (C_2H_6) and acetylene (C_2H_2) were first detected [Moos and Clarke, 1979; Tokunaga et al., 1975]: as relatively abundant by-products, they are highly observable. These hydrocarbons emit strongly at infrared wavelengths and are thus important species in the radiative balance of the stratospheres of giant planets in general [Yelle et al., 2001]. Only in more recent observations with more sophisticated

instruments have other photochemical species been detected. For example, detections of ethylene (C_2H_4) were initially ambiguous [Encrenaz et al., 1975] due to the low spectral resolution of observations available in 1974. However, the development of instruments with a high spectral resolving power such as the ISO-SWS (the Short-Wavelength Spectrometer on the Infrared Space Observatory, de Graauw et al. 1996), the TEXES instrument (Texas Echelon Cross Echelle Spectrograph, Lacy et al. 2002) and the Celeste spectrograph [Jennings et al., 2009; Moran et al., 2007] have allowed the detection and study of minor species such as ethylene, propane (C_3H_8), methlyacetylene (C_3H_4) and diacetylene (C_4H_2) [Bezard, 1998; Bézard et al., 2001; Greathouse et al., 2006; Hesman et al., 2012].

1.3.2 Vertical distributions of hydrocarbons

Observations of the spectral features of hydrocarbons probed a limited altitude range in the stratosphere when the planet is viewed in nadir. In modelling the observed spectral features of hydrocarbon species, earlier studies were only able to determine the concentration or volume mixing ratio of a hydrocarbon molecule at a single pressure level. This method applied to observations of hydrocarbon spectral features in different regions of the electromagnetic spectrum, which probed different pressure levels, provided initial clues of the vertical distributions of photochemical species. For example, Courtin et al. [1984] and Noll et al. [1986] used thermal infrared spectra of C_2H_2 and C_2H_6 emission which is most sensitive to the lower stratosphere (at approximately the 1 mbar level) while Winkelstein et al. [1983] used ultraviolet observations which were most sensitive to the upper stratosphere (at approximately the 10^{-3} mbar level). The development of photochemical models have allowed the full vertical distributions of photochemical species to be modelled. Figure 1.2 shows the vertical distributions of CH_4, C_2H_2, C_2H_6, C_2H_4, C_3H_8, CH_3C_2H, C_4H_2 and C_6H_6, as predicted by a photochemical model presented in Moses et al. [2000].

Ultraviolet photolysis is strongest in the upper stratosphere at pressures of approximately

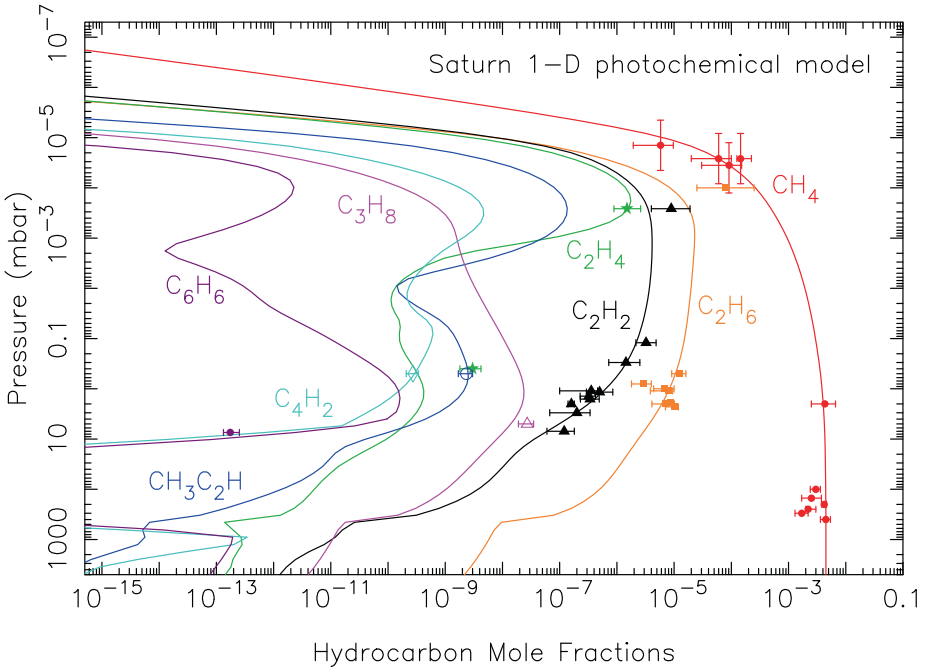

Figure 1.2: Vertical profiles of CH_4 (red), C_2H_6 (orange), C_2H_2 (black), C_2H_4 (green), C_3H_8 (light purple), CH_3C_2H (blue), C_4H_2 (cyan) and C_6H_6 (benzene) as predicted by Moses et al. [2000]. Data points with error bars show concentrations derived from Voyager-IRIS observations [Courtin et al., 1984], UVS (Ultraviolet Spectrometer) observations [Smith et al., 1983] and a reanalysis of ISO-SWS observations [Moses et al., 2000]. (Figure 5.5 of Esposito and Krimigis [2009]).

1 μbar leading to the fastest production rates of higher-order hydrocarbons at this level. Short wave radiation is strongly attenuated by Saturn's atmosphere and thus production rates decrease with higher pressures. Hydrocarbons produced by the photochemistry in the upper stratosphere are transported to the lower stratosphere initially by molecular diffusion and then by eddy mixing below the homopause of each species. This gives rise to large vertical gradients in the concentrations of photochemical by-products, as demonstrated in Figure 1.2.

1.4 Variability in Saturn's stratosphere

The variability of Saturn's stratosphere is the main theme of this thesis. Using the findings of previous studies, this Section presents an hypothesis of processes in the stratosphere of Saturn which are likely to produce variability in temperature and composition that may be observed.

1.4.1 Radiative processes

Saturn experiences seasons like Earth and thus each hemisphere undergoes a heating and cooling as the subsolar latitude moves north and south of the equator. A number of earlier studies presented radiative climate models of Saturn's stratosphere to support the interpretation of Voyager observations of Saturn in 1980 (for example, Cess and Caldwell [1979], Carlson et al. [1980], Bézard and Gautier [1985]). These earlier models were however very simple and computed with the little knowledge of the properties of the stratosphere known at the time. For example, the vertical distributions of C_2H_2 and C_2H_6 were not well known at this time and these hydrocarbons are highly significant in the radiative balance of the stratosphere.

In this thesis, the radiative climate model computed by T. Greathouse was used to predict the magnitude of temperature changes in the stratosphere as a result of changes in solar insolation alone. This model was first presented in Fletcher et al. [2010], who compared its results with observed temperature changes determined from Cassini-CIRS observations acquired from 2004 to early 2009. The model adopts a multi-layer radiative transfer treatment to compute heating by absorption of sunlight by CH_4 gas and cooling via the emission bands of CH_4, C_2H_2, C_2H_6 as well as emission induced by H_2-H_2, H_2-He and H_2-CH_4 collisions. In addition, the attenuation of sunlight by Saturn's rings and the effects of orbital eccentricity were included. In contrast to earlier models, T. Greathouse computed

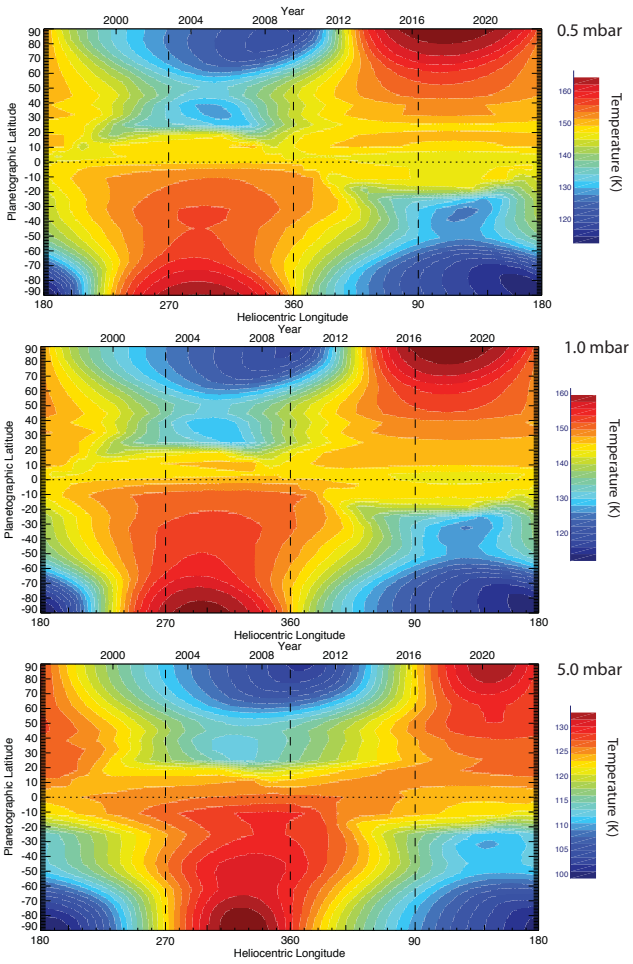

Figure 1.3: Meridional and temporal variations of temperature predicted by a radiative climate model by T. Greathouse at 0.5 mbar, 1.0 mbar and 5.0 mbar. The dashed vertical lines mark the positions of solstices and equinoxes.

the model using two different sets of meridional distributions of C_2H_2 and C_2H_6 derived from observations. The first set were derived from IRTF-TEXES observations in 2002 [Greathouse et al., 2005] and the second set were derived from limb-viewed Cassini-CIRS observations in 2005/2006 [Guerlet et al., 2009]. In both distributions, the vertical profiles

of C_2H_2 and C_2H_6 reflect those of Moses et al. [2000], which were used as initial guesses in their respective analyses. This model does however hold these concentrations (both vertical and meridionally) as fixed over the entire Saturnian year. As demonstrated later in this thesis, the concentrations of acetylene and ethane at the 1-2 mbar level vary with time due to dynamical motion. However, this model by T. Greathouse best parameterises the known radiative processes that affect Saturn's stratospheric temperatures at present.

Figure 1.3 shows the predicted meridional and temporal temperature trends at three different altitudes in the lower stratosphere. In 2005, the model predicts an overall 40 K pole-to-pole contrast in temperature at the 1 mbar level, which is in good correspondence with Fletcher et al. [2007] and Guerlet et al. [2009] who probed temperatures at this altitude using Cassini-CIRS observations acquired at a similar time. At the 1 mbar level, temperatures in the southern hemisphere peak in approximately 2005/2006, over two years after southern summer solstice. This demonstrates the phase lag of Saturn's stratospheric temperatures to changes in the solar insolation. As shown in Figure 1.3, this phase lag is intuitively longer at higher pressures.

The magnitude of seasonal temperature changes predicted by the model were generally consistent with temperature changes found in Fletcher et al. [2010] where the evolution of temperature from 2004 to 2009 was determined from Cassini-CIRS observations. Polar and equatorial latitude were, however, the exception since these regions are host to strong dynamical forcing, as discussed in Section 1.4.3. From 2005 to 2012, mid-northern latitudes are expected to emerge from ring shadow and warm by approximately 10 K at the 1 mbar level. Over the same time period, mid-southern latitudes are expected to cool by approximately 12 K at the same altitude.

The contrasts in temperature changes during summer in each hemisphere should also be compared. Southern summer generally produces a larger warming in the southern hemisphere compared to northern summer in the northern hemisphere. Yet, at high

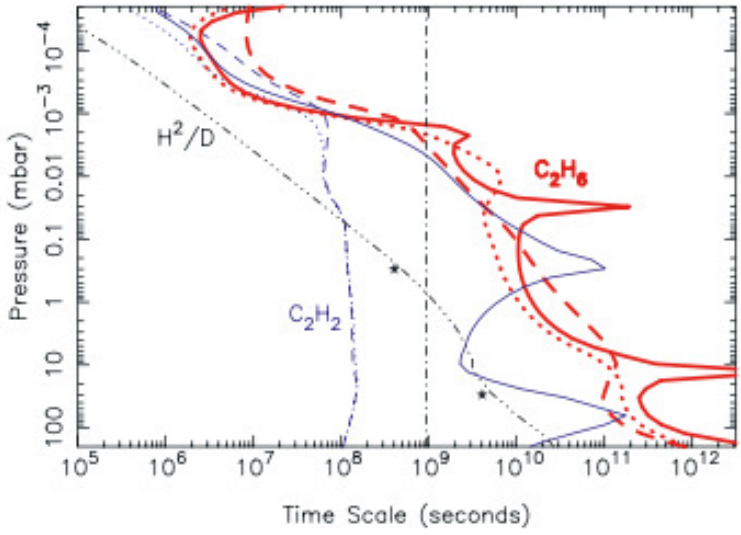

Figure 1.4: The calculated photochemical time constants (in seconds) for C_2H_2 (thin blue) and C_2H_6 (thick red) with height (mbar) in Saturn's atmosphere (Figure 7 of Moses and Greathouse [2005]). These have been calculated during southern summer solstice (L_s ~270°) at -36°S. Dashed lines indicate the photochemical loss timescales (n/L, where n is the species concentration (cm^{-3}) and L is the loss rate (cm^{-3} s^{-1})), dotted lines the production timescales (n/Q, where Q is the production rate) and solid lines indicate the net lifetime ($n/|Q-L|$). The vertical dot-dashed line is Saturn's orbital period (29.4 years). Stars show estimates of the meridional transport timescale and the triple dot-dashed line represents the vertical diffusion timescale.

latitudes, which undergo the largest changes in solar insolation, it is evident that northern summer appears to last longer than southern hemisphere. These two contrasts can be attributed to Saturn's orbital eccentricity and the occurrence of perihelion during southern summer and aphelion during northern summer.

1.4.2 Photochemical processes

A time-dependent model of Saturn's photochemistry was first presented in Moses and Greathouse [2005]. In particular, this model focused on how the concentrations of C_2H_2 and C_2H_6 ware modulated by changes in the solar insolation.

Figure 1.4 shows the predicted photochemical lifetimes of C_2H_2 and C_2H_6 as a function

of altitude. At 10^{-3} bar pressures, where photochemical reaction rates are fastest, the net photochemical lifetimes of both hydrocarbons are *short*: on the order of 10^7 s, which is approximately 0.5 (Earth) years. Thus, at this altitude, the abundances of these species respond to short term variations in the solar ultraviolet flux due to the season as well as the 11 year solar cycle, the shadow of Saturn's rings and Saturn's orbital eccentricity.

However, in the lower stratosphere at the 1 mbar level, photochemical lifetimes are much longer. The photochemical production and loss timescales of C_2H_2 at 1 mbar are approximately 10^8 seconds. However, the similarity of these two timescales essentially demonstrates that C_2H_2, although readily photochemically lost, is efficiently recycled and reproduced, as concluded in Moses and Greathouse [2005]. This effectively lengthens the net photochemical lifetime of C_2H_2 to approximately 90 years or three times longer than a Saturn year, as indicated in Figure 1.4. C_2H_6 is even more stable than C_2H_2 with a net photochemical lifetime of approximately 600 years or over 20 times longer than a Saturn year. Photochemical variations in C_2H_2 and C_2H_6 at higher altitudes where these species are less stable will also not propagate to the 1 mbar level since the vertical diffusion timescale at the 1 mbar level is comparable with the length of a Saturn year, as indicated in Figure 1.4.

Moses and Greathouse [2005] concluded that the concentrations of acetylene and ethane exhibit no temporal changes at the 1 mbar level as a result of photochemistry alone. Therefore, the concentrations of these species are expected to be maximum at the equator, where the most sunlight is received annually, and to decrease in concentration to higher latitudes. Any observed deviation from this predicted meridional trend or any temporal changes in concentration observed at a given latitude are likely to be the result of vertical motion associated with dynamics. As we will see, the thermal infrared observations used in this thesis probe C_2H_2 and C_2H_6 at approximately the 1 mbar level where these hydrocarbons, in particular C_2H_2, are predicted to exhibit strong vertical gradients (Section 1.3.2). Any

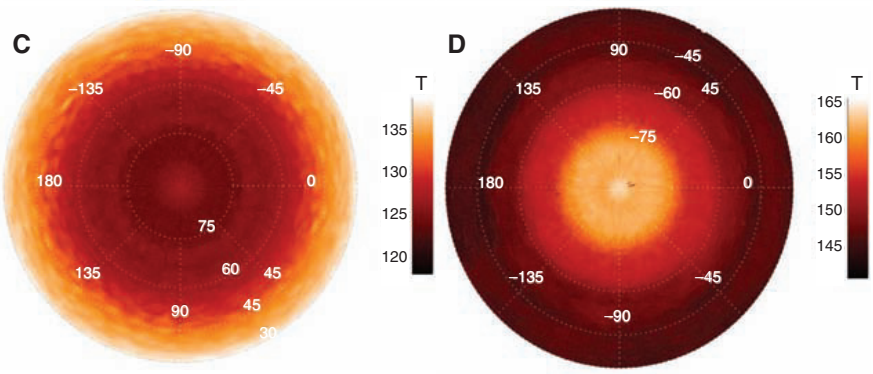

Figure 1.5: Orthogonal projections of Saturn's polar temperatures at 1 mbar in the northern hemisphere (left) and southern hemisphere (right), as shown in Fletcher et al. [2008].

vertical motion covering this altitude range will therefore yield an observable change in the concentrations of both species. For example, upwelling will advect air from higher pressures which is relatively depleted in hydrocarbon abundance. Thus, the concentration of acetylene and ethane in regions of upwelling would be observed to be lower in comparison to adjacent regions where there is no vertical motion. Or, the concentration of acetylene and ethane would be observed to decrease with time in the region host to upwelling. Similarly, downwelling would advect hydrocarbon-richer air. Thus, the concentration of acetylene and ethane would be observed to be larger in comparison to adjacent regions or an increase in concentration would be observed with time. Acetylene is predicted to exhibit a larger vertical gradient than ethane and therefore is expected to exhibit a larger change in concentration as a result of vertical motion.

1.4.3 Dynamical processes

1.4.3.1 Polar vortices

The south pole of Saturn was host to a polar vortex during southern summer. Thermal infrared observations made by Cassini's CIRS instrument revealed temperatures south of

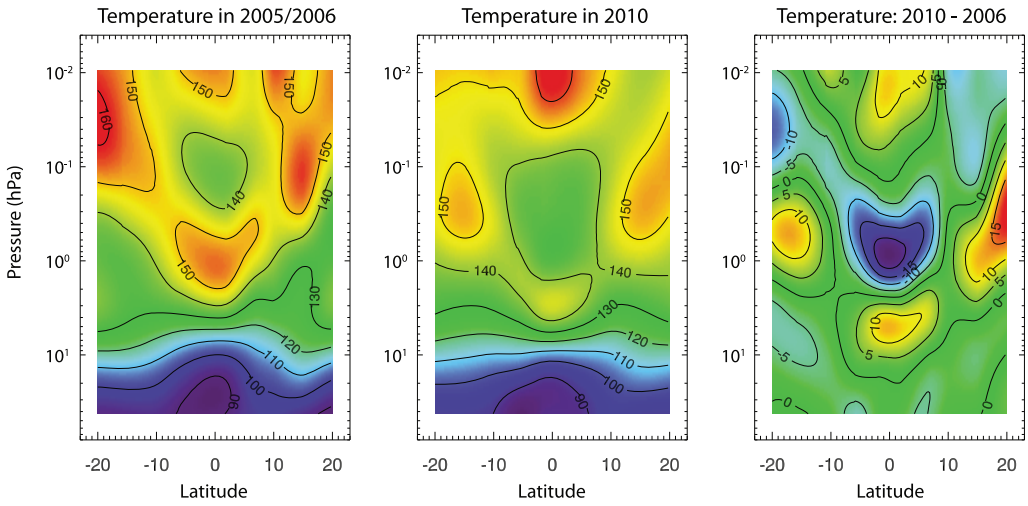

Figure 1.6: Latitudinal-vertical distributions of temperature retrieved from limb-viewed Cassini-CIRS observations in 2005 (left), 2010 (right) and their differences, as shown in Guerlet et al. [2011].

75°S to be considerably warmer with temperatures at the pole of greater than 160 K at the 1 mbar level (Figure 1.5). However, similar warm features at Saturn's northern pole were not observed at this altitude. Fletcher et al. [2008] concluded that these warm temperatures were a result of a polar vortex at Saturn's south pole. Parcels of air subsiding in this vortex are heated adiabatically as they are compressed at higher pressure yielding the observed warming. The presence of photoabsorbing aerosols providing localised heating at the 1 mbar level was also noted as a possible contributor to these warm temperatures.

The fact that warm temperatures associated with a polar vortex were only observed at Saturn's south pole indicates that the vortex only forms at the summer pole. In this thesis where the evolution of Saturn's stratosphere is investigated from 2005 to 2012, a dissipation of Saturn's south polar vortex was perhaps expected as the southern hemisphere moved into Autumn. The emergence of a northern polar vortex would also be expected as northern summer solstice approaches.

1.4.3.2 The equatorial oscillation

Saturn's equator is host to a wave-driven oscillation. Using Cassini-CIRS observations acquired in a limb-viewing geometry in 2005 and 2006, Fouchet et al. [2008] derived latitudinal-vertical temperature fields at low latitudes and showed vertically-alternating temperature minima and maxima associated with this oscillation (left panel of Figure 1.6). These results demonstrate that the oscillation modulates the temperature, and thus zonal wind, fields from 15°S to 15°N. Guerlet et al. [2009] also observed a local maxima in the meridional profiles of C_2H_2 and C_2H_6 at Saturn's equator in 2005 using the same limb-viewed Cassini-CIRS observations. This was attributed to downward vertical motion at this time advecting hydrocarbon-richer air from higher in the stratosphere. This perhaps indicates vertical motion associated with the oscillation that behaves in a way that is similar to that observed in oscillations on Earth. Baldwin et al. [2001] demonstrated that downward and upward motion occur at altitudes coinciding with temperature maxima and minima respectively in a quasi-biennial oscillation (QBO) on Earth.

The evolution of this oscillation has also been investigated in previous studies. By deriving brightness temperatures from CH_4 emission (7.8 μm) and C_2H_6 emission (12.2 μm) from several different thermal infrared datasets from 1980 to 2008, Orton et al. [2008] determined that the period of the oscillation was 14.7 years or approximately half a Saturn year, as demonstrated in Figure 1.7. Thus, the oscillation appears to be semiannual in period and has been described, and will be described throughout this thesis, as Saturn's semiannual oscillation or SSAO. Observations from the Cassini spacecraft have also tracked the most recent evolution of the oscillation from 2005 to 2010. From radio occultation measurements in 2005 and 2009/2010, the structure of the SSAO was seen to descend with a cooling of up to 18 K observed at the 1 mbar level. Guerlet et al. [2011] similarly deduced the evolution of the SSAO from limb-viewed Cassini-CIRS measurements acquired from 2005 to 2010. Figure 1.6 shows their retrieved latitudinal-vertical temperature distribu-

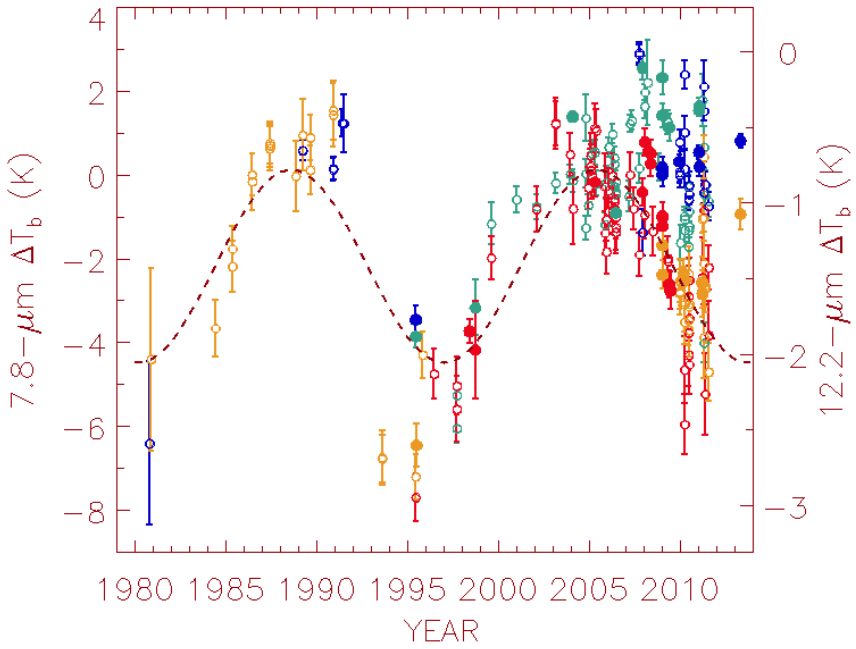

Figure 1.7: The difference in CH_4 (7.8 μm) brightness temperature between 15.5°N and 3.5°N (blue) and 15.5°S and 3.5°S (green) and C_2H_6 (12.2 μm) brightness temperature between 15.5°N and 3.6°N (orange) and 15.5°S and 3.6°S (red). Open and filled symbols indicate different observatories. This plot is Figure 3 of Orton et al. [2008] but has been updated to include more recent data.

tions in 2005/2006 and 2010. As shown, the temperature maximum at the 1 mbar level in 2005 has descended to a higher pressure in 2010 while a temperature minimum descends from above. Thus, there is a cooling of approximately 20 K at the 1 mbar level.

The SSAO was therefore considered responsible in interpreting any observed evolution at equatorial latitudes.

1.4.3.3 The beacon

A massive thunderstorm emerged in Saturn's northern (spring) hemisphere in December 2010. This feature was initially born in the troposphere but produced effects which penetrated into the stratosphere [Fischer et al., 2011; Fletcher et al., 2011; Sánchez-Lavega

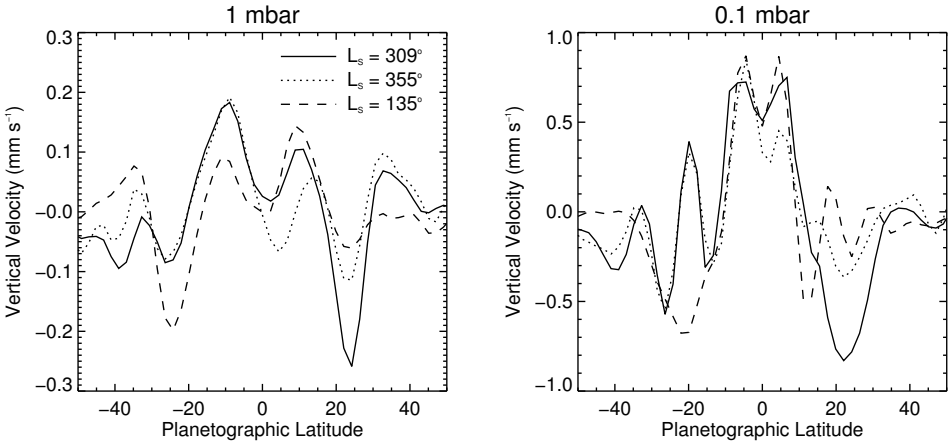

Figure 1.8: The vertical velocity as a function of planetographic latitude (left) and 0.1 mbar (right) at $L_s = 309°$ (solid), $L_s = 355°$ (dotted) and $L_s = 135°$, as predicted by a GCM of Saturn's stratosphere [Friedson and Moses, 2012].

et al., 2011]. Following the merger of two warm air masses in May 2011, a stratospheric vortex now dominates latitudes from 20°N to 50°N over a longitude range of approximately 80°. Downwelling within this vortex has adiabatically heated this region to temperatures as high as 180 K and strongly enhanced the concentrations of trace species such as C_2H_2 and C_2H_4 which were advected from hydrocarbon-richer, lower pressures [Fletcher et al., 2012; Hesman et al., 2012].

1.4.3.4 Meridional overturning

Polar, equatorial latitudes and mid-northern latitudes are known to be host to local dynamical processes. However, the overall hemispheric contrast in temperature observed in 2005 and predicted by a radiative climate model (Section 1.4.1) is likely to induce a larger-scale, hemisphere-to-hemisphere circulation in an effort of the atmosphere to redistribute heat from the summer hemisphere to the winter hemisphere.

Notable behaviour which might indicate the existence of large-scale circulation is an overall increase in the concentration of ethane with latitude in Saturn's southern hemisphere, as

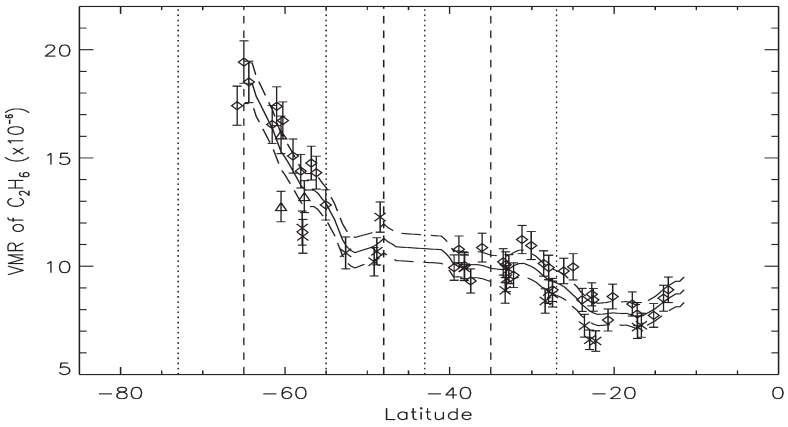

Figure 1.9: The volume mixing ratios of ethane at 2.0 mbar in Saturn's southern hemisphere, retrieved by Howett et al. 2007 using Cassini-CIRS observations in 2004. Diagonal crosses, triangles and diamond markers indicate MIRCMPST, COMPSIT and ISSPCKT datasets respectively.

shown in Figure 1.9. This feature has been by Greathouse et al. [2005] who used ground-based observations in 2002, by Howett et al. [2007] who used Cassini-CIRS COMPSIT ($\Delta\tilde{\nu} = 0.5$ cm^{-1}) observations in 2004 (shown in Figure 1.9) and Hesman et al. [2009] who determined this trend using both Cassini-CIRS and IRTF-Celeste observations in 2005/2006. Guerlet et al. [2009] also observed an increase but this was not significant with respect to the uncertainties on their results. The magnitude of increase in ethane's concentration differed with study however this can be attributed to the differing sources of C_2H_6 line date used in each study. While Greathouse et al. [2005] and Howett et al. [2007] used existing versions of the C_2H_6 line data available from the HITRAN database [Rothman et al., 2009], Guerlet et al. [2009],Hesman et al. [2009] have used an updated version of the line data [Vander-Auwera et al., 2007]. As detailed in Table 3.1, Vander-Auwera et al. [2007] line data for C_2H_6 is used in this work.

An observed meridional enrichment of ethane to higher-southern latitudes is in contrast with the poleward decrease in concentration that would be expected given the long photochemical lifetime of this species (Section 1.4.2). The observed deviation from this trend in

the southern hemisphere implies a large-scale dynamical mechanism at work. The fact that such a trend is exhibited only by ethane, and not acetylene, rules out many physical explanations. For example, general downwelling in the southern hemisphere or transport by meridional diffusion would enrich the concentrations of both hydrocarbons with latitude, as demonstrated in Moses et al. [2007]. Previous studies have concluded the presence of a meridional wind system which advects hydrocarbon-richer air from the equator to higher southern latitudes. In order to provide a meridional enrichment of ethane only, transport by this wind system must occur on a timescale longer than acetylene's photochemical lifetime but shorter than ethane's lifetime, suggesting the transport timescale is longer than 3 Saturn years. By symmetry, a similar wind system, and thus meridional enrichment of C_2H_6, would be expected in the northern hemispheres and the long lifetimes of C_2H_6 would imply this feature would remain observable irrespective of the season. Yet, such an enrichment in the northern hemisphere is not observed in 2005. This hemispheric asymmetry in ethane's meridional enrichment at this time implies that the mechanism producing it is seasonal in nature and must therefore act on a timescale more comparable with half a Saturn year (15 years approximately). The timescale of the mechanism producing this observed behaviour of ethane may be tested by tracking concentrations of ethane in both hemispheres.

In this thesis, the general circulation model (or GCM) presented in Friedson and Moses [2012] served as a hypothesis of the meridional circulation in Saturn's stratosphere. This model uses the OPGCM (Outer Planet General Circulation Model) code, which is an adaptation of 'CAM-3' (Community Atmosphere Model 3.1, Hurrell et al. [2006]) that was initially developed to model Earth's climate system. A similar scheme was also used to model the circulation in Titan's atmosphere [Friedson et al., 2009]. A previous challenge in producing 2D (latitudinal-vertical) dynamical models of the outer planet stratospheres was an adequate parameterisation of 3D processes such as eddies [Friedson et al., 1999; Liang et al., 2005]. Friedson and Moses [2012] uses the Plumb & Mahlman method [Plumb

and Mahlman, 1987] which best allows 3D processes such as eddies to be represented in zonally-averaged simulations. However, this method is not valid at high latitudes: results of this GCM were only presented from 50° to 50°N. At short wavelengths ($\lambda < 5\mu$m), the radiative transfer model implemented CH_4 opacity and opacities from upper tropospheric (2000 mbar to 200 mbar) and stratospheric (50 mbar to 24 μbar) haze layers assuming observationally-constrained particle sizes and refractive indices from Karkoschka and Tomasko [2005]. At longer wavelengths, opacities due to H_2-H_2, H_2-He collisions, PH_3, CH_4, C_2H_2, C_2H_4, C_2H_6 were included. The effects of Saturn's ring shadow were also included in the radiative transfer model. The meridional distributions of C_2H_6 and C_2H_2 were assumed from Guerlet et al. [2009] but held fixed in the model. perihelion

Figure 1.8 shows the vertical velocities predicted at the 0.1 mbar and 1 mbar levels predicted by this GCM in three different seasons. At $L_s = 309°$ (*shortly* after southern summer solstice), the model shows upwelling from 20°S to 5°S with the strongest upwelling centred on approximately 10°S. As discussed in Friedson and Moses [2012], this upwelling produces cross-equatorial meridional flow and pronounced subsidence at 25°N. Upon approach to the vernal equinox ($L_s = 355°$), upwelling at 10°S at 1 mbar remains mostly constant while subsidence at 25°N begins to weaken. At $L_s = 135°$ (*shortly* after northern summer solstice), the direction of this circulation has reversed with general upwelling from approximately 10°N to 15°N and strong subsidence centred at 25°S, at 1 mbar. This pattern of upwelling in the summer hemisphere, cross-equatorial flow and subsidence in the winter hemisphere is described as *seasonally-reversing Hadley circulation*. This circulation is weaker in northern summer than in southern summer due to the hemispheric asymmetry in seasonal forcing as a result of Saturn's orbital eccentricity ($e \approx 0.055$) and the occurrence of perihelion during summer. This Hadley circulation is therefore likely to dominate the circulation at low latitudes. The lack of confidence in the GCM results at higher latitudes prevents a comparison of observed and modelled behaviour in these regions.

1.5 Summary

Observed and modelled results from previous literature indicate a wealth of processes that make Saturn's stratosphere highly variable with time. The evolution of stratospheric temperatures was investigated at equatorial latitudes from 2005 to 2010 (Section 1.4.3.2) and global temperature changes with season have also been observed from 2004 to early 2009 (Section 1.4.1). However, with the exception of the recent focus on the beacon in the northern hemisphere from 2011 onwards (Section 1.4.3.3), seasonal temperature changes in Saturn's stratosphere beyond the spring equinox in August 2009 are yet to be investigated.

In addition, previous studies have only provided a snapshot of the distributions of acetylene and ethane. As discussed in Section 1.4.2, these are predicted to be photochemically invariant with season at the 1 mbar level where photochemical and diffusive timescales are longer than a Saturn year. Thus, observed changes in concentration of these species is can only be explained by vertical motion as a result of dynamics. In this thesis, C_2H_2 and C_2H_6 were therefore used as chemical tracers of vertical motions. By simultaneously tracking the evolution of temperature and the concentrations of these species from thermal infrared observations, this work aims to investigate variability in Saturn's stratosphere over the course of a season and from year-to-year.

1.6 Thesis overview

Chapter 2 provides an overview of the Voyager-IRIS and Cassini-CIRS datasets used in this thesis (and tables of the CIRS datasets are presented in Appendix A). A radiative transfer model and the analysis procedure used to determine the vertical temperature profile and concentrations of acetylene and ethane from these observations is presented in Chapter 3.

These properties are initially determined from Cassini-CIRS observations acquired in 2005 and the results compared with previous studies (Chapter 4). Subsequently, Cassini-CIRS observations from 2005 to 2010 are analysed in Chapter 5 in order to assess variability over this time period. Chapter 6 aims to determine the extent of interannual variability by comparing results derived from Voyager-IRIS observations in 1980 with Cassini-CIRS observations in 2009 and 2010 that capture Saturn in the same season but one *year* apart. Observations performed by the ground-based Celeste spectrograph in 2012 are reduced and calibrated in Chapter 7. This involves modelled transmission spectra of Earth and dayside spectra of Venus and Mars: these models are shown in Appendix B. An analysis of these observations in addition to Cassini-CIRS observations in 2012, is presented in Chapter 8 in order to determine the most recent evolution of Saturn's stratosphere.

Chapter 2

Thermal infrared observations of Saturn from Voyager and Cassini

In order to assess the extent of variability in Saturn's stratosphere, infrared datasets which sample the planet at many different seasonal phases were required. This chapter serves as an introduction of the thermal infrared datasets available from the Voyager and Cassini spacecraft which are analysed later in this thesis to determine seasonal and interannual variability.

2.1 Voyager-IRIS

2.1.1 The Voyager Mission

The Voyager mission has provided, and continues to provide a wealth of knowledge of the properties of our Solar System and beyond. The mission refers to twin probes, Voyager 1 and Voyager 2, which were launched from Cape Canaveral, Florida in 1977. Following successful flybys of Jupiter and Saturn, the mission was extended to explore the outer solar system and Voyager 2 remains the only spacecraft to have observed the ice giants Uranus and Neptune. Voyager 1 is believed to have entered interstellar space in August 2012 [Burlaga et al., 2013] and, in April 2013 (only a few months prior to the writing of this thesis), became the most distant man-made object from Earth beating Pioneer 10, which had previously held this record.

The scientific payload of both Voyager probes feature a variety of *in-situ* and remote

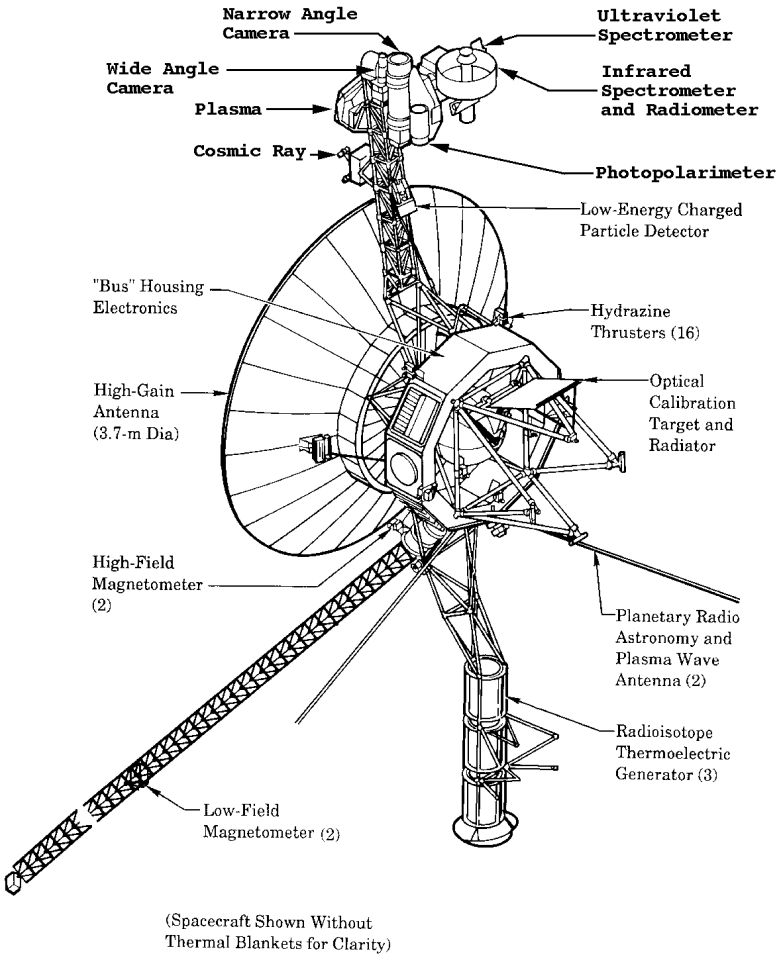

Figure 2.1: A schematic of the various remote sensing and *in situ* instruments aboard the Voyager 1 and Voyager 2 spacecraft.

sensing instruments. The Cosmic Ray Sub-system (CRS), Low-Energy Charged Particles (LECP), Magnetometer (MAG), Plasma Science (PLS) and Plasma Wave Subsystem (PWS) form the set of instruments designed for *in-situ* measurements of the magnetic and plasma fields of a planet. The Infrared Interferometer Spectrometer (IRIS), Imaging Science System (ISS), Planetary Radio Astronomy Investigation (PRA), Photopolarimeter System (PPS), Radio Science System (RSS) and the Ultraviolet Spectrometer (UVS) form the remote-sensing payload of the spacecraft. Figure 2.1 shows a schematic of the

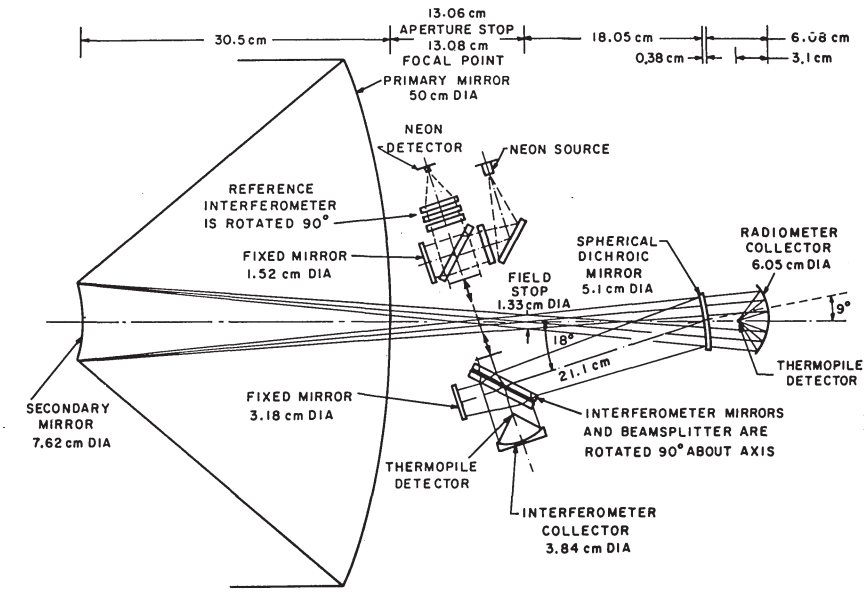

Figure 2.2: A schematic of the IRIS instrument on both Voyager 1 and Voyager 2 spacecraft. Credit: [Hanel et al., 1980]

Voyager spacecraft and the positions of the above instruments on board. In this thesis, I use the infrared observations of Saturn acquired by the IRIS instrument.

2.1.2 The IRIS instrument

The IRIS instrument provided observations of Saturn in an effective spectral range from 180 cm^{-1} to 2500 cm^{-1} at an apodized spectral resolution of 4.3 cm^{-1}. Figure 2.2 shows a schematic of the IRIS instrument. A 50 cm Cassegrain telescope with a field-of-view of 0.25° focuses light from the target upon a dichroic mirror. This divides the radiation into a visible/near-infrared (0.33 - 2 μm) and a thermal infrared component (>2.5 μm) which are then incident on a single channel radiometer and Michelson interferometer, respectively.

In the interferometer, a dieletrically coated Caesium Iodide substrate splits the incident infrared component to a moving and stationary mirror which is subsequently superimposed

for interference. An auxiliary interferomter splits a 0.59 μm neon source for reference. A thermopile records the signal and each interferogram represents an integration time of 45.6 seconds.

2.1.3 Voyager-IRIS observations of Saturn

The encounters with Saturn of Voyager 1 and 2 occured in November 1980 and August 1981 respectively. Both spacecraft began acquiring spectra of Saturn as early as 3 weeks before their closest approach with the planet where the disc of the planet was just filling the field-of-view of the IRIS instrument. While Voyager 2 generally viewed the planet in its ecliptic plane, Voyager 1's trajectory onwards to Saturn's moon, Titan, took it slightly north of Saturn's ecliptic plane. In both spacecraft, a north-south mapping procedure was conducted where the IRIS detectors were scanned on the sub-spacecraft meridian and the rotation of Saturn was used to obtain longitudinal coverage. In addition to on-target observations, deep-space observations were performed periodically for use as radiance calibration and in order to characterise the sensitivity of the instrument.

Raw observations are acqiured initially as interferograms. Their calibration by the IRIS pipeline involves an initial symmetrisation of interferograms in order to correct for the fact that they are not sampled at zero path difference and to also remove the asymmetry due to residual dispersion in the beamsplitter and compensator. The symmetrized interferograms were then apodized using a Hamming function and have been cosine-transformed to produce spectra. The responsivity obtained from the deep-space observations and knowledge of the instrument temperature are then used to obtain calibrated radiances. In addition to target spectra, the noise-equivalent spectral radiance or NESR spectra of the IRIS instruments on both spacecrafft have been provided. These represent the standard deviation at each wavenumber of all deep-space observations acquired during the Saturn encounter. Figure 2.3 shows the NESR spectra of Voyager 1-IRIS and Voyager 2-IRIS. As shown, the

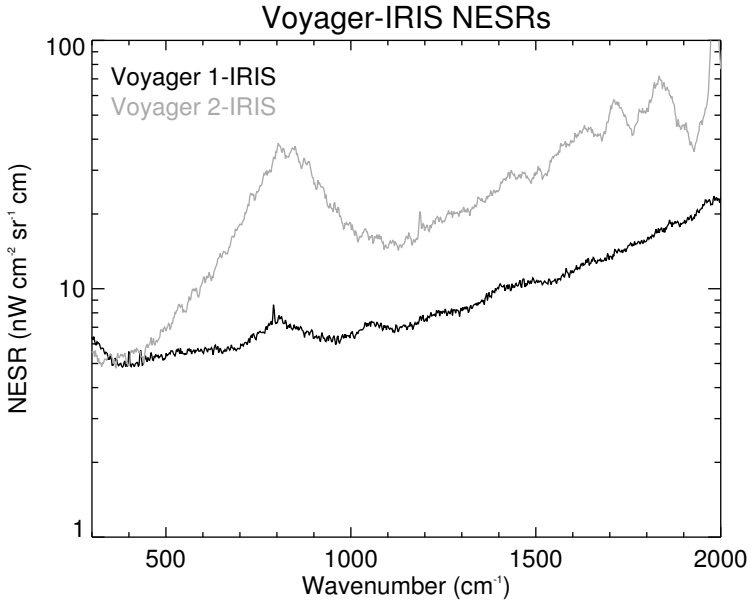

Figure 2.3: The noise-equivalent spectral radiance or NESR of the IRIS instrument in Voyager 1 (black) and Voyager 2 (grey), as provided by PDS Atmospheres Nodes.

NESR of Voyager 2-IRIS is considerably higher, in particular at higher wavenumbers: this is because of an interferometer misalignment which occured during the Saturn encounter [Hanel et al., 1982].

2.1.3.1 Selection of IRIS spectra

Calibrated IRIS spectra of Saturn from Voyager 1 and Voyager 2 were downloaded from the PDS Atmospheres Node[1], henceforth described as PDS. There were approximately 2990 and 1460 individual observations of Saturn from Voyager 1-IRIS and Voyager 2-IRIS, respectively, however a subset of these were deemed unsuitable for further analysis:

Calibration faults: Approximately 10% of IRIS spectra had been flagged by the database as poor quality due to there being too many remaining spikes in the interferogram, missing data in the interferogram, zero peaks in the interferogram, no data or issues with

[1] http://pds-rings.seti.org/voyager/iris/expanded_volumes.html

the symmetrisation described above. All such observations were discarded from further use.

Large field-of-view: The IRIS database includes observations which were acquired up to three weeks before the Voyager spacecrafts' closest approach to Saturn. At such long ranges from the planet, a large spatial region on the planet illuminate the IRIS detectors and such observations are unsuitable for the analysis presented in Chapter 6 where meridional variations in atmospheric properties aim to be resolved. In some cases, the instrument's field-of-view is illuminated both by deep space and the planet disk and so the resultant spectrum does not represent signal from the planet alone. Figure 2.4 shows an approximation of the viewing geometry of Voyager-IRIS on Saturn and demonstrates the correspondence of spacecraft range and the field-of-view of the instrument on the planet. In order to omit problematic observations as described above from further analysis and to yield observations with a desired field-of-view on the planet, spectra acquired beyond a cutoff spacecraft range from Saturn were removed. For example, using only bservations acquired within 17 R_s would achieve a latitudinal field-of-view of 1 - 2° (comparable with the Cassini-CIRS instrument introduced later in this Chapter) however an insufficient number of observations were acquired within such a range. In order to maintain an adequate number of observations for averaging in order to improve the signal-to-noise ratio whilst maintaining a reasonable latitudinal resolution, a spacecraft distance of ∼43 R_s, corresponding to an equatorial latitude range of 10° illuminating the detector, was chosen as the distance cutoff. Approximately 2500 Voyager 1-IRIS spectra and 2450 Voyager 2-IRIS spectra were acquired within such a distance.

2.1.3.2 Zonal averaging

A nominal assessment of the suitability of the remaining Voyager 1-IRIS and Voyager 2-IRIS spectra is presented here ahead of the analysis in Chapter 6.

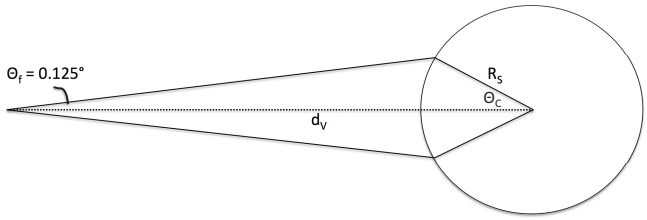

Figure 2.4: (Approximate) viewing geometry of the IRIS spacecraft on Saturn (with radius R_s) at a distance d_V from the planet. Θ_C represents the latitude corresponding to the field-of-view Θ_f.

In order to increase the signal-to-noise ratio of IRIS spectra for analysis, individual IRIS spectra were sorted into 10° planetographic latitude bins (with a Nyquist overlap of 5°) and coadded together. Latitude bins of this size were deemed suitable given the latitudinal field-of-view effectively chosen by the removal of observations acquired beyond a spacecraft range of 43 R_s described in the previous section. The resultant spectral noise on these coadds would normally be calculated by scaling the NESR spectrum by a factor of $1/\sqrt{N}+1/\sqrt{M}$, as demonstrated in Equation 2.1.

$$\begin{aligned}
\sigma_{\mathrm{coadd}}(\tilde{\nu}) &= \frac{1}{N}\sqrt{\sum_{i}^{N}\sigma_i^2(\tilde{\nu})} + \frac{1}{M}\sqrt{\sum_{i}^{M}\sigma_i^2(\tilde{\nu})} \\
&= \frac{1}{N}\sqrt{N\sigma_{\mathrm{nesr}}^2(\tilde{\nu})} + \frac{1}{M}\sqrt{M\sigma_{\mathrm{nesr}}^2(\tilde{\nu})} \\
&= \left(\frac{1}{\sqrt{N}} + \frac{1}{\sqrt{M}}\right)\sigma_{\mathrm{nesr}}(\tilde{\nu}) \qquad (2.1) \\
\sigma_{\mathrm{coadd}}(\tilde{\nu}) &\sim \frac{\sigma_{\mathrm{nesr}}(\tilde{\nu})}{\sqrt{N}} (\text{for } N << M) \qquad (2.2)
\end{aligned}$$

N is the number of target spectra coadded, M is the number of deep-space spectra used in the calibration, $\sigma_{\mathrm{nesr}}(\tilde{\nu})$ is the NESR spectrum of the IRIS instrument (Figure 2.3) and $\sigma_{\mathrm{coadd}}(\tilde{\nu})$ is the resultant noise on the coadded spectrum. IRIS observations are calibrated using a grand-average of deep-space observations, however, the number of deep

space spectra combined in this average was not available from the IRIS database. In the absence of such information and given the likelihood that far fewer target spectra are averaged than deep-space spectra ($N << M$), the noise of the coadded spectra has been estimated by scaling the NESR spectrum by a factor of $1/\sqrt{N}$ (Equation 2.2).

Figure 2.5 and 2.6 show the distributions of coadded spectra from Voyager 1-IRIS and Voyager 2-IRIS. As expected, the spectra from Voyager 2 appear noisier than those from Voyager 1 due to the misalignment of the interferometer in the former's flyby of Saturn. In terms of the signal-to-noise ratio, there was little/no advantage in combining Voyager 1-IRIS and Voyager 2-IRIS observations and thus the latter dataset was discarded. In Voyager 1-IRIS observations, features from Saturn's collision-induced spectrum (600 cm^{-1} to 700 cm^{-1}), the acetylene ν_5 ($\sim$730 cm^{-1}), ethane ν_9 ($\sim$820 cm^{-1}) and methane ν_4 ($\sim$1300 cm^{-1}) features are clearly visible. There is poorer signal-to-noise at high-northern latitudes since Voyager 1-IRIS captures Saturn at a solar longitude of $L_s \sim 8°$. High-northern latitudes are therefore in the depths of winter and are thus not bright in the thermal infrared. In addition, there were very few observations available to coadd north of 75°N. Results derived from observations north of 70°N should therefore be treated with caution. Similarly, results derived from the observations at 80°S, 65°S and 60°S will be treated with caution since, even though this region is bright in the thermal infrared in the aftermath of southern summer, it is unlikely that the signal-to-noise ratio has been increased sufficiently for analysis due to the lower number of coadds.

As shown, negative radiances are present in the observations, in particular at wavenumbers higher than 900 cm^{-1}. Given the fact that the NESR of the IRIS instrument (Figure 2.3) increases with higher wavenumber, the fact that the negative radiances are most occurent in latitude bands where fewer individual spectra have been coadded and the fact that negative radiances are most prevalent in the Voyager 2-IRIS dataset (which is noisier), it is highly likely that the negative radiances are simply a result of noise. However,

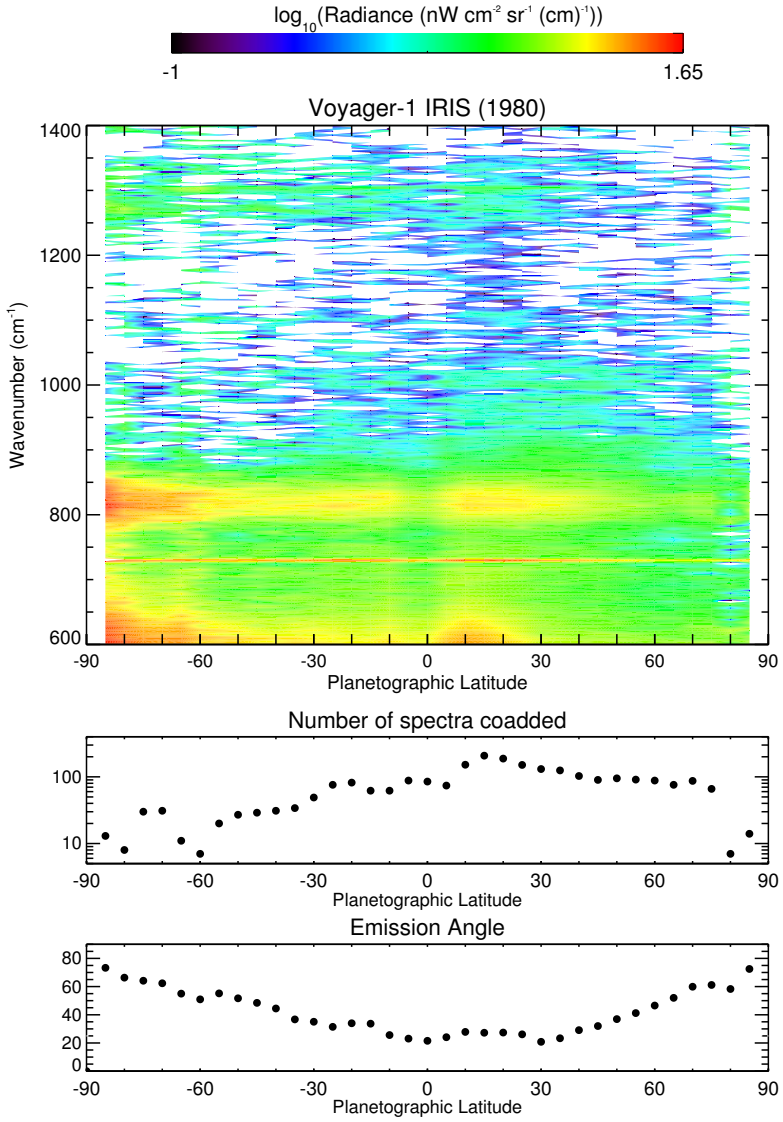

Figure 2.5: The Voyager 1-IRIS coadds: the spectra at a spectral resolution of $\Delta\tilde{\nu} = 4.3$ cm^{-1}, number of individual spectra coadded (middle) and the resultant emission angle (bottom) with planetographic latitude. White regions in the top plot indicate radiances which are negative.

negative radiances can also be produced by a thermal drift in the instrument temperature between acquiring target and deep-space observations. Thus, when the latter are used in the calibration of the former, the instrument's responsivity is improperly characterised

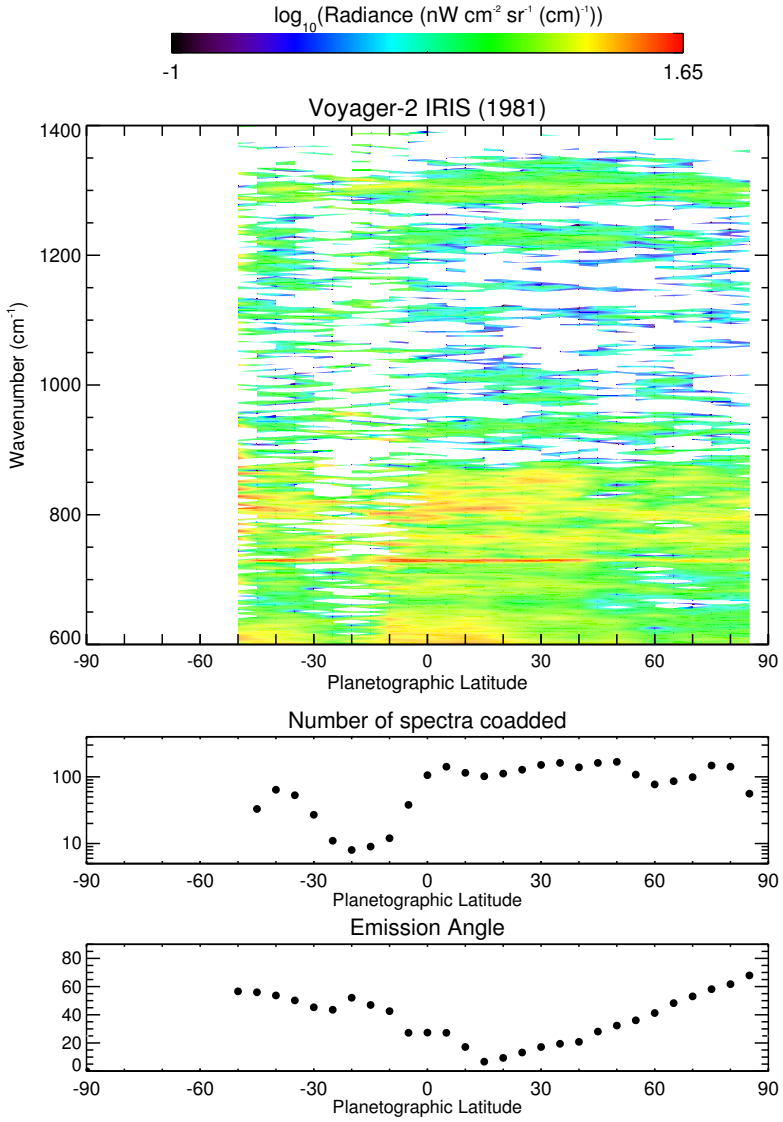

Figure 2.6: The Voyager 2-IRIS coadds: the spectra at a spectral resolution of $\Delta\tilde{\nu} = 4.3$ cm^{-1}, the number of individual spectra coadded (middle) and the resultant emission angle (bottom) with planetographic latitude. White regions in the top plot indicate radiances which are negative.

leading to baseline shifts in the target spectra. Negative radiances can be a result of baseline shifts in the spectrum, an issue which is also prevalent in Cassini-CIRS spectra (see Section 2.2.5). PDS does note a thermal drift in instrument temperature of up

to 0.2K/day during the Saturn encounter and so a thermal drift cannot be ruled out. However, in the absence of an obvious correction or an alternative means of calibration, the observations were analysed as they are presented in Figure 2.5.

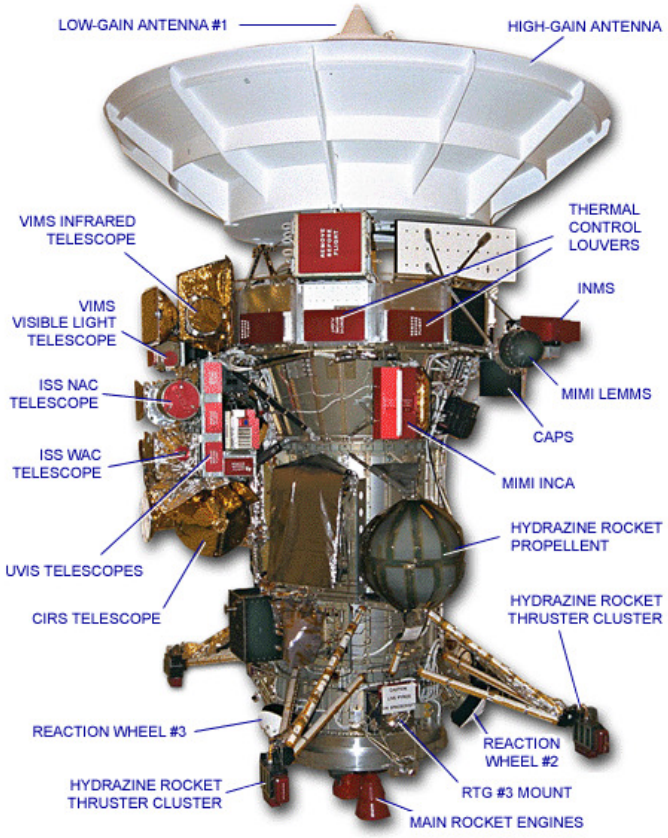

Figure 2.7: A schematic of the various remote sensing and *in situ* instruments aboard the Cassini orbiter.

2.2 Cassini-CIRS

2.2.1 The Cassini-Huygens Mission

Blasting off from Cape Canaveral, Florida in 1997, the Cassini-Huygens spacecraft started its 7 year journey to the Saturnian system. In 2000/2001, the spacecraft performed a gravity-assisted flyby of Jupiter and, in doing so, obtained observations of the largest gas giant. The spacecraft successfully entered Saturn's orbit on the 1st July, 2004 and began 4 years of initial data acquisition, which would later become known as the *prime mission*. In these four years, the spacecraft performed 74 orbits of Saturn, 45 flybys of Titan and

flybys of other large Saturnian satellites such as Enceladus, Phoebe, Dione, Rhea and Iapetus. The mission has fortunately been extended past its nominal four year lifetime. A two year extension, which became known as the *equinox mission*, was granted in order to observe Saturn at its vernal equinox in August 2009. The *solstice mission* describes the current extension to the Cassini mission where the planet will be observed up to its northern summer solstice in 2017.

The spacecraft was initially comprised of both an orbiter (Cassini) and probe (Huygens), both of which are host to a suite of instruments. The Huygens probe featured 6 instruments which obtained *in situ* measurements of Titan's surface, atmospheric compsition, structure and radiation fields: the Gas Chromatograph and Mass Spectrometer (GCMS), the Aerosol Collector and Pyrolyzer (ACP), the Descent Imager and Spectral Radiometer (DISR), the Huygens Atmospheric Structure Instrument (HASI), the Doppler Wind Experiment (DWE) and the Surface Science Package (SSP). Huygens is now longer operational and remains on the surface of Titan. The orbiter features 12 instruments, 6 of which are designed to perform in-situ measurements of Saturn's magnetic, dust and plasma fields - the Cassini Plasma Spectrometer (CAPS), the Cosmic Dust Analyze (CDA), the Ion and Neutral Mass Spectrometer (INMS), the Magntometer (MAG), the Magnetospheric Imaging Instrument (MIMI) and the Radio and Plasma Wave Science (RPWS). The remaining 6 instruments are designed for remote-sensing of atmospheres in the Saturnian system at various regions of the electromagnetic spectrum - the Composite Infrared Spectrometer (CIRS), the Imaging Science Sunsystem (ISS), the Ultraviolet Imaging Spectrograph (UVIS), the Visible and Infrared Mapping Spectrometer (VIMS), RADAR, and the Radio Science Subsystem (RSS). Figure 2.7 shows the location of all these instruments on the Cassini orbiter. In this thesis, I have used infrared observations acquired by the CIRS instrument.

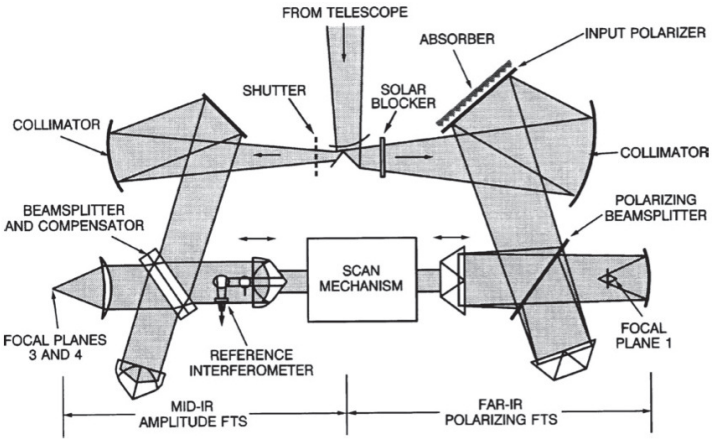

Figure 2.8: A schematic of the CIRS instrument. (Credit: Kunde et al. [1996])

2.2.2 The CIRS Instrument

The CIRS instrument aboard the Cassini orbiter is a remote-sensing Fourier transform spectrometer (FTS), which measured/continues to measure the thermal radiation from the Saturnian system. The instrument has an effective spectral range from 10 cm^{-1} to 1400 cm^{-1} and can operate at spectral resolutions as high as 0.5 cm^{-1} [Calcutt et al., 1992; Flasar et al., 2004; Kunde et al., 1996]. The CIRS instrument was designed and built by an international collaboration led by the NASA Goddard Spaceflight Centre and can be considered a successor of the IRIS instrument described in the previous section of this chapter.

Figure 2.8 shows a schematic of the CIRS instrument and the paths taken by radiation. A beryllium Cassegrain telescope consisting of a 50.8 cm paraboidal primary mirror and a 7.6 cm hyperboloidal secondary mirror, focuses light from the target into the instrument (at the top-centre of the Figure). The incoming radiation is then divided by a field-splitting mirror onto a mid-infrared and far-infrared interferometer. The mid-infrared interferometer (600 - 1400 cm^{-1}) is a Michelson interferometer which comprises the FP3

Specifications	Far-IR	Mid-IR	
Focal Planes	FP1	FP3	FP4
Interferometer type	Martin-Puplett polarising	Michelson	Michelson
Spectral Range (cm^{-1})	10 - 600	600 - 1100	1100 - 1400
Spectral Resolution (cm^{-1})	0.5 - 15.5	0.5 - 15.5	0.5 - 15.5
Integration time (s)	2 - 50	2 - 50	2 - 50
Detectors	Thermopile	PC HgCdTe	PV HgCdTe
Pixels	2	10	10
Pixel field-of-view (mrad)	3.9	0.273	0.273
Peak detectivity (cm $Hz^{1/2}$ W^{-1})	4 x 10^9	2 x 10^{10}	5 x 10^{11}

Table 2.1: Specifications of the far-infrared and mid-infrared components of the CIRS instrument aboard Cassini. 'PC' means photoconductive and 'PV' means photovoltaic.

and FP4 focal planes. The far-infrared FP1 interferometer (10 - 600 cm^{-1}) is a Martin-Puplett polarising interferomter. Table 2.1 details the specifications of all three focal planes and Figure 2.9 shows their NESR spectra. In this thesis, only observations of the FP3 and FP4 focal planes are used since they cover the spectral features used in the retrieval process described in Chapter 3.

2.2.3 CIRS Calibration

The reduction and calibration of CIRS observations is conducted using an established pipeline at the Goddard Space Flight Center. Interferograms of deep space and an internal shutter within the instrument, henceforth described as *calibration spectra*, are used as reference cold and warm sources for characterising the spectral response of the instrument and for conducting the intensity calibration. The corrected interferograms are then cosine-transformed into infrared spectra and apodised with a Hamming function of width appropriate for the spectral resolution of the observation. These spectra are available in a series of binary tables which can be extracted using the Vanilla database tool (provided by L. Fletcher and other members of the CIRS analysis team).

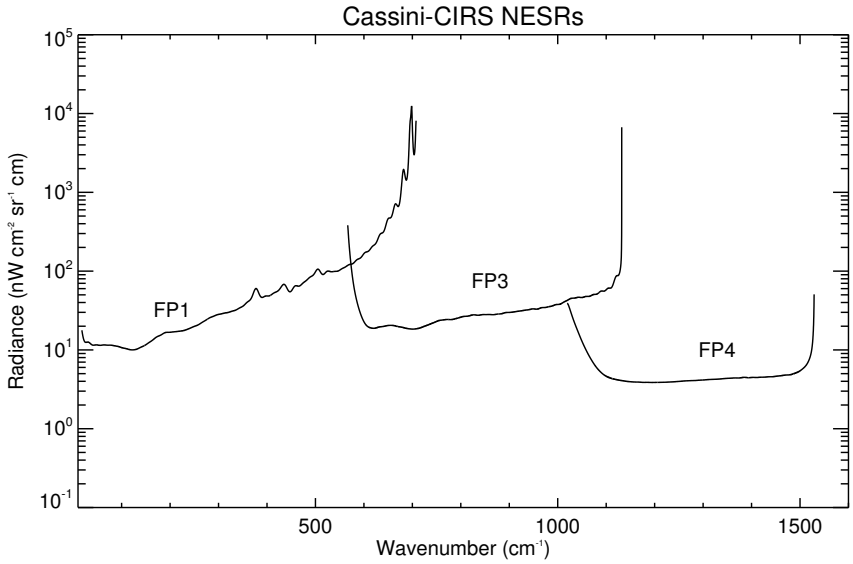

Figure 2.9: The NESRs (noise-equivalent spectral radiances) of the FP1, FP3 and FP4 focal planes when operating at a spectral resolution of $\Delta\tilde{\nu} = 0.5$ cm^{-1}. These spectra represent the standard deviation of all deep-space observations obtained during the spacecraft's cruise to Saturn.

The calibration of CIRS observations is under constant revision. There also exists different versions of CIRS spectra that have been calibrated using a different sampling of deep-space spectra and also where a phase correction has been applied to the interferograms. The v3.2, v4.2 and v4.3 calibration versions are used in this thesis and are described in further detail in Section 2.2.5 where calibration issues are discussed.

2.2.4 CIRS observations of Saturn

2.2.4.1 Observing Modes

The CIRS instrument can operate in several different observing modes which offer different advantages and disadvantages depending on the scientific goal. These are described below and Tables A.1, A.2, A.3 and A.4 lists all observations of Saturn in these modes from 2004 to 2013.

Compositional mapping or COMPSITs: This mode represents the highest spectral resolution (FWHM = 0.48 cm^{-1}) offered by the CIRS instrument. In order to maximise the signal-to-noise ratio when operating at this spectral resolution, long integrations are performed with the Cassini spacecraft positioned at a further orbital distance from the planet (typically 50 - 60 R_s). At such spacecraft distances, the latitudinal field-of-view of the far-IR and mid-IR focal planes are 10° and 0.8° respectively. Individual COMPSIT observations will generally 'sit-and-stare' on a particular latitude band and the rotation of the planet is used to build up longitudinal coverage. The higher spectral resolution of COMPSIT observations are obviously advantageous in resolving smaller features in the infrared spectrum of Saturn including those from isotopes thus allowing isotopic ratio such as the CH_4/CH_3D ratio to be determined.

Medium resolution mapping or MIRMAPs: Operating at a spectral resolution of 2.5 cm^{-1}, the detector arrays focus on a latitude band on the central meridian and spectra are obtained whilst the planet rotates underneath the spacecraft. The spacecraft is positioned at ∼30 R_s from the planet which results in a field-of-view of 1-2° in latitude. MIRTMAPS are very similar to MIRMAPs except the detector arrays are stepped across several latitude bands in one observation.

Low resolution mapping or FIRMAPs: FIRMAPs represent the lowest spectral resolution offered by the CIRS instrument (FWHM = 15.5 cm^{-1}). The detector arrays are scanned north-south on the planet's central meridian and the rotation of Saturn is used to build up longitudinal coverage. As with MIRMAP observations, a latitudinal field-of-view of 1-2° is achievable in the FP3 and FP4 focal planes.

2.2.4.2 Coaddition

CIRS spectra are individually too noisy for analysis and thus coaddition (or averaging together) of individual spectra over space and/or time is required. Given the 1-2° latitu-

dinal field-of-view of the FP3 and FP4 focal planes, CIRS observations can be sorted and coadded into 2° planetographic latitude bins. Thus, such coadded observations or *coadds* represent zonal averages of the planet over a 2° latitude range. Individual observations could additionally be coadded over time as well as latitude. For example, in Hurley et al. [2012], COMPSIT observations from 2005 to 2009 were averaged together in 2° latitude bins in order to increase the signal-to-noise ratio to the high levels required for their analysis. However, in this thesis, temporal averaging has been avoided in order to best resolve variability in Saturn's atmosphere over time.

In this coaddition procedure, the resultant noise of the spectrum is calculated by scaling the NESR spectrum (Figure 2.9 as in Equation 2.3).

$$\sigma_{\mathrm{coadd}}(\tilde{\nu}) = \sigma_{\mathrm{NESR}}(\tilde{\nu}) \left(\frac{1}{\sqrt{N}} + \frac{1}{\sqrt{M}} \right) \left(\frac{0.5 \text{ cm}^{-1}}{\mathrm{FWHM}} \right)^{1/2} \left(\frac{50\mathrm{s}}{\Delta t} \right)^{1/2} \tag{2.3}$$

The first scale factor represents the improvement to the signal-to-noise ratio by the coaddition of N target spectra which each have been calibrated using M deep-space spectra. The NESR spectra shown in Figure 2.9 describe the sensitivity of the instrument when operating at a spectral resolution of $\Delta\tilde{\nu} = 0.5$ cm^{-1} where each target interferogram is integrated for a time $\Delta t = 50$s. Thus, the latter two scale factors adjust the NESR spectrum for observations acquired with a different spectral resolution and integration time.

2.2.4.3 Latitudinal-temporal distribution of CIRS observations

One goal of this project is to determine the variability in Saturn's atmosphere with time over the course of the Cassini mission. Ideally, observations (upon coaddition into latitude bands) should yield an adequately high signal-to-noise ratio for analysis whilst continuing to exhibit a sufficiently high temporal sampling such that seasonal changes on the planet may be resolved.

A nominal inspection of FP4 observations of the observing modes described in Section 2.2.4.1 was conducted in order to determine which dataset might best suit the goal of this project. All individual COMPSIT, MIRMAP and FIRMAP observations (as detailed in Appendix A) were sorted into 2° planetographic latitude bins. Thus, such spectra only represent a zonal coadd at the time each observation was taken. Spectra from the v4.2 calibration release (where up to 4000 deep-space observations have been used in the calibration of each target spectrum) were used such that the signal-to-noise ratio on the target spectra is proportional to the number of target spectra acquired.

Figure 2.10 shows the latitude-temporal distribution of these observations. As shown, COMPSIT observations have generally focused on equatorial-to-mid latitudes with less sampling at high latitudes, in particular after 2010. The emission angles of COMPSIT observations are generally greater than 40°, which is advantageous in the retrieval of trace species such as CH_4, C_2H_2 and C_2H_6 as their spectral features are more prominent at higher emission angles where the contribution of the tropospheric continuum is reduced. In a particular latitude band over time, coadds have very similar emission angles which also means observations/results in different years can be directly compared since differences in the emission angle can be ruled out as a cause of any observed variability with time. However, as is expected given their higher spectral resolution, the signal-to-noise of these spectra (even after coaddition into 2° latitude bands) is poor ($\sim$10).

MIRMAP observations have similarly focused on low-to-mid latitudes. MIRMAPs can approximately be divided into three groups temporally - 2005/2006, 2007/2008 and 2010 onwards. In comparison to COMPSIT observations, the signal-to-noise ratio in these observations is higher (up to 100) with exception at high-northern latitudes which were captured in late winter. Emission angles are at a minimum at the equator and generally increase with latitude. FIRMAP observations exhibit the most regular sampling of Saturn with latitude and time. Whilst sacrificing spectral resolution, the signal-to-noise ratio

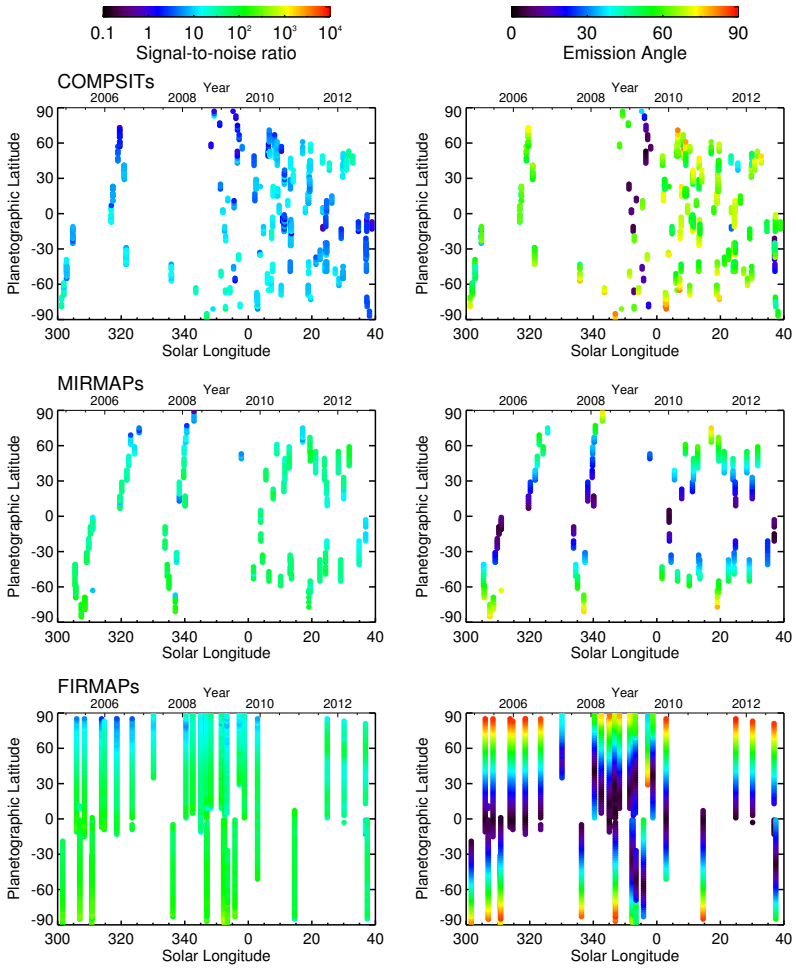

Figure 2.10: The distribution of COMPSITs (top), MIRMAPs (middle) and FIRMAPs (bottom) with planetographic latitude and time. Left-hand plots show 2° planetographic latitude coadds coloured according to the signal-to-noise ratio in the methane band (1230 cm^{-1} to 1380 cm^{-1}) as indicated in the colour bar. Right-hand plots show the same but for emission angle.

of 2° coadds is generally very high (∼100) with again the exception of high-northern latitudes. Observations are also minimum in emission angle at the equator and increase with latitude and so observations within a latitude band can be directly compared in different years.

Due to their high signal-to-noise ratio and regular temporal sampling, FIRMAP observa-

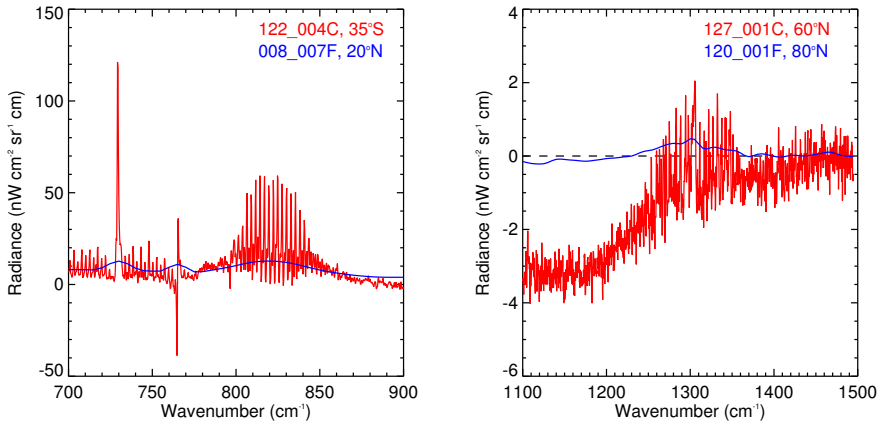

Figure 2.11: Low-resolution ($\Delta\tilde{\nu} = 15.5$ cm^{-1} in blue) and high-resolution ($\Delta\tilde{\nu} = 0.5$ cm^{-1} in red) examples of CIRS spectra of Saturn containing electrical spectral spikes (left) and negative radiances, indicating a negative baseline shift (right). The observation names and (planetographic) latitudes are shown, as summarised in Appendix A.

tions were deemed the most suitable dataset for resolving temporal changes in Saturn's atmosphere.

2.2.5 Calibration Issues

Whilst the CIRS calibration pipeline has been developed to best remove unphysical features in the target spectrum as a result of instrumental artefacts, some features continue to remain. Spectral spikes and baseline shifts are considered to be the most relevant in this project. Figure 2.11 shows examples of these two calibration issues in coadded target spectra.

2.2.6 Spectral spikes

Spectral spikes occur as a result of electrical interference. Whilst these spikes have been known to occur in several different regions of the three focal planes, those that occur at approximately 765 cm^{-1} and 790 cm^{-1} are of relevance due to their proximity to the

acetylene ν_5 and ethane ν_9 emission features. The former spike lies between the acetylene ν_5 and ethane ν_9 emission features and thus the 750 - 770 cm^{-1} region of the spectrum can simply be omitted from analysis. The latter spike at 790 cm^{-1} can similarly be omitted. Although this involves removing $\sim$10 cm^{-1} of the ethane ν_9 feature from the analysis, there is adequate information content in the remaining feature.

2.2.7 Baseline shifts

2.2.7.1 Thermal drift

Baseline shifts in radiance can be produced by changes in the temperature of the instrument during the course of an observation. This results in differences in the instrument temperature at times when target spectra and deep-space spectra were obtained. Thus, when the latter are used to calibrate the former, the detector's responsivity and self-emission are improperly characterised leading to offsets in the calibrated target spectrum. Negative baseline shifts are most obvious since radiances can become negative in some spectral regions, as exemplified in Figure 2.11. Negative radiances are particularly prevalent in proximity to the CH_4 ν_4 band (1230 to 1380 cm^{-1}) at high latitudes where the thermal infrared signal from Saturn is low (as shown in Figure 2.11). Positive baseline shifts are likely as occurrent as negative baseline shifts though, in contrast to negative baseline shifts which can be indicated by negative radiances, there is little evidence to indicate which observations have been affected by such a positive baseline shift.

In the v3.2 calibration approach, target spectra are calibrated using the temporally-closest calibration (deep-space and internal shutter) spectra. This method is likely to best characterise the instrument responsivity at the time the target observations were acquired and thus minimise the effects of a thermal drift on the calibrated radiances. However, far fewer deep-space spectra are used to calibrate each target spectrum ($N >> M$ in Equation 2.1)

and thus the signal-to-noise ratio on the target spectrum is limited by the number of deep-space observations, which is not ideal. The v4.2 calibration approach uses a grand-average of up to 4000 calibration spectra to calibrate each target spectrum. Thus, the drift in instrument temperature is potentially larger where target and calibration spectra have been acquired over a larger time range compared to v3.2. However, the significant advantage of the v4.2 method is that the signal-to-noise ratio is limited instead by the number of target spectra acquired.

2.2.7.2 Asymmetric interferograms

Baseline shifts in the radiance of the spectrum can further be caused by 1) the CIRS calibration pipeline improperly identifying the centre of the interferogram and/or 2) the interferogram being asymmetric around the central burst of zero path difference. Both these artefacts can result in offsets in the spectrum once the interferogram is transformed into spectral space.

The v4.3 calibration releases also uses a grand-average of 4000 deep-space observations to calibrate each target spectrum but additionally includes a phase correction developed by the CIRS calibration team to best remove any asymmetry in the interferograms. The v4.3 calibration is therefore thought to best minimise the effects of radiance baseline shifts however this calibration scheme is still in the stages of development.

In order to quantify the improvement made to observations by the phase correction, observations from the v4.2 (without correction) and v4.3 (with correction) were compared. For all COMPSITs, MIRMAPs and FIRMAPs detailed in Tables A.1, A.2 and A.1, individual spectra were sorted into 2° (planetographic) latitude bins and coadded. The mean radiances from 1100 to 1200 cm^{-1} and from 1400 to 1470 cm^{-1} were computed for the v4.2 and v4.3 coadds and the fractional change in signal from v4.2 to v4.3 (Equation 2.4) was

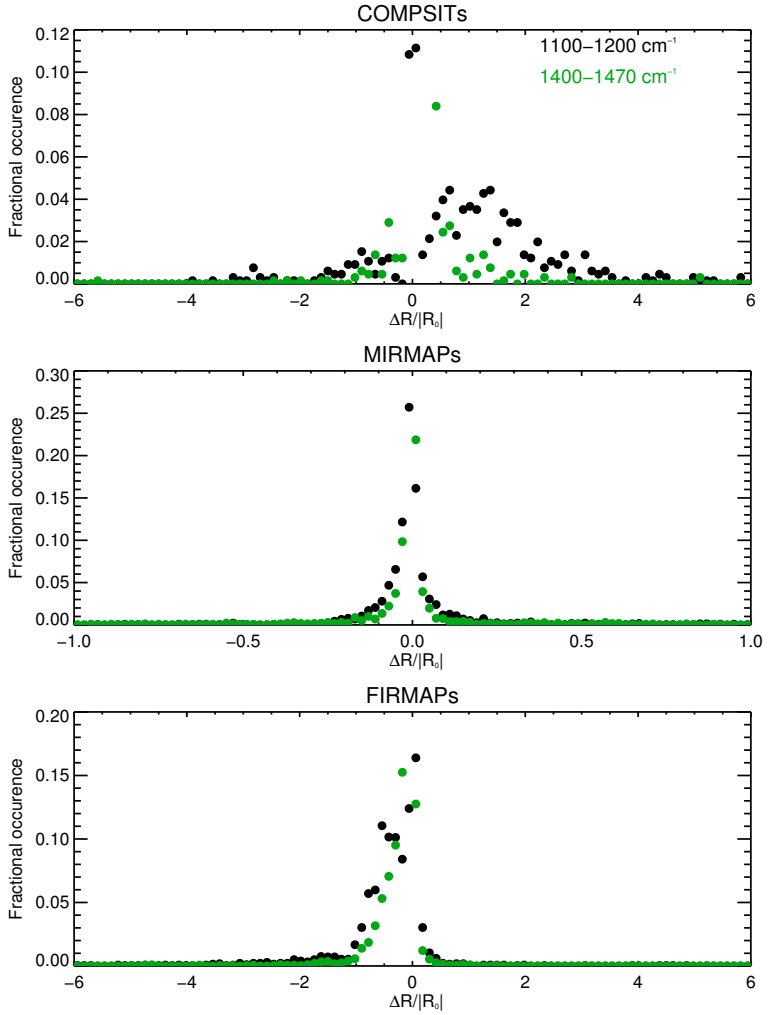

Figure 2.12: The distribution of values of $\Delta\bar{R}/\bar{R}_0$ over the entire FIRMAP dataset (Table A.4).

computed in order to assess the change made to the coadds by the phase correction.

$$\frac{\Delta\bar{R}}{|\bar{R}_0|} = \frac{\bar{R}_{v4.3}(\tilde{\nu_1} : \tilde{\nu_2}) - \bar{R}_{v4.2}(\tilde{\nu_1} : \tilde{\nu_2})}{|\bar{R}_{v4.2}(\tilde{\nu_1} : \tilde{\nu_2})|} \tag{2.4}$$

$\bar{R}_{v4.2}(\tilde{\nu_1} : \tilde{\nu_2})$ and $\bar{R}_{v4.3}(\tilde{\nu_1} : \tilde{\nu_2})$ are the spectrally-averaged radiances from wavenumbers $\tilde{\nu_1}$ to $\tilde{\nu_2}$ of coadds from the v4.2 and v4.3 calibrations respectively. Thus, a positive value of $\Delta\bar{R}/|\bar{R}_0|$ describes an increase in the mean signal from v4.2 to v4.3 whilst a negative

value would describe a decrease. Figure 2.12 shows the distribution of the values of $\Delta\bar{R}/\bar{R}_0$ over all three CIRS datasets at wavenumber ranges of 1100 - 1200 cm^{-1} and 1400 - 1470 cm^{-1}. As shown, the phase correction implemented in the v4.3 calibration appears to have had some success for COMPSIT observations at both spectral bands since its distribution is biased towards values greater than zero. The distribution for MIRMAP observations is centred at approximately zero which indicates that as many observations have been shifted to higher radiances as those shifted to lower radiances. However, for FIRMAP observations, there is a general bias towards values less than zero, which indicates that the v4.3 calibration has generally yielded spectra with lower radiances in the 1100 - 1200 cm^{-1} and 1400 - 1470 cm^{-1} regions. It is unclear whether this is a successful correction of positive baseline shifts in the v4.2 calibration or an unsuccessful correction of negative baseline observations which have potentially been worsened. However, this calibration improvement is still in the early stages of development.

2.2.7.3 Negative baseline removal?

An obvious approach to correcting the presence of negative baseline observations would be to omit any individual spectra that are negative in the 1100 - 1200 cm^{-1} region from the coaddition procedure (Section 2.2.4.2). However, this likely only removes the worst observations from the coaddition: spectra with a baseline shift (either negative or positive) may still remain. In addition, this filter could only be applied to FP4 observations since the typical thermal infrared signal in the FP3 focal plane was well above zero. Yet, given that FP3 and FP4 observations are generally acquired simultaneously, a baseline shift present in the FP4 focal plane is suggestive of a similar shift in the FP3 observation. Applying the filter of negative radiances to FP4 spectra alone partially removes the issue of negative baselines from FP4 but does not remove the issue from FP3 spectra. This is highly problematic since spectral regions of both focal planes can be analysed simultaneously in

the retrieval of temperature and hydrocarbon abundances (see Chapter 4).

No attempt at correcting the presence of baseline shifts in the observations has therefore been made in this thesis. Instead, the potential presence of baseline shifts is noted as a source of uncertainty in the retrieval of temperature and hydrocarbon abundances. In the subsequent chapters which present an analysis of CIRS observations, all three calibration releases (v3.2, v4.2 and v4.3) were used independently in order to account for the sensitivity of derived atmospheric properties with respect to the calibration version.

2.3 Summary

In summary, Voyager and Cassini provide a wealth of infrared observations of Saturn which may be analysed. Voyager 2-IRIS observations are significantly noisier due to the misalignment of the its interferometer during data acquisition and thus only Voyager 1-IRIS observations are deemed adequate for analysis. Even so, the Voyager 1-IRIS dataset have a high noise level and testing with synthetic spectra will be conducted in Chapter 6 in order to determine how retrievable atmospheric information is from these observations.

FIRMAP ($\Delta\tilde{\nu} = 15.5$ cm^{-1}) observations from Cassini-CIRS exhibit the best temporal sampling of Saturn across the Cassini mission and, as a result of their lower spectral resolution, exhibit a high signal-to-noise ratio. Thus, FIRMAPs are nominally considered the best dataset for resolving seasonal changes on the planet and an analysis of these observations forms the bulk of this thesis. The spectra of the v3.2, v4.2 and v4.3 calibration versions were analysed independently to test the robustness of results with respect to differing calibration approaches.

Chapter 3

Radiative transfer modelling and inversion

In situ measurements allow direct determination of a planet's atmospheric properties such as the temperature, chemical composition and dynamics. However, in the study of a planet besides Earth, such measurements are impractical and expensive, with the entry of the Galileo probe into Jupiter's atmosphere representing a rare example. The most practical way to study the atmosphere of another planet is therefore through the analysis of their electromagnetic spectra which can be measured remotely by instruments either mounted on ground-based telescopes or those on orbiting/nearby spacecraft.

Electromagnetic radiation propagating through the atmosphere of the planet is absorbed, scattered emitted by gases and aerosols. Different chemical species exhibit characteristic features in the spectrum and their shape and strength are sensitive to the atmospheric conditions in the region of the atmosphere at which the line is formed. This process can be modelled using the equations of radiative transfer and laboratory measurements of the strengths of lines of chemical species in the gas. Synthetic spectra of the planet or a *forward model* can thus be computed assuming an initial best guess of the atmospheric conditions and compared with the observed spectrum. The atmospheric conditions used in the forward model may be modified from the initial guess until the synthetic spectrum exhibits a good fit to the observed spectrum. This latter step is often described as a *retrieval* or *inversion* model. In this chapter, a radiative transfer model of Saturn's atmosphere and the procedures used to retrieve atmospheric quantities from observations of Saturn's atmosphere are outlined.

3.1 Radiative transfer model of Saturn's atmosphere

3.1.1 Equations of radiative transfer

For light with a radiance of $I_{\tilde{\nu}}$ (measured typically in W cm^{-2} sr^{-1} (cm^{-1})$^{-1}$) travelling through a planetary atmosphere at an angle θ to the zenith, a path of vertical thickness, dz, containing material of number density, n and with an absorption coefficient $k_{\tilde{\nu}}$, the absorption of radiation is given by Equation 3.1 (Lambert's law),

$$dI_{\tilde{\nu}} = I_{\tilde{\nu}} k_{\tilde{\nu}} n dz/\mu \tag{3.1}$$

where $\mu = cos(\theta)$. Thus, if the radiance is $I_{\tilde{\nu}0}$ at a base height of z_0, the total radiance emitted at a height z_1 is

$$I_{\tilde{\nu}1} = I_{\tilde{\nu}0} \exp\left(-\int_{z_0}^{z_1} \frac{k_{\tilde{\nu}} n dz}{\mu}\right) = I_{\tilde{\nu}0}\tau_{\tilde{\nu}}(z_0, z_1)$$

where $\tau_{\tilde{\nu}}(z_0, z_1) = \exp\left(-\int_{z_0}^{z_1} k_{\tilde{\nu}} n dz/\mu\right)$ is the transmission from z_0 to z_1 and $\mu = \cos\theta$. The atmosphere is also emitting infrared radiation in addition to absorbing it. By Kirchoff's law, the layer of thickness, dz, has an emissivity equal to its absorptivity thus, the radiance emitted is

$$dI_{\tilde{\nu}}^{\text{emm}} = +k_{\tilde{\nu}} B(\tilde{\nu}, T) n dz/\mu$$

where $k_{\tilde{\nu}}$, n and μ are as before and $B(\tilde{\nu}, T)$ is the Planck function at wavenumber, $\tilde{\nu}$ (Equation 3.2).

$$B(\tilde{\nu}, T) = \frac{2hc^2\tilde{\nu}^3}{\exp(hc\tilde{\nu}/kT) - 1} \tag{3.2}$$

Here, h is Planck's constant, c is the speed of light, k is Boltzmann's constant and T is the temperature of the atmosphere. This emitted radiation will itself be absorbed before

leaving the top of the planet's atmosphere. Thus, the contribution of emitted radiance reaching the top of the atmosphere is

$$dI_{\tilde{\nu}}^{\text{emm}} = \frac{k_{\tilde{\nu}} B(\tilde{\nu}, T) n dz}{\mu} \exp\left(-\int_{z_0}^{z_1} \frac{k_{\tilde{\nu}} n dz}{\mu}\right) = B(\tilde{\nu}, T) d\tau_{\tilde{\nu}}(z_0, z_1) \tag{3.3}$$

Therefore, the total thermal emission reaching the top of the atmosphere is

$$\begin{aligned} I_{\tilde{\nu}} &= I_{\tilde{\nu}} \tau_{\tilde{\nu}}(\mu, z_0, z_1) + \int_{\tau_{\tilde{\nu}}(z_0, z_1)}^{1} B_{\tilde{\nu}}(z) d\tau_{\tilde{\nu}}(\mu, z, z_1) & (3.4) \\ &= I_{\tilde{\nu}} \tau_{\tilde{\nu}}(\mu, z_0, z_1) + \int_{z_0}^{z_1} B_{\tilde{\nu}}(z) \frac{d\tau_{\tilde{\nu}}}{dz} dz & (3.5) \end{aligned}$$

The first term of Equation 3.4 represents the radiance that is emitted by the bottom layer that escapes the atmosphere. The second term of Equation 3.4 describes the subsequent contribution of the radiance emitted by some layer which itself is attenuated by the absorption of each level. As it is rewritten in Equation 3.5, $d\tau_{\tilde{\nu}}/dz$ is the *transmission weighting function* and the product $B_{\tilde{\nu}}(z) d\tau_{\tilde{\nu}}/dz$ is often called the *contribution function*. In general, the weighting function varies smoothly as a function of height in the atmosphere and peaks at an altitude corresponding to an optical depth of approximately unity.

3.1.2 Opacity modelling

There are different methods of calculating the opacity or τ in the equations shown in the previous section. The choice of method is generally a balance between the desired accuracy and the computational expense.

3.1.2.1 Line-by-line modelling

Line databases such as HITRAN [Rothman et al., 2009] and GEISA [Jacquinet-Husson et al., 2005] can be used to compute the absorption coefficients of every spectrally-active gas in a spectral range. The mean transmission in an atmospheric path of a wavenumber interval, $\Delta\tilde{\nu}$, is calculated as a summation of all individual line strengths in a given wavenumber interval, as shown in Equation 3.6. This can involve summing the contribution of thousands of narrow lines in one interval.

$$\bar{\tau}(m) = \frac{1}{\Delta\tilde{\nu}} \int_{\tilde{\nu}_0}^{\tilde{\nu}_0+\Delta\tilde{\nu}} \exp\left(-m \sum_j k_j(\tilde{\nu})\right) d\tilde{\nu} \tag{3.6}$$

Here, m is the total amount of absorber (molecule cm^{-2}), k_j is the j^{th} line in the wavenumber window, $\Delta\tilde{\nu}$. The above calculation must be conducted at a sufficiently small wavenumber step, $\Delta\tilde{\nu}$, such that individual lines are resolved. While this method best characterises the contribution to opacity of each individual line and is therefore the most accurate treatment of opacity, it is also computationally very expensive and thus very time consuming. In particular, this method is impractical when several subsequent spectra need to be calculated in an iterative approach towards a best fit solution, as described in Section 3.2. At high spectral resolutions where individual lines are resolved and only a forward model is required, the line-by-line method has been used (see Appendix A). However, the retrieval or *inversion* of atmospheric profiles from spectra is conducted using the faster *correlated-k* method described in the next section.

3.1.2.2 Correlated-k modelling

In the correlated-k method, line strengths within the averaging window are instead sorted in order of strength and the transmission is calculated as in Equation 3.7.

$$\bar{\tau}(m) = \int_0^\infty f(k)\, \exp(-km) dk \tag{3.7}$$

Here, $f(k)$ is the fraction of lines in the wavenumber domain with a strength between k and $k + dk$. The cumulative function can be defined as

$$g(k) = \int_0^k f(k) dk$$

$g(k)$ is a smooth, monotonically increasing function ranging from 0 to 1 and therefore its inverse, $k(g)$, also known as the k-distribution, can be calculated. Thus, the calculation of the transmission becomes

$$\bar{\tau}(m) = \int_0^1 f(k)\, \exp(-k(g)m) dg \tag{3.8}$$

Unlike $k(\tilde{\nu})$ in Equation 3.7, $k(g)$ is a smooth function which means integration over the wavenumber range can be conducted using far fewer integration intervals. The k-distribution can be divided into N points of quadrature and n approximation of the mean transmission calculated as

$$\bar{\tau} = \sum_{i=1}^{N} \exp\left(-k_i m\right) \Delta g_i \tag{3.9}$$

where k_i and Δg_i is the k-distribution value and the quadrature weight at the ith point of quadrature respectively. This treatment of opacity is therefore computationally much less expensive and therefore faster. In a planetary atmosphere, the temperature, pressure

and thus transmission vary as a function of height. Thus, the transmission (Equation 3.9) must be evaluated seperately at a suitable number of layers in the atmosphere. For an atmosphere composed of M layers, the total transmission at the top of the atmosphere is given by

$$\bar{\tau} = \sum_{i=1}^{N} \exp\left(-\sum_{j=1}^{M} k_{ij} m_j\right) \Delta g_i \tag{3.10}$$

where m_j is the density of absorbers at the jth layer, k$_{ij}$ is the k-distribution value of the jth layer at the ith quadrature point. The equation of radiative transfer (Equation 3.5) becomes

$$I_{\tilde{\nu}0} = \sum_{i}^{N} \left(\bar{B}_{\tilde{\nu}0}(T_0)\tau_{i1} + \sum_{j=1}^{M} \bar{B}_{\tilde{\nu}0}(T_j)(\tau_{i,j+1} - \tau_{i,j})\right) \Delta g_i \tag{3.11}$$

In general, the correlated-k method is the chosen treatment of line opacities throughout this thesis such that forward models and retrievals can be conducted efficiently. The correlated-k method is highly valid in the modelling of Voyager-IRIS and Cassini-CIRS observations which are of a lower spectral resolution. For IRTF-Celeste observations, individual lines are resolved. Retrievals of IRTF-Celeste spectra are conducted initially using correlated-k but with a final iterative step using the line-by-line method as described in further detail in 8.2.5.

3.1.3 Opacity sources in Saturn's atmosphere

Gaseous sources: At thermal infrared wavelengths ($\lambda > 5\mu$m), photons do not have sufficient energy to induce electronic transitions within atoms. Instead, infrared photons interact with the rotational and vibrational modes of molecules. Diatomic molecules, such as molecular hydrogen, have only one mode of vibration and one mode of rotation and thus rotational and vibrational transitions are not possible in such molecules. However,

in general, linear and non-linear molecules made of N atoms respectively have $3N-5$ and $3N-6$ modes of vibrations between which vibration transitions occur. Non-diatomic molecules also have rotational degrees of freedom with linear molecules such as C_2H_2 having two while non-linear molecules have three. Trace species in Saturn's atmosphere such as PH_3, NH_3, CH_4, C_2H_2 and C_2H_6 exhibit a range of vibrational, rotational and ro-vibrational transitions and their corresponding spectral features dominate the thermal infrared spectrum of Saturn.

Scattering sources: The effects of Rayleigh scattering are considered to be negligible in the thermal infrared. Clouds and aerosols represent non-Rayleigh scattering sources in Saturn's atmosphere and can significantly modify the radiance reaching the top of the atmosphere. HST (Hubble-space telescope) observations have revealed that Saturn's atmosphere is host to a vertically-discrete and/or continuously stratified tropospheric haze and a stratospheric haze with optical depths at 0.67 μm of the order of 10^1 and 10^{-2} respectively [Muñoz et al., 2004]. A preliminary analysis of limb-viewed ISS images of Saturn taken in 2011 constrained the presence of a vertically discrete haze layer to the ∼2 mbar level in the southern hemisphere [Rages and Barth, 2012]. However, it is likely that this haze is optically too thin in the thermal infrared to have any effect on the observed radiances. Thus, the effects of scattering by Rayleigh and non-Rayleigh sources are considered negligible in the thermal infrared.

Collisional sources of opacity: Purely rotational transitions are not possible in diatomic molecules such as H_2 since they have a zero dipole moment. However, collision of an H_2 molecule with another molecule/atom can deform the molecule such that it has a transient dipole moment which yields weak absorption. Whilst this is normally a weak form of opacity, given the sheer bulk of molecular hydrogen and helium in Saturn's atmosphere, H_2-H_2 and H_2-He collision-induced absorption form a significant feature in the spectrum of Saturn at longer wavelengths.

Line Broadening: The spectral lines associated with vibrational, rotational and ro-vibrational molecular transitions are broadened due to physical processes in the atmosphere of Saturn. The random motions of gas molecules in the atmosphere as they emit or absorb produces Doppler broadening which results in a gaussian line shape. The absorption coefficient, $k_{\tilde{\nu}}$ at wavenumber $\tilde{\nu}$ due to a Doppler-broadened line at wavenumber $\tilde{\nu}_0$ is given by

$$k_{\tilde{\nu}} = \frac{s}{\gamma_D \pi^{1/2}} \exp\left(-\left(\frac{\tilde{\nu}-\tilde{\nu}_0}{\gamma_D}\right)^2\right) \text{ where } \gamma_D = \gamma_{D_0}\left(\frac{T}{T_0}\right)^{1/2}$$

where s is the total line strength ($= \int_0^\infty k_{\tilde{\nu}} d\tilde{\nu}$) and γ_{D_O} is a reference Doppler line width at a reference temperature, T_0. Collisional or pressure broadening occurs when the emission or absorption of a photon is interrupted by a collision of the molecule with another atom or molecule producing a lorentzian line shape. The absorption coefficient, $k_{\tilde{\nu}}$ at wavenumber $\tilde{\nu}$ due to a collision-broadened line at wavenumber $\tilde{\nu}_0$ is given by

$$k_{\tilde{\nu}} = \frac{s\gamma_L}{\pi((\tilde{\nu}-\tilde{\nu_0})^2 + {\gamma_L}^2)} \text{ where } \gamma_L = \gamma_{L_0}\frac{p}{p_0}\left(\frac{T_0}{T}\right)^n$$

where γ_{L_0} is the collision-broadened linewidth at a reference pressure p_0 and temperature T_0 and n is the temperature coefficient which is determined empirically from laboratory measurements. While doppler broadening dominates at lower pressures and collisional broadening dominates at higher pressures, in general, the observed line shape is a result of both doppler and collisional broadening which together produce a Voigt lineshape (Equation 3.12).

$$k_{\tilde{\nu}} = \frac{sy}{\gamma_D \pi^{3/2}} \int_{-\infty}^{\infty} \frac{exp(-t^2)}{(x-t)^2 + y^2} dt \tag{3.12}$$

Here, s is as before, $x = (\tilde{\nu} - \tilde{\nu}_0)/\gamma_D$ and $y = \gamma_L/\gamma_D$ and t is the mean time between collisions..Natural broadening also occurs as a result of the Heisenberg uncertainty principle though it is negligible with respect to the broadening mechanisms described above.

Gas	Line intensities	Broadening half width	Temperature dependence
H_2-H_2 CIA	Orton et al. [2007]	-	-
H_2-He CIA	Borysow et al. [1988]	-	-
H_2-CH_4 CIA	Borysow and Frommhold [1986]	-	-
CH_4-CH_4 CIA	Borysow and Frommhold [1987]	-	-
CH_4, CH_3D	Brown et al. [2003]	H_2 broadened with half-width of 0.059 cm^{-1} atm^{-1} at 296 K	n =0.44 [Margolis, 1993]
PH_3	Kleiner et al. [2003]	γ_{H_2} = 0.1078 - 0.0014 J cm^{-1} atm^{-1} γ_{He} = 0.0618 - 0.0012 J cm^{-1} atm^{-1} [Bouanich et al., 2004; Levy et al., 1993]	n = 0.70 - 0.01 J [Salem et al., 2004]
NH_3	Kleiner et al. [2003]	Brown and Peterson [1994]	-
C_2H_2	Jacquinet-Husson et al. [2005]	Using fits to data in Varanasi [1992]	-
$^{12}C_2H_6$,$^{13}C^{12}CH_6$	Vander-Auwera et al. [2007] but with updates to $^{12}C/^{13}C$ line strengths according to Sada et al. [1996]	0.11 cm−1 atm^{-1} at 296 K [Blass et al., 1987]	[Halsey et al., 1988]

Table 3.1: The sources of line data used in the radiative transfer modelling of Saturn's thermal infrared spectrum together with the line-broadening parameters assumed.

Table 3.1 lists all sources of line data used in the radiative transfer forward model of Saturn, including the collision-induced opacities and the line broadening assumed for each molecule.

This line data is used to generate k-distributions for modelling of the observations used throughout this thesis using the correlated-k method. These are computed using different convolution functions appropriate for the spectral resolution and instrument line function of the observations being modelled. This procedure is detailed in the analysis sections of Chapters 4, 5, 6 and 8.

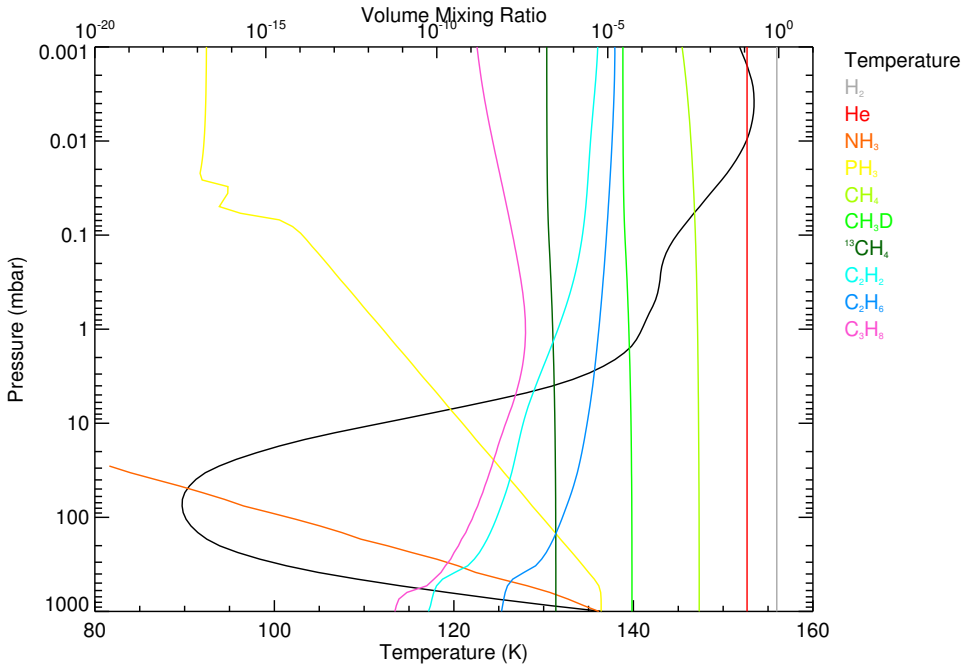

Figure 3.1: The reference vertical profiles of temperature and volume mixing ratios of trace species as indicated by the legend.

3.1.4 Reference atmosphere of Saturn

Figure 3.1 shows the reference vertical profiles of temperature and the volume mixing ratios of all spectrally-active gases used in this thesis. The reference atmosphere is defined on 100 pressure levels equally spaced in logarithmic pressure from approximately 10 bar to 1 μbar.

The reference temperature profile incorporates a mean of nadir-retrieved temperature profiles from Cassini-CIRS data (sensitive from 1 - 800 mbar) between 45°S and 45°N [Fletcher et al., 2010] together with limb-retrieved temperature profiles from Guerlet et al. [2009] over a similar latitude range (sensitive from 20 mbar to μbar). H_2 and He are assumed to be vertically well-mixed and the values for volume mixing ratios are assumed from those derived from a reanalysis of Voyager-IRIS measurements [Conrath and Gautier, 2000]. The f_P or ortho-to-para H_2 ratio has been set to be at local thermal equilibrium

using the calculation described in Borysow et al. [1985].

The NH_3 vertical profile is parameterised using a deep value of 5.5 x 10^{-5} (which assumes the deep value of 1.1 x 10^{-4} from Grossman et al. [1989] and a 50% saturation from de Graauw et al. [1997]) at pressures higher than 1 bar and a logarithmic extrapolation to negligible concentration at lower pressures. The PH_3 profile has been taken from Orton et al. [2000] and uses a deep volume mixing ratio of 6.4 ppmv. The vertical profiles of CH_4, $^{13}CH_4$ and CH_3D were assumed from Fletcher et al. [2009] The vertical profiles of all remaining hydrocarbon species were taken from Moses et al. [2000]. In particular, the vertical profiles of C_2H_2 and C_2H_6 retrieved from Guerlet et al. [2009] were not adopted in the reference atmosphere. This was to avoid placing a dependence on the results of this work with those from a previous study that also used Cassini-CIRS observations.

Aerosols and haze profiles have not been included in the reference atmospheric model since their effect on radiances at thermal infrared wavelengths is estimated to be negligible, as discussed previously in Section 3.1.3.

3.2 Nemesis

The inversion or *retrieval* of atmospheric profiles will be conducted using Nemesis [Irwin et al., 2008]. Nemesis is a retrieval tool which was initially developed to model and retrieve Cassini-CIRS observations of Saturn and Titan. However, the code can now generally be used to model and retrieve information from spectra of any planetary atmosphere including those from exoplanets [Lee et al., 2012]. Nemesis has recently been developed to operate in line-by-line mode as well as correlated-k however, retrievals in thesis were conducted using Nemesis in the latter mode.

Using the equations of radiative transfer, NEMESIS initially computes a forward model spectrum based on the *a priori* atmosphere (such as the reference atmosphere described

in Section 3.1.4) and the consistency of the modelled and observed spectrum is calculated by evaluation of the cost function, ϕ (Equation 3.13).

$$\phi = (\mathbf{y} - \mathbf{F}(\hat{x}))^T \mathbf{S}_\epsilon{}^{-1} (\mathbf{y} - \mathbf{F}(\hat{x})) + (\hat{\mathbf{x}} - \mathbf{x_a})^T \mathbf{S_a}{}^{-1} (\hat{\mathbf{x}} - \mathbf{x_a}) \tag{3.13}$$

By allowing an atmospheric parameter (such as temperature or the concentration of a chemical species) to vary, the aim is to iterate towards a solution atmospheric profile, $\hat{\mathbf{x}}_\mathbf{n}$, which produces a synthetic spectrum, $\mathbf{F}(\hat{\mathbf{x}})$ which is most consistent with the measured spectrum, $\mathbf{y}$ whilst minimising departure from the *a priori* profile, $\mathbf{x_0}$. $\mathbf{S}_\epsilon$ and $\mathbf{S_a}$ are respectively the measurement and *a priori* covariance matrices. The former term contains both errors associated with the noise on the observed spectrum together with the *forward modelling error* which is an estimate of the uncertainties associated with the radiative transfer forward model such as use of the correlated-k method and uncertainties in the spectroscopic line data. The latter term contains errors on the *a priori* information.

Nemesis then updates the trial atmospheric profile, $\hat{\mathbf{x}}_\mathbf{n}$, according to Equation 3.14 and again computes a forward model spectrum using this profile.

$$\mathbf{x}_{n+1} = \mathbf{x}_0 + \hat{\mathbf{S}}_\mathbf{x} \mathbf{K_n}^T (\mathbf{K}_n \hat{\mathbf{S}}_\mathbf{x} \mathbf{K_n}^T + \mathbf{S}_\epsilon)^{-1} (\mathbf{y} - \mathbf{F}(\hat{x}) - \mathbf{K}_n(\mathbf{x}_0 - \mathbf{x}_n)) \tag{3.14}$$

Here, $\mathbf{K}_n$ is the Jacobian or matrix of functional derivatives which describes the rate of change of radiance at a wavenumber with respect to an atmospheric quantity at the ith pressure/height ($dR_{\tilde{\nu}}/dx_i$). This essentially describes how sensitive the radiance at a particular wavenumber is to the magntitude of an atmospheric parameter (such as temperature or the concentration of a gas species). The Jacobians are used to compute the functional derivatives as a measure of the sensitivity of different spectral regions throughout this thesis. It is through calculation of this quantity that Nemesis knows how to

adjust the trial atmosphere $\mathbf{x_n}$ to calculate $\mathbf{x_{n+1}}$ in order to better improve the consistency of the measured and synthetic spectrum. For each iteration, a forward model spectrum is computed and compared with the observed spectrum by evaluation of the cost function, ϕ. Nemesis will continue to iterate until the cost function converges within a desired limit where an optimal atmospheric profile has been determined. In this thesis, convergence to such a solution was considered once ϕ differded by less than 1% between successive iterations. At this point, the desired atmospheric parameter is said to have been *retrieved*.

In conducting this retrieval, it is important to weight *a priori* information together with information in the spectrum equally. This can be seen more clearly in the evaluation of the cost function, ϕ (Equation 3.13), where the relative sizes of $\mathbf{S}_\epsilon$ and $\mathbf{S_a}$ dictate how each of the two terms is weighted. For example, in setting $\mathbf{S_a}$ to be large, which assumes little confidence in the *a priori* profile, the second term of Equation 3.13 becomes much smaller than the first term. In this case, Nemesis will seek to retrieve a solution atmospheric profile such that the modelled spectrum exhibits a very good fit to the observed spectrum. However, without the weighting of the first term, the solution atmospheric profile may be very different from the *a priori* profile and potentially unphysical. On the other hand, if the data is very noisy or a large forward modelling error is assumed, the first term of Equation 3.13 becomes very small and Nemesis will seek a solution atmospheric profile which is very similar to the *a priori* profile in order to minimise the second term. In this case, very little information in the observation is used and the retrieved atmospheric profile is very similar to the *a priori*. Ideally, an atmospheric solution which weights these two extremes equally is sought such that information from the observation is used whilst ignoring retrieved profiles that are highly different from the *a priori* profile and potentially unphysical. The results presented throughout this thesis correspond to retrievals where the *a priori* uncertainty and the forward modelling error have been adjusted such that both are weighted equally.

Nemesis is used throughout this thesis to retrieve the vertical temperature profile and concentrations of stratospheric acetylene and ethane. The procedures used to retrieve these atmospheric parameters differed depending on the dataset being modelled. The analysis sections of Chapters 4, 6 and 8 detail the procedures used in modelling Cassini-CIRS, Voyager-IRIS and IRTF-Celeste observations.

3.3 Summary

A radiative transfer model of Saturn's atmosphere has been developed which allows for thermal infrared spectra of Saturn to be computed at the spectral resolutions used in this thesis. While opacity data can be modelled using either the line-by-line method and correlated-k method, the latter has been chosen for forward modelling in this work due to its lesser computational expense and suitability for the spectral resolution used in this work. Nemesis is used to retrieve or invert observations to derive atmospheric information such as the vertical temperature profile and the stratospheric concentrations of acetylene and ethane. These quantities will serve as metrics of the structure and circulation of the stratosphere.

The collision-induced spectrum and methane ν_4 band are chosen as spectral sensors of the tropospheric and stratospheric temperature respectively. These spectral regions sound the 100 - 200 mbar level and 10 - 0.1 mbar levels respectively (but also with some sensitivity to lower pressures at high spectral resolutions). In CIRS and IRIS observations, the C_2H_2 ν_5 (710 - 750 cm^{-1}) and C_2H_6 ν_9 (770 - 890 cm^{-1}) emission features are used as sensors of the stratospheric concentrations of these hydrocarbons. These features generally provide greatest sensitivity to the 1-2 mbar level. However, in IRTF-Celeste observations where only a single emission line of these hydrocarbons is observed, there is a differing vertical sensitivity.

Chapter 4

Saturn's stratosphere in 2005 from Cassini-CIRS

Before assessing seasonal change on Saturn from 2005 onwards, it was necessary to first look at the results in 2005, corresponding to late summer and late winter (L_s ~310°) in Saturn's southern and northern hemispheres, and infer the state of the stratosphere at this time. The properties of Saturn's thermal structure and composition have previously been determined from Cassini-CIRS observations acquired from 2004 - 2006 in many studies such as Howett et al. [2007], Fletcher et al. [2007], Hesman et al. [2009] and Guerlet et al. [2009]. This section therefore serves as a reproduction and comparison of results determined in these studies and a discussion of the inferred properties of Saturn's stratosphere at that time. The results of this Chapter have also been published in Sinclair et al. [2013] but are presented in greater detail in this thesis.

4.1 Observations

As demonstrated in Chapter 2, Cassini-CIRS FIRMAP ($\Delta\tilde{\nu}$ = 15.5 cm^{-1}) observations, though offering a lower spectral resolution, provide a regular sampling of Saturn with time at a high signal-to-noise ratio. Thus, FIRMAP observations were used in Chapter 5, which investigates evolution from 2005 to 2010, and thus for consistency, FIRMAP observations acquired in 2005 were used in this Chapter. The 006_005BF and 008_007F FIRMAPs (Table A.4) acquired in April-May 2005 ($L_s = 307°$) were chosen to respectively capture the southern and northern hemispheres of Saturn in 2005. Individual spectra of

the v4.2 calibration were sorted into 2° (planetographic) latitude bins (with a 1° Nyquist overlap) and coadded. As discussed in Chapter 2, there are available different calibrated versions of the CIRS dataset that can result in slightly different radiance baseline levels, in particular for the $\Delta\tilde{\nu} = 15.5$ cm^{-1} observations. In order to assess possible differences in the retrieved results as a result of calibration and to rule out any significant results being an artefact of a particular calibration set, the coaddition procedure described above and the subsequent analysis has been reproduced for the same observations of the v3.2 and v4.3 calibrations. Only the results of v4.3 observations were presented in Sinclair et al. [2013].

4.2 Analysis

4.2.1 Radiative transfer modelling

K-distributions for CH_4, PH_3, NH_3, C_2H_2, C_2H_6 were generated using a triangular instrument line function with a FWHM = 15.5 cm^{-1} in order to model the FIRMAP observations of this spectral resolution. Although the line function of the CIRS instrument is actually a Hamming line function, a triangular line function was found to be a very good approximation of a Hamming function at these lower spectral resolutions (L. Fletcher, private communication).

4.2.2 Retrieval of temperature

In accordance with previous studies (e.g., Greathouse et al. [2005]; Guerlet et al. [2009]; Hesman et al. [2009]; Howett et al. [2007]), the collision-induced H_2-H_2 and H_2-He spectrum from 600 - 680 cm^{-1} and the methane ν_4 band (1230 to 1380 cm^{-1}) are selected as spectral regions of tropospheric and stratospheric temperature sensors respectively. Molec-

ular hydrogen and helium form the bulk of Saturn's composition and were considered to be well-mixed both vertically and meridionally.

It is similarly assumed throughout this thesis that CH_4 exhibits no meridional variation: the vertical profiles of CH_4 and its isotoplogues as described in Section 3.1.4 are assumed as the vertical profile of CH_4 at all latitudes. Photochemically, no variation in methane is expected in the lower stratosphere at pressures from 10 mbar to 0.1 mbar [Moses and Greathouse, 2005] which represents the altitude at which the methane ν_4 band is most sensitive (see Figure 4.1). However, at the 1 mbar level, vertical motion in the stratosphere might advect methane from lower or higher altitudes and thus induce differences in the volume mixing ratio of methane with latitude. As shown in Figure 3.1, the concentration of CH_4 (and its isotopes) decreases slightly with height. Thus, downwelling in the stratosphere would, for example, advect air which is less concentrated in methane and the overall concentration of methane at the 1 mbar level would be decreased. However, the vertical gradient in methane's concentration is comparably much smaller than that of C_2H_2 and C_2H_6 and thus changes in concentration of CH_4 as a result of vertical motion would likely be much smaller in magnitude than those observed of C_2H_2 and C_2H_6, as detailed in in Chapter 5. Ideally, the concentration of methane and any possible variation with latitude could be retrieved and such results assumed in further retrievals requiring knowledge of its volume mixing ratio. However, a retrieval of methane's concentration would require a prior or simultaneous retrieval of stratospheric temperature since the radiance emitted by a molecular species is a result of both the concentration of species and the temperature of the line-forming region. Unfortunately, methane is used as the sensor of stratospheric temperature and so such a retrieval would be highly degenerate. Meridional or temporal variations in methane's concentration can therefore not be ruled out. However, in the absence of current results or methods, which could determine the extent of its meridional variation and given the fact that any meridional variations are likely to be small in magnitude, it is assumed that CH_4 exhibits no variation with latitude or time.

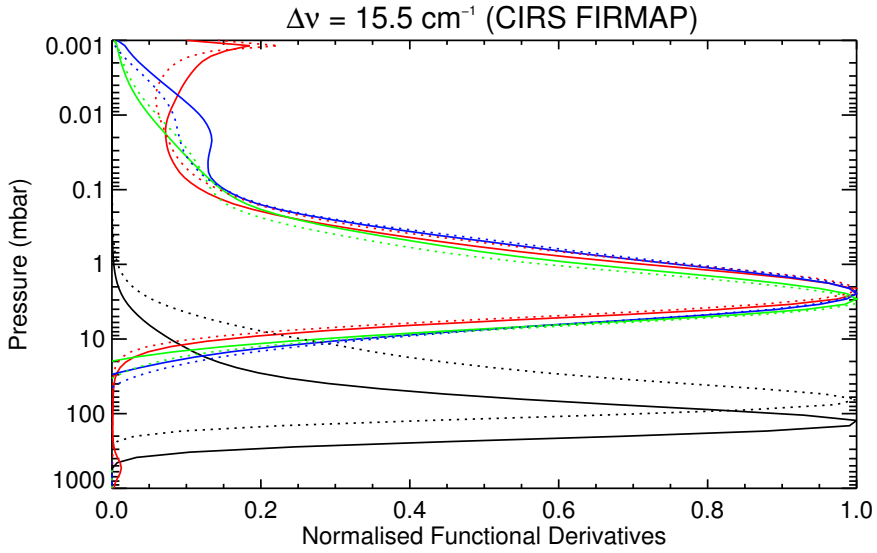

Figure 4.1: The vertical functional derivatives averaged over the collision-induced spectrum (600 - 680 cm^{-1}, the sensor of tropospheric temperature, black), the CH_4 ν_4 band (1230 - 1380 cm^{-1}, the sensor of stratospheric temperature, red) and the C_2H_2 ν_5 (710 - 750 cm^{-1}, blue) and C_2H_6 ν_9 (770 - 890 cm^{-1} green) bands used as sensors of the concentrations of these species. Solid and dashed profiles show contribution functions corresponding to low emission angle (<15°) and high emission angle (>60°) observations respectively.

4.2.3 Retrieval of stratospheric acetylene and ethane

The concentrations of acetylene and ethane are retrieved from their ν_5 (710 - 750 cm^{-1}) and ν_9 (770 - 890 cm^{-1}) emission features respectively. Given that the radiance of a molecular species is dependent on both the concentration of the species and the temperature in the line-forming region, retrieval of temperature (as in the previous section) must be conducted prior or simultaneously with retrieval of acetylene and ethane. In this Chapter, concentrations of acetylene and ethane were retrieved simultaneously with temperature as described in the previous Section.

4.2.4 Vertical information content

Figure 4.1 shows the functional derivatives of these spectal features at a spectral resolution of $\Delta\tilde{\nu} = 15.5$ cm^{-1} observations. There is greatest sensitivity to tropospheric temperature at approximately the 200 mbar level but with a systematic shift to higher altitudes when higher emission angle are used. There is greatest sensitivity to both stratospheric temperature and the concentrations of acetylene and ethane from 10 - 0.1 mbar with peak sensitivity ocurring at the 2-mbar level with little change when higher emission angle observations are used. Therefore, retrieved results of stratospheric temperature and the concentrations of acetylene and ethane were interpreted at the 2.1 mbar level.

4.3 Results

Figure 4.2 shows the retrieved vertical-latitudinal distributions of temperature in 2005 and Figure 4.3 shows the meridional distributions of tropospheric and stratospheric temperature and the stratospheric concentrations of acetylene and ethane. With the exception of high-northern latitudes, temperatures and concentrations retrieved from observations of the v4.2 calibration were generally in agreement (within the retrieval uncertainty) with those retrieved from the v3.2 and v4.3 calibrations. In 2005, the thermal infrared signal from high-northern latitudes is low. Small changes in the radiance baseline level with differently calibrated spectra therefore form a larger proportion of the signal emitted at these latitudes and so, retrieved quantities exhibit the greatest difference in this region. In Figure 4.3, results are shown for observations using the v4.2 calibration. However, error bars on these results reflect both retrieval uncertainty and any possible range as a result of the calibration version.

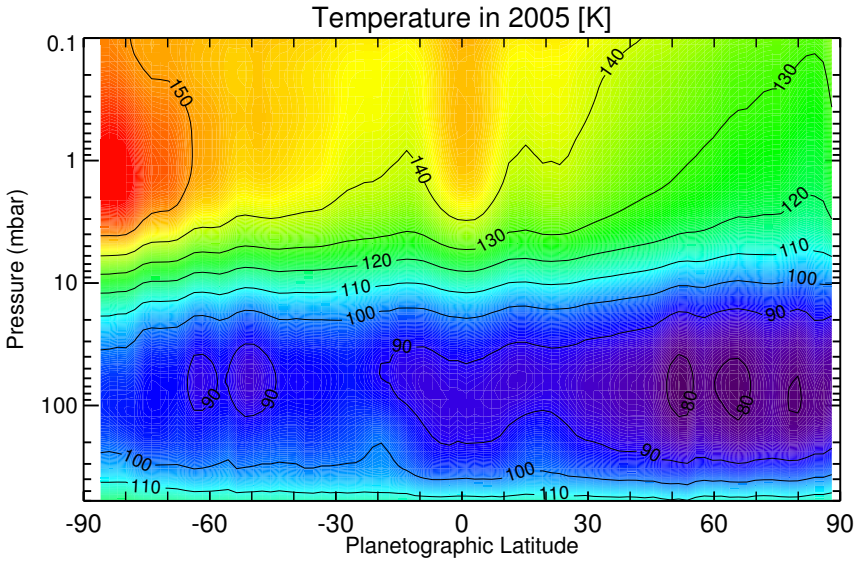

Figure 4.2: The retrieved distributions of the vertical temperature profile in 2005 as a function of planetographic latitude.

4.3.1 Meridional trends

To first order, the meridional profile of stratospheric temperature at the 2.1 mbar level exhibits a thermal hemispheric asymmetry with high-southern latitudes being approximately 40 K warmer than high-northern latitudes. This thermal contrast is consistent with Fletcher et al. [2007] who retrieved temperatures from near-nadir observations and Guerlet et al. [2009] who used limb Cassini-CIRS observations acquired in 2005/2006 (the results from the latter are also shown in Figure 4.3). This pole-to-pole temperature variation is also consistent with the findings of a radiative climate model computed by T. Greathouse (Figure 1.3) as detailed in Section 1.4.1. This indicates that the general meridional trend of temperature can be explained by the seasonal forcing. There are anomalies superimposed on this general trend at the south pole and the equator which indicate local dynamical processes at work in this regions: these are discussed in Sections 4.3.2 and 4.3.3 respectively.

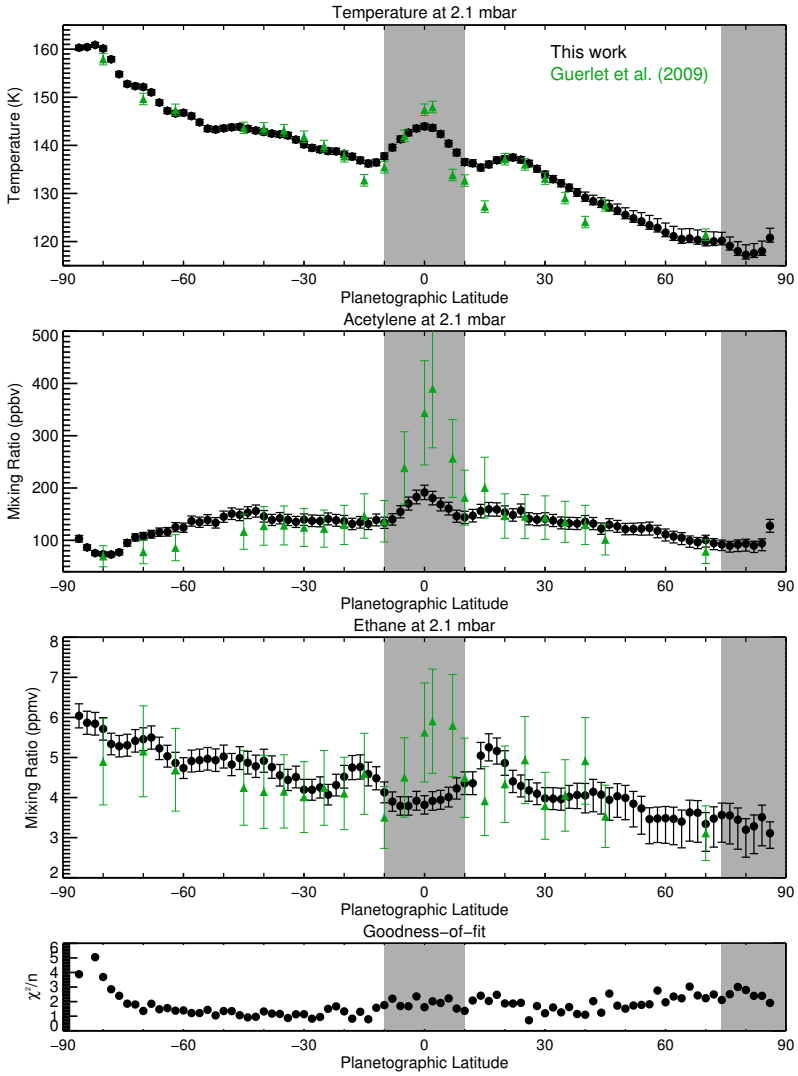

Figure 4.3: The meridional distributions of the retrieved temperatures and concentrations of C_2H_2 and C_2H_6 at 2.1 mbar from CIRS observations and the goodness-of-fit values are shown for comparison. Results are shown for retrievals of v4.2 calibrated FIRMAP observations however, the error bars on these values have been increased to include the values retrieved from v3.2 and v4.3 observations if these differed from the v4.2 result by greater than 1σ. The shaded regions at equatorial latitudes indicate less confidence in these results due to the limited sensitivity of nadir observations in resolving the equatorial thermal structure as discussed in Section 4.3.2. The shaded regions at high latitudes indicate little confidence in these results due to the poor signal-to-noise in the observations. Where available, results retrieved from limb observations in 2005/2006 (green triangles, Guerlet et al. [2009]) are also shown.

In general, the meridional trend of acetylene's concentration at the 2.1 mbar level exhibits a maximum at the equator and decreases to higher latitudes. The maximum at the equator is very much confined to equatorial latitudes which is also suggestive of local dynamics at work as discussed in Section 4.3.2. However, the overall decrease to higher latitudes is consistent in magnitude with results from limb observations by Guerlet et al. [2009] as shown in Figure 4.3. The trend is also consistent with the work published in Greathouse et al. [2005] who used ground-based IRTF-TEXES observations of Saturn in 2002 and Hesman et al. [2009] who used IRTF-Celeste observations acquired in 2006. This behaviour is in agreement with photochemical models [Moses and Greathouse, 2005], which predict acetylene's concentration to be highest at the equator where the most sunlight is received annually. A similar trend would also be expected of ethane though this is not observed in this work or previous work and this is discussed further in Section 4.3.4.

4.3.2 The equatorial oscillation

At the 2.1 mbar level, the meridional temperature profile exhibits a maximum at the equator. As discussed in Section 1.4.3.2, this is a result of a semiannual oscillation, which modulates temperatures at latitudes from 15°S to 15°N. In 2005, a temperature maximum associated with the oscillation occupies the 1 mbar level (Figure 1.6) thus giving rise to the maximum in the meridional profile of temperature.

The meridional trend of acetylene at the 2.1 mbar level also exhibits an equatorial maximum. While acetylene's concentration at this altitude is expected to be maximum at the equator where the greatest sunlight is receieved annually and to decrease to higher latitudes, the maximum in its meridional profile is very much confined to equatorial latitudes suggesting a link to the equatorial oscillation. As shown in Figure 4.3, Guerlet et al. [2009] also found a similar result (though with a more significant enhancement of acetylene at the equator) in addition to an equatorial maximum in ethane's concentration and they

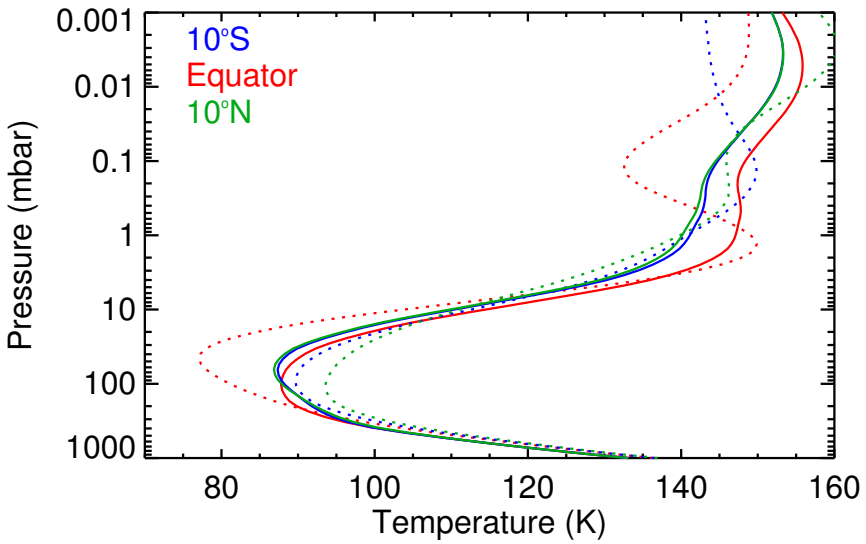

Figure 4.4: The retrieved vertical profiles of temperature (solid) and those retrieved from limb observations in Fouchet et al. [2008] (dotted) at 10°S (blue), the equator (red) and 10°N (green).

attribute this to equatorial downwelling associated with the oscillation. The evolution of this equatorial oscillation is investigated in Chapter 5.

Figure 4.4 compares the vertical temperature profiles retrieved at equatorial latitudes in this work with those from Fouchet et al. [2008]. The profile retrieved by Fouchet et al. [2008] at the equator will henceforth be described as *F08*. As shown, there are considerable differences which are most likely a result of the differing vertical sensitivity in the near-nadir observations used in this study and the limb-viewed observations used in their study. The limb observations sounded the Saturnian stratosphere at several different tangent heights from 10 mbar to 0.01 mbar and thus can readily resolve the vertically-alternating thermal stucture associated with the SSAO. In this thesis, the nadir observations used provide a broad sensitivity from 10 mbar to 0.1 mbar with the greatest sensitivity at the 1-2 mbar level (Figure 4.1). In 2005, this pressure range is occupied by a temperature maxima associated with the SSAO and a maximum is observed in the thermal meridional

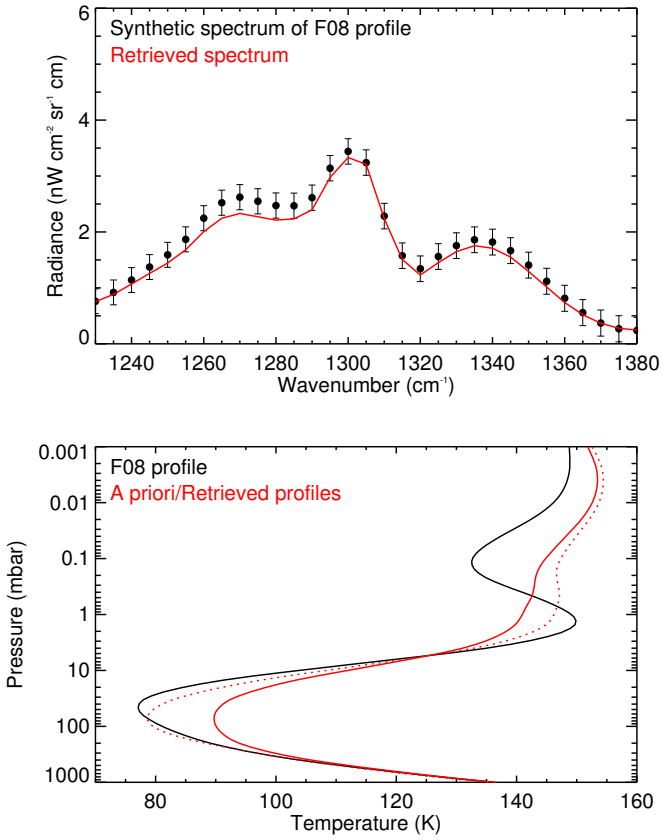

Figure 4.5: A synthetic spectrum (black) forward modelled using the vertical temperature retrieved at the equator in Fouchet et al. [2008] shown in the same colour in the bottom plot. The red solid and dashed profiles respectively indicate the *a priori* and temperature profile retrieved from the synthetic spectrum. The modelled spectrum is also shown for comparison in the same colour.

trend. However, it can be seen that retrieved temperatures from nadir CIRS observations are inconsistent with those retrieved from limb observations in Fouchet et al. [2008].

Synthetic FP3 and FP4 spectra were computed using the *F08* temperature profile. The aim here is to retrieve temperature from these synthetic spectra and assess how different the temperature profiles are with respect to the *F08* profile as a measure of the incosistencies in vertical information content. The spectra were computed at zero emission angle and at a spectral resolution of $\Delta\tilde{\nu} = 15.5$ cm^{-1} and random noise was added in order to

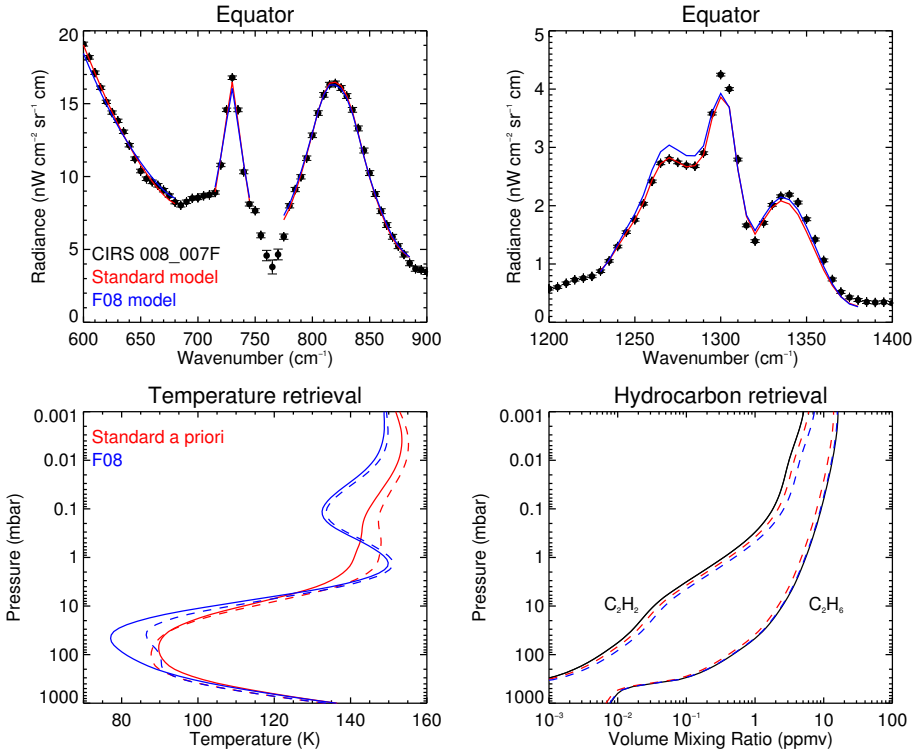

Figure 4.6: Retrievals of the vertical temperature profile and concentrations of acetylene and ethane at the equator starting from different temperature *a priori* profiles. The top plots show Cassini-CIRS FIRMAP observations of the equator in May 2005 (black) and the corresponding modelled spectra starting from the standard temperature *a priori* (red) and the profile retrieved by Fouchet et al. [2008] in 2005 (blue). Error bars indicate the noise on the spectra however this is generally negligible on the scale of the plot. The bottom plots show the *a priori* (solid) and retrieved (dashed) profiles of temperature, acetylene and ethane.

simulate an observed spectrum. However, this was of a magnitude such that the spectrum was high in signal-to-noise such that noise was not a limiting factor in the retrieval. A retrieval of temperature was then conducted of this synthetic spectrum using our reference temperature profile as the *a priori*. Figure 4.5 compares the observed and synthetic spectra together with the modelled and retrieved temperature profiles. As shown, the discrepancy in the retrieved temperature profile with the *F08* profile remains confirming that near-nadir observations cannot resolve the fine-scale structure of the SSAO. In particular, the broad contribution function in the nadir cannot fully resolve the maximum in temper-

ature derived in Fouchet et al. [2008] and so a cooler temperature is retrieved at the 1-2 mbar level. The SSAO is seen to modify the stratospheric thermal structure at latitudes from 15°S to 15°N [Fouchet et al., 2008]. Thus, temperatures retrieved in this latitude range will be treated with less confidence. In addition, retrievals of the concentrations of acetylene and ethane, which rely on an adequate characterisation of the temperature, will also be treated with caution at latitudes from 15°S to 15°N. Indeed, retrieved temperatures, acetylene and ethane concentrations from this work appear inconsistent with those from Guerlet et al. [2009] over this latitude range (Figure 4.3) whilst exhibiting good agreement within error bars at other latitudes.

A retrieval of the vertical temperature profile and the concentrations of acetylene and ethane at the equator was repeated. Whilst the same acetylene and ethane *a priori* profiles are used, the *F08* temperature profile was instead adopted as the temperature *a priori*. This serves to retrieve a temperature profile which will retain the shape of the original *F08* profile whilst Nemesis applies small deviations in order to provide the best match between the modelled and observed spectra. The concentrations of acetylene and ethane were also allowed to vary in this retrieval in order to assess their sensitivity to the temperature prior. Figure 4.6 compares retrievals of temperature and the concentrations of acetylene and ethane of a 008_007F spectrum of the equator starting from the standard and *F08* temperature *a priori*. Retrieval of temperature starting from the standard temperature profile is found to yield a modelled spectrum which exhibits a better fit to the observation. However, richer concentrations of acetylene and ethane are retrieved when the *F08* profile is adopted as the temperature prior. This partly reconciles the discrepancy in the retrieved concentrations of these hydrocarbons in this work with Guerlet et al. [2009].

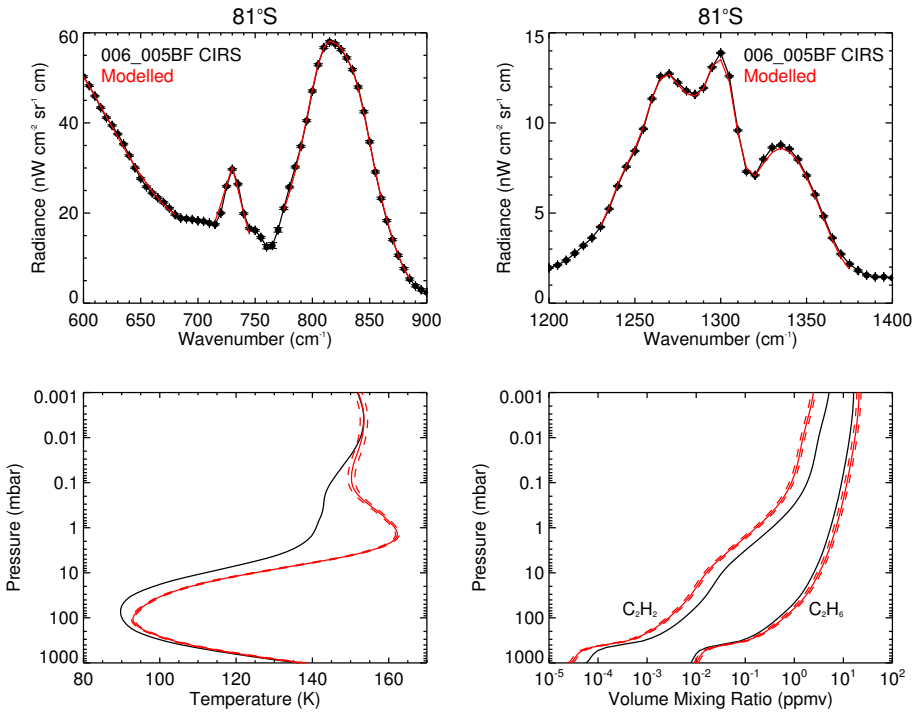

Figure 4.7: Observed (black) and modelled (red) spectra at 81°S in 2005 and the corresponding retrieved profiles of temperature and the concentrations of acetylene and ethane (red, with dashed profiles of the same colour outlining the 1σ uncertainty) with respect to *a priori* (black, solid) profiles.

4.3.3 South polar hot spot

The meridional trend in temperature at the 2.1 mbar level exhibits a sharp increase south of 75 °S with temperatures greater than 160 K. This is consistent with Fletcher et al. [2008] who attributed this behaviour to the presence of a polar vortex at the south pole in the aftermath of southern summer. This thesis also indicates a similar marked increase in the concentrations of acetylene and ethane south of 75°S. This behaviour also supports the presence of a polar vortex advecting hydrocarbon-richer air from higher in the stratosphere.

Although retrievals in this region have larger χ^2/n values (Figure 4.3), this is a result of a very high signal-to-noise ratio in the observations rather than a poorer fit of the modelled

spectra to the observed. Figure 4.7 shows an example retrieval at 81°S and demonstrates that there is a good fit to the observations at these latitudes.

4.3.4 Ethane's meridional enrichment

Ethane exhibits an increase in concentration towards higher southern latitudes during southern summertime conditions in the absence of a similar increase in acetylene. This is in accordance with Greathouse et al. [2005], Howett et al. [2007], Hesman et al. [2009] and Guerlet et al. [2009]. The magnitude of the increase with latitude in this work differs from that in the former three studies whilst there is agreement in the results with those from Guerlet et al. [2009] within error bars, as indicated in Figure 4.3. This attributed to the spectroscopic line data of C_2H_6 where updated line data from Vander-Auwera et al. [2007] was used in this work and Guerlet et al. [2009] while older versions were used in other studies.

4.4 Summary

In 2005, Saturn's thermal structure exhibited a hemispheric asymmetry with considerably warmer temperatures in the southern hemisphere since this year captures Saturn shortly after southern summer solstice. As discussed in Fletcher et al. [2010], the general temperature variations with latitude at this time are consistent with a radiative climate model which indicates that seasonal forcing is responsible for much of the observed thermal meridional trend.

Superimposed on this general trend is a maximum in the temperature profile at the equator, which indicates the presence of a semi-annual oscillation, or SSAO, as seen in previous studies. However, the nadir observations used in this work only broadly sound a single stratospheric pressure range and do not resolve the entire vertical structure. Warm tem-

peratures at high-southern latitudes together with enriched concentrations of acetylene and ethane in this latitude region with respect to lower latitudes are suggestive of downwelling associated with a south polar vortex.

Acetylene's global meridional trend is consistent with photochemical prediction while in contrast, ethane's concentration exhibits a hemispheric asymmetry which suggests its concentration is governed by a mechanism with a timescale comparable with half a Saturn year. Further study of this feature and its evolution may more clearly indicate the timescales associated with the emergence and dissipation of this feature and thus the physical processes at work.

Chapter 5

Seasonal variablity from 2005 to 2010 from Cassini-CIRS

This chapter presents the results of the vertical temperature profiles and stratospheric concentrations of acetylene and ethane retrieved from Cassini-CIRS observations acquired from 2005 to 2010. These results, with respect to those presented in Chapter 4, are used to assess the seasonal change occurring in Saturn's stratosphere over this period. As with Chapter 4, these results have also been published in Sinclair et al. [2013] but are presented in greater detail in this thesis.

5.1 Observations & Analysis

Observations: The 120_001F (November 2009, $L_s \sim 3°$) and 139_002F (October 2010, $L_s \sim 14°$) FIRMAPs (Table A.4) have been chosen: both observations were required in order to cover both the southern and northern hemispheres. Results from these observations together with those from 2005 (Chapter 4) are used to directly compare the planet in late summer and after the equinox. However, all intermediate FIRMAP observations were used to assess the evolution of Saturn's atmosphere over this time, in particular at latitudes where a signficant change in temperature and/or the concentrations of acetylene and ethane were observed. Observations of the v4.2 calibration were sorted into 2° planetographic latitude bins, stepped in 1° increments, and coadded. As was done for 2005 observations in Chapter 4, observations of the v3.2 and v4.3 calibrations were also selected and the coaddition procedure and the subsequent analysis reproduced in order to assess

any possible differences in the results due to the calibration version.

Analysis: The vertical temperature profile and the concentrations of acetylene and ethane were retrieved simultaneously using the same retrieval procedure described in Section 4.2 of the previous Chapter. As demonstrated in Figure 4.1, there is greatest sensivity to temperature and the concentrations of acetylene and ethane at 2.1 mbar and so seasonal change was assessed at this pressure level.

5.2 Results

Figure 5.1 shows the latitudinal distributions of the vertical temperature profile in 2005, 2009 and 2010 and their differences and Figure 5.2 shows the meridional distributions of temperature and the concentrations of acetylene and ethane at the 2.1 mbar level.

The differences in results retrieved from v4.2 observations and those from v3.2 and v4.3 observations were generally negligible, or at least to within the uncertainty on the retrieved quantities. As was seen in Chapter 4, high-northern latitudes were an exception since small changes in the radiance baseline level represent a larger proportion of the overall signal in this region which is still cool in late winter/early spring and thus not bright in the thermal infrared. Error bars in Figure 5.2 reflect both the retrieval uncertainty and any possible range as a result of the calibration version. Figure 5.3 shows the differences between 2005 and 2009/2010 concentrations of acetylene and ethane in units of 2σ (where σ is the uncertainty in the retrieved concentration). A change in the concentration of acetylene or ethane in excess of the 2σ level is considered to be physically significant.

5.2.1 Equatorial evolution

In comparing 2005 and 2009/2010 temperatures, the equator exhibits a cooling of 5.3 ± 0.1 K at the 2.1 mbar level (Figures 5.1, 5.2 and 5.3). Equatorial cooling over a similar time

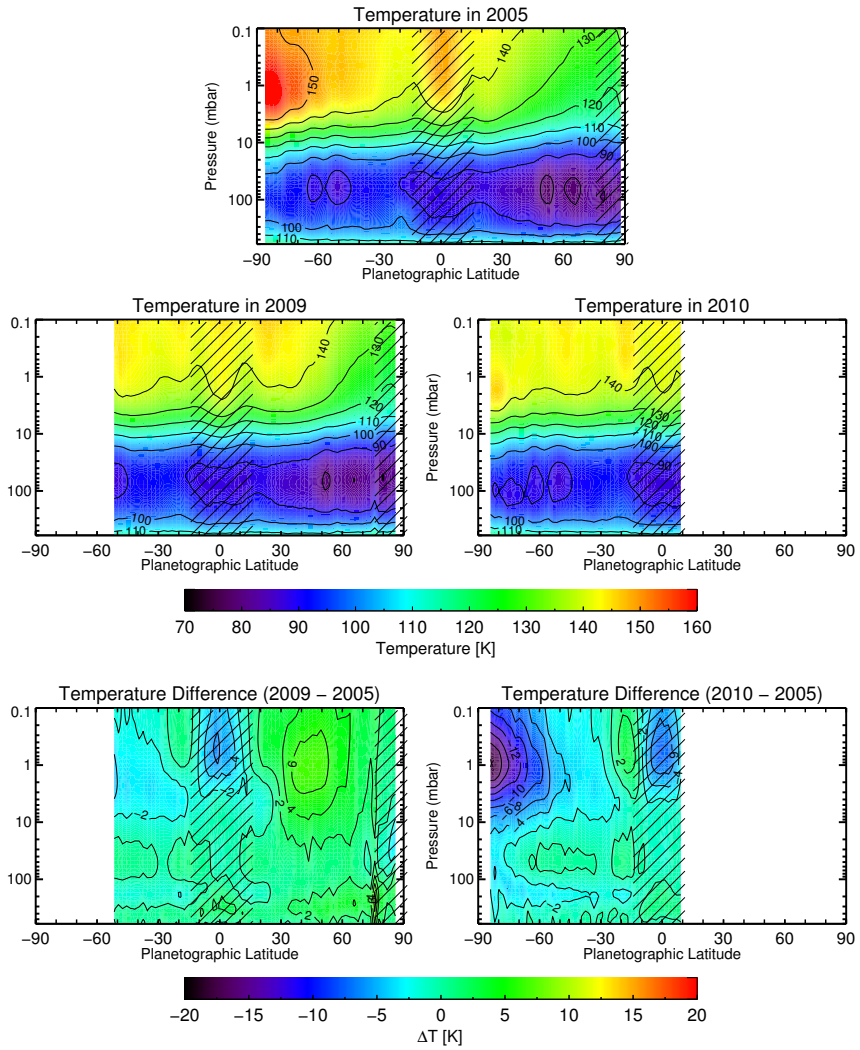

Figure 5.1: The retrieved latitudinal-vertical temperature profiles in 2005 ($L_s \sim 308°$), 2009 ($L_s \sim 3°$) and 2010 ($L_s \sim 14°$) and their differences. The shaded regions at high latitudes indicate less confidence in these results due to the poor signal-to-noise ratio of these observations.

range has previously been observed and is attributed to the vertical structure of the SSAO descending with time as detailed in Section 1.4.3.2. From 2005 to 2010, a temperature maximum associated with the SSAO at 1 mbar descends to higher pressures at which there is less/no sensitivity in these observations and is replaced by a temperature minimum from lower pressures. Thus, at the 1-2 mbar level, a cooling is observed.

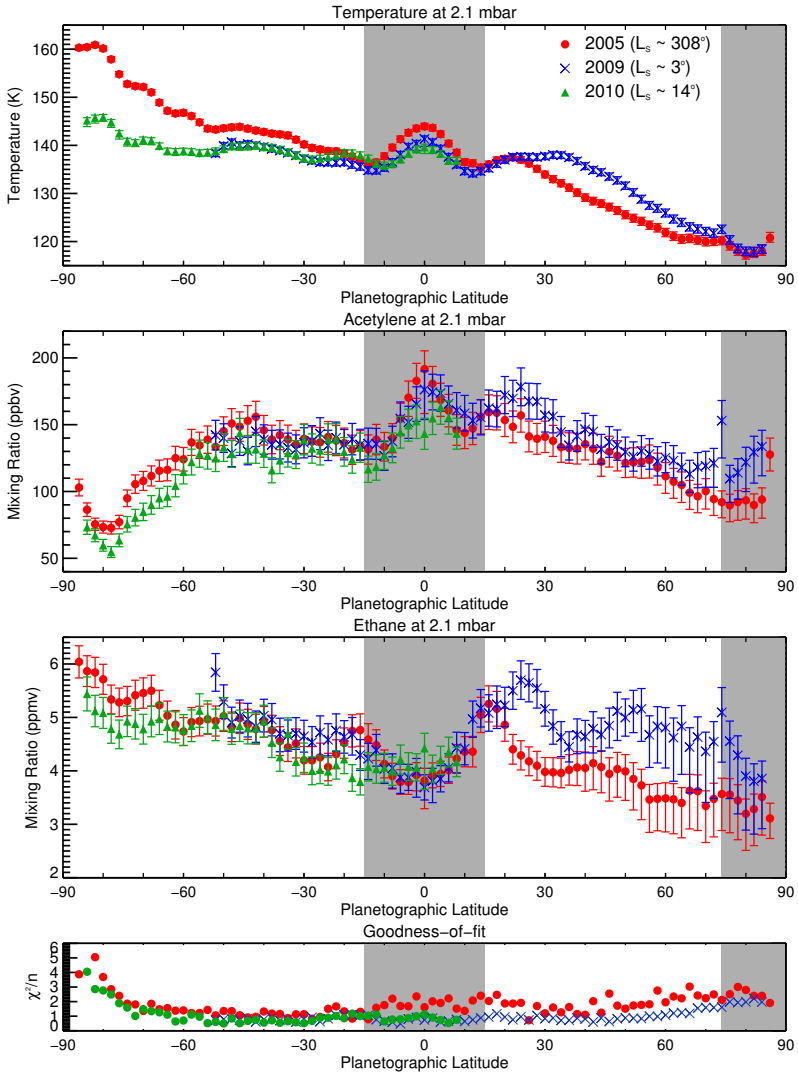

Figure 5.2: The meridional profiles of temperature and the concentrations of acetylene and ethane at 2.1 mbar and the corresponding goodness-of-fit values. Red circles indicate 2005 results, blue crosses indicate 2009 results and green triangles indicate 2010 results. Results are shown for retrievals of v4.2 observations. However, the error bars on these values have been increased to include the value retrieved from v3.2 and v4.3 observations if these valued differed by greater than 1σ. The shaded regions at equatorial latitudes indicate less confidence in these results due to the limited resolution of the SSAO from nadir observations and the shaded regions at high-northern latitudes indicate less confidence in these results due to the lower signal-to-noise ratio of these observations.

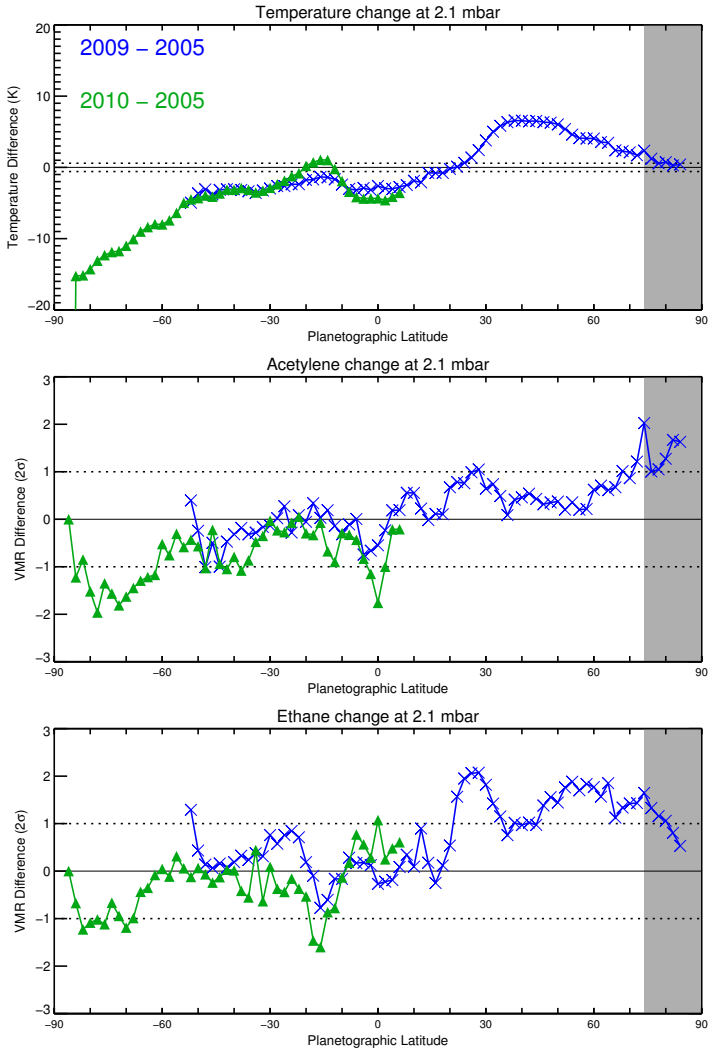

Figure 5.3: The differences in the retrieved temperature (top), acetylene (middle) and ethane (bottom) concentrations at 2.1 mbar between 2005 and 2009 (blue) and 2005 and 2010 (green). Temperature differences are in units of K and the dashed horizontal mark the mean error in the retrieved temperature. Concentration changes are in units of 2σ (where σ is the uncertainty in the retrieved concentration) and dotted lines show the $\pm 2\sigma$ levels. The shade regions at high-northern latitudes indicate less confidence in these results due to the low signal-to-noise ratio of these observations. In particular, the difference in acetylene concentration at 75°N between 2005 and 2009 is unphysical.

Figure 5.4 shows the variations of temperature, acetylene and ethane with time from 2005 to 2010. The mid-2008 temperatures appear to significantly differ from the general trend and this result was ignored in the subsequent interpretation. The temperature at 2.1 mbar

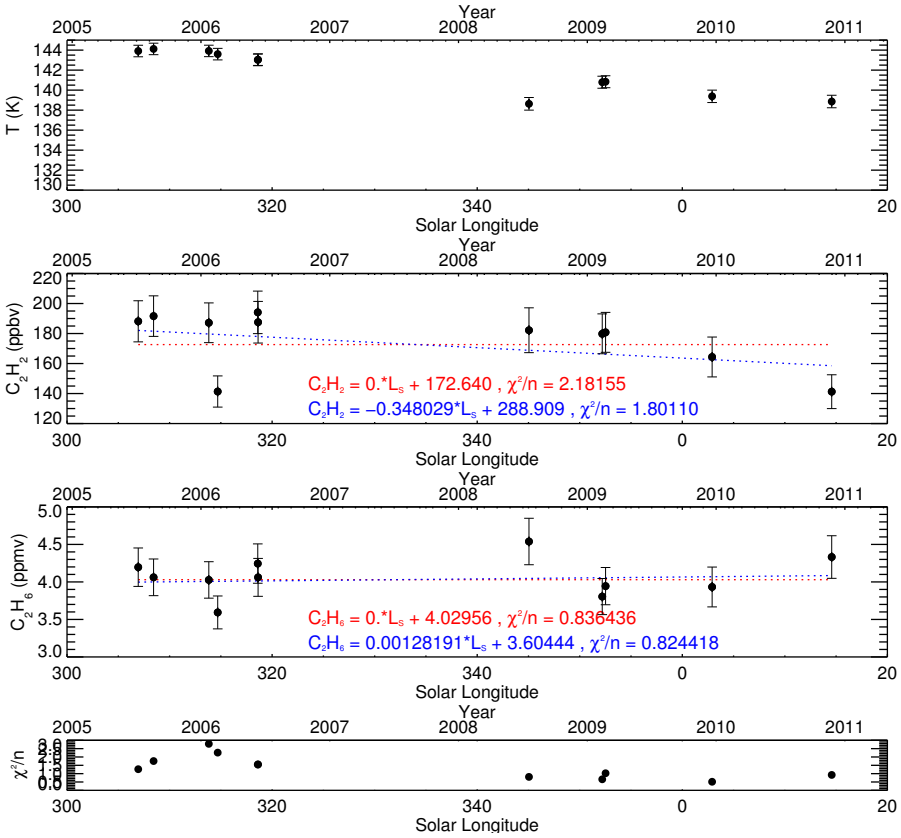

Figure 5.4: The equatorial evolution of temperature, acetylene and ethane at 2.1 mbar and the χ^2/n values of each retrieval. For hydrocarbon trends, red dotted lines show the best fit constant trend while blue dotted lines show the best-fit straight line. The equations of these lines and the reduced χ^2 with the data are shown.

appears constant (within error bars) from 2005 to late 2006 and subsequently exhibits a general decrease from 2009 onwards (with no data coverage at this latitude between late 2006 and mid 2008). Acetylene's concentration at the equator is seen to decrease from 188.2 ± 13.7 ppbv to 141.3 ± 11.3 ppbv from 2005 to 2010. The temporal variation in acetylene over this time range is better fit a decreasing trend (Figure 5.4), rather than a constant one, which reinforces the conclusion of a decrease in concentration. However, ethane's abundance exhibits almost no change from 2005 to 2010 and the variation of ethane's concentrations exhibits a good correspondence with a constant trend. Results from a preliminary analysis of limb observations in 2005 and 2010 also indicate a decrease in

acetylene's concentration at the 1 mbar level with time while ethane maintains a constant concentration within error bars (S. Guerlet, private communication).

The magnitude of cooling observed in this work is comparable to the approximate 6 K cooling observed by Fletcher et al. [2010] who used similar nadir Cassini-CIRS observations from 2005 to 2008. However, Guerlet et al. [2011] and Schinder et al. [2011] (using limb-viewed Cassini-CIRS observations and radio occultation data over the 2005 - 2010 time range) derived a larger magnitude of cooling. This discrepancy is most likely due to the differing altitudinal sensitivity of the nadir observations used in this work and the limb/occultation observations used in their studies. As demonstrated in Section 4.3.2, nadir viewing does not provide a sufficient vertical resolution such that the full structure of the SSAO can be resolved, unlike the limb observations used in Guerlet et al. [2011], which sounded the atmosphere at several different pressure levels. The temperature profile retrieved by Guerlet et al. [2011] at the equator in 2010 will henceforth be described as G11.

In order to test the effects of different vertical resolutions on the retrievability of the equatorial temperature evolution, synthetic FP3 and FP4 spectra at a spectral resolution of $\Delta\tilde{\nu} = 15.5$ cm^{-1} and at zero emission angle were computed using the G11 temperature profile. Random noise was subsequently added to the spectrum in order to simulate a synthetic spectrum. However, with the aim of quantifying the uncertainty introduced by the differing vertical resolution, this noise was of a small magnitude such that it was not the limiting uncertainty. A retrieval of temperature was then conducted of this synthetic spectrum using the reference temperature profile as the *a priori*. These results, together with a similar analysis conducted of the equator in 2005 in Chapter 4, allow for the evolution of the SSAO, as determined in Guerlet et al. [2011], to be simulated at a nadir viewing geometry. Figure 5.5 shows the synthetic and modelled observations in 2005 and 2010 and the corresponding model and retrieved profiles of temperature. As shown,

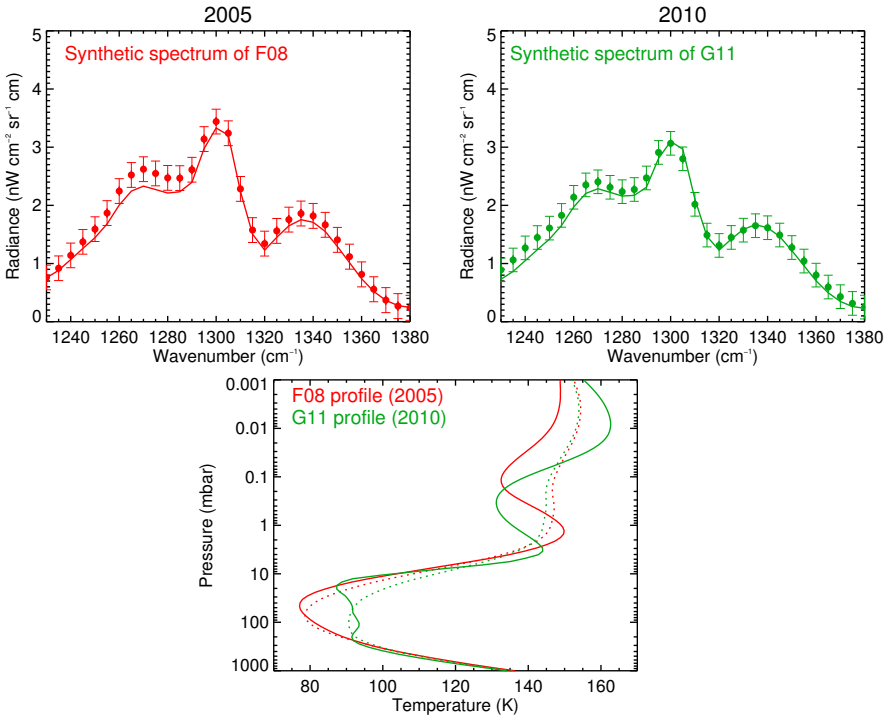

Figure 5.5: Synthetic spectra produced from the F08 temperature profile of the equator in 2005 (red) and the G11 temperature profile of the equator in 2010 (green). The modelled spectra and corresponding retrieved temperature profiles of these synthetic spectra are shown as dashed lines.

although the synthetic spectra in 2005 and 2010 have been produced using modelled temperature profiles which are approximately 15 K different in temperature at the 1-2 mbar level, retrievals of temperature from these spectra using the standard temperature *a priori* yields only an approximate 6 K temperature difference. These results confirm that the limited vertical resolution of the nadir observations is the cause of the disrepancy in the magnitude of cooling observed in this work and in Guerlet et al. [2011] and Schinder et al. [2011].

Retrievals of the vertical temperature profile at the equator in 2010 were repeated, but instead using the G11 temperature profile as the *a priori*. Use of this prior serves to retrieve a vertical temperature profile which retains features of the original prior whilst

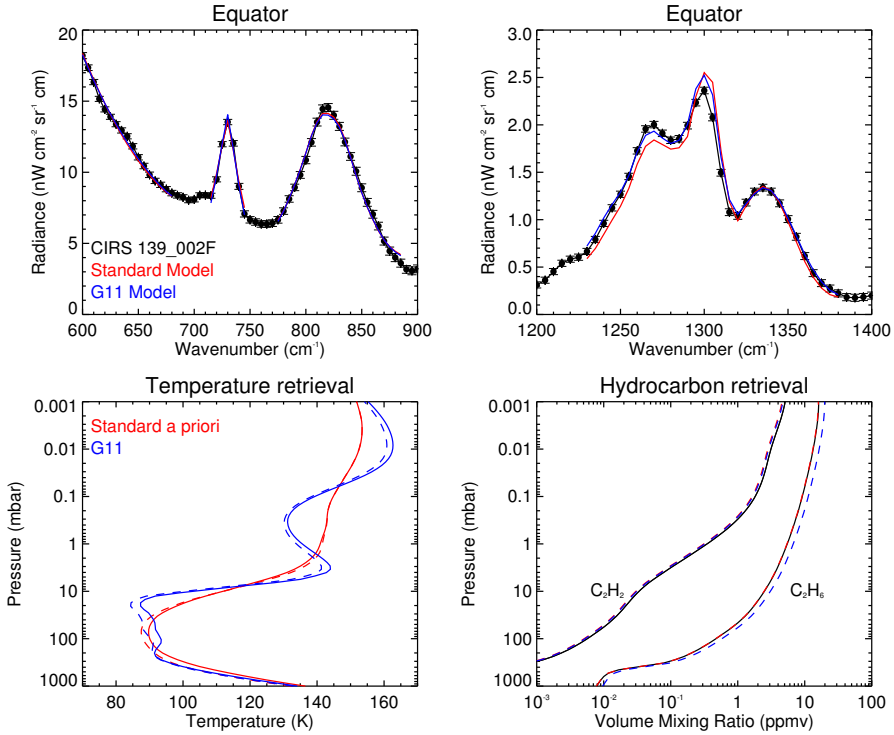

Figure 5.6: Retrievals of the vertical temperature profile and concentrations of acetylene and ethane at the equator starting from different temperature *a priori* profiles. The top plots show Cassini-CIRS FIRMAP observations in October 2010 (black) and the corresponding modelled spectra starting from the standard temperature *a priori* (red) and the the profile retrieved by Guerlet et al. [2011] in 2010 (blue). The bottom plots show the *a priori* (solid) and retrieved (dashed) profiles of temperature, acetylene and ethane.

applying deviations in order to provide the best match between observed and modelled spectra. Figure 5.6 compares retrievals of temperature and the concentrations of acetylene and ethane in 2010 using the standard and G11 temperature profiles as the *a priori*. Table 5.1 compares the retrieved temperatures and concentrations of acetylene and ethane in 2010 using both priors with those from 2005 where the standard and F08 temperature profiles were similarly tested as *a priori* (Section 4.3.2). As shown, use of the F08 and G11 temperature profiles as *a priori* yields a larger magnitude of cooling at the equator at the ∼1 mbar level, which is more comparable with the magnitude of cooling observed in Guerlet et al. [2011] and Schinder et al. [2011], thus partly reconciling this discrepancy.

Year	Temperature *A priori*	Results at 2.1 mbar			
		T (K)	C_2H_2 (ppbv)	C_2H_6 (ppmv)	χ^2/n
2005	Standard	143.9 ± 0.6	188.7 ± 13.7	4.20 ± 0.26	0.77
	F08	148.2 ± 0.6	208.0 ± 15.5	4.43 ± 0.25	1.69
2010	Standard	141.3 ± 0.6	137.0 ± 11.3	4.33 ± 0.28	0.92
	G11	139.5 ± 0.6	145.6 ± 12.1	5.56 ± 0.26	1.12
2010-2005	Standard	-5.0 ± 0.8	-46.9 ± 17.7	0.13 ± 0.38	-
	F08/G11	-8.7 ± 0.8	-62.4 ± 19.7	1.13 ± 0.36	-

Table 5.1: Retrieved temperatures and the concentrations of acetylene and ethane at the equator using the standard, F08 and G11 temperature profiles as *a priori* profiles. The goodness-of-fit values are also shown for each retrieval.

The choice of temperature *a priori* yields significantly different acetylene and ethane concentrations with systematically higher concentrations retrieved when the F08 and G11 temperature profiles are used. In particular, the increase in ethane's concentration from 2005 to 2010 is significant with respect to error bars when comparing results in 2005 and 2010 using the F08 and G11 *a priori* temperature profiles. A decrease in acetylene's concentration from 2005 to 2010 is yielded by both the standard and limb temperature *a priori*. Given the decrease in acetylene's concentration observed from 2008 onwards, the agreement with unpublished findings by S. Guerlet and the consistency of this result with respect to the temperature *a priori* used, the reduction of acetylene's concentration at the equator from 2005 to 2010 at the 2.1 mbar level is believed to be robust. In contrast, the increase in ethane's concentration is interpreted with caution since its concentration is constant within error bars until the 2010 result and S. Guerlet did not find a similar trend in ethane from unpublished results from limb observations in 2005 and 2010. In addition, an increase would be puzzling given the observed decrease in acetylene's concentration. Thus, an interpretation of the observed evolution of acetylene and ethane is presented below but assuming ethane is constant in concentration from 2005 to 2010.

The role of Saturn's ring shadow at the equator in 2009 was initially considered. The onset of darkness underneath the rings would halt photochemical production of acetylene and ethane and so their concentrations might be expected to decrease. This would occur on a chemical, rather than photochemical, timescale in the absence of sunlight. A larger decrease might be expected in acetylene compared to ethane since the latter is a saturated hydrocarbon and likely to be chemically more stable. However, it is unlikely that acetylene is unstable on a timescale shorter than the duration of ring shadow on the equatorial latitude band. In addition, the decrease in acetylene's concentration occurs before the ring shadow passes over the equator. Thus, the role of Saturn's ring shadow has been ruled out as an explanation of the observed evolution of acetylene and ethane at the equator.

Instead, a dynamical explanation is favoured. A decrease in acetylene's concentration from 2005 to 2010 without any significant change in ethane's concentration is consistent with upwelling at the equator over this time range advecting hydrocarbon-depleted air from lower altitudes. A significant change is only observed of acetylene owing to its larger vertical gradient in concentration and thus increased sensitivity to vertical motion in comparison to ethane. The maximum in acetylene's concentration at the equator in 2005 is suggestive of downwelling at this time and so the subsequent evolution of equatorial acetylene indicates a reversal in the direction of vertical winds at the equator between this year and 2010. In equatorial oscillations on Earth, downwelling is produced at pressure levels corresponding to temperature maxima while upwelling is observed at pressure levels corresponding to temperature minima (for example, see Baldwin et al. [2001]). The observed meridional maximum in temperature at the equator in 2005 and the subsequent cooling indicates a thermal maximum at the 1-2 mbar level in 2005 descending to lower altitudes and being replaced by a temperature minimum in 2010. Thus, the inferred reversal of vertical winds implied by acetylene's evolution is consistent with the observed thermal evolution of the SSAO from 2005 to 2010 and the observed behaviour of vertical winds in

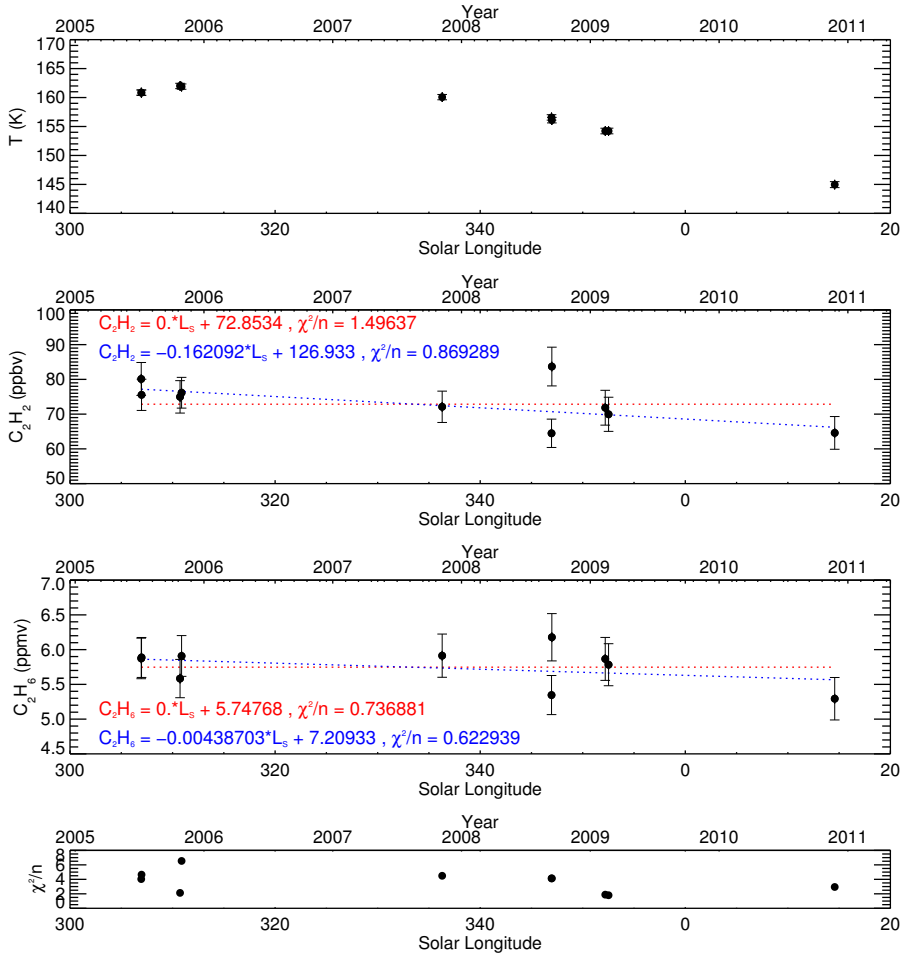

Figure 5.7: The evolution of temperature, acetylene and ethane at 2.1 mbar at 82°S with respect to 2005 results. and the χ^2/n values of each retrieval. For hydrocarbon trends, red dotted lines show the best fit constant trend while blue dotted lines show the best-fit straight line. The equations of these lines and the reduced χ^2 with the data are shown.

equatorial oscillations here on Earth.

5.2.2 Evolution of the south polar vortex

Significant stratospheric cooling at high-southern latitudes is the most striking result in comparing 2005 and 2010 temperatures in Figure 5.1. In addition, a decrease in the concentrations of both acetylene and ethane is observed at latitudes south of 75°S (Figures

5.2 and 5.3). For example, at 82°S, the temperature at the 2.1 mbar level falls by 17.1 ± 0.8 K from 2005 to 2010 and the concentrations of acetylene and ethane decrease from 80.1 ± 4.7 ppbv to 64.6 ± 4.7 ppbv and 5.87 ± 0.29 ppmv to 5.29 ± 0.31 ppmv respectively. Figure 5.7 shows the temporal trends of temperature and the concentrations of acetylene and ethane at 2.1 mbar. As shown, the goodness-of-fit values are generally higher at high-southern latitudes. However, again, this is simply due to the high signal-to-noise ratio of these observations rather than poor fits between modelled and observed spectra as previously exemplified in Figure 4.7 which shows a high-southern latitude retrieval in 2005. In the absence of data coverage from 2006 to late 2007, the temperature appears generally constant from 2005 to 2008 then exhibits a cooling from 2008 onwards. Acetylene's concentration appears to exhibit a general decrease in concentration from 2005 to 2010: the observed temporal variation exhibits a better fit to a decreasing trend rather than a constant one. Ethane's concentrations is constant within error bars from 2005 to early 2009 and the late 2010 result shows a significant decrease with respect to the 2005 result. The observed evolution of ethane's concentration is better fit with a decreasing trend but only with a small improvement with respect to a constant trend.

The significant decrease in temperatures and the changes in acetylene and ethane abundance are possible indications of changes in the structure or strength of the polar vortex. In addition, the southern hemisphere moved from late summer to late Autumn in the 2005 to 2010 time range and so an associated radiative cooling is also expected to have taken place in this date range. In order to assess how much of the observed cooling is radiative or dynamical in cause, a radiative climate model has been computed for this region (computed and provided by T. Greathouse by private communication). This model is the same as that presented in Section 1.4.1. However, in this case, the model was run with the retrieved vertical profiles of temperature, acetylene and ethane in 2005 determined in this work (Figure 4.7). Acetylene and ethane are highly efficient stratospheric coolants and are important to the radiative balance of the stratosphere. Their retrieved

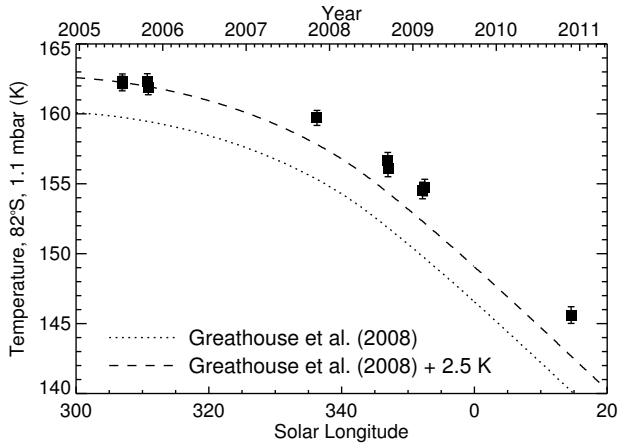

Figure 5.8: A comparison between the observed temperature trend at 82° at 2.1 mbar (points with error bars) and the trend predicted by a radiative climate model (dotted). An offset of 2.5 K has also been added to the model trend (dashed) so that 2005 temperatures match.

concentrations from this work have been used in the climate model for consistency in calculating the cooling rates. The model was run for three consecutive Saturn years until the temperature trends converged. Figure 5.8 compares the observed temperature trend with that predicted by the climate model. At a solar longitude of $L_s = 300°$ (2005), the climate model converges to a thermal profile approximately 2.5 K cooler than observed temperatures. This further suggests that another heating source is required to explain observed temperatures at high-southern latitudes at this time, either in the form of dynamical heating by a polar vortex or possibly a contribution by photoabsorbing aerosols as suggested in Fletcher et al. [2008]. A 2.5 K offset has been added to the model trend in Figure 5.8 for ease of comparison. As shown, the radiative climate model predicts cooling of up to 20 K from a solar longitude of 300° (2005) to 20° (mid 2011) and thus, we can nominally assess the observed cooling at the south pole to be radiative in origin.

However, the observed decrease in the concentrations of acetylene and ethane might imply dynamical changes also taking place in the 2005 to 2010 time range. The shallower profile

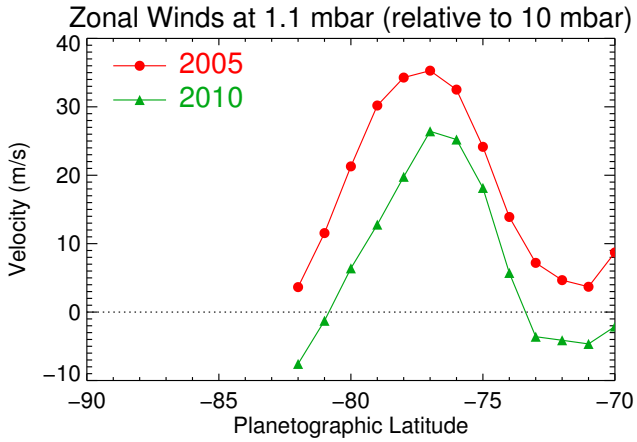

Figure 5.9: The zonal winds at 1.1 mbar in 2005 (red circles) and 2010 (green triangles) at high-southern latitudes (derived from the thermal wind equation). No data was available south of 82°S. These velocities should only be interpreted qualitatively since their derivation relies on integration over an altitude in which there is variable sensitivity in the Cassini-CIRS observations.

in the meridional temperature gradient in 2010 suggest that zonal winds associated with the vortex have weakened. The thermal wind equation (Equation 5.1) has been integrated to assess seasonal changes in the zonal wind field at high-southern latitudes.

$$\Delta u(z_0, z) = \int_{z_0}^{z} \frac{du}{dz} dz' = -\int_{z_0}^{z} \frac{g}{fT} \frac{dT}{dy} dz' \tag{5.1}$$

$\Delta u(z_0, z)$ is the difference in zonal wind speed at altitude, z, with respect to a reference altitude, z_0, $g = GM/R^2_{pole}$ is the polar gravity, $f = 2\Omega sin\Theta$ is the Coriolis parameter (where Θ is latitude), T is temperature and y is the physical distance in the meridional direction. The integration of this equation was computed from 10 mbar up to 0.1 mbar which represents the range of altitudinal sensitivity in the observations. Thus, the derived zonal winds are relative to those at the 10 mbar level. Figure 5.9 compares the derived zonal winds in 2005 and 2010 at high-southern latitudes. As shown, a jet centred on 77°S weakens in strength and wind speeds even become negative/prograde between 2005 and 2010. Thus, the horizontal winds within the polar vortex seem to have weakened in

strength.

However, it is uncertain whether a change in the vertical motion within the vortex has taken place between 2005 and 2010. In 2005, the sharp rise in the meridional profiles of both hydrocarbons indicates the presence of downwelling advecting hydrocarbon-richer air from higher in the stratosphere. Even if the downwelling ceased and the source of hydrocarbon-richer air was removed, the concentrations of both hydrocarbons at this altitude would be expected to remain stable since their photochemical lifetimes predicted to be stable on longer than the 5 year duration of the observations analysed. Thus, if the observed decrease in acetylene and ethane is robust, only upwelling and the dynamical advection of hydrocarbon-depleted air could lead to an overall decrease in concentration. However, upwelling of this sort would also be expected to induce adiabatic cooling as the parcels of air ascend to lower pressures and expand. Yet, the magnitude of observed cooling over this time range is matched (if not exceeded) by a radiative climate model which suggests the observed cooling trend is governed purely by radiative cooling. Thus, vertical motion yielding a decrease in the concentrations of acetylene and ethane does not seem to be consistent with the thermal evolution.

A further possible explanation might be the effects of auroral-induced chemistry on the concentrations of acetylene and ethane. The 2005 to 2009/2010 time period marks the approach to solar minimum and thus auroral activity would be expected to decrease as a result. On Jupiter, auroral processes have been seen to produce spatially-discrete 'hotspots' in CH_4 and C_2H_6 emission, which indicate significant warming and possible chemical enrichments of C_2H_6 in these features (e.g., Kim et al. [1985]). Possible effects of auroral chemistry on the concentrations of acetylene and ethane on Saturn has been suggested in Guerlet et al. [2010]. However, the magnitude of such effects and whether they would propagate to the altitudes sounded on Saturn in this work is yet to be tested in photochemical modelling. Any possible modulation of the concentrations of photochemical species like

acetylene and ethane by the aurora is likely to be larger at lower pressures where these hydrocarbons are less photochemically stable and the atmosphere is more tenuous and thus provides less shielding from charged particles. The vertical diffusion timescale at the 1 mbar level (approximately a Saturn year in length, Moses and Greathouse 2005) is longer than the ∼11 year solar cycle. Therefore, a modulation of hydrocarbons at the 1 mbar level by the effects of the solar cycle at lower pressures is not possible by vertical diffusion alone. However, with the inferred downwelling at the south pole advecting parcels of air from lower pressures where such auroral effects could be taking place, it is possible that the observed decrease in acetylene and ethane is not linked to the polar vortex and in fact would be a reaction to the diminishing auroral activity on approach to solar minimum. Development of photochemical models which couple auroral and seasonal effects on the concentrations of acetylene and ethane may further indicate whether this explanation is likely.

5.2.3 25°N

An enrichment of both acetylene and ethane is observed at 25°N from 2005 to 2009 (Figures 5.2 and 5.3). Figure 5.10 shows observation-model comparisons of the retrievals at 25°N in 2005 and 2009 - the contrast in emission between these two dates is evident in the C_2H_2, C_2H_6 and CH_4 bands. As demonstrated in the retrieved profiles in the same Figure, retrievals indicate the changes in radiance are a result of both temperature and hydrocarbon enrichment. Figure 5.11 shows the evolution of the temperature, acetylene and ethane concentrations at this latitude. There is an initial decrease in temperature from 2005 to late 2006 followed by a subsequent increase with a net temperature increase of 1.1 ± 0.9 K from 2005 to 2010. The initial drop in temperature can be attributed to the ring shadow passing over this latitude band. The subsequent increase in temperature from 2007 onwards is consistent with the magnitude of seasonal warming predicted by

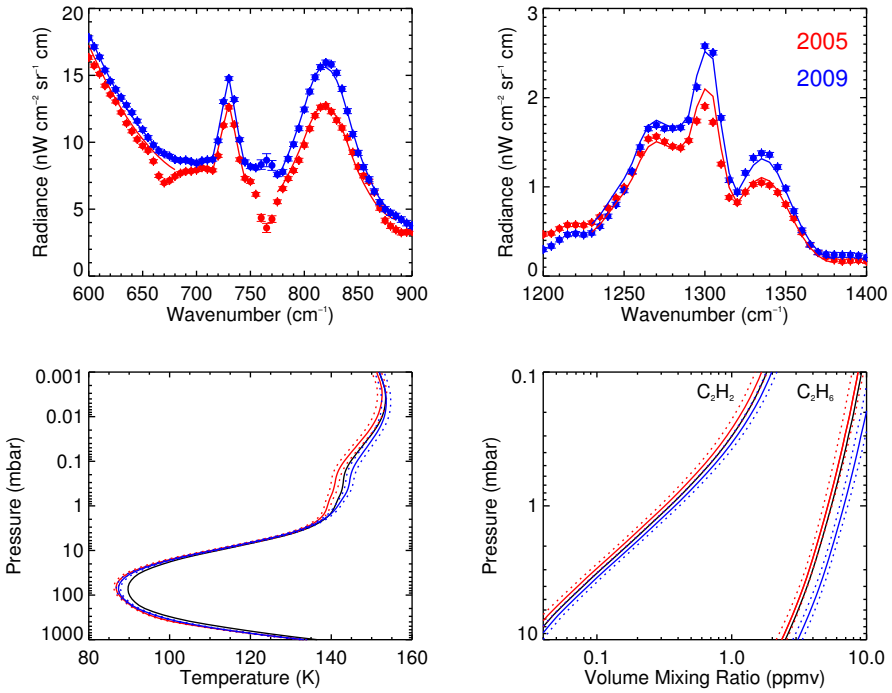

Figure 5.10: Observation-model comparisons and the corresponding retrievals of acetylene and ethane at 25°N in 2005 (red) and 2009 (blue). Black profiles indicate the *a priori* profile, coloured solid profiles show retrieved profiles and dotted profiles indicate the uncertainty on these retrievals.

the radiative climate model by T. Greathouse (Figure 1.3). Acetylene's concentration increases from 144.9 ± 11.8 ppbv to 175.0 ± 13.9 ppbv (21%) and ethane's concentration increases from 4.22 ± 0.27 to 5.36 ± 0.34 ppmv (27%), which is fractionally a larger increase than for acetylene. For both hydrocarbons, the temporal variation from 2005 to 2010 exhibits a better fit to an overall increasing trend rather than a constant one. This reinforces the conclusion of a general increase in their concentration over the 2005 to 2010 time range.

The enrichment of acetylene and ethane from 2005 to 2009 is attributed to be a result of downwelling at this latitude advecting hydrocarbon-richer air from higher in the stratosphere. This result is consistent with the GCM of Saturn's stratosphere presented in

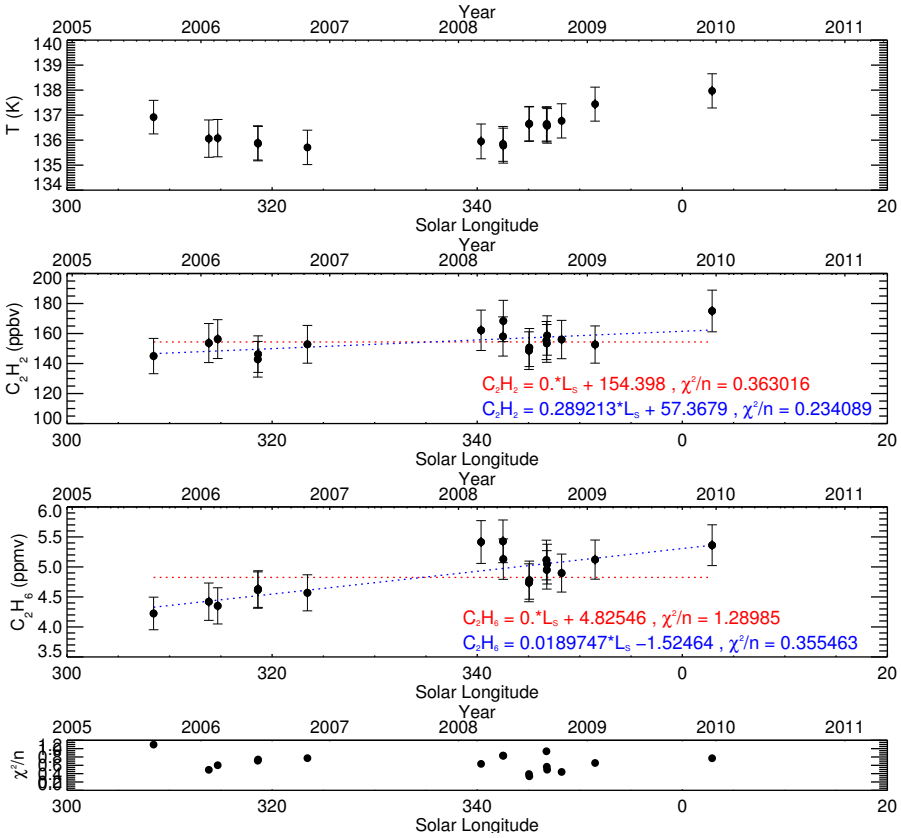

Figure 5.11: The evolution of temperature, acetylene and ethane at 2.1 mbar at 25°N with respect to 2005 results and the χ^2/n values of each retrieval. For hydrocarbon trends, red dotted lines show the best fit constant trend while blue dotted lines show the best-fit straight line. The equations of these lines and the reduced χ^2 with the data are shown.

Section 1.4.3.4. This model is compared with these results in greater detail in Section 5.2.6. It is puzzling that ethane exhibits a larger fractional enrichment with time than acetylene: the latter's vertical gradient in concentration is predicted to be stronger [Moses et al., 2000] and so it would be expected to exhibit a larger response to vertical motion. It is possible that the vertical gradients of acetylene and ethane at this latitude are significantly different from those predicted in Moses et al. [2000] and so the expected relative changes are no longer valid. A further explanation might be that acetylene is chemically unstable upon transport to higher pressures (J. Moses, private communication) and therefore is being chemically lost in the descending air parcels at 25°N.

With parcels of air descending to higher pressures and being compressed, adiabatic heating would also be expected to accompany the hydrocarbon enrichment at this latitude. However, the evolution of temperature at the 2.1 mbar level from 2005 to 2009 is consistent in magnitude with a radiative climate model. This suggests the increasing solar insolation alone can explain the temperature change from 2005 to 2009. However, the meridional profiles of temperature at the 2.1 mbar level in both 2005 and 2009 show a maximum at 25°N, which perhaps indicates the presence of adiabatic heating through downwelling at this latitude.

5.2.4 15°S

Unlike at 25°N, at 15°S, acetylene and ethane exhibit a decrease in concentration from 2005 to 2010 (Figures 5.2 and 5.3). Figure 5.12 shows the evolution of temperature, acetylene and ethane at 15°S from 2005 to 2010. From 2005 to the vernal equinox, the temperature shows an initial decrease of approximately 1.5 K followed by a subsequent increase of 2 K. Ethane's concentration from 4.49 ± 0.31 ppmv in 2005 to 4.28 ± 0.29 ppmv in 2010 (5%) and thus its decrease in concentration is not significant with respect to error bars. Indeed, ethane's temporal variation is best fit with a trend that is approximately constant. Acetylene's concentration decreases from 135.0 ± 11.2 ppbv to 109.1 ± 9.3 ppbv (19.1%) and thus a decrease is significant with respect to error bars when comparing 2005 and 2010 values. However, in considering the overall evolution in acetylene concentrations from 2005 to 2010, the observed variation exhibits a good correspondence to a constant trend with only a marginal improvement in fit to a decreasing trend. A decrease in concentration of acetylene and ethane at 15°S is therefore less obvious from these results. However, an unpublished analysis of limb observations from 2005 to 2010 also indicate a decrease in acetylene and ethane from 2005 to 2010 which adds weight to the validity of a decrease in both species over this time (S. Guerlet, private communication).

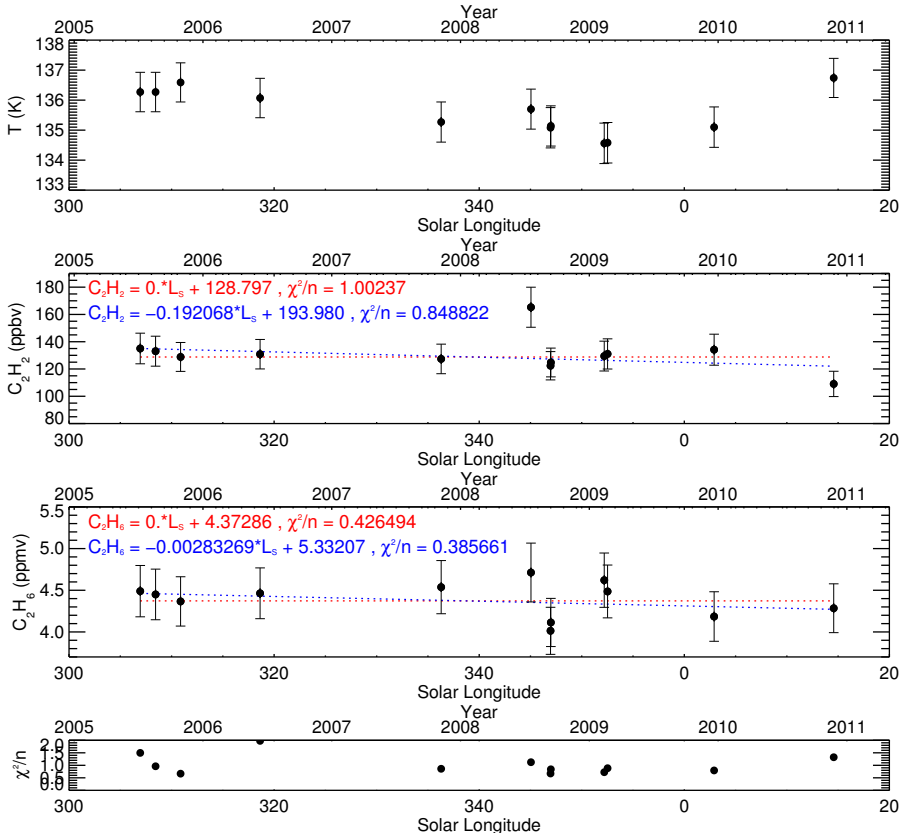

Figure 5.12: The evolution of temperature, acetylene and ethane at 2.1 mbar at 15°S with respect to 2005 results (using retrievals where the standard temperature *a priori* were used) and the χ^2/n values of each retrieval. For hydrocarbon trends, red dotted lines show the best fit constant trend while blue dotted lines show the best-fit straight line. The equations of these lines and the reduced χ^2 with the data are shown.

Figure 5.13 shows observation-model comparisons of the retrievals at 15°S in 2005 and 2010. Unlike the observations at 25°N (Figure 5.10), changes in the concentration of acetylene and ethane are not obvious from the observations alone since the chemical depletion has been accompanied by a slight warming and so radiances in the acetylene and ethane emission features have remained approximately constant. The poorer fit of the model spectrum to the methane band (1230 - 1380 cm^{-1}) in the 2010 observation is noted. This latitude is at the boundary of the region of Saturn's stratosphere modulated by the SSAO and as indicated in Section 5.2.1, retrievals of temperature using our

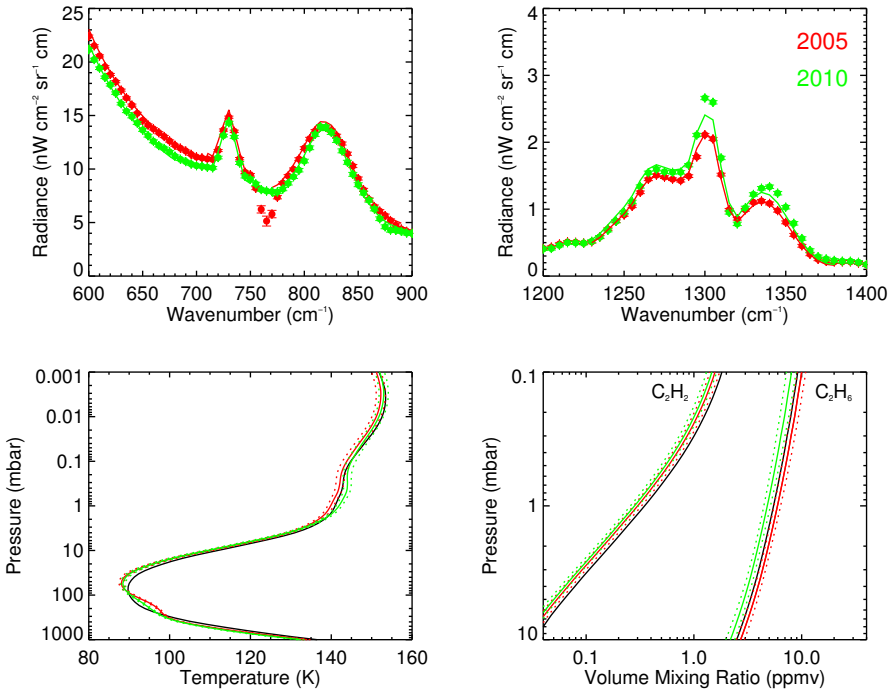

Figure 5.13: Observation-model comparisons and the corresponding retrievals of acetylene and ethane at 15°S in 2005 (red) and 2010 (blue). Black profiles indicate the *a priori* profile, coloured solid profiles show retrieved profiles and dotted profiles indicate the uncertainty on these retrievals. For temperature retrievals, the standard temperature *a priori* profiles has been used. The dip in emission in the 2005 observation at 770 cm^{-1} is not physical and is a result of a calibration spike - this spectral region was not included in the analysis.

standard temperature prior poorly resolve the vertical structure of the SSAO. Retrieval of the vertical temperature profile and the concentrations of acetylene and ethane have therefore been repeated, but instead starting from limb-retrieved temperature profiles at 15°S in 2005 and 2010 [Fouchet et al., 2008; Guerlet et al., 2011] and the result is shown in Figure 5.14. As shown, the fit to the methane feature in 2010 is significantly improved. A decrease in ethane's concentration from 2005 to 2010 is also retrieved using these temperature priors. However, an insignificant change in acetylene's concentration remains - in fact the retrieved concentration is actually higher in 2010 than in 2005 but is constant within the retrieval uncertainty.

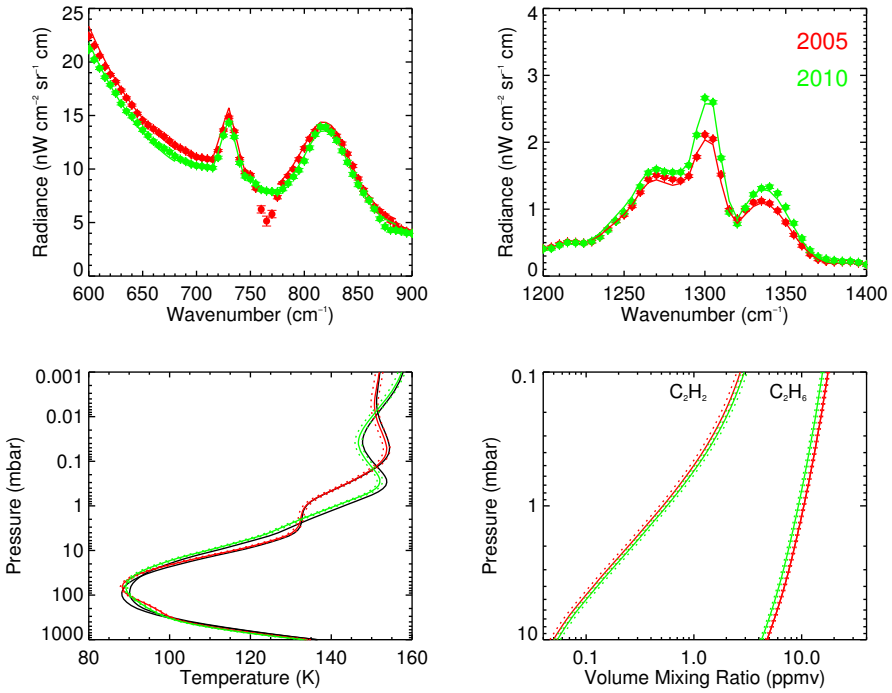

Figure 5.14: The same as for Figure 5.13 but where the limb-retrieved temperature profiles at 15°S in 2005 and 2010 [Fouchet et al., 2008; Guerlet et al., 2011] have been adopted as the temperature *a priori*.

The observed decrease in both hydrocarbon species is suggestive of upwelling at 15°S from 2005 to 2010 which advects hydrocarbon-depleted air from higher pressures. The upwelling induces a larger change in concentration in acetylene compared to ethane due to the former's larger vertical gradient in concentration. As discussed in Section 5.2.6, this result is consistent with a cell of upwelling predicted by a global circulation model [Friedson and Moses, 2012]. Adiabatic cooling would be expected to accompany the upwelling at 15°S as parcels of raise ascend to lower pressures and expand. While the observed temperature trend exhibits an initial cooling, the magnitude of this cooling is consistent with a radiative climate model which predicts a ∼1 K cooling over this time range. The subsequent rise in temperature after the vernal equinox is most likely linked to the evolution of the SSAO which has been seen to modulate the thermal structure from 15°S to 15°N. Adiabatic

cooling associated with upwelling is potentially being masked by the signature of the SSAO.

5.2.5 Northern hemispheric enrichment of ethane

Ethane exhibits an overall enrichment in concentration from approximately 20°S to 75°N in comparing 2005 and 2009 concentrations (Figures 5.2 and 5.3) with the largest enrichments exhibited at 25°N (as discussed in Section 5.2.3) and approximately 57°N. Although the errors bar on ethane concentrations retrieved at these latitudes are larger (indicating larger differences in the concentration retrieved from different calibrated versions of the CIRS datasets), this enrichment still appears robust.

Figure 5.15 shows the evolution of temperature, acetylene and ethane at 57°N as an example. Accompanying an overall increase in temperature, which is consistent in magntitude with that of a radiative climate model (Figure 1.3), is a similar increase in the concentration of ethane. The overall evolution of C_2H_6 is better with an increasing trend rather than a constant trend. Although acetylene also increases in this time and at this latitude, the overall evolution of C_2H_2 can be adequately fitted with a constant trend.

Extensive downwelling is a nominal explanation of the observed increase in ethane in the northern hemisphere from 2005 to 2009. Seasonally-varying Hadley circulation is responsible for the upwelling at 15°S and downwelling at 25°N and it is possible that a similar circulation scheme extends to higher latitudes. Perhaps there is a general hemisphere-to-hemisphere circulation circulation which modulates mid-to-high latitude hydrocarbon concentrations, transporting ethane and other trace species back and forth between the hemispheres on a timescale of half a Saturn year. South of 60°S, both hydrocarbons do exhibit a decrease in concentration from 2005 to 2010 which might indicate the upwelling branch of such a hemisphere-to-hemisphere cell. Oddly, acetylene does not exhibit a similar increase over the latitude range where ethane is shown to increase. However, in the

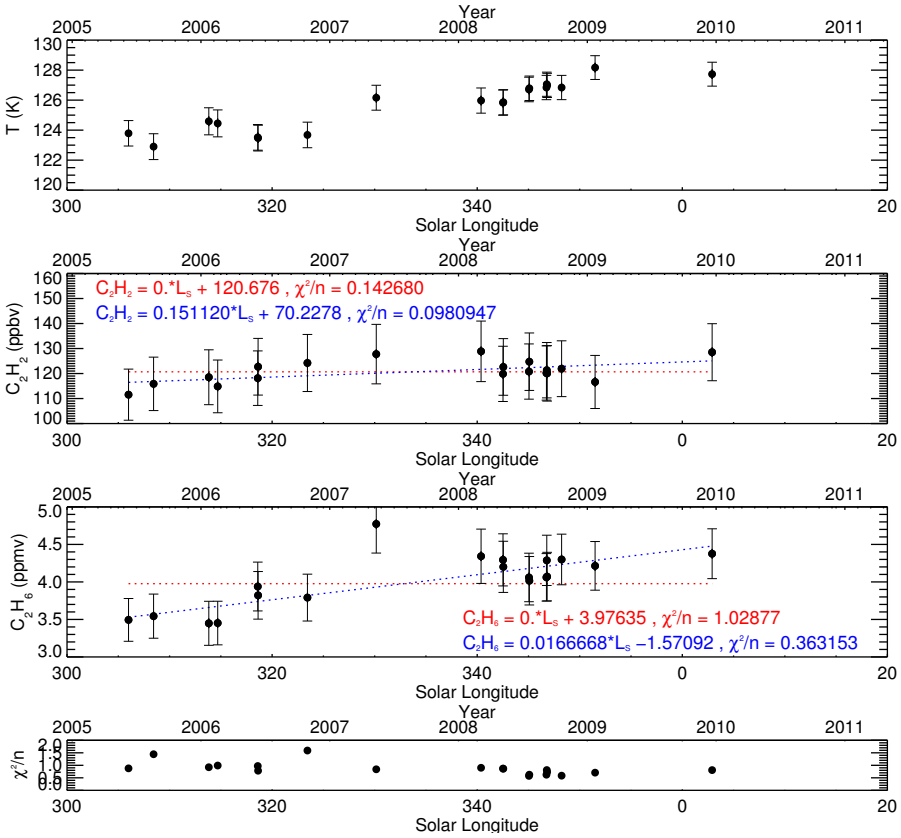

Figure 5.15: The evolution of temperature, acetylene and ethane at 2.1 mbar at 57°N with respect to 2005 results and the χ^2/n values of each retrieval. For hydrocarbon trends, red dotted lines show the best fit constant trend while blue dotted lines show the best-fit straight line. The equations of these lines and the reduced χ^2 with the data are shown.

downwelling at 25°N (Section 5.2.3), acetylene exhibited a lesser enrichment than ethane which was attributed to the former's vulnerability to destruction upon transport to higher pressures. Perhaps this effect is more pronounced at higher northern latitudes.

If this feature in ethane is robust, this enrichment might show early indications of northern hemisphere ethane mimicking the same increase towards the pole as exhibited by the molecule in the southern hemisphere during southern summertime conditions (Figure 5.2). This would confirm that the mechanism producing ethane's meridional enrichment is in fact seasonal in nature and thus has a timescale on the order of half a Saturn year (approximately 15 years) and not on the order of ∼100 years as suggested in previous studies.

As the northern and southern hemispheres continue to evolve upon approach to summer and winter solstices, respectively, and the enrichment of ethane at mid-to-high northern latitudes and the depletion of both hydrocarbons at high-southern latitudes carries on, a reversal of the current hemispheric enrichment in ethane may be observed by 2017. Ethane's meridional enrichment in the southern hemisphere was observed as early as 2002 at the height of southern summer solstice [Greathouse et al., 2005] and so perhaps there was similar transport from the northern to southern hemispheres in southern spring.

5.2.6 Comparison with global-circulation model

The vertical motions implied by the results in Section 5.2.3, 5.2.4 and 5.2.1 were compared with the GCM of Saturn's upper troposphere and stratosphere that was presented in Section 1.4.3.4. The vertical velocities predicted by the model are shown in Figure 1.8.

At 15°S, 25°N: This model shows agreement with the downwelling and upwelling suggested by the observed changes in the concentrations of acetylene and ethane in Sections 5.2.3 and 5.2.4. The results of this work indicate an enrichment of both hydrocarbons (and thus the inferred latitudinal extent of the cell of downwelling) from approximately 18°N to 35°N. However, the model in fact shows positive vertical velocities north of 30°N, which would be expected to induce a decrease in the hydrocarbon abundances. This represents one discrepancy between the results of this work and the GCM. In addition, whilst the model predicts the strongest upwelling to be centred at approximately 10°S, our observed decrease in ethane is most pronounced at 15°S. Results from limb observations also show a decrease in concentration at 15°S, with no significant change at 10°S or 20°S (S. Guerlet, private communication). Friedson and Moses [2012] do acknowledge that their GCM does not fully capture the SSAO and so perhaps in reality waven-driven dynamics at the equator force the cell of upwelling further south. In order to determine the vertical velocities

required to produce the observed changes in concentration of acetylene and ethane in this work, the vertical continuity equation (Equation 5.2 taken from Guerlet et al. [2009]) is solved.

$$\left(\frac{\partial}{\partial t} + \bar{\omega}^* \frac{\partial}{\partial z}\right) \bar{\chi}_i = \bar{S} + \bar{D} \tag{5.2}$$

Here, $\bar{\omega}^*$ is the average vertical velocity over time t, $\bar{\chi}_i$ is the volume mixing ratio of a chemical species i, $\bar{S}$ refers to photochemical sources and sinks and $\bar{D}$ refers to vertical transport by eddy diffusion. For the sake of the calculation, photochemical sources and sinks are assumed to be negligible over the 2005 to 2010 time range. Similarly, vertical diffusion timescales are approximately a Saturn year at the $\sim$1 mbar level [Moses and Greathouse, 2005] and thus can be considered to have negligible effect over the 5 year duration of our observations. Thus, the right-hand size of Equation 5.2 has been set to zero. Under these assumptions, comparison of the vertical velocity from the observed evolution of acetylene and ethane with that of the GCM will highlight whether vertical advection alone can explain the observed evolution of these species. The vertical concentration gradient ($\partial\bar{\chi}_i/\partial z$) was calculated in two different ways - 1) using the retrieved profile in 2005 from this work which represents a constant scale factor applied to the photochemically-predicted profiles from Moses et al. [2000] 2) using vertical profiles retrieved from limb observations at 15°S and 25°N in 2005/2006 by Guerlet et al. [2009] and applying a scale factor such that the 2.1 mbar concentrations were equal to those retrieved in this work.

Table 5.2 shows the derived vertical profiles and the scaling factor applied to the latter set of profiles and the vertical velocities predicted by the GCM for comparison. The vertical velocities derived from the changes in ethane's concentration using both sets of vertical profiles show agreement with the vertical velocities calculated in the GCM. In particular, those derived using the scaled vertical profiles from Guerlet et al. [2009] show

Species	Latitude	Vertical profile	Derived Vertical Velocities (mm/s)	GCM predicted velocity (mm/s)
C_2H_2	15°S	This work	0.014 ± 0.034	0.19
		Guerlet et al., (2009) x 0.91	0.016 ± 0.039	
	25°N	This work	-0.07 ± 0.04	-0.26
		Guerlet et al., (2009) x 0.97	-0.06 ± 0.04	
C_2H_6	15°S	This work	0.15 ± 0.11	0.19
		Guerlet et al., (2009) x 1.00	0.20 ± 0.15	
	25°N	This work	-0.37 ± 0.17	-0.26
		Guerlet et al., (2009) x 0.85	-0.24 ± 0.10	

Table 5.2: The vertical velocities at 15°S and 25°N as derived from the observed changes in acetylene and ethane's concentration between 2005 and 2009/2010.

the best agreement which is expected given the vertical gradients of these species have been constrained by observations at these latitudes. The consistency between vertical velocities derived from the observed changes in ethane and the global circulation models (which does not account for time dependent chemistry) is testament to the fact that ethane's evolution is governed by dynamics. In contrast, the vertical velocities derived from acetylene's observed evolution at both latitudes are inconsistent by almost an order of magnitude. This suggests that chemistry and dynamics both play a role in the evolution of acetylene's concentration at the 2.1 mbar level. At 15°S, a chemical source of acetylene is required to derive a vertical velocity more comparable with the GCM though the form of such a source remains uncertain. At 25°N, a chemical sink of acetylene is required to derive a vertical velocity more comparable to the GCM and that derived from ethane results. As discussed earlier, acetylene is likely being removed by some process as the parcels of air descend to higher pressures.

Equator: The GCM predicts a vertical velocity which, although is positive, is relatively small and therefore unlikely to yield the observed decrease in acetylene's concentration at the equator (Figures 5.2, 5.4). Again, Friedson and Moses [2012] acknowledge that their model has not fully captured the SSAO and so there is less confidence in the predicted

vertical velocities at the equator.

Further qualitative disrepancies exist between the results in this work and those shown in the GCM at other latitudes. For example, the GCM predicts upwelling at 10°N in 2005 and downwelling at 25°S in 2005 and 2009 yet no signficant change in concentration of either hydrocarbon is observed at these latitudes. The vertical motion is likely too weak and/or does not extend a sufficient vertical range to produce an observable change in the hydrocarbon concentrations. Unfortunately, the results of the GCM are not valid at high latitudes and thus no comparison can be drawn with results in Sections 5.2.2 and 5.2.5. At high-southern latitudes where the results imply the presence of a polar vortex, dynamical modelling remains a challenge due to the convergence of grid points. A model which couples a photochemical and dynamical scheme would be ideal in interpreting the observed changes in the concentrations of acetylene and ethane over time.

5.3 Summary

The evolution of temperature and the concentrations of acetylene and ethane from 2005 to 2010 has been derived in this chapter as a measure of variations in the structure and circulation of Saturn's stratosphere over this time period.

A stratospheric cooling is exhibited at the equator from 2005 to 2010 which is attributed to the structure of the SSAO descending with time, as determined in previous studies. The nadir observations struggle to resolve the small-scale vertical structures of the SSAO which is why the magnitude of cooling from 2005 to 2010 was not consistent with Guerlet et al. [2011] and Schinder et al. [2011]. However, use of limb-retrieved temperature profiles at the equator from Guerlet et al. [2011] as *a priori* profiles partly reconciled this discrepancy.

At high-southern latitudes, where the results of Chapter 4 imply the presence of a polar

vortex, a significant cooling of approximately 17 K is observed from 2005 to 2010. The observed cooling trend is matched in magnitude by that predicted from a radiative climate model which nominally suggests this cooling can simply be explained by the seasonal changes in solar insolation and this region cooling radiatively. However, integration of the thermal wind equation showed decreased zonal wind strengths in 2010 compared to 2005 which might suggest a weakening of the polar vortex between these two years. In addition, the concentrations of acetylene and ethane were seen to decrease though it is uncertain whether this is linked with dynamical changes in the vortex or perhaps linked to the diminishing auroral chemistry.

Decreases and increases in the concentrations of acetylene and ethane are observed at 15°S and 25°N respectively. These changes imply upwelling and downwelling at these latitudes respectively. Indeed, a global circulation model predicts this pattern of vertical motion as a result of a seasonally-reversing Hadley circulation. Derivation of the vertical velocities required to explain the observed changes in ethane's concentration from 2005 to 2009 were consistent with that of the GCM which implies ethane's evolution is governed by dynamical advection alone. For acetylene, derived vertical velocities were largely inconsistent with those from the GCM which suggests both chemistry and dynamics play a role in this chemical's evolution.

Chapter 6

Interannual variability in Saturn's stratosphere

Over a Saturn year (approximately 29.5 years) has now passed since the Voyager spacecraft made flybys of Saturn. These spacecraft made their closest approaches to Saturn in November 1980 and July 1981,which correspond to heliocentric solar longitudes of approximately 8° and 17° respectively. These observations, together with those from Cassini-CIRS in the 2009-2010 time range (corresponding to solar longitudes from approximately 355° to 15°), therefore capture Saturn in approximately the same season, but one Saturn year apart. Any differences in Saturn's atmospheric properties implied by a comparison of these two datasets could therefore reveal the extent of interannual variability. In order to investigate any potential interannual differences in Saturn's stratosphere, retrievals of the vertical temperature profile and stratospheric concentrations of acetylene and ethane were conducted from Voyager-IRIS observations and Cassini-CIRS observations in 2009-2010 and compared. These atmospheric quantities serve as metrics of the structure and circulation of the stratosphere as they were used in Chapters 4 and 5.

This work has also been published in Sinclair et al. [2014] though the results are discussed in greater detail in this thesis.

6.1 Observations

6.1.1 Voyager-IRIS

As discussed in Chapter 2, the Voyager 2-IRIS observations are signficantly noiser than those from Voyager 1-IRIS since the interferometer during the former's flyby of Saturn was misaligned. IRIS observations from Voyager 2 have therefore been omitted. Voyager 1-IRIS observations ($\Delta\tilde{\nu} = 4.3$ cm^{-1}) coadded into 10° planetographic latitude bins stepped in increments of 5° have been chosen.

6.1.2 Cassini-CIRS

There was considerable choice in the Cassini-CIRS observations in the 2009 - 2010 time range which could be chosen for comparison. Observations from December 2010 onwards were avoided due to the onset of the northern spring storm at mid-northern latitudes after this time (discussed further in Chapter 8). The 120_001F (November 2009, $L_s \sim 3°$) and 139_002F (October 2010, $L_s \sim 15°$) FIRMAPs were chosen since they offered a latitude sampling and viewing angles most comparable with the IRIS observations, in contrast to the higher spectral resolution datasets from Cassini-CIRS. These observations were similarly sorted into 10° planetographic latitude bins, stepped in increments of 5°, and coadded, as was conducted for Voyager 1-IRIS observations. Observations from the v4.2 calibration were nominally selected. However, coaddition and the subsequent analysis has been repeated for observations of the v3.2 and v4.3 calibrations in order to assess potential sensitivity in the results to the different calibration procedures.

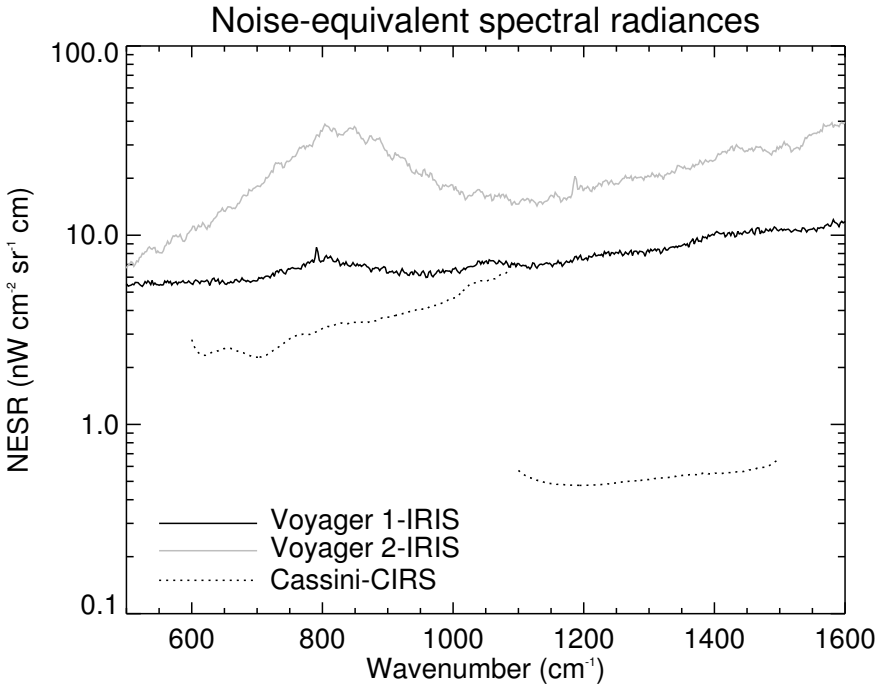

Figure 6.1: A comparison of the noise-equivalent spectral radiances or NESR spectra from Voyager 1-IRIS (black) and Voyager 2-IRIS (grey), as provided by PDS Atmosphere Nodes. These have been calculated as the standard deviation in signal of all deep-space spectra acquired during the Saturn encounter. The NESRs of Cassini-CIRS spectra, which have been scaled for the IRIS spectral resolution, are also shown for comparison.

6.2 Analysis

6.2.1 Radiative transfer modelling

Using the line data shown in Table 3.1, k-distributions for CH_4, PH_3, NH_3, C_2H_2 and C_2H_6 were generated using a Hamming line convolution function of FWHM = 4.3 cm^{-1} in order to model Voyager-IRIS observations of this spectral resolution. The k-distributions used in Chapters 4 and 5 using a triangular line function of 15.5 cm^{-1} were also used in this Chapter to model FIRMAP observations of this spectral resolution.

6.2.2 Testing the retrievability of IRIS observations

A comparison of the CIRS and IRIS datasets of Saturn involved comparing observations with different spectral resolutions and a large difference in the signal-to-noise ratio. In particular, IRIS spectra are significantly noisier at longer wavenumbers. As shown in Figure 6.1, the NESR of the Voyager 1-IRIS data is up to ten times higher than that of Cassini-CIRS at approximately 1300 cm^{-1} in the methane ν_4 band, from which stratospheric temperature is retrieved. In addition, there were fewer IRIS observations available to coadd in each latitude bin in order to increase the signal-to-noise ratio. It was thus important to test whether stratospheric temperature and the concentrations of acetylene and ethane could be retrieved from Voyager 1-IRIS observations, as they are presented in Chapter 2, and compared with the results from FIRMAP observations. In order to test the retrievability of these atmospheric properties from IRIS observations and how comparable such results were with those from CIRS FIRMAP observations, synthetic spectra of these two datasets were forward modelled, using known vertical profiles of temperature and the volume mixing ratios of acetylene and ethane, and random noise consistent with the NESR of both instruments was added to simulate an observed spectrum. Subsequently, the vertical temperature profile and the stratospheric concentrations of acetylene and ethane were retrieved from these synthetic observations: a comparison of the retrieved results with those used to model the synthetic spectrum provided a direct determination of how retrievable the information is from the spectrum.

6.2.2.1 Generating noisy synthetic observations

It was important to generate sets of synthetic spectra using a representative range of stratospheric conditions. 100 model atmospheres were produced each representing a random deviation in temperature and the volume mixing ratios of acetylene and ethane from the reference atmosphere described in Section 3.1.4. A random temperature shift in the

range $-20K < \Delta T < 20K$ was applied to the reference temperature profile in order to signify the approximately 40 K global range in 1-2 mbar temperature observed in this work (Figures 4.3 and 5.2) and previous studies [Fletcher et al., 2010; Guerlet et al., 2009]. Similarly, random scaling factors in the ranges $0.4 < \alpha < 1.3$ and $0.75 < \beta < 1.45$ were applied to the reference profiles of acetylene and ethane, respectively, in order to simulate the meridional variations at the 1-2 mbar level observed (Figures 4.3 and 5.2) and Guerlet et al. [2009]. In addition, a random emission angle in the range $0 < \theta_{emm} < 85$ was associated with each model atmosphere: this range represents the range in emission angle of the Voyager-IRIS and Cassini-CIRS FIRMAP datasets.

Adopting each of these model atmospheres and associated emission angles in turn, 100 synthetic Voyager 1-IRIS observations (at a spectral resolution of ($\Delta\tilde{\nu} = 4.3$ cm^{-1}) and CIRS FIRMAP observations ($\Delta\tilde{\nu} = 15.5$ cm^{-1}) were produced using NEMESIS in forward-model mode with the subsequent addition of random noise. For synthetic IRIS spectra, in order to characterise the range of noise levels on IRIS observations, the Voyager-IRIS NESR spectrum (Figure 2.3) was scaled by a randomised factor of $1/\sqrt{N}$ ($10 < N < 300$) and adopted as the forward modelling error so as to simulate the quality of a Voyager-IRIS spectrum produced from coaddition of N individual spectra. The range in value of N is in accordance with the range of individual IRIS observations coadded (Figure 2.5). For synthetic CIRS spectra, the FP3 and FP4 focal planes were forward-modelled separately and similarly, these spectra were simulated using a range of spectral noise levels representative of the FIRMAP dataset. The Cassini-CIRS NESR spectra (Figure 2.9) was scaled using random factors of $(1/\sqrt{N} + 1/\sqrt{M})$, as detailed in Equation 2.3. This is in order to simulate the noise on a coadded spectrum produced from coaddition of N target spectra which have been calibrated using M deep-space spectra. Ranges of this term were from $1/\sqrt{4443} + 1/\sqrt{4000}$ to $1/\sqrt{12} + 1/\sqrt{315}$ which represent the ranges in N and M of the FIRMAP dataset (Table A.4) which minimise and maximise this factor respectively.

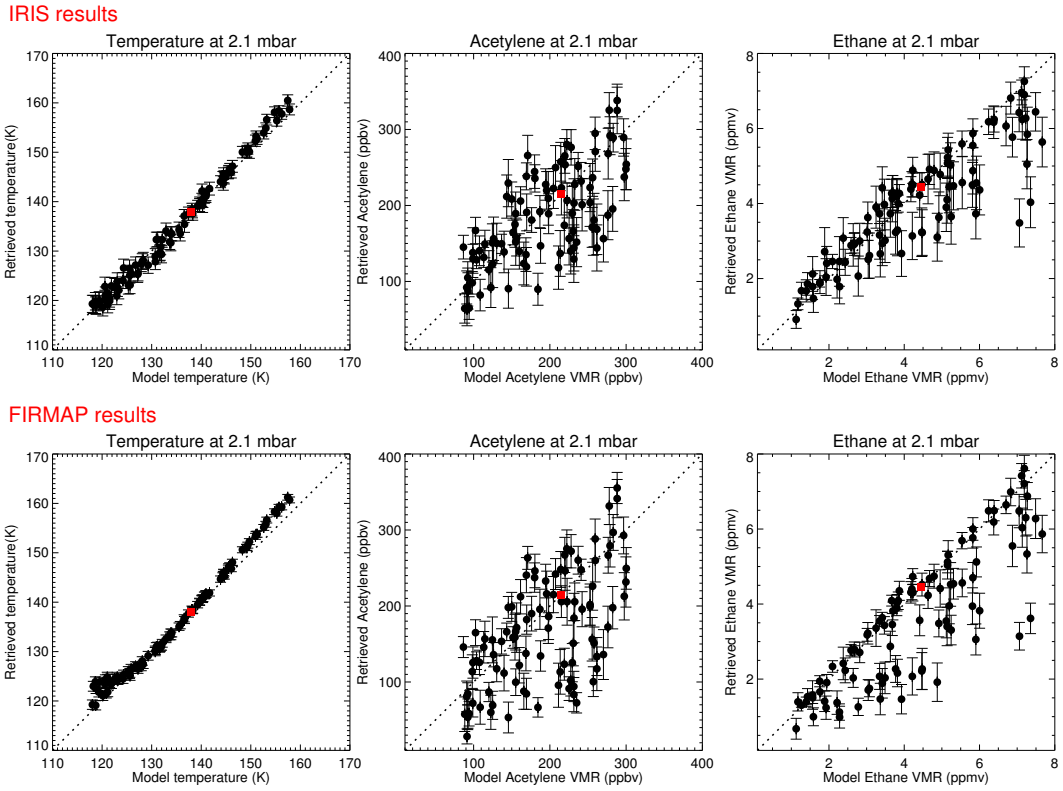

Figure 6.2: A comparison of modelled and retrieved temperatures, acetylene and ethane concentrations at 2.1 mbar from synthetic IRIS ($\Delta\tilde{\nu} = 4.3$ cm^{-1}) and CIRS FIRMAP ($\Delta\tilde{\nu} = 15.5$ cm^{-1}) observations. Red squares indicate the *a priori* value at that altitude.

6.2.2.2 Test retrievals

Using the procedure outlined in Section 4.2, the vertical temperature profile and volume mixing ratios of acetylene and ethane were retrieved from these synthetic IRIS and FIRMAP observations. Figure 6.2 compares the modelled and retrieved values of temperature and the concentrations of acetylene and ethane at 2.1 mbar retrieved from the two synthetic datasets. As shown, a significant number of retrievals reproduce the modelled values within error bars. Figures 6.3 and 6.4 show low and high signal-to-noise ratio examples of retrievals from IRIS and CIRS spectra. However, there are a number of outliers, in particular for retrievals of acetylene and ethane. These outlying retrievals were further

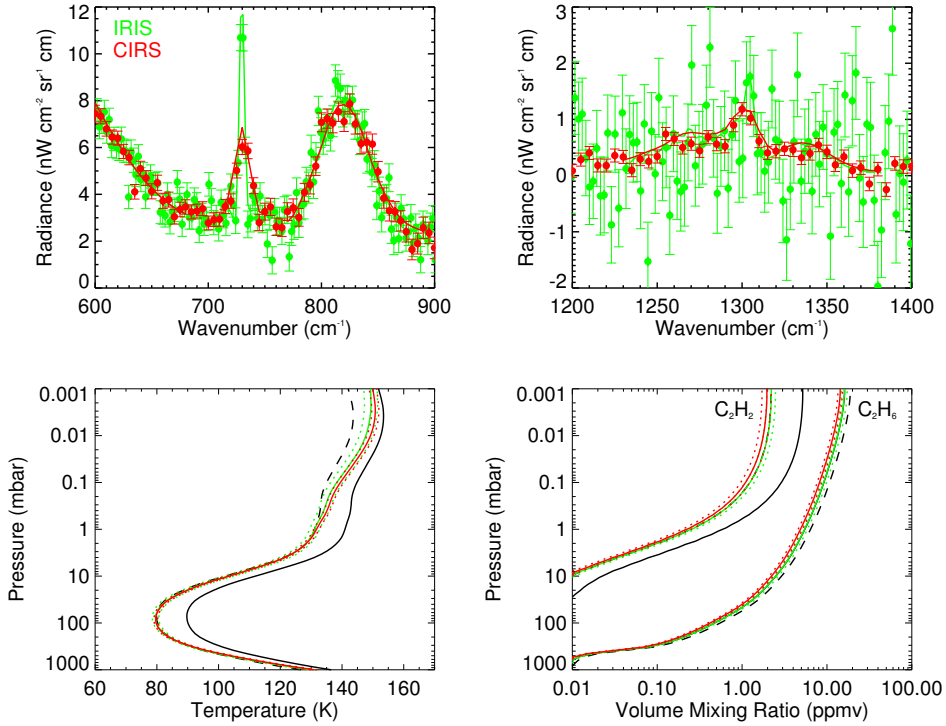

Figure 6.3: An example retrieval from a synthetic IRIS spectrum of a low signal-to-noise ratio and CIRS FIRMAP spectrum using a cooler temperature profile. Green shows IRIS spectra/retrievals and red shows CIRS spectra/retrievals. Solid profiles indicate the reference/*a priori* profile used in the retrieval and and dashed indicate those used to compute the synthetic spectra.

investigated. In order to quantitatively assess the accuracy of each retrieval, the values of $\chi_Y(p)$ (Equation 6.1) were computed.

$$\chi_Y(p) = \frac{|Y_{\text{model}}(p) - Y_{\text{retr}}(p)|}{\sigma_{Y_{retr}}(p)} \tag{6.1}$$

Y_{model} and Y_{retr} are, respectively, the modelled and retrieved values of either temperature or the concentrations of acetylene or ethane at pressure level, p, and $\sigma_{Y_{retr}}$ is the uncertainty in the retrieved value. In retrievals from IRIS observations, it is found that 94% of χ_{T}(2.1 mbar), 65% of $\chi_{\text{C}_2\text{H}_2}$(2.1 mbar) and 85% of $\chi_{\text{C}_2\text{H}_6}$(2.1 mbar) values were less

	χ_{T}	$\chi_{\mathrm{C_2H_2}}$	$\chi_{\mathrm{C_2H_6}}$	T	$\mathrm{C_2H_2}$	$\mathrm{C_2H_6}$	θ_{EMM}	$1/\sqrt{N}$	χ^2/n
χ_{T}	-	0.41	0.11	-0.56	-0.03	-0.31	0.34	-0.1	-0.18
$\chi_{\mathrm{C_2H_2}}$	0.41	-	-	-0.86	0.34	0.1	0.2	-0.01	0.13
$\chi_{\mathrm{C_2H_6}}$	0.11	-	-	-0.57	0.22	0.63	0.1	0.01	0.13
T	-0.56	-0.86	-0.57	-	-	-	-	-	-0.22
$\mathrm{C_2H_2}$	-0.03	0.34	0.22	-	-	-	-	-	-0.05
$\mathrm{C_2H_6}$	-0.31	0.1	0.63	-	-	-	-	-	-0.12
θ_{EMM}	0.34	0.2	0.1	-	-	-	-	-	-0.15
$1/\sqrt{N}$	-0.1	-0.01	-0.01	-	-	-	-	-	0.84
χ^2/n	-0.18	0.13	0.13	-0.22	-0.05	-0.12	-0.15	0.84	-

Table 6.1: Correlation coefficients of the values of χ_{T}, $\chi_{\mathrm{C_2H_2}}$ and $\chi_{\mathrm{C_2H_6}}$ (as defined in Equation 6.1), the temperature, T, acetylene, $\mathrm{C_2H_2}$, and ethane, $\mathrm{C_2H_6}$, concentrations at 2.1 mbar, the emission angle, θ_{EMM}, the scaling factor applied to the NESR, $1/\sqrt{N}$, which serves as a measure of the noise on the synthetic spectrum, and the goodness-of-fit value, χ^2/n for retrievals from synthetic IRIS observations.

	χ_{T}	$\chi_{\mathrm{C_2H_2}}$	$\chi_{\mathrm{C_2H_6}}$	T	$\mathrm{C_2H_2}$	$\mathrm{C_2H_6}$	θ_{EMM}	$1/\sqrt{N}+$ $1/\sqrt{M}$	χ^2/n
χ_{T}	-	0.30	0.17	-0.40	0.01	0.04	0.4	-0.11	-0.58
$\chi_{\mathrm{C_2H_2}}$	0.30	-	-	-0.88	0.22	-0.01	0.24	-0.18	0.38
$\chi_{\mathrm{C_2H_6}}$	0.17	-	-	-0.85	0.02	0.20	0.16	-0.15	0.48
T	-0.40	-0.88	-0.85	-	-	-	-	-	-0.39
$\mathrm{C_2H_2}$	0.01	0.22	0.02	-	-	-	-	-	-0.08
$\mathrm{C_2H_6}$	0.04	-0.09	0.20	-	-	-	-	-	-0.07
θ_{EMM}	0.40	0.24	0.16	-	-	-	-	-	-0.05
$1/\sqrt{N}$	-0.11	-0.18	-0.15	-	-	-	-	-	0.39
χ^2/n	-0.58	0.38	0.48	-0.39	-0.08	-0.07	-0.05	0.39	-

Table 6.2: Correlation coefficients of the values of χ_{T}, $\chi_{\mathrm{C_2H_2}}$ and $\chi_{\mathrm{C_2H_6}}$ (as defined in Equation 6.1), the temperature, T, acetylene, $\mathrm{C_2H_2}$, and ethane, $\mathrm{C_2H_6}$, concentrations at 2.1 mbar, the emission angle, θ_{EMM}, the scaling factor applied to the NESR, $1/\sqrt{N} + 1/\sqrt{M}$, which serves as a measure of the noise on the synthetic spectrum, and the goodness-of-fit value, χ^2/n for retrievals from synthetic CIRS FIRMAP observations.

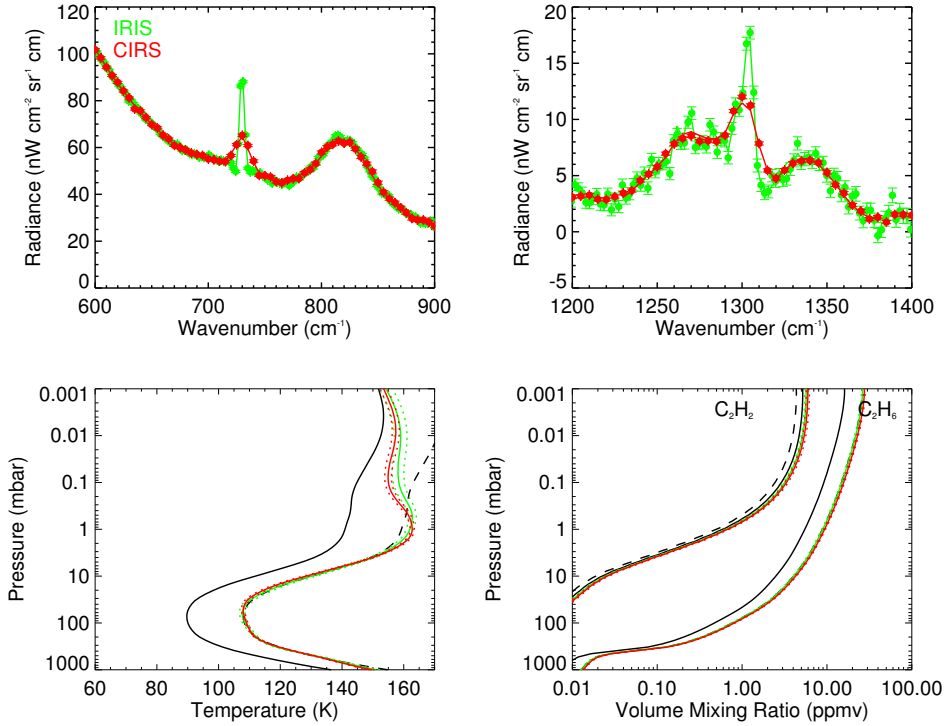

Figure 6.4: An example retrieval from a synthetic IRIS spectrum of a high signal-to-noise ratio and CIRS FIRMAP spectrum using a warmer temperature profile. Green shows IRIS spectra/retrievals and red shows CIRS spectra/retrievals. Solid profiles indicate the reference/*a priori* profile used in the retrieval and and dashed indicate those used to compute the synthetic spectra.

than 2, which signifies modelled and retrieved results matching within 2σ. In retrievals from FIRMAP observations, 63% of χ_{T}(2.1 mbar), 49% of $\chi_{\mathrm{C_2H_2}}$(2.1 mbar) and 49% of $\chi_{\mathrm{C_2H_6}}$(2.1 mbar) values are less than 2. Nominally, this would suggest that stratospheric temperature and the concentrations of acetylene and ethane are more retrievable from IRIS observations, however, Figure 6.2 displays a similar scatter in the retrieval of all three parameters from both datasets. The fewer number of retrievals with values of $\chi < 2$ appears to be an artefact of the higher signal-to-noise ratio of FIRMAP observations and thus smaller error bars on the corresponding retrieved results.

A correlation analysis was conducted in order to investigate whether certain sets of pa-

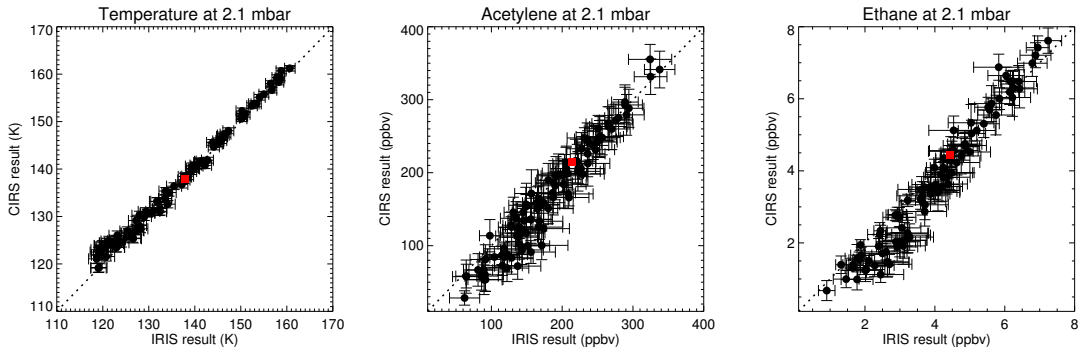

Figure 6.5: A comparison of temperatures, acetylene and ethane concentrations retrieved at the 2.1 mbar level from synthetic IRIS and CIRS FIRMAP observations of the same model atmosphere. Red squares indicate the *a priori* value at that altitude.

rameters of the synthetic spectra yielded a poorer comparison of modelled and retrieved results. Tables 6.1 and 6.2 shows correlation coefficients of the values of χ_{T}, $\chi_{\mathrm{C_2H_2}}$ and $\chi_{\mathrm{C_2H_6}}$ with the properties of the synthetic spectra. As shown for the retrievals of both datsets, there is a correlation of $\chi_{\mathrm{T}}(2.1\ \mathrm{mbar})$ with $\chi_{\mathrm{C_2H_2}}(2.1\ \mathrm{mbar})$ which suggests that slight discrepancies in the retrieval of temperature can similarly induce discrepancies in the retrieval of acetylene's concentration. The correlation coefficient of $\chi_{\mathrm{T}}(2.1\ \mathrm{mbar})$ with $\chi_{\mathrm{C_2H_6}}(2.1\ \mathrm{mbar})$ is smaller indicating that retrievals of ethane's concentrations are less vulnerable to discrepancies in the retrieved temperature. However, χ_{T}, $\chi_{\mathrm{C_2H_2}}$ and $\chi_{\mathrm{C_2H_6}}$ exhibit significant negative correlations with the modelled temperature atmosphere at the 2.1 mbar level: retrievals from spectra of a cooler stratosphere are generally less accurate. This is intuitive given a cooler atmosphere emits less signal in the thermal infrared and so the signal-to-noise of the observation is lower. There is also a negative correlation of χ^2/n (goodness-of-fit) to the modelled temperature: a poorer fit of the modelled spectra to the observations can partly indicate which retrievals have less accurately inverted the stratospherc temperature and concentrations of acetylene and ethane.

For retrievals of synthetic IRIS spectra, there is negligible correlation between the value of $1/\sqrt{N}$ (which serves as a proportional measure of the noise on the spectrum) with the

values of χ_{T}, $\chi_{\mathrm{C_2H_2}}$ and $\chi_{\mathrm{C_2H_6}}$. This suggests the noisier nature of IRIS observations does not immediately hinder the retrievability of stratospheric temperature, acetylene and ethane. For retrievals of synthetic FIRMAP observations, $1/\sqrt{N}+1/\sqrt{M}$, which similarly describes the noise on the synthetic spectrum), exhibits a small, negative correlation with χ_{T}, $\chi_{\mathrm{C_2H_2}}$ and $\chi_{\mathrm{C_2H_6}}$ which indicates that retrievals from observations of a higher signal-to-noise ratio are less accurate. This is most likely an artefact of the higher signal-to-noise resulting in smaller error bars on the retrieved quantities which, from Equation 6.1, results in a higher value of χ.

In conclusion, it appears that stratospheric temperature, acetylene and ethane are generally retrievable from the Voyager 1-IRIS and Cassini-CIRS FIRMAP datasets. Retrievals of temperature of a cooler atmosphere are less accurate and this is in turn introduces errors into the retrievals of the concentrations of acetylene and ethane. This potential source of error is noted in interpreting results in Section 6.3. However, this potential source of error is true of retrievals from both synthetic datasets. Figure 6.5 compares the results retrieved from the synthetic IRIS and synthetic FIRMAP observations. As shown, there is very good correspondence in the retrieved temperatures and concentrations at the 2.1 mbar level. Although the retrieval procedure in some cases does not return the modelled value within 2σ for reasons as described above, it appears these sources of discrepancy are systematic. Thus, despite the differing spectral resolution and noise levels on the IRIS and FIRMAP observations, it seems that results retrieved from these datasets can be directly compared.

6.2.3 Brightness temperature variations

Results of retrievals of the stratospheric temperature and the concentrations of acetylene and ethane are presented in Section 6.2.5. However, variations in the brightness at certain spectral regions in the observations alone can provide an initial assessment of potential

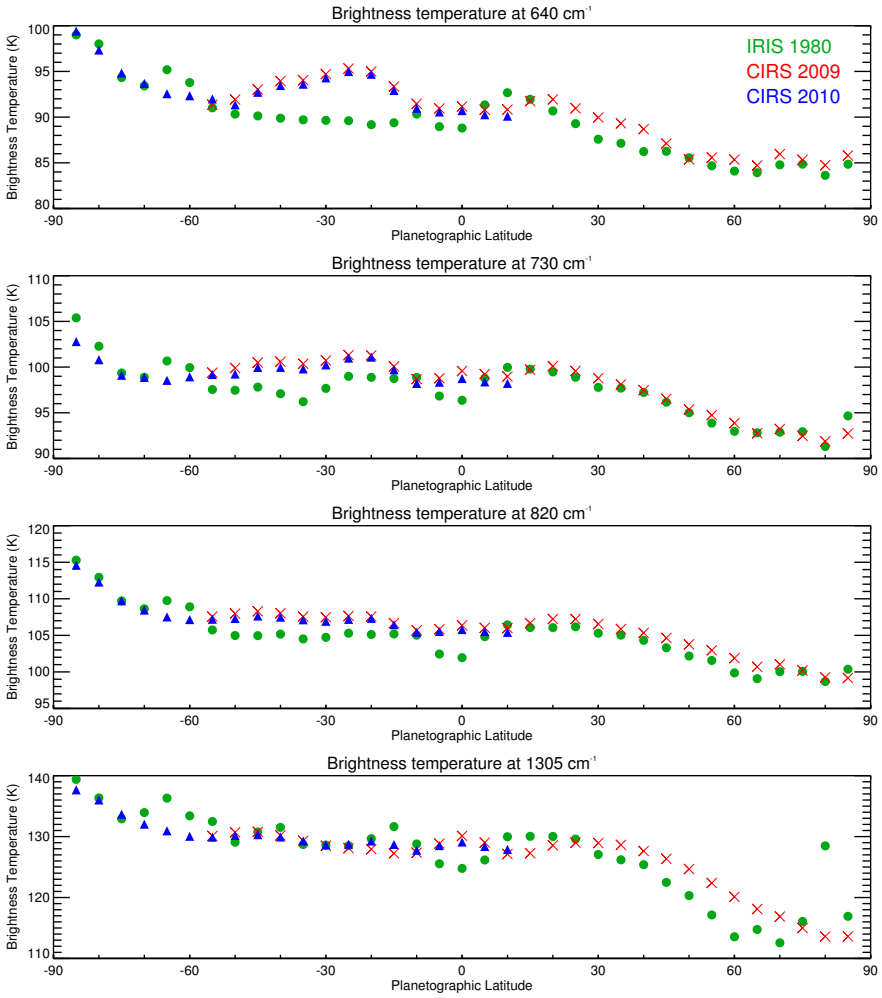

Figure 6.6: The brightness temperatures from collision-induced absorption (averaged from 600 to 680 cm^{-1}), the acetylene band (averaged from 710 to 750 cm^{-1}), the ethane band (averaged from 770 to 890 cm^{-1}) and methane band (averaged from 1230 to 1380 cm^{-1}) from IRIS observations in 1980 (green circles) and CIRS observations in 2009 and 2010 (red crosses and blue triangles respectively).

differences between the CIRS and IRIS datasets. Figure 6.6 compares the brightness temperatures from these datasets in the collision-induced spectrum ($\sim$640 cm^{-1}), acetylene ($\sim$730 cm^{-1}), ethane ($\sim$820 cm^{-1}) and methane bands ($\sim$1300 cm^{-1}). As shown, there are generally higher brightness temperatures in the southern hemisphere which was expected given that both Voyager-IRIS and Cassini-CIRS datasets capture Saturn in late southern

summer/early southern autumn. There appeared to be discrepancies in the brightness temperatures at all three spectral regions at the equator between CIRS and IRIS observations which nominally indicated differences in the stratospheric thermal structure between 1980 and 2009/2010. This was explored further in Section 6.3.1.

6.2.4 Convolving Voyager-IRIS observations

In order to increase the signal-to-noise ratio of these observations and for consistency with the spectral resolution of the FIRMAP observations chosen for comparison (Section 6.1.2), the $\Delta\tilde{\nu} = 4.3$ cm^{-1} IRIS observations were convolved to a spectral resolution of $\Delta\tilde{\nu} = 15.5$ cm^{-1} to produce a second set of higher signal-to-noise ratio but lower spectral resolution observations. Both the Cassini-CIRS and Voyager-IRIS instruments exhibit a Hamming line function, which at low spectral resolutions can be approximated by a triangular line function. Thus, in order to convolve the Voyager-IRIS spectra to $\Delta\tilde{\nu} = 15.5$ cm^{-1}, they were smoothed twice using a moving boxcar average, which resulted in a triangular smoothing.

A χ^2 analysis of a synthetic, convolved $\Delta\tilde{\nu} = 4.3$ cm^{-1} spectrum and a synthetic $\Delta\tilde{\nu} = 15.5$ cm^{-1} spectrum was conducted in order to determine the width of the boxcar with which to smooth by twice. Synthetic spectra of the reference Saturnian atmosphere (Section 3.1.4) at zero emission angle were computed at $\Delta\tilde{\nu} = 4.3$ cm^{-1} and $\Delta\tilde{\nu} = 15.5$ cm^{-1} using Hamming and triangular line functions respectively: these are shown in Figure 6.7. Using a boxcar of varying widths from 8 cm^{-1} to 25 cm^{-1}, the synthetic IRIS spectrum was smoothed twice and χ^2 calculated each time to determine how well the smoothed synthetic IRIS spectrum matched the synthetic FIRMAP spectrum. Figure 6.7 shows the results of the χ^2 analysis: a boxcar smoothing width of 14.30 cm^{-1} was found to yield a smoothed spectrum most consistent with the synthetic FIRMAP spectrum. All Voyager 1-IRIS coadded spectra at their original spectral resolution of $\Delta\tilde{\nu} = 4.3$ cm^{-1}

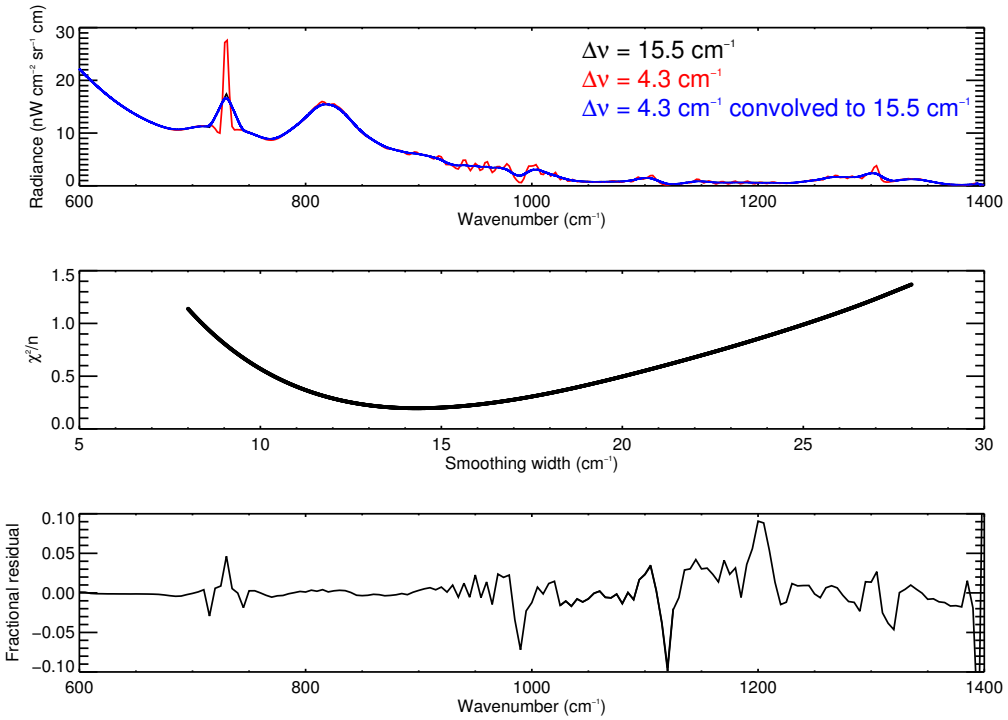

Figure 6.7: The synthetic $\Delta\tilde{\nu} = 15.5$ cm^{-1} (black) and $\Delta\tilde{\nu} = 4.3$ cm^{-1} (red) spectra. The blue spectrum is the $\Delta\tilde{\nu} = 4.3$ cm^{-1} spectrum convolved to $\Delta\tilde{\nu} = 15.5$ cm^{-1} using a double boxcar of width 14.3 cm^{-1}. This best fit width was determined by a χ^2/n analysis (middle). The fractional residual between the $\Delta\tilde{\nu} = 15.5$ cm^{-1} and the convolved $\Delta\tilde{\nu} = 4.3$ cm^{-1} spectrum is shown in the bottom plot.

were smoothed twice using a boxcar of width 14.3 cm^{-1} in order to produce spectra of a spectral resolution of 15.5 cm^{-1}. In order to estimate the noise on the convolved IRIS observation, the NESR spectrum (Figure 2.3) was similarly smoothed twice using a boxcar 14.30 cm^{-1} in width and then scaled by a factor of $\sqrt{4.3/15.5N}$ where N is the number of spectra coadded that were initially coadded and the factor of $\sqrt{4.3/15.5}$ accounts for the increase in signal-to-noise ratio at the lower spectral resolution.

6.2.5 Retrievals

The vertical temperature profile and the stratospheric concentrations of acetylene and ethane were retrieved simultaneously using the procedure and spectral regions described in Chapter 3. Retrievals from IRIS observations were conducted at both their original spectral resolution of $\Delta\tilde{\nu} = 4.3\text{cm}^{-1}$ and from the observations which have been convolved down to $\Delta\tilde{\nu} = 15.5\text{cm}^{-1}$. Retrievals from CIRS observations were conducted independently using the v3.2, v4.2 and v4.3 calibrated spectra.

6.3 Results

Figure 6.8 shows the distribution of retrieved vertical temperature profiles in 1980, 2009 and 2010. Figure 6.9 compares the meridional distributions of tropopausic temperature at 145.1 mbar, stratospheric temperatures and concentrations of acetylene and ethane at 2.1 mbar, at which there is greatest sensitivity.

Retrievals of Voyager 1-IRIS observations are their original spectral resolution of $\Delta\tilde{\nu} = 4.3$ cm^{-1} and those convolved to $\Delta\tilde{\nu} = 15.5$ cm^{-1} were generally very similar. Figure 6.9 shows the results using retrievals of 4.3 cm^{-1} observations however the error bars on these values reflect differences in retrieved quantities when the $\Delta\tilde{\nu} = 15.5$ cm^{-1} observations were used instead. Similarly, results are shown for retrievals of Cassini-CIRS observations of the v4.2 calibration however error bars include the values retrieved from alternative calibrations. As was seen in Chapters 4 and 5, small differences in the radiance baseline level with different calibration versions has a larger effect at high-northern latitudes where the thermal infrared signal is low and thus error bars on CIRS measurements are large in this region, and in some latitude bands, appear larger than those on IRIS measurements. This might give the impression that IRIS measurements have a better sensitivity than CIRS, however, as demonstrated in Figure 6.1, the opposite is true. The available of several

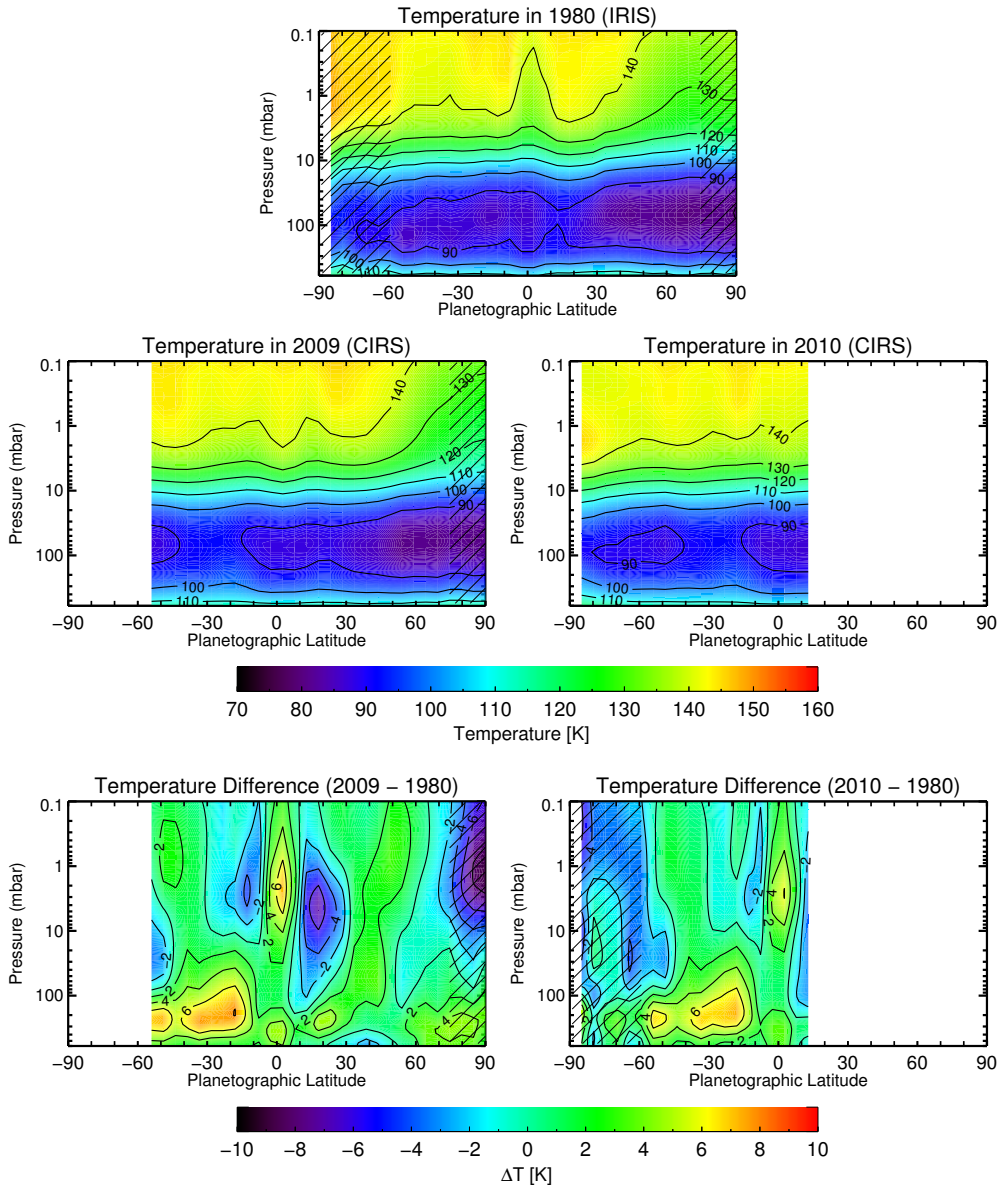

Figure 6.8: The retrieved distributions of the vertical temperature profile in 1980, 2009 and 2010 and their differences.

calibration versions of CIRS measurements have allowed differing calibration approaches in the CIRS pipeline to be characterised as an uncertainty on a retrieved quantity. However, only one calibration version of IRIS measurements was available from PDS.

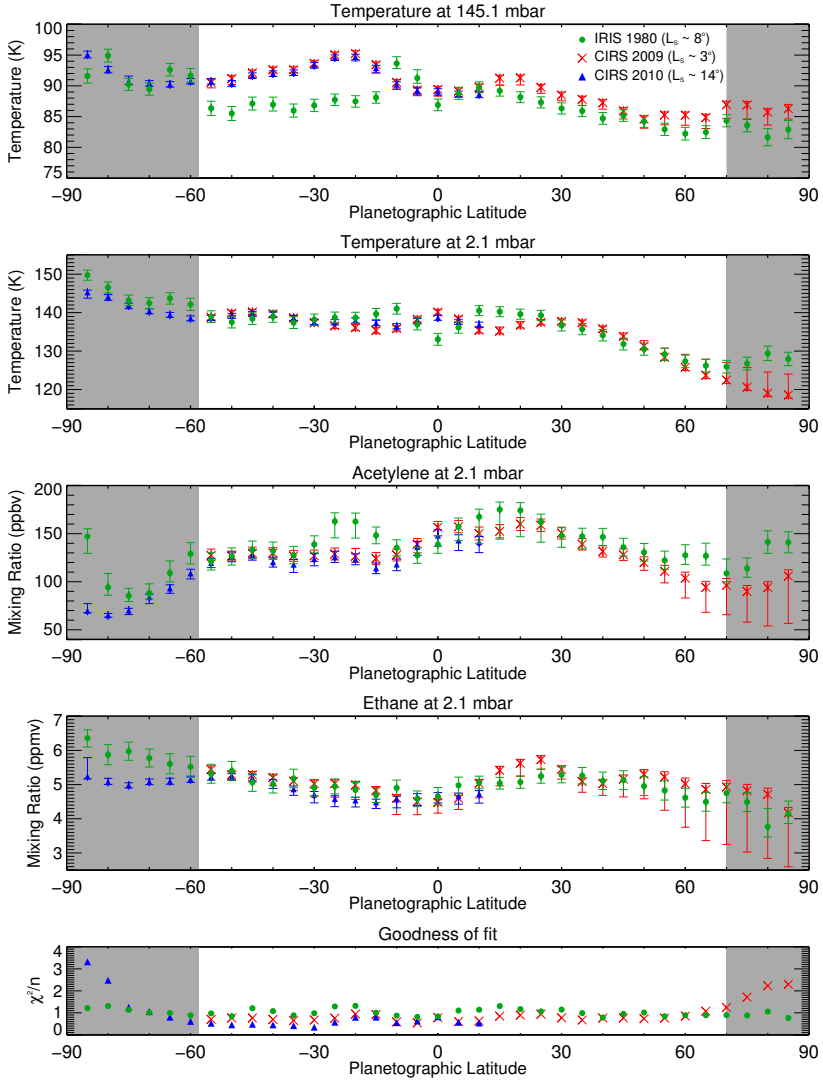

Figure 6.9: The temperatures at 145.1 mbar and 2.1 mbar and the concentrations of acetylene and ethane at 2.1 mbar, as a function of planetographic latitude from Voyager-IRIS observations in 1980 (green circles), Cassini-CIRS in 2009 (red crosses) and 2010 (blue triangles). Results from Cassini-CIRS observations using the v4.3 calibration are shown, but the error bars have been increased in size to include the result retrieved from the v3.2 calibration if this outlied by greater than 1σ. Similarly, results retrieved from Voyager 1-IRIS observations at the original spectral resolution of $\Delta\tilde{\nu} = 4.3$ cm^{-1} are shown, but error bars have been increased to include the value retrieved from the convolved $\Delta\tilde{\nu} = 15.5$ cm^{-1} IRIS spectra if this outlied by greater than 1σ. The shaded regions at high latitudes indicate little confidence in the results due to the low signal-to-noise of these observations.

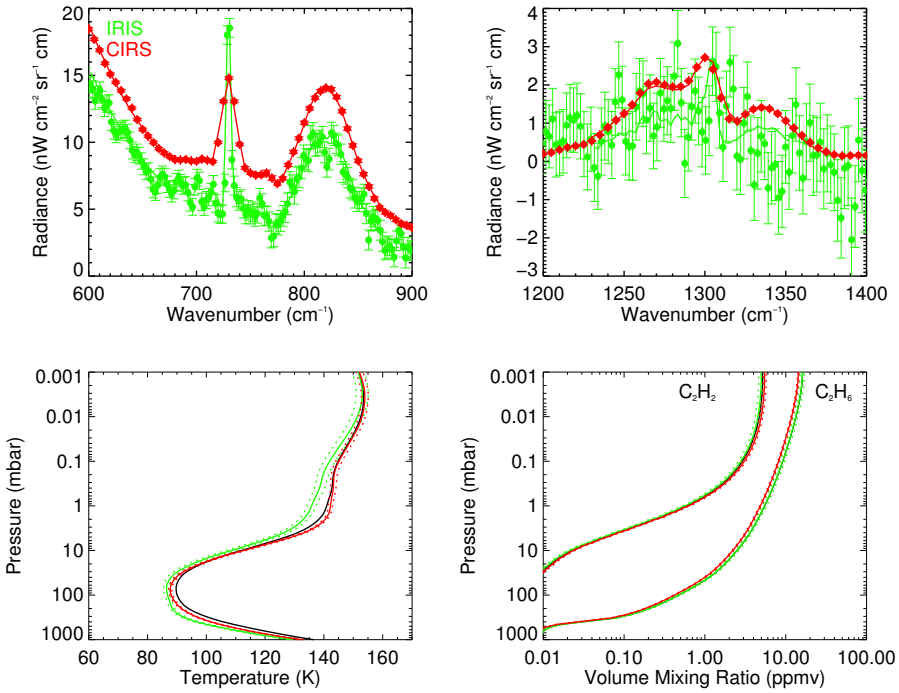

Figure 6.10: Observation-model comparisons at the equator: Voyager 1-IRIS observations (blue points) and Cassini-CIRS observations in 2009 (red points) and the corresponding modelled spectra (solid) in the same colours. The *a priori*, retrieved profiles and their uncertainty are shown as black solid, coloured solid (using colours as above) and coloured dotted lines.

6.3.1 Equatorial thermal anomalies

There are differences in the stratospheric thermal structure from approximately 20°S to 20°N. At the equator, temperatures at the 2.1 mbar level are 7.5 ± 1.6 K warmer in 2009 with respect to 1980 while at 10°S and 10°N, temperatures at the same altitude are respectively 2.5 ± 1.6 K and 4.8 ± 1.4 K *cooler* in 2009 with respect to 1980.

Figure 6.10 shows the retrieved temperature profile at the equator in 1980 and the corresponding modelled and observed spectra. While the modelled spectra exhibit a good fit to the observations at wavenumbers of less than 900 cm^{-1}, the data is significantly noisier and the model fits poorer in the methane ν_4 band from which the stratospheric temperature

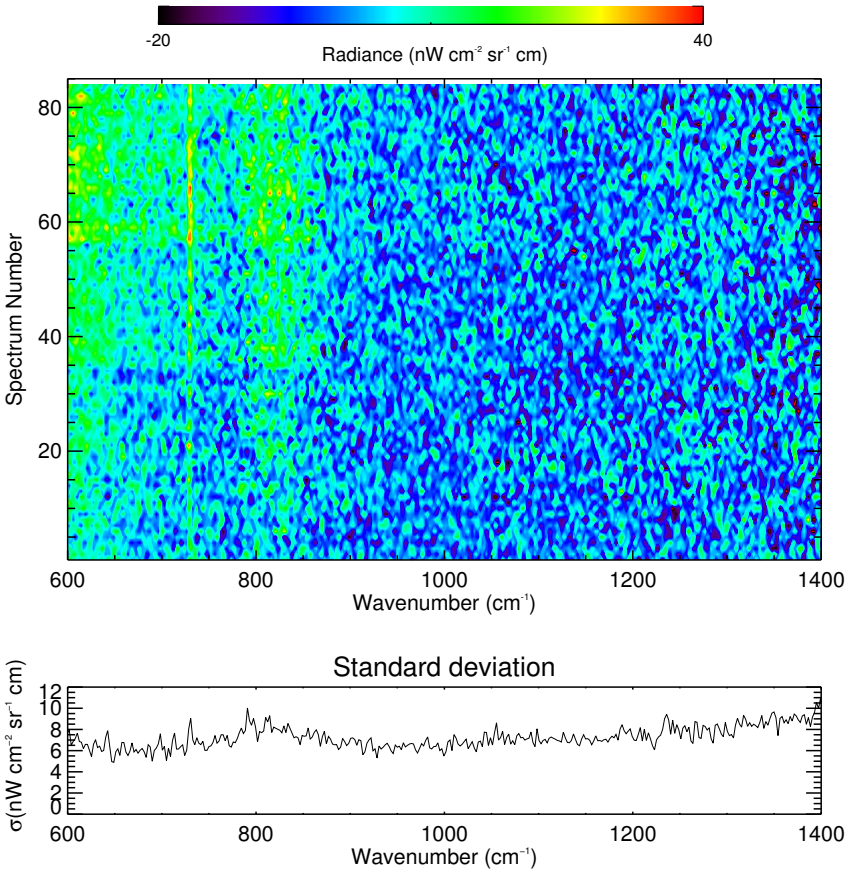

Figure 6.11: All individual Voyager 1-IRIS observations acquired from 5°S to 5°N which were coadded to produce the equatorial observation.

is retrieved. However, despite the poorer quality IRIS spectra and corresponding model fits at the equator, the observed contrasts in the thermal structure between 1980 and 2009/2010 are still considered to be robust and not artefacts of the observations and/or retrieval procedure as will now be discussed.

6.3.2 Is this result an artefact of the observations?

Figure 6.11 shows an image of all individual spectra obtained between 5°S and 5°N which have been averaged together to produce the coadded spectrum at the equator. It is

comforting that all individual spectra used to produce the equatorial IRIS coadd are generally consistent and there is a low standard deviation in the radiance. For instance, one spectrum obtained in this latitude range could be unphysical or low in radiance and offsetting radiances to be lower in the coadded spectrum. However, this does not appear to be the case for the IRIS observation at the equator. Even after coaddition of these observations, the resultant, averaged spectrum is still noisy due to the the limited number of observations in this latitude range and the higher NESR of the IRIS instrument. A comparison of this observation with those from Cassini-CIRS does involve comparing two spectra of highly different noise levels. However, as demonstrated in the test retrievals of synthetic observations in Section 6.2.2, which simulate the differing sensitivites of the two datasets, retrievals of temperature from these two datasets are directly comparable. The validity of the Voyager-IRIS observations and their comparability with those from Cassini-CIRS can also be assessed by the agreement in the retrieved results at other latitude ranges. Retrieved stratospheric temperatures at mid-southern and mid-northern latitudes exhibit good agreement between 1980 and 2009/2010. In particular, mid-southern observations from Voyager-IRIS have been produced from coaddition of even fewer observations (Figure 2.5) and are thus noisier than those from the equator. The agreement between IRIS and CIRS temperature results breaks down from 20°S to 20°N. The SSAO is known to modulate the stratospheric temperature structure from 15°S to 15°N [Fouchet et al., 2008], but the 10° latitudinal binning of observations of both datasets effectively stretches the influence of the SSAO to slightly higher latitudes. Thus, the discrepancies in the stratospheric thermal structure exist from 20°S to 20°N, which represents the effective range of the SSAO, and the agreement in temperatures at mid latitudes does suggest this feature is robust and is a result of forcing by the SSAO. In addition, Figure 1.7 (Figure 3 of Orton et al. [2008] but with more recent results) shows the contrast between ±4° and ±16° of brightness temperature at 7.8 μm and 12.2 μm: also using Voyager-IRIS observations in 1980, they determined 16°N to be approximately 5.5 K warmer in brightness temperature

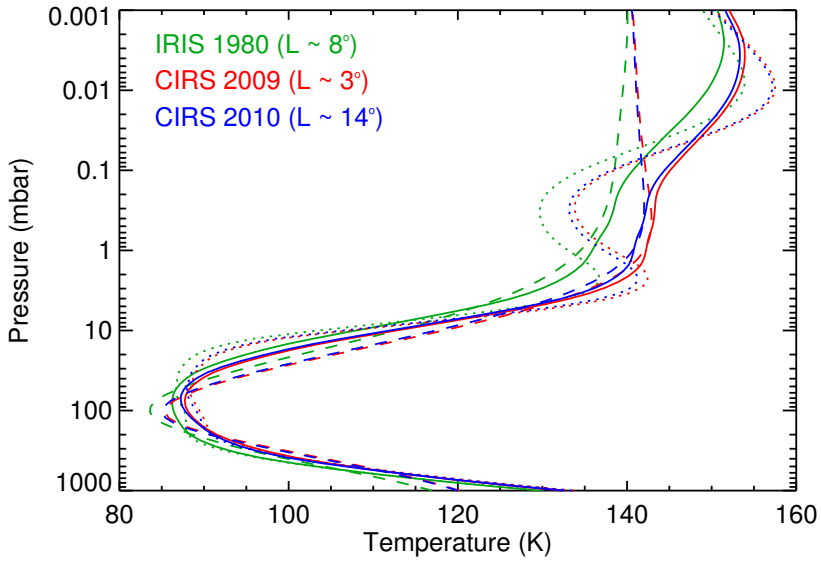

Figure 6.12: Retrieved temperature profiles at the equator in 1980 (green), 2009 (red) and 2010 (blue). Solid, dotted and dashed profiles indicate those retrieved using the standard, limb and isothermal temperature *a priori* profiles respectively.

at 7.8 μm (1280 cm^{-1}) than 3°N which is consistent with the behaviour observed in Figure 6.6. Thus, the reduction of IRIS spectra presented in this work and in Orton et al. [2008] both suggest a cooler stratospheric equator in 1980.

6.3.3 Is this result an artefact of the retrieval process?

The latitudinal profile of brightness temperature in the methane band (Figure 6.6) indicates lower stratospheric temperatures in IRIS spectra at the equator compared with CIRS observations but a reverse of this at 5°S and 5°N and so a contrast in the thermal structure is apparent from the observed spectra alone. As demonstrated in Sections 4.3.2 and 5.2.1, the nadir viewing geometries of the Cassini-CIRS spectra and corresponding vertically-broad contribution functions struggled to resolve the vertical structure of the SSAO and the observed cooling trend determined in Guerlet et al. [2011] using limb-viewed Cassini-CIRS observations. Thus, retrievals of temperature and the concentrations of acetylene

Year	Temperature *A Priori*	Equator results at 2.1 mbar			
		T (K)	C_2H_2 (ppbv)	C_2H_6 (ppmv)	χ^2/n
1980 (IRIS)	Standard	132.9 ± 1.0	140.5 ± 6.8	4.27 ± 0.18	0.95
	Isothermal	130.5 ± 1.0	147.5 ± 7.1	4.40 ± 0.18	1.12
	Limb	136.7 ± 0.9	138.5 ± 6.7	4.40 ± 0.18	0.94
2009 (CIRS)	Standard	140.1 ± 0.6	166.8 ± 7.5	3.94 ± 0.10	0.73
	Isothermal	138.6 ± 0.3	163.9 ± 6.8	3.57 ± 0.08	4.95
	Limb	142.5 ± 0.3	176.5 ± 6.4	4.43 ± 0.10	0.90
2010 (CIRS)	Standard	138.8 ± 0.7	148.7 ± 7.3	4.14 ± 0.11	0.86
	Isothermal	137.2 ± 0.3	139.1 ± 6.5	3.75 ± 0.09	5.35
	Limb	141.2 ± 0.3	152.0 ± 5.9	4.58 ± 0.10	0.85
2009-1980	Standard	7.1 ± 1.2	26.3 ± 10.1	-0.33 ± 0.21	-
	Isothermal	8.1 ± 1.0	16.4 ± 9.8	-0.83 ± 0.20	-
	Limb	5.8 ± 0.9	38.0 ± 9.3	0.03 ± 0.21	-
2010-1980	Standard	5.9 ± 0.7	8.2 ± 10.0	-0.13 ± 0.21	-
	Isothermal	6.7 ± 0.3	-8.4 ± 9.6	-0.65 ± 0.20	-
	Limb	4.5 ± 0.3	13.5 ± 8.9	0.18 ± 0.10	-

Table 6.3: Retrieved temperatures and the concentrations of acetylene and ethane at 2.1 mbar at the equator in 1980, 2009 and 2010 using the *standard*, *isothermal* and *limb* temperature profiles as *a priori* profiles and differences between 2009/1980 and 2010/1980 results. Results from IRIS are those using the convolved $\Delta\tilde{\nu} = 15.5$ cm^{-1} observations for consistency in spectral resolution with Cassini-CIRS. The goodness-of-fit values are also shown for each retrieval.

and ethane were repeated from Voyager-IRIS spectra in 1980 and Cassini-CIRS observations in 2009/2010 starting from different *a priori* temperature profiles.

Firstly, a vertically-isothermal temperature profile of 140 K, henceforth described as the *isothermal* profile, was tested. Use of an isothermal *a priori* serves to minimise the possibility that features in the retrieved vertical profile are an artefact of those in the initial *a priori*. Secondly, a mean of temperature profiles retrieved at 5°S, 0° and 5°N in February 2010 [Guerlet et al., 2011] was adopted as the *a priori*: this profile will henceforth be described as the *limb* profile. Figure 6.12 compares the temperature profiles retrieved from the different *a priori* and Table 6.3 compares retrieved results at the 2.1 mbar level. The *isothermal* and *limb* profiles yield temperature differences of 8.1 ±1.0 K and 5.8 ± 0.9 K at the 2.1 mbar level respectively. Thus, a significantly cooler stratosphere at the equator

in 1980 with respect to 2009/2010 is true irrespective of the temperature *a priori* used. It should, however, be noted that use of the *isothermal a priori* resulted in significantly poorer fits to the observations (Table 6.3) and thus there is less confidence in these results. The limb *a priori* however produced fits to all three sets of observations of a comparable quality with that of the standard prior. As expected, the choice of temperature *a priori* alters the retrieved concentrations of acetylene and ethane. The concentrations retrieved from the isothermal priors generally disagree with those retrieved from the standard and limb *a priori*. However, as discussed above, there is less confidence in these results due to the high goodness-of-fit values. Acetylene concentrations retrieved from the standard and limb *a priori* agree within each year. Similarly, ethane concentrations retrieved from IRIS observations in 1980 using the standard and limb temperature *a priori* agree within error bars. However, ethane concentrations retrieved from CIRS observations in 2009 and 2010 using the limb *a priori* are significantly higher than those retrieved using the standard.

Thus, the conclusion a different in the stratospheric thermal structure at the equator from 1980 to 2009/2010 is considered to be a robust result. The SSAO is expected to drive the thermal evolution of the equator as demonstrated in Chapter 6. However, by definition, the period of the SSAO is half a Saturn year (approximately 15 years) and so, after the $\sim$30 year difference between the CIRS and IRIS observations, the phase of the SSAO would be expected to be very similar. Although IRIS observations in 1980 and CIRS observations in 2009 and 2010 do not capture the planet at exactly the same solar longitude, it is unlikely that temperature differences of greater than 4 K can be explained by the small differences in the season. These results thus imply the SSAO has been captured in a slightly different phase, which suggests its period is more quasi-semiannual.

6.3.4 Tropospheric anomalies at mid-southern latitudes

Retrieved tropospheric temperatures at 25°S at approximately 100 mbar are 8 K warmer in 2009/2010 compared to 1980 (Figures 6.9) and this is also consistent with brightness temperature contrasts in the observations alone (Figure 6.6). This thermal contrast in the tropospheric temperature between the Cassini and Voyager datasets extends from 45°S to 15°S with the largest temperature difference exhibited at 25°S. A similar temperature difference is not observed of stratospheric temperatures in the same latitude range, which suggests this feature is physically limited to tropospheric altitudes.

The 10° latitudinal binning does not utilise the 1 - 2° latitudinal field-of-view of the $\Delta\tilde{\nu} = 15.5$ cm^{-1} Cassini-CIRS observations and thus the ability to resolve meridional structures of this size. Figure 6.13 shows the meridional profile of the tropospheric temperature at 145.1 mbar using the retrieved results in Chapter 5 where observations were binned into 2° latitude bins instead. The higher spatial resolution binning indicates several temperature maxima at the 145.1 mbar level at 55°S, 45°S and 20°S. Prograde tropospheric jets are known to exist at 40°S and 54°S and retrograde jets are known to exist at 32°S and 49°S [Porco et al., 2005]: these positions are consistent with larger meridional gradients in the temperature as is expected. However, the fact that a similar profile is not observed in the Voyager-IRIS results implies a differing structure of the zonal winds from 1980 to 2009/2010.

An analysis conducted by Li et al. [2013] found a similar result. Their method of retrieving temperature used the hydrogen S(0) and S(1) lines, which peak in sensitivity at higher pressures than the collision-induced absorption and methane band used to respectively retrieve tropospheric and stratospheric temperature in this work. This is likely why the magnitude in temperature difference between the Voyager and Cassini eras differ between our studies however, qualitatively, our results agree. Li et al. [2013] suggest wave activity

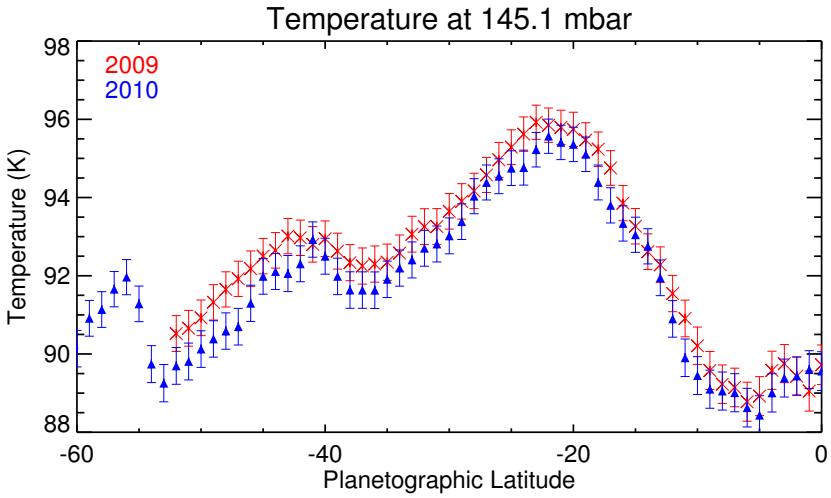

Figure 6.13: The meridional profiles of temperature at 145.1 mbar in 2009 (red crosses) and 2010 (blue triangles) using the results of Chapter 5 where Cassini-CIRS observations were instead binned into 2° latitude bins.

as a source of interannual variability on the tropospheric thermal structure. In particular, they attribute the warmer Cassini temperatures at mid-southern latitudes to be the lasting effects of wave activity induced by the 1990 equatorial storm [Sanchez-Lavega et al., 1991]. In the absence of another obvious source of interannual variability, wave forcing is similarly concluded as the source of differences in the tropospheric temperature field at mid-southern latitudes between the Voyager and Cassini era in this work.

6.3.5 25°S

A significantly richer concentration of acetylene is retrieved at 25°S in 1980 (164.6 ± 6.4 ppbv) compared to 2009/2010 (122.1 ± 7.1 ppbv) in the absence of a similar enrichment of ethane. Figure 6.14 compares the observed and modelled CIRS and IRIS observations at this latitude. Again, the Voyager-IRIS observation is signficantly noisier than the Cassini-CIRS observation. However, as discussed in Section 6.3.1, the comparable results of test retrievals of synthetic observations (Section 6.2.2 and the fact that retrieved temperatures

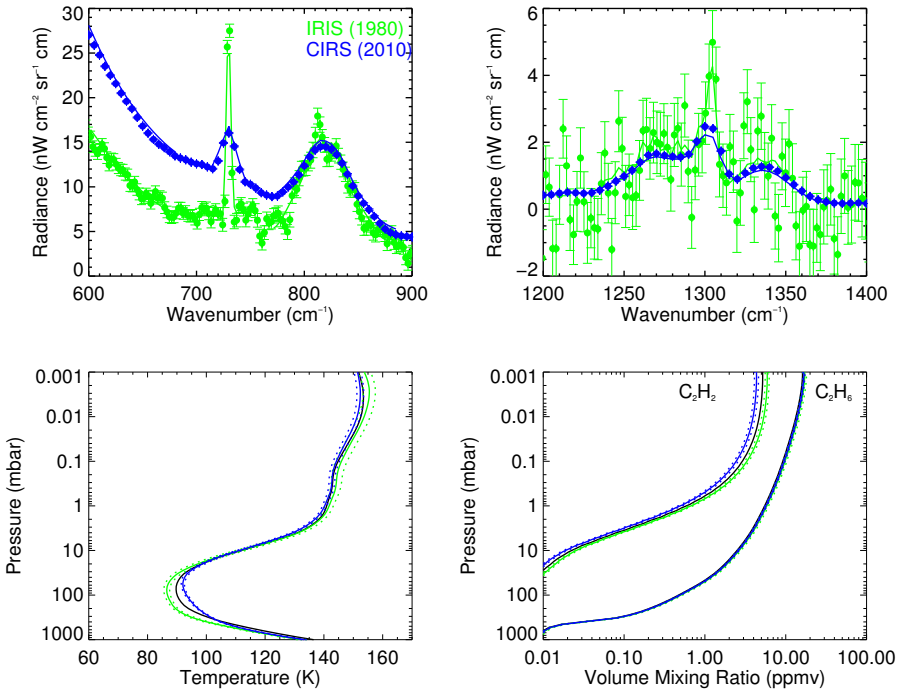

Figure 6.14: Observation-model comparisons at 25°S: Voyager 1-IRIS observations (blue points) and Cassini-CIRS observations in 2009 (red points) and the corresponding modelled spectra (solid) in the same colours. The *a priori*, retrieved profiles and their uncertainty are shown as black solid, coloured solid (using colours as above) and coloured dotted lines.

and concentrations from real observations match in other latitude ranges (30°S to 55°S and 30°N to 60°N) suggests that the noisier nature of IRIS spectra does not nominally appear to hinder the retrievability of temperature and the concentrations of acetylene and ethane. However, this result would not nominally be expected from the brightness temperatures of the observations alone: Figure 6.6 actually shows higher brightness temperatures at 730 cm^{-1} in CIRS observations than in Voyager-IRIS observations. This is likely due to the significantly warmer troposphere in 2009/2010 at mid-southern latitudes as discussed in Section 6.3.4. The warmer tropospheric temperatures have increased continuum radiances upon which the acetylene emission feature is superimposed and thus brightness temperatures computed over 710 to 750 cm^{-1} are significantly increased. Figure 6.15 compares

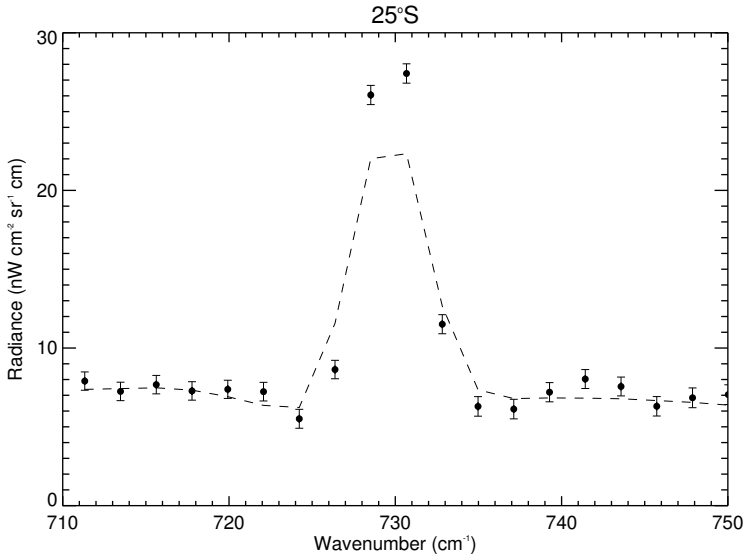

Figure 6.15: The Voyager 1-IRIS spectrum of 25°S from 710 - 750 cm^{-1} (points with error bars) and a synthetic IRIS spectrum computed using the retrieved temperature profile in 1980 and the retrieved concentration of acetylene in 2009.

the Voyager 1-IRIS observation of the acetylene emission feature at 25°S with a synthetic IRIS spectrum which has been computed using the retrieved temperature profile in 1980 but the retrieved concentration of acetylene in 2009. The peak of the forward modelled acetylene emission feature does not match the strength of the same feature in the observation and thus demonstrates that an enrichment of acetylene in 1980, with respect to 2009, is required to fit the Voyager 1-IRIS observation at 25°S.

An enrichment of acetylene at 25°S in 1980 with respect to 2009/2010 would nominally imply that there is increased downwelling in the former year. A similar enrichment of ethane is not observed, though this can perhaps be attributed to its smaller vertical gradient in concentration in comparison to acetylene. 25°S marks the position of a cell of downwelling associated with seasonally-reversing Hadley circulation, as demonstrated by the GCM (Figure 1.8). Downwelling at this latitude persists throughout the whole Saturn year but varies in strength. In the aftermath of southern summer, the Hadley circulation takes the form of upwelling at 15°S, cross-equatorial flow at high altitudes and

subsidence at 25°N. The concentrations of acetylene and ethane were seen to decrease and increase at 15°S and 25°N respectively from 2005 to 2010, which provides observational evidence that this circulation taking place. A half-Saturn year later, this circulation is predicted to reverse with upwelling at 15°N and downwelling increasing in strength at 25°S. Although downwelling is predicted at 25°S, it is puzzling that the implied strengths of the downward motion are different from 1980 to 2009/2010 since these years capture Saturn at approximately the same season. If the behaviour of the SSAO is different from 1980 to 2009/2010 (as discussed in Section 6.3.1), perhaps its differing dynamical forcing at low latitudes has resulted in stronger subsidence at 25°S.

6.3.6 High latitudes

Figures 6.16 and 6.17 show example retrievals at high-southern and high-northern latitudes. As these Figures demonstrate, the Voyager-IRIS observations poorly sample high latitudes and thus there are fewer observations to combine/average together to increase the signal-to-noise ratio. This, in addition to the low thermal infrared signal from high-northern latitudes which are captured in late winter/early spring in both datasets is problematic for observations in this region. In addition, testing of the retrieval procedure on synthetic IRIS observations (Section 6.2.2) revealed larger errors on retrieved temperatures and acetylene and ethane concentrations from observations of a cooler stratosphere which is true for high-northern latitudes. A discussion of the results at high latitudes is presented below, but should be interpreted with caution.

Systematically higher hydrocarbon concentrations are observed in IRIS results at high-southern latitudes (<60°) in comparison to those from CIRS (Figure 6.9). As discussed in Section 4.3.3, the considerably warmer temperatures and sharp meridional increases in the concentrations of acetylene and ethane at high-southern latitudes are indicative of the south polar vortex. In Chapter 6 (Section 5.2.2), we saw a strong cooling in the

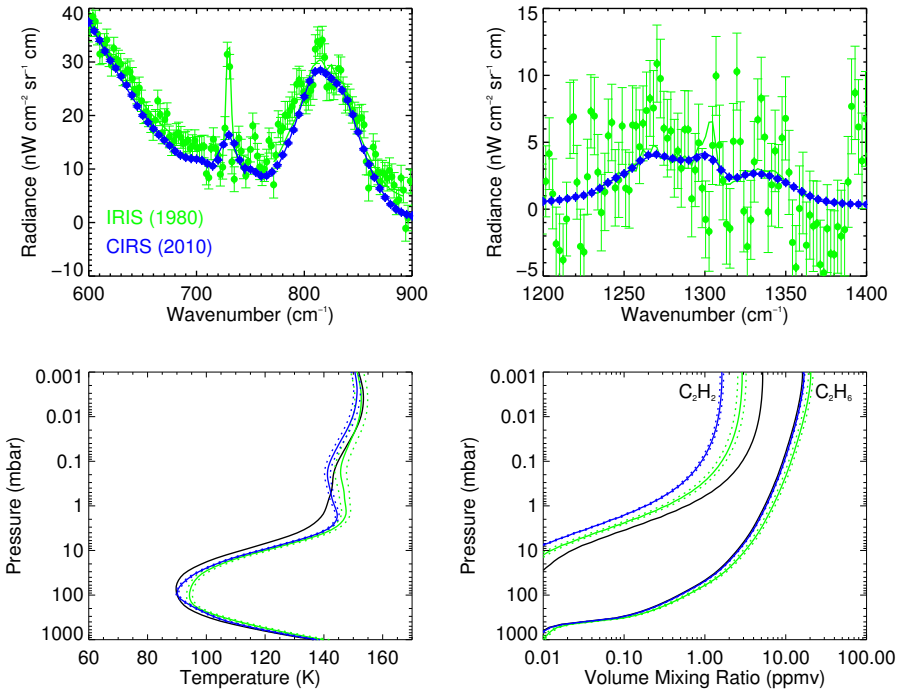

Figure 6.16: Observation-model comparisons at 80°S: Voyager 1-IRIS observations (blue points) and Cassini-CIRS observations in 2010 (red points) and the corresponding modelled spectra (solid) in the same colours. The *a priori*, retrieved profiles and their uncertainty are shown as black solid, coloured solid (using colours as above) and coloured dotted lines.

south polar region from 2005 to 2010 which was consistent in magnitude with a radiative climate model of this region. This, and a similar contrast in hydrocarbon concentration within and outside the south polar region suggests that a polar vortex remains in 2010. Equivalently, the presence of a polar vortex a Saturn year earlier in the same season would be expected: a similar meridional increase in the concentrations of acetylene and ethane at high-southern latitudes in 1980 is suggestive of this. The stronger concentrations of acetylene and ethane in 1980 with respect to 2009/2010 might suggest there is stronger downwelling in the former year. However, the retrieved temperatures in 1980 are consistent (within error bars) with those from 2010 and so there is no evidence of increased adiabatic heating associated with the stronger downwelling. An alternative explanation is

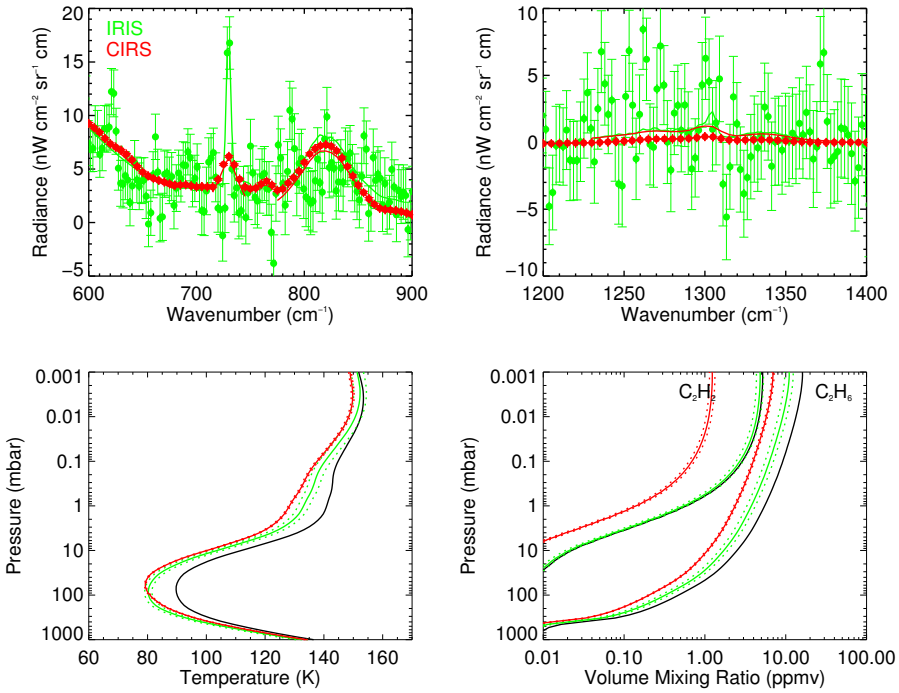

Figure 6.17: Observation-model comparisons at 80°N: Voyager 1-IRIS observations (blue points) and Cassini-CIRS observations in 2009 (red points) and the corresponding modelled spectra (solid) in the same colours. The *a priori*, retrieved profiles and their uncertainty are shown as black solid, coloured solid (using colours as above) and coloured dotted lines.

the proximity of solar maximum in 1980 and the associated auroral effects that may play a role in hydrocarbon photochemistry. Charged-particle chemistry from the aurora has been suggested as a possible source of enhanced hydrocarbon production [Guerlet et al., 2010]. Auroral processes on Jupiter are seen to produce *auroral hot spots* or discrete regions of enhanced CH_4 and C_2H_6 emission (e.g., Kim et al. [1985]). Though these features are spatially-discrete, the coaddition of Voyager-IRIS observations into 10° latitude bins could effectively stretch the influence of these hot spots spatially.

Stratospheric temperatures and the concentrations of acetylene appear enhanced at high-northern latitudes with respect to 2009. Ethane's concentration appears consistent between these two years however, as discussed above and in Section 6.2.2, there are poten-

tially errors in the retrieval of temperature, acetylene and ethane in regions where the stratosphere is significantly cooler. With the presence of a south polar vortex during, and in the aftermath of, southern summer, by symmetry a similar polar vortex would be expected to form at the north pole as northern summer approaches (with northern summer solstice in 2017). Downwelling within the vortex would provide adiabatic heating and advection of hydrocarbon-richer air and thus temperatures and hydrocarbon concentrations would be expected to be elevated with respect to the general meridional trend, as has been observed of the southern polar vortex. However, there is no evidence of the onset of a northern polar vortex in 2010 (and not even in 2013 - L. Fletcher, private communication) and thus, one would not be expected to form a Saturn year previously in 1980. Increased auroral activity during solar maximum in 1980 would also be expected at high-northern latitudes and could induce hot spots in CH_4 and C_2H_6 emission that would manifest as enhanced temperatures and concentrations. Modelling of the effects of auroral chemistry on the concentrations of photochemical species would better indicate whether auroral processes could alter lower stratospheric temperature and hydrocarbon concentrations in this way.

6.4 Summary

A comparison of atmospheric properties derived from Voyager 1-IRIS observations in 1980 and Cassini-CIRS observations in 2009/2010 has highlight the extent of interannual variability. A comparison of these two datasets involved comparing spectra of different spectral resolutions and highly different signal-to-noise ratios. However, the retrieval analysis has been conducted twice, once using Voyager 1-IRIS spectra at their original spectral resolution of 4.3 cm^{-1}, and second using the same observations convolved to 15.5 cm^{-1}. Temperatures and the concentrations of acetylene and ethane retrieved from the 4.3 cm^{-1} and 15.5 cm^{-1} were generally very similar and so differences in the spectral resolution

can be ruled out as a possible source of discrepancy. An analysis of retrievals on noise synthetic spectra of the Voyager-IRIS and Cassini-CIRS observations was conducted and retrieved quantites exhibited a good correspondence between these two datasets. It was thus concluded that results from these two datasets could be directly compared.

Diffferences in the stratospheric thermal structure were found at the equator between 1980 and 2009/2010 which suggested the two datasets have captured Saturn's semiannual oscillation (SSAO) in a different phase which suggests its period is more quasi-semiannual. Elevated concentrations of acetylene at 25°S may also be explained by a difference in the phase of the SSAO and its dynamical forcing at low latitudes.

Stratospheric temperatures and hydrocarbon concentrations appear elevated in 1980 with respect to 2009/2010 at high-southern and high-northern latitudes. This is likely an artefact of the low signal-to-noise ratio of the IRIS observations; however, dynamical differences at polar regions from 1980 to 2009/2010 or increased auroral activity during solar maximum in 1980 and its effect on temperatures and hydrocarbons cannot be ruled out.

Chapter 7

Reduction and calibration of IRTF-Celeste observations in 2012

Celeste is a cryogenic grating spectrometer which operates in the thermal infrared (5μm to 25μm) at a high resolving power. The instrument was initially developed for resolving Zeeman split magnesium lines in the solar corona, thus allowing for magnetic field strengths to be determined [Moran et al., 2007]. However, more recently, Celeste has been used to provide ground-based support to the Cassini mission in the study of the Saturnian system.

It is ideal that spacecraft and ground-based observations are used in conjunction since they each offer different advantages. The Cassini spacecraft provides observations of Saturn within 60 Saturn radii and thus a high spatial resolution represents one significant advantage of spacecraft observations. Even once observations are coadded within latitude bins to improve the signal-to-noise ratio, a 2° latitudinal resolution is achievable, allowing for small-scale meridional variations in the thermal structure and composition of the planet to be resolved. Spacecraft observations are also advantaegous in that a range of orbits around the planet can be executed allowing for high-latitude/polar regions, unobservable from Earth, to be viewed and for limb viewing geometries to be achieved at low latitudes. A further obvious advantage of space-borne spectroscopy is that observations are made outside the Earth's atmosphere which absorbs heavily in some regions of the infrared (see Figure 7.1).

In order to be practical as a payload on a spacecraft, space-borne instruments are de-

[2]http://www.gemini.edu/?q=node/10789#Mid-IR

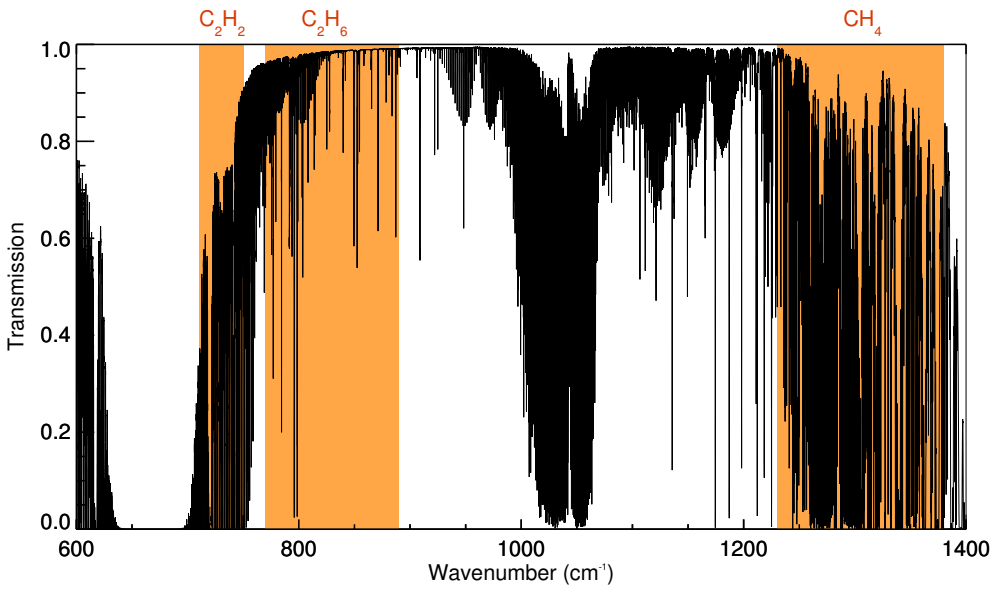

Figure 7.1: The transmission through the Earth's atmosphere in the thermal infrared at an airmass of 1, a PWV (precipitable water vapour) of 1 mm and at the altitude of the Mauna Kea observatory of 4.2 km, as provided by the Gemini observatory[2].

signed with a limited size which ultimately limits the spectral resolution. In Cassini's case, the best spectral resolution (FWHM) available from the CIRS instrument is 0.5 cm^{-1} and many observations are required to average together to improve the signal-to-noise ratio, often sacrificing spatial and temporal resolution. However, Celeste can achieve spectral resolutions of approximately 0.1 cm^{-1} at a high signal-to-noise ratio in wavenumber regions where there is little telluric absorption.. Spectral resolving power therefore represents the main advantage of ground-based spectroscopy. The high spectral resolution offered by Celeste provides observability to smaller, weaker features in the target spectrum, which can allow for isotopic ratios to be determined, such as the $^{12}C/^{13}C$ ratio (as has been determined from Celeste observations of Titan in Jennings et al. [2009]), and for trace species not observable at lower spectral resolutions to be studied. In contrast to spacecraft observations, absorption by the Earth's atmosphere can form a significant disadvantage in ground-based observing. Figure 7.1 shows the transmission through the

Earth's atmosphere over the spectral range at which Saturn is studied in this thesis: even when observing at high altitude sites such as the Mauna Kea observatory, observing in some infrared bands is not viable/near impossible. Luckily, certain emission features from acetylene and ethane in Saturn's spectrum occur at wavenumbers of a relatively high transmission through the Earth's atmosphere ($> 50\%$) which allows these species to be studied from Earth.

7.1 The Celeste Instrument

Celeste has historically been mounted on the NASA IRTF (Infrared Telescope Facility) at the Mauna Kea observatory in Hawaii, USA and the McMath-Pierce telescope at the Kitt Peak observatory in Arizona, USA . Only observations of Celeste when mounted on the IRTF are used in this thesis.

When mounted on the IRTF, the infrared part of the f/37 beam from the telescope is reflected by a dichroic mirror, the focal ratio of the beam changed to f/8 by an lens and the beam is then focused on to window of the instrument dewar. The dichroic mirror also focuses a visible beam to a guide camera for tracking on the target. The infrared beam incident on the dewar passes through a circular variable filter and an image is formed at a slit of variable size. The beam is expanded, collimated by Cassegrain optics and diffracted by a 18 x 33 cm^2 echelle grating with 31.6 rulings/mm which is blazed at angles of 40° to 60° (depending on the chosen wavenumber band). The diffracted beam is then focused onto a 128 x 128 Si:As blocked impurity band detector array. The detector and the optics of the instrument are cooled to temperatures of approximately 6 K by liquid nitrogen and helium.

7.2 Observations using Celeste

Generally, on an awarded night of telescope time, the grating number (an arbitary number range which changes the blaze angle of the grating and thus the wavenumber of photons reaching the detector) is set to observe a wavenumber range (typically 3 cm^{-1} in size) corresponding to a spectral feature of a chosen molecular species. Target and calibration spectra are obtained. In this thesis, spectra from approximately 742.5 cm^{-1} to 744.5 cm^{-1} (C_2H_2 emission) and from 820.5 cm^{-1} to 823 cm^{-1} (C_2H_6 emission), which are henceforth described as the *743 cm^{-1}* and *822 cm^{-1}* band were used. On the IRTF, the slit length corresponds to approximately 50" on the sky. Thus, even for planetary targets as large as Jupiter (30" to 45") and Saturn (15" to 20"), the slit covers both the disc of the planet and deep space simultanesouly. The width of the slit is adjusted appropriately for the diffraction-limited resolving power ($\theta = 1.22\lambda/D$ ~1" in the thermal infrared on the IRTF) and the spectral resolution. In this analysis, observations using a 300μm slit are used which results in spectral resolutions of approximately 0.1 cm^{-1} and 0.17 cm^{-1} in the 743 cm^{-1} and 822 cm^{-1} bands respectively.

Integrations on the target are performed with the slit of the spectrometer aligned north-south along the central meridian of the planet. The secondary mirror moves back and forth at two positions at a set frequency such that the telescope chops between the target planet and dark sky 40" clear of the target. This describes an 'A-chop'. Subsequently, the telescope is nodded to another position and the process repeated but in reverse (chopping from dark-sky to the target), which describes a 'B-chop'. Subtraction of A-chop and B-chop serves to remove telluric sky emission and any emission from the telescope thus leaving signal which is proportional to that observed from the target alone.

For observations of Saturn, A-B chop pairs were acquired continuously and the rotation of the planet is used to obtain longitudinal coverage. Observations obtained using this

procedure are advantageous for subsequent reduction and analysis: all visibile latitudes can be viewed in a wavenumber band simultaneously and observations within a latitude band will be approximately equivalent in emission angle and thus can be averaged together to produce zonal averages with an increased signal-to-noise ratio. Observations on flatfield objects and calibration standards are acquired in addition to those obtained from the target. Venus and Mars have historically been used as calibration standards and, as bright objects in the thermal infrared, only a few A-B chop pairs are required to obtain an adequate signal-to-noise ratio. Thermal radiation from the Moon is approximately blackbody and is approximately flat in radiance over the 3 cm^{-1} bandwidth of a typical Celeste spectrum. Any variation in pixel signal when viewing the Moon is therefore a result of differences in the pixel sensitivity or regions of the spectrum where there is more or less telluric absorption. Spectra of the Moon are therefore used with the aim of 1) characterising the pixel-to-pixel sensitivity of the detector array and 2) correcting for telluric absorption.

Table 7.1 summaries the Celeste observations used in this thesis. The airmasses, solar longitudes, sub-observer latitudes, longitudinal ranges and radial velocities have been determined using the JPL Horizons ephemeris computation service[3] which will henceforth be named *Horizons*. The IRTF-Celeste dataset is extensive: many spectra of the 743 cm^{-1}, 822 cm^{-1} and other bands have been acquired in July 2009, other nights in March 2012 and also in April 2013. However, only the 822 cm^{-1} and 743 cm^{-1} data acquired on 31/03/12 and 01/04/12 respectively were reduced and analysed in this thesis. This was for the sake of brevity, the fact that there very good (dry and cloud-free) observing conditions on these nights compared to other nights and the coincidence of the 163_001MT CIRS observation acquired on 01/04/12 which has allowed a comparison of CIRS and Celeste results.

[3]http://ssd.jpl.nasa.gov/?horizons

Date (yyyy-mm-dd)	Time	Target	Band (cm^{-1})	Number of A-B chop pairs	Airmass	Solar Longitude	v_{target} (km/s)	Sub-observer Latitude	Longitudal Coverage
2012-03-31	11:35 - 15:05	Saturn	822	44	1.1 - 2.0	32°	-21.1 to -20.8	17°N	131° to 244°
2012-04-01	04:50	Moon	822	20	1.0	-	-	-	-
	05:04 - 05:12	Venus	822	4	1.6	-	-13.1	5°S	222
	05:20 - 05:30	Mars	822	4	1.3	90°	8.3	22°N	78°
	05:35	Moon	743	20	1.0	-	-	-	-
	05:55 - 06:03	Venus	743	4	2.2	-	-13.1	5°S	222
	06:13 - 06:27	Mars	743	4	1.1	90°	8.6	22°N	90°
	07:35 - 15:15	Saturn	743	102	1.1 to 2.1	32°	-20.9 to -20.7	17°N	88° to 340°

Table 7.1: A summary of the Celeste data used in this project. All latitudes are planetographic and longitudes given for Saturn are System III longitudes.

7.3 Reduction

The following subsections outline the reduction procedure applied to all A-B chop pairs of targets including Saturn and radiance calibrating targets such as Venus and Mars.

7.3.1 Offset subtraction and flatfielding

Each chop on the target produces a spectral-spatial image of 128 pixels in both dimensions. Initially, a sigma filter was applied where the image was searched with a 3x3 pixel width box and any pixels where the signal outlied the mean signal in the box by 2σ was replaced with the mean signal in the box. This serves to remove *hot pixels*. Each chop pair was then subtracted and flatfield corrected as described by Equation 7.1.

$$R(x,y) = \frac{A(x,y) - B(x,y)}{M_{\text{norm}}(x,y)} \tag{7.1}$$

x and y represent the spectral and spatial dimensions respectively and $A(x,y)$, $B(x,y)$, $M_{\text{norm}}(x,y)$ and $R(x,y)$ represent the A-chop, B-chop, normalised moon flat field and the resultant image respectively. The subtraction of the chops serves to remove offset signal (such as sky emission and emission from the instrument-telescope system). Division by the normalised flatfield then adjusts the signal in each pixel to account for the varying pixel-to-pixel sensitivity across the detector.

Figure 7.2 shows the resultant spectral-spatial image of an example A-B chop pair observed on 31/03/12 of Saturn in the 822 cm^{-1} band. Spatial pixel numbers from approximately 8 to 92 have been illuminated by the slit. Spatial pixel numbers from approximately 28 to 55 have been illuminated by the disc of Saturn while all other pixels illuminated by the slit capture dark sky north and south of the planet (under the assumption that the subtraction described above has removed telluric emission).

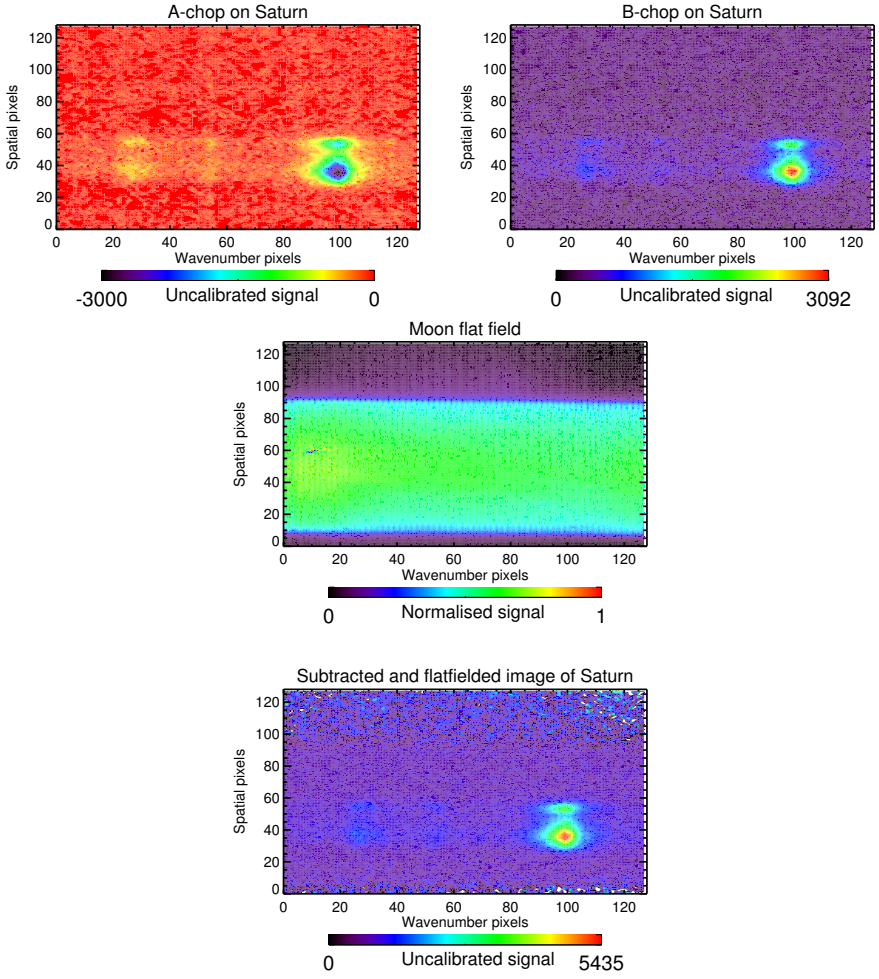

Figure 7.2: An example A-chop (top left), B-chop (top right), moon flat field (middle) and the resultant subtracted and flatfielded image (bottom) of an observation of Saturn in the 822 cm^{-1} band on 31/03/12. The image is inverted spatially and so the y-axis represents south in the direction of the planet's meridian.

7.3.2 Geometry of target spectra

Latitudes and emission angles: In each spectral-spatial image of a target, the range of spatial pixel values corresponding the disc of the target were identified. This was found to vary slightly from image to image due to the limited tracking accuracy of the IRTF telescope. Using the mean number of spatial pixels occupied by the planet together with

the observed polar anglar diameter (determined from *Horizons*), the angular size of one spatial pixel was calculated. This was found to be 0.55" which is consistent with Hesman et al. [2009] who also used IRTF-Celeste observations. This corresponds to a latitudinal field-of-view of 2-3° at the sub-observer latitude, increasing to 6 - 7° at higher emission angles. The pixel corresponding to the centre of the planet disc was then identified and the angular offset of all remaining on-disc spatial pixels were thus calculated. On Saturn and Mars where the slit of the spectrometer was aligned along the central meridian, this corresponded to simply an offset in the polar direction. However, on Venus, the day-night terminator was close to the central meridian and so the slit was aligned north-south on the dayside of the planet at an offset from the disc centre. Using this information, latitudes were associated with each on-disc pixel using a procedure developed by Pat Irwin. This procedure models the surface of the planet target as an ellipsoid (or sphere for planet targets with no oblateness) and finds the coordinates of intersection of a straight line representing the line of sight of the observer. The angle subtended by this point from the equatorial plane of the planet as viewed at the centre of the planet thus determines the (planetocentric) latitude of each pixel. Similarly, the angle between the zenith of these coordinates and the line of sight thus determines the emission angle.

Longitudes: The exact date and time of each A-B chop pair was noted in the observing logbook. For observations of Saturn and Mars where the slit of the spectrometer was aligned along the central meridian of the planet, the longitude was simply determined by finding the sub-observer longitude at the time of each observation from *Horizons*. In this thesis, System III longitudes of Saturn are quoted. For Venus, the slit of the spectrometer was instead aligned north-south on the day side of the planet at a slight offset from the disc centre due to the proximity of the terminator at this position. Using the observed pole-to-pole angular diameter of Venus, the observed size of the Venus disc in pixels and the known angular size of 1 pixel as mentioned previously in this section, the longitudinal offset from the disc centre was determined. This was found to be approximately 30° in

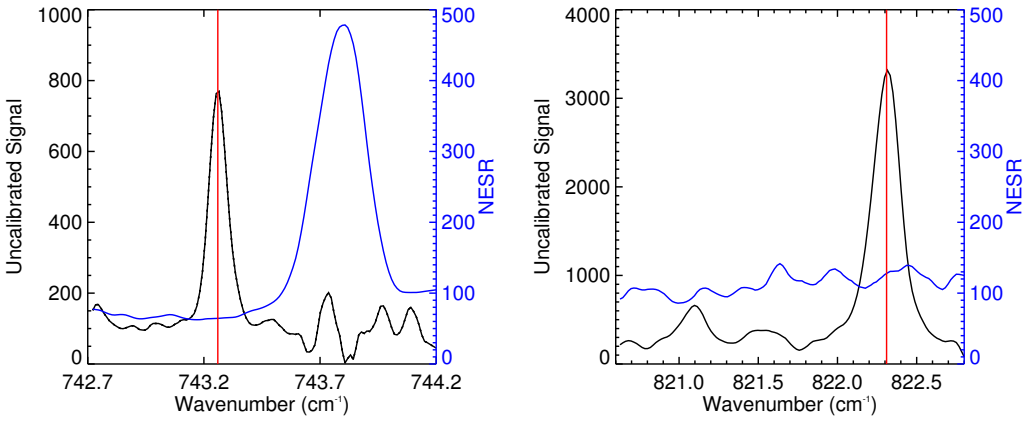

Figure 7.3: Example (uncalibrated) Celeste observations (black) in the 743 cm^{-1} (left) and 822 cm^{-1} bands upon smoothing, colocation and wavenumber calibration. The vertical red lines indicate the reference wavenumber used for the wavenumber calibration. The NESR spectra (blue) are also shown for comparison.

longitude.

7.3.3 Noise, spectral smoothing & colocation

Spectral noise: Having identified the on-disc pixels in the previous section, the off-disc pixels were used to determine the noise equivalent spectral radiance spectrum or NESR, initially in uncalibrated radiance units. This was estimated by finding the standard deviation in the signal at each spectral pixel for all dark sky pixels, whilst avoiding pixels close to the disc of the planet. This was calculated separately for each A-B chop image on the planet such that any small changes in the detector/instrument temperature or further possible variations in the instrument's sensitivity in the course of one night were characterised for each individual observation.

Smoothing & Colocation: In spectral pixel space, the spectrum of the planet moved slightly from observation to observation. This was deemed to be a result of the changing airmass in the course of the observations being taken and flexure in the instrument-telescope system changing the spectral pixels illuminated by the slit. In the spectral dimension, all target

Band	Grating Number	Order	θ_B	$\Delta\tilde{\nu}$/pixel (cm^{-1})	Reference Spectral Feature	$\tilde{\nu}_{0,ref}$ (cm^{-1})
743 cm^{-1}	2078	4	58.18°	0.0118	C_2H_2 ν_5 R(5)	743.26
822 cm^{-1}	4474	4	50.29°	0.0174	C_2H_6 ν_9 ${}^RQ_0$	822.31

Table 7.2: The instrument grating setting, the corresponding spectral pixel dispersion and the reference spectral features used to acquire wavenumber grids for the 743 cm^{-1} and 822 cm^{-1} data.

spectra and NESR spectra are smoothed using a triangular convolution with a FWHM of 4 spectral pixels (since slit width/pixel size = 300μm/75μm =4). A standard spectrum was chosen at a minimum in airmass and at a latitude on the centre of the target. A cross-correlation analysis was then conducted of all other observations acquired in order to determine which shift in spectral pixel space provided the best match with the standard spectrum.

Figure 7.3 shows examples of target and NESR spectra in the 743 cm^{-1} and 822 cm^{-1} bands following smoothing, colocation and the wavenumber calibration described in the next section.

7.3.4 Wavenumber calibration

For a given grating number, the order, Blaze angle, θ_B and spectral pixel dispersion, $\Delta\tilde{\nu}$/pixel, were computed using the Cigar procedure provided by Brigette Hesman. Table 7.2 shows these properties for the grating numbers used to observe at 743 cm^{-1} and 822 cm^{-1}. Using the calculated value of $\Delta\tilde{\nu}$/pixel and the known wavenumber position of line features, spectral pixel numbers were transformed into wavenumber space as described by Equation 7.2.

$$\tilde{\nu} = \left(\frac{\Delta\tilde{\nu}}{\text{pixel}}\right)(\textbf{pixel} - \text{pixel}_0) + \left(1 - \frac{\text{v}_{\text{planet}}}{c}\right)\tilde{\nu}_{0,ref} \tag{7.2}$$

$\tilde{\nu}$ and **pixel** are the wavenumber and spectral pixel number vectors respectively and $\Delta\tilde{\nu}$/pixel is the spectral pixel dispersion. pixel_0 is the spectral pixel number at which a feature in the spectrum is observed and $\tilde{\nu}_{0,ref}$ is the wavenumber of this feature (as determined from line data). The scaling factor applied to $\tilde{\nu}_{0,ref}$ describes a correction to this reference wavenumber due to the doppler shift of the planet at the time observations were acquired, where v_{planet} is the radial velocity of the planet with respect to an observer on Earth and c is the speed of light. The radial velocities of target planets at the time observations were acquired was determined using *Horizons*. Table 7.2 details the instrument grating setting and the above parameters used in acquiring wavenumber grids for the 743 cm^{-1} and 822 cm^{-1} data. Figure 7.3 shows examples of 743 cm^{-1} and 822 cm^{-1} spectra after wavenumber calibration.

7.3.5 Accounting for telluric absorption

Figure 7.4 shows the transmission through the Earth's atmosphere in the 743 cm^{-1} and 822 cm^{-1} bands as a function of airmass and the PWV (Precipitable Water Vapour). These transmission spectra have been computed using the radiative transfer model detailed in Appendix B.1. In the 822 cm^{-1} band, there is almost perfect transmission through the Earth's atmosphere and there is very little dependence on the transmission as a function of airmass or the PWV. Planetary targets and the Moon are generally viewed at different airmasses. However, given the transmission spectrum exhibits little variation with airmass, any offsets in the signal in the 822 cm^{-1} band will be cancelled out in the subtraction and flatfield procedure (Equation 7.1).

In contrast, the transmission in the 743 cm^{-1} band is poorer in particular at 743.8 cm^{-1}

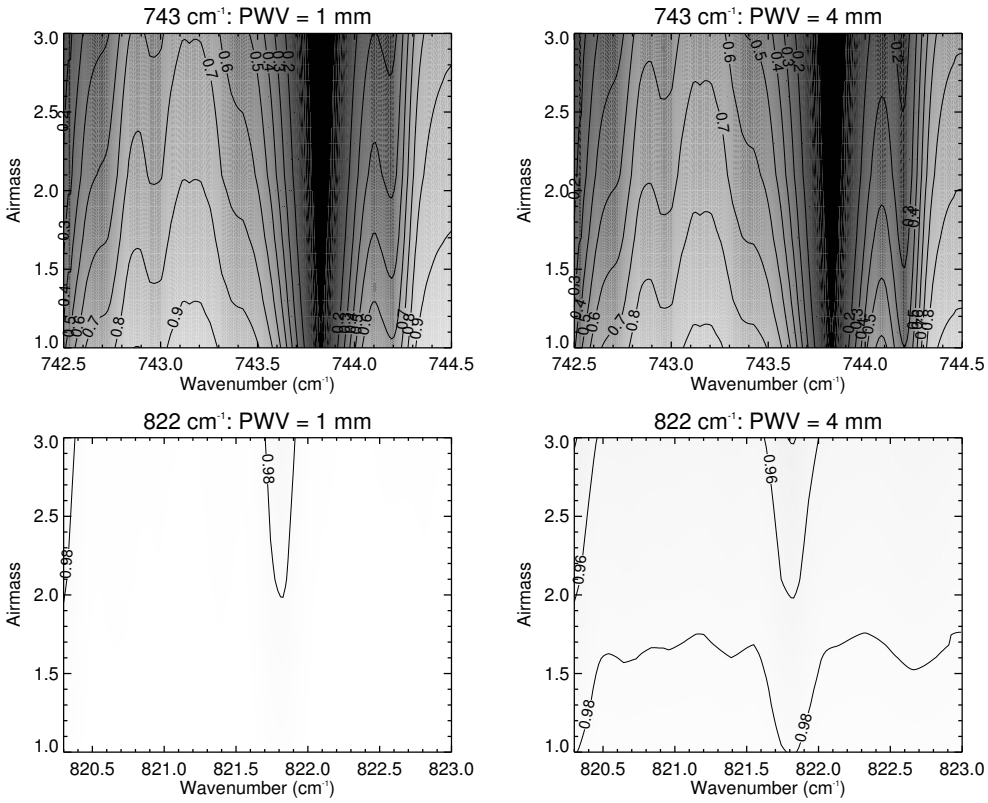

Figure 7.4: The transmission through the Earth's atmosphere (from an altitude of 4.2 km) as a function of wavenumber and airmass in the 743 cm^{-1} band (top) and 822 cm^{-1} band using a Precipitable Water Vapour or PWV of 1 mm (left) and 4 mm (right).

where there is strong CO_2 absorption. There is also significant variation in the transmission over the zenith angles at which Celeste data was acquired. Given the fact that moon and target observations were often acquired at different airmasses, it is possible that telluric absorption has not been removed by the subtraction and flatfield procedure described in Section 7.3.1. However, the noise or NESR on each target spectrum is anti-correlated with the transmission through the Earth's atmosphere and therefore was used to assess and essentially ignore spectral regions affected by the Earth's atmosphere. As described in Section 7.3.3, the NESR spectrum is determined by finding the standard deviation of signal in dark-sky pixels. Given the subtraction and flatfield procedure (Section 7.3.1), the signal from dark-sky pixels and thus the numerator of Equation 7.1 is small. There is a high

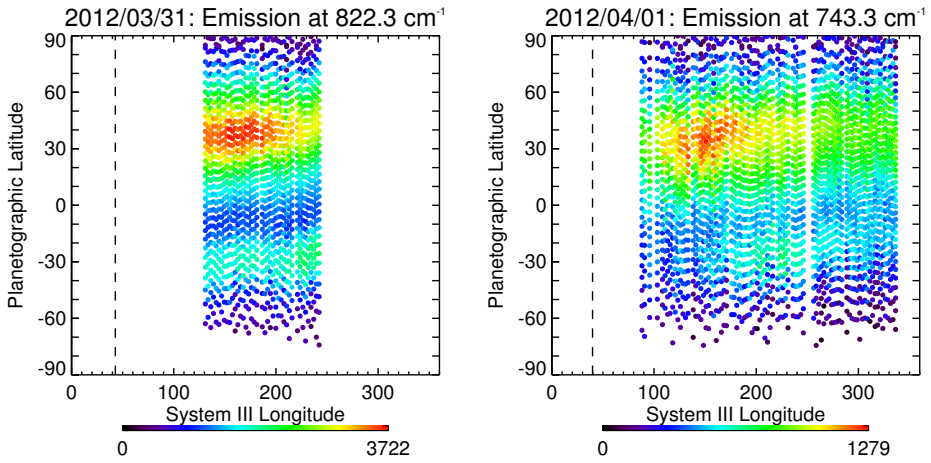

Figure 7.5: Cylindrical maps of emission at 822.3 cm^{-1} on 2012/03/31 (left) and 743.3 cm^{-1} on 2012/04/01. Each point represents a pixel and has been coloured according to the uncalibrated signal.

signal from the Moon except at wavenumbers where there is poor transmission through the Earth's atmosphere. Thus, once observations of the Moon are normalised for use as a flatfield, the denominator of Equation 7.1 is small at wavenumbers corresponding to telluric absorption. Therefore, the subtracted and flatfielded signal from dark sky pixels, and thus their standard deviation, is large in regions of low transmission. The noise on the resultant target spectrum can thus indicate which spectral regions are affected by absorption through the Earths' atmosphere. In addition, in the optimal estimation retrieval procedures described in Section 3, these spectral regions will be weighted less in the fitting of modelled spectra to the observations.

7.3.6 Zonal Coaddition

Figure 7.5 shows the resultant maps of acetylene and ethane emission on Saturn on 31/03/2012 and 01/04/2012 following the reduction procedure outlined above. As shown for both species, emission is maximum at a latitude of approximately 40°N, which is consistent with the position of the storm which enriched hydrocarbon concentrations at

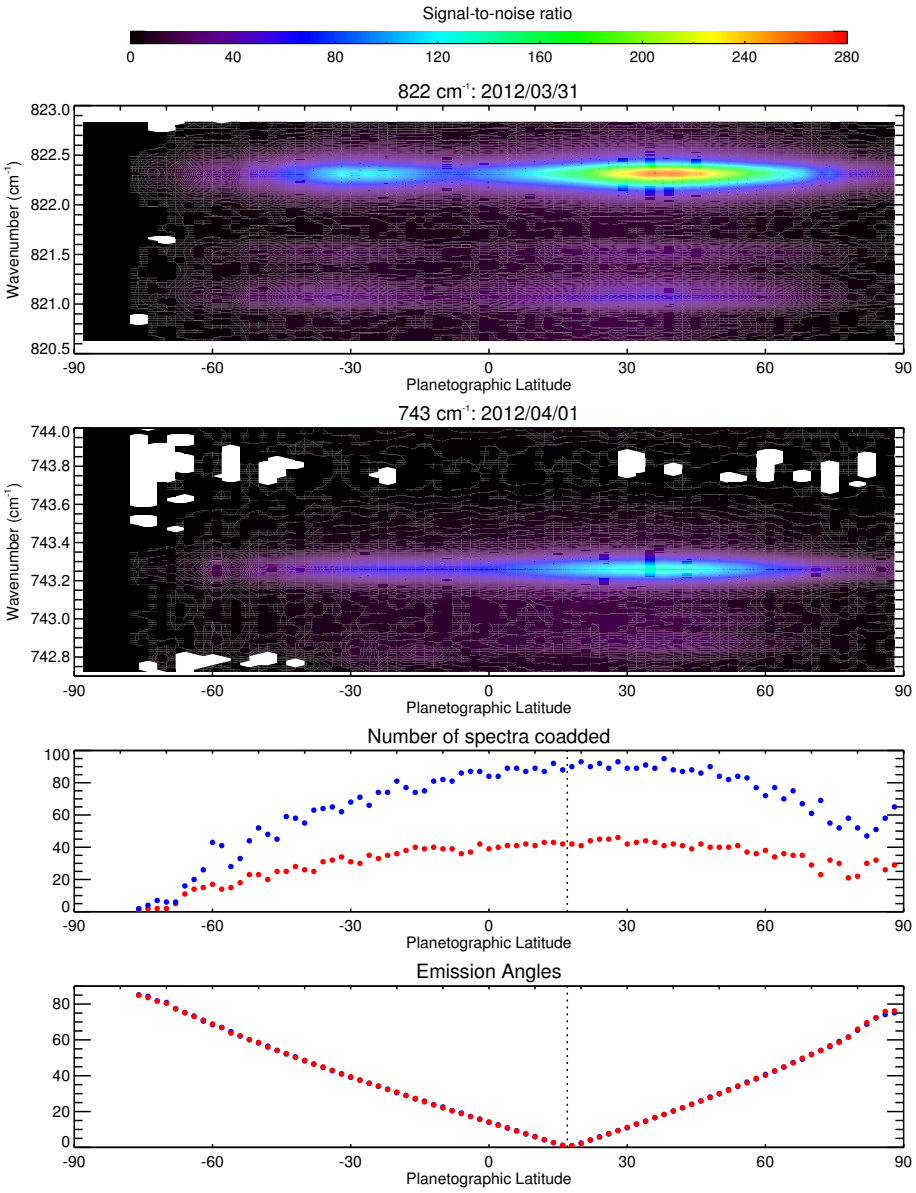

Figure 7.6: The coadded observations at 822 cm^{-1} on 2012/03/31 and 743 cm^{-1} on 2012/04/01 as a function of planetographic latitude. The top plots show the uncalibrated spectra in units of the signal-to-noise ratio, the middle plots show the number of spectra coadded in each latitude bin and the bottom plots show the resultant emission angle. The vertical dotted lines indicate the sub-observer latitude at the time these observations were acquired.

this latitude [Fletcher et al., 2012]. There is a dip in the emission from the equator to approximately 25°S due to obscuration by the rings at these latitude ranges.

In order to demonstrate the signal-to-noise ratio that may be acheieved, all spectra in both bands were sorted into latitude bins that were 4° (planetographic) in size with a nyquist overlap of 2° and coadded or averaged together. Given the procedure in acquiring data where the rotation of the planet has been used to obtain longitudinal coverage, averaging over latitude bands in this way involves coaddition over a small range in emission angle and thus different viewing geometries are not being mixed. The effective noise on the coadded spectra, $\sigma_{\text{eff}}(\tilde{\nu})$, is estimated as given in Equation 7.3.

$$\sigma_{\text{eff}}(\tilde{\nu}) = \frac{1}{N}\sqrt{\sum_{i}^{N} \text{NESR}_i^2} \tag{7.3}$$

Here, N is the total number of spectra coadded in each latitude bin and $\text{NESR}_i(\tilde{\nu})$ is the noise on the ith spectrum used in the coadd. Figures 7.6 shows the resultant signal-to-noise ratios of coadded spectra in the 822 cm^{-1} and 743 cm^{-1} bands, the number of spectra coadded and their emission angles. As shown, the signal-to-noise ratio in both bands peaks at approximately 40°N, which is consistent with the thermal and chemical enrichments of C_2H_2 and C_2H_6 at this latitude due to the storm [Fletcher et al., 2012]. In general, fewer A-B chop pairs were acquired in the 822 cm^{-1} data than in the 743 cm^{-1} band and thus fewer individual observations in the former band were available to coadd into each latitude bin. Yet, the signal-to-noise in the 822 cm^{-1} band (>250 at ∼822.3 cm^{-1} at 40°N) exceeds that of the 743 cm^{-1} band (∼140 at 743.3 cm^{-1} at 40°N). This is due to the higher level of telluric absorption in the 743 cm^{-1} band and the earth's atmosphere limiting the signal reaching the instrument.

It is unlikely that observations south of the equator can be further analysed due to the obscuration by Saturn's rings. Unobscured latitudes further south of the rings are also

within the diffraction limit of the southern limb of the planet and thus signal from the planet and dark sky are likely mixed together. Similarly, latitudes north of 70°N are within the diffraction limit of the northern limb. Thus, only observations north of the equator and south of 70°N are further analysed (Chapter 8).

7.4 Calibration

The radiometic calibration was conducted in order to convert the IRTF-Celeste observations of Saturn into units of radiance (power received per unit area per unit solid angle per wavenumber interval).

Venus and Mars have historically been chosen as calibration targets in previous Celeste runs for several reasons. Firstly, they are bright targets in the thermal infrared and thus very little integration time was required to obtain an adequate signal-to-noise ratio, thus leaving more awarded telescope time on the target of scientific interest. Secondly, as spatially-extended sources, they illuminated the slit of Celeste in a similar way to Saturn: use of point sources as radiance calibration standards such as stars or asteroid targets has proven problematic in previous Celeste runs since they illuminate the slit of the instrument differently.

Using Venus and Mars as calibration standards, several different methods for conducting the radiometric calibration have been explored. In accordance with previous Celeste data reductions, the calibration scale factors have been derived by scaling the uncalibrated Celeste observations of Venus and Mars to infrared observations of these planets from Venera 15 and Mariner 9. However, Venus has only been used to calibrate the 822 cm^{-1} data since it was viewed at too high an airmass in the 743 cm^{-1} band (Table 7.1). The Mariner-9 and Venera 15 infrared spectra were of considerably lower spectral resolutions than those of Celeste and represent averages over large spatial regions and viewing angles. In order

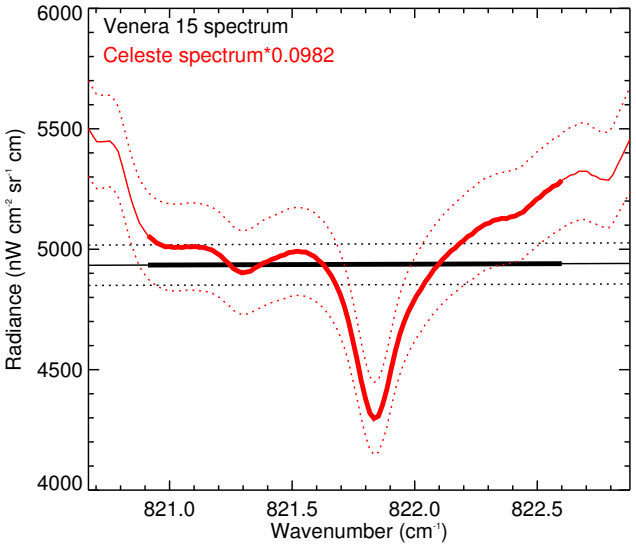

Figure 7.7: Calibration using Venera 15: An average of 55 spectra between 66°S and 16°N from Venera 15 (black, solid). The solid line indicates the observed spectrum with dotted lines outlining the noise (which is characterised as the NESR of the instrument divided by a factor of $1\sqrt{55}$ to account for coaddition of 55 spectra). Spectral regions with thicker lines in both spectra indicate the wavenumber ranges used to calculate the calibration scaling factor.

to remove these sources of uncertainty, radiative transfer models of Venus and Mars at spectral resolutions and emission angles of Celeste were produced and the calibration also attempted by scaling the uncalibrated Celeste observations to these forward models. Ultimately, IRTF-Celeste spectra calibrated using all the above methods were not analysed in this thesis in favour of spectra calibrated using an alternative approach that is presented in Section 8.2.3 of the next Chapter. As discussed in 8.2.3, spectra calibrated using Venus and Mars are too high in radiance. The calibration methods using Venus and Mars and a discussion of possible sources of error are presented below.

7.4.1 Calibration using Venus

Using the Venera 15 spectrum: Venera 15 was a spacecraft sent to Venus by the Soviet Union. The spacecraft was launched in June 1983 and reached an orbit around Venus in October 1983 where it observed the planet for two months. The spacecraft was host to radar instruments, detectors for measuring cosmic rays and solar plasma fields as well as an infrared fourier transform radiometer instrument [Zasova et al., 2006]. The infrared radiometer operates in a spectral range from approximately 300 cm^{-1} to $\sim$1600 cm^{-1} at a spectral resolution of approximately 3.5 cm^{-1}. A spectrum of Venus from this instrument, which is an average over latitudes from 66°S to 16°N, was provided by the Celeste team. For consistency in latitude sampling, Celeste observations of Venus in the 822 cm^{-1} band were coadded over a similar latitude range. This resulted in averaging over 26 spatial pixels and emission angles ranging from approximately 30° to 70°. Figure 7.7 compares the (scaled) observed Celeste spectrum of Venus with that of Venera 15. While the Celeste spectrum shows spectral features including a CO_2 absorption feature at $\sim$821.8 cm^{-1}, the Venera 15 spectrum is flat over the $\sim$2 cm^{-1} range shown due to the comparably lower spectral resolution. Thus, the calibrating scale factor is calculated as a crude ratio of the signal in the Venera 15 spectrum with that of Celeste averaged over the spectral ranges indicated in Figure 7.7.

Using forward model of Venus: The IRTF-Celeste spectra of 4 spatial pixels centred on the sub-observer latitude of Venus (approximately the equator) were selected and averaged together. Given the alignment of the slit of the spectrometer west of the Venus' central meridian, the emission angle of this spectrum is approximately 30°. A forward model of Venus at an emission angle of 30° was computed using the radiative transfer model outlined in Appendix B.2 (adopting the *high cloud opacity* model as the cloud model). Figure 7.8 compares the scaled Celeste coadded spectrum with this forward model. Given the consistency in the forward model and the Celeste coadd, the calibration scale factor

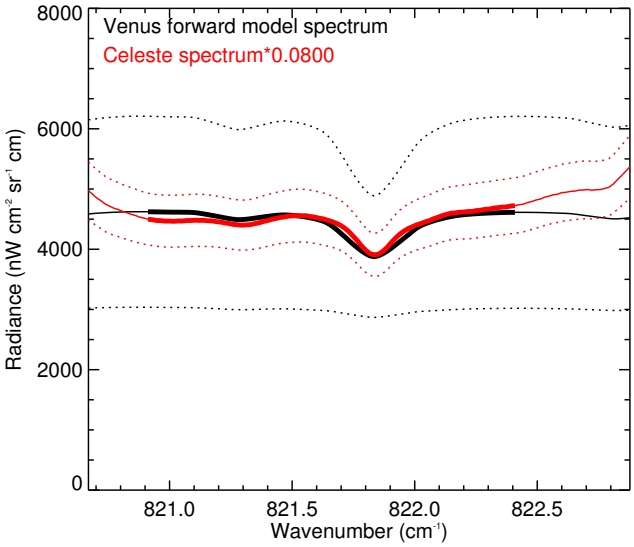

Figure 7.8: Calibration using forward model of Venus: The forward modelled spectrum (black) and an equatorial coadd of Celeste observations (red) of Venus at 822 cm^{-1}. Solid lines indicate spectra while dotted lines outline the noise on each spectra. Spectral regions with thicker lines in both spectra indicate the wavenumber ranges used to calculate the calibration scaling factor.

has been calculated over a large spectral range as indicated in the Figure.

7.4.2 Calibration using Mars

Using Mariner 9-IRIS: Mariner 9 was a NASA space orbiter which was launched in May 1971 and arrived in orbit around Mars in November of the same year. The spacecraft arrived at Mars during a planet-wide dust storm. However once the storm settled, a variety of remote sensing and imaging instruments aboard began taking observations. The Infrared Interferometer Spectrometer (IRIS, Hanel et al. [1972]) onboard operated in a spectral range from approximately 200 cm^{-1} to 2200 cm^{-1} at a spectral resolution of approximately 1.2 cm^{-1}. A global coadd of all Mariner 9-IRIS spectra acquired was provided by the Celeste team. Whilst avoiding two spatial pixels (each of an angular size of approximately 0.55") at the northern and southern limb of the planet which are within

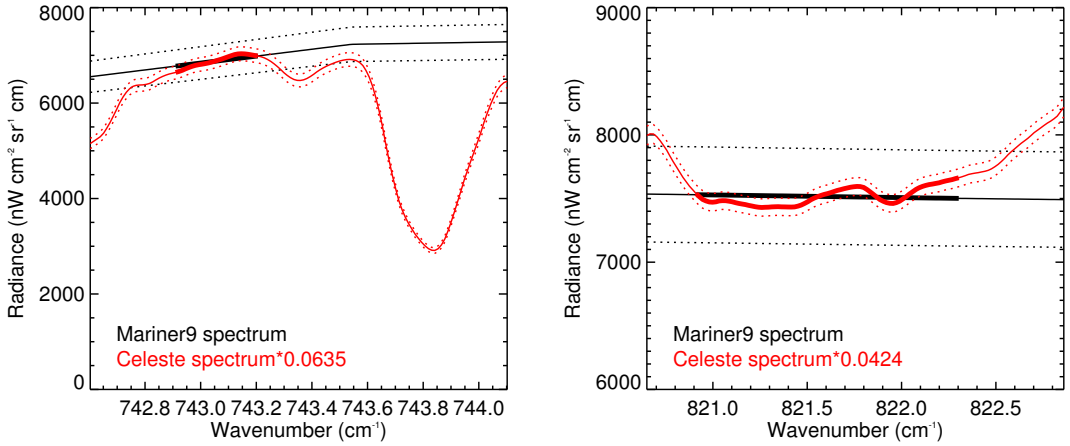

Figure 7.9: Calibration using Mariner 9-IRIS: Calibration of globally-averaged Celeste observations of Mars (red) and the Mariner 9-IRIS spectrum (black) at 743 cm^{-1} (left) and 822 cm^{-1} (right). Solid lines indicate spectra and dotted line show the corresponding noise. Spectral regions with thicker lines in both spectra indicate the wavenumber ranges used to calculate the calibration scaling factor.

the diffraction limit (1") of dark sky, Celeste spectra of all visible latitudes on Mars were coadded in the 743 cm^{-1} and 822 cm^{-1} bands. This resulted in an average over 17 spatial pixels of spectra with a range in emission angle from 0° to 50°. It should be noted that the sub-observer latitude on Mars was 22°N during the March 2012 observing run (Table 7.1) and thus a global coadd of visible Celeste spectra is considerably biased to the northern hemisphere. Figure 7.9 compares the global Celeste coadds in both bands with those from Mariner 9-IRIS. In the 822 cm^{-1} band, the Martian spectrum is approximately flat and thus the calibrating scale factor is determined simply by the ratio of the Mariner 9-IRIS signal with that of Celeste over the broad spectral range indicated in the figure. In the 743 cm^{-1} band, the feature at approximately 743.9 cm^{-1} is a superposition of CO_2 absorption in both the Martian and telluric atmospheres. As was the case for calibration using the Venera 15 spectrum, the comparably lower spectral resolution of the Mariner 9-IRIS spectrum cannot resolve this feature. Thus, the calibrating scale factor was determined from a continuum region (as indicated in the Figure) avoiding this absorption feature.

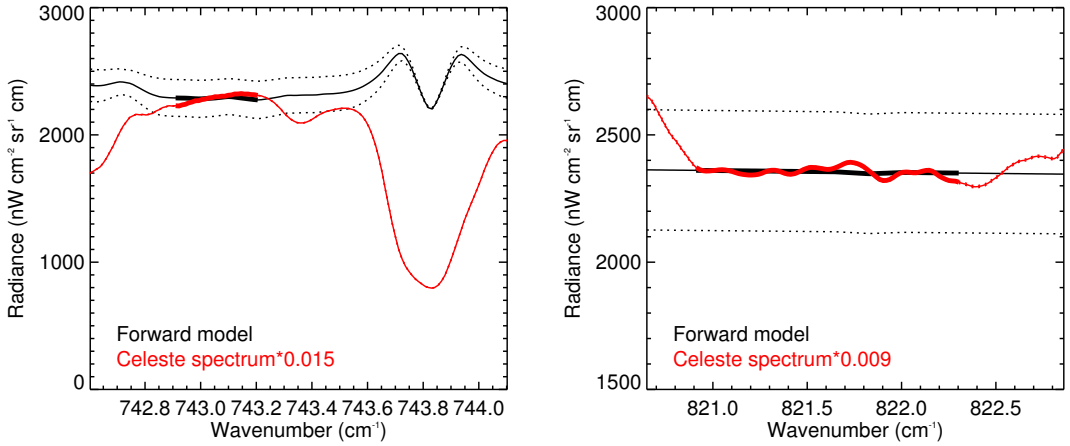

Figure 7.10: Calibration using forward model of Mars: A forward model (black) and an equatorial coadd of Celeste observations (red) of Mars at 743 cm^{-1} (left) and 822 cm^{-1} (right). Solid lines indicate spectra while dotted lines outline the noise on each spectra. Spectral regions with thicker lines in both spectra indicate the wavenumber ranges used to calculate the calibration scaling factor.

Using forward model of Mars: Celeste spectra of 4 spatial pixels centred on the sub-observer latitude of Mars (approximately 22°N) were averaged together in order to produce a coadd which was approximately zero in mean emission angle. Forward models of Mars in the 743 cm^{-1} and 822 cm^{-1} bands at zero emission angle were computed using the radiative transfer forward model detailed in Appendix B.3. Figure 7.10 compares the forward modelled and coadded (scaled) Celeste observations of Mars. Again, the CO_2 absorption feature at approximately 743.9 cm^{-1} dominates the Martian spectrum in the 743 cm^{-1} band. The inconsistent width of the CO_2 feature between Celeste and the forward model is because the former is the result of both telluric and martian CO_2 absorption. Thus, the calibration scale factor in the 743 cm^{-1} band has been calculated using the continuum at 743 cm^{-1}, as indicated in the Figure. In the 822 cm^{-1} band, the Martian spectrum is approximately flat and thus a wide spectral region has been chosen for determining the calibration scale factor in this band.

Date	Calibrating Target	Standard Spectrum	Band	Calibrating Scaling Factors x 10^2
2012/03/31	Venus	Venera 15	822	9.82 ± 0.03
		Forward model	822	8.00 ± 0.50
	Mars	Mariner 9	822	42.37 ± 0.39
		Forward model	822	9.17 ± 0.07
2012/04/01	Mars	Mariner 9	743	63.46 ± 1.31
		Forward model	743	14.98 ± 0.21

Table 7.3: A summary of derived calibration scaling factors to be applied to Celeste observations of Saturn at 743 cm^{-1} and 822 cm^{-1} using different calibrating targets and standard spectra. All latitudes for Saturn are planetographic. The scale factors describe the calibration into radiance units of nW cm^{-2} sr^{-1} cm.

7.4.3 Discussion of calibration methods

Table 7.3 summarises the calibration scale factors determined from the methods outlined above in Sections 7.4.1 and 7.4.2. As shown, there is a considerable range in calibration scaling factors. As demonstrated in Section 8.2.3, all scaling factors shown in Table 7.3 are over a factor of 4 higher than scaling factors derived from an alternative calibration approach using Cassini-CIRS results.

In using infrared observations from Venera 15 and Mariner 9 to calibrate IRTF-Celeste spectra, the large differences in the spectral resolutions (of greater than a factor of 10) is likely a considerable source of error. In particular, the 822 cm^{-1} band of Venus and the 743 cm^{-1} band of Mars both include a CO_2 absorption feature which is not resolved by either Venera 15 or Mariner 9-IRIS which show approximately flat spectra in these bands. Further likely sources of error in using these spacecraft observations as calibration standards are the differences in the latitudinal sampling and thus the emission angles of the observations. Both the Venera 15 and Mariner 9 spectra are averages of observations over large ranges in latitude and emission angle. In replicating these spatial ranges with

IRTF-Celeste spectra that are acquired from Earth, spectra of different emission angles are averaged. IRTF-Celeste spectra of Venus and Mars are averages of observations acquired within 30 minutes. However, the Venera 15 and Mariner 9 spectra are averages over much larger time ranges during which atmospheric conditions such as temperature and aerosol concentration may have changed. In particular, the Mariner 9 spectrum is an average over half a Martian year during which surface and atmospheric temperatures on Mars vary significantly. Thus, differences in the temporal sampling between IRTF-Celeste and Venera 15 and Mariner 9 spectra is an additional source of uncertainty. For this reason, Mars is not considered a viable calibration standard.

Calibration using radiative transfer forward models of Venus and Mars removes the sources of uncertainty due to differences in the spectral resolution and emission angles. However, the main limitation in computing forward models of terrestrial planets as calibration spectra is the uncertainty in atmospheric properties at the required position/time such as temperature, cloud/aerosol concentrations and opacities which affect the modelled radiances. This source of uncertainty is reflected in the large error bars on the modelled radiances.

7.5 Summary

IRTF-Celeste data of C_2H_2 and C_2H_6 emission on Saturn provide observations of a high spectral resolution to complement the lower resolving power of Cassini-CIRS. In particular, the 822 cm^{-1} band data are acquired in a relatively clear window of the Earth's transmission spectrum (>90%) and thus observations in this band exhibit a high signal-to-noise ratio. Spectra in this band contain both a $^{12}C_2H_6$ and $^{13}C^{12}CH_6$ feature which will potentially allow for the $^{12}C/^{13}C$ ratio to be determined in future work. Telluric transmission is lower in the 743 cm^{-1} band: these observations exhibit a lower signal-to-noise

ratio and an improper removal of telluric absorption cannot be ruled out.

As is true for ground-based observing in the thermal infrared in general, the radiometric calibration represents a signficant source of uncertainty on the observations. An attempt was made at calibrating the data using Venus and Mars as standards. However, as we will see in Chapter 8, these derived calibration scale factors yield radiances which are considerably higher than those using a calibration from Cassini-CIRS results. Spectra calibrated using Venus and Mars are therefore not analysed in this thesis.

Chapter 8

Saturn's northern hemisphere in 2012 from Cassini-CIRS and IRTF-Celeste observations

The most recent evolution of Saturn's northern hemisphere is investigated in this chapter, both from Cassini-CIRS observations and spectra obtained by Celeste on the IRTF. At this time, the northern hemisphere was dominated by a vortex 'beacon', which emerged in December 2010. The thermal and chemical properties of this feature has been the focus of much recent work [Fletcher et al., 2011, 2012; Hesman et al., 2011]. Fletcher et al. [2012] investigated the evolution of the beacon up to March 2012 using Cassini-CIRS observations. The aim of this Chapter was to reproduce these results using instead IRTF-Celeste spectra of C_2H_2 and C_2H_6 emission that were acquired in March/April 2012. This was attempted in this Chapter, but as demonstrated, there is little confidence in these results due to calibration uncertainties and the poor consistency with CIRS results. However, the results retrieved from CIRS observations in 2012 alone provided insight into the most recent seasonal changes in the northern hemisphere.

8.1 The northern stratosphere in 2012 from Cassini-CIRS

Modelling the C_2H_2 and C_2H_6 features in the IRTF-Celeste observations requires knowledge of the stratospheric temperature since the strength of emission in these features is dependent on both the gas concentration and the temperature of the line forming re-

gion. However, observations of CH_4 emission, which serve as a sensor of stratospheric temperature, were not acquired by IRTF-Celeste in 2012. In the absence of CH_4 spectra from Celeste, there was no choice but to use Cassini-CIRS observations to determine the temperature field in Saturn's northern hemisphere in this year. The vertical temperature profiles were therefore retrieved from Cassini-CIRS observations in 2012 and also using similar observations in 2009 to compare atmospheric properties before and after the eruption of the beacon.

In addition, the stratospheric concentrations of acetylene and ethane were also retrieved from these Cassini-CIRS observations. Nominally, this was conducted simply with the aim of allowing for a comparison of CIRS and Celeste results. However, as demonstrated in Section 8.2.3, the calibration of IRTF-Celeste spectra using Venus or Mars as standards (Section 7.4) yielded radiances which were too high. Stratospheric temperature and the concentrations of acetylene and ethane were also required in order to produce synthetic IRTF-Celeste spectra for use in an alternative calibration procedure.

8.1.1 Observations

As conducted in Chapters 4, 5 and 6, the analysis of Cassini-CIRS observations was repeated three times using spectra from the v3.2, v4.2 and v4.3 calibrations. This was done in order to assess the sensitivity of atmospheric properties to the different calibration procedures. The selection, coaddition and analysis of Cassini-CIRS observations described below has been in this years described below has been applied to the observations from these three calibration versions.

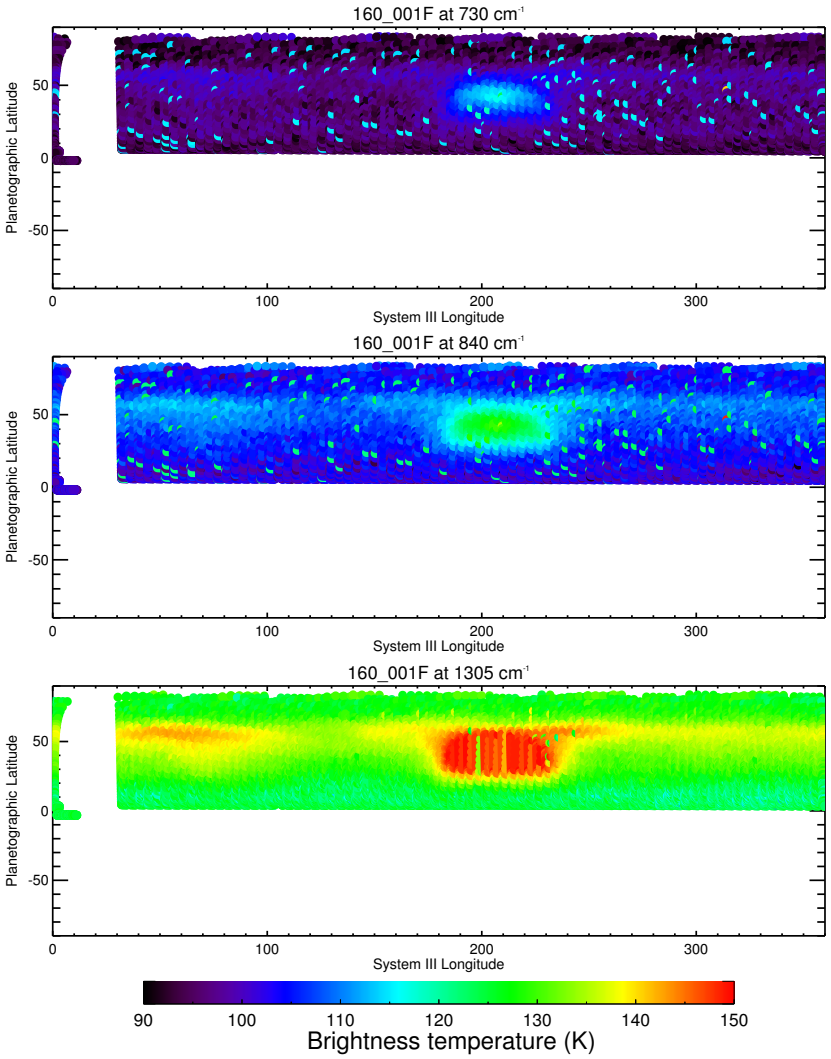

Figure 8.1: Brightness temperature maps of the 163_001F observation (2012/01/27) at 720 cm^{-1} (the C_2H_2 band), 830 cm^{-1} (the C_2H_6) band and 1305 cm^{-1} (the CH_4 band).

8.1.1.1 2009

An analysis of the 120_001F FIRMAP (December 2009) observation has previously been presented in Chapter 5 and Chapter 6. However, the results of these Chapters have used observations binned in latitude differently from the latitudinal binning applied to IRTF-

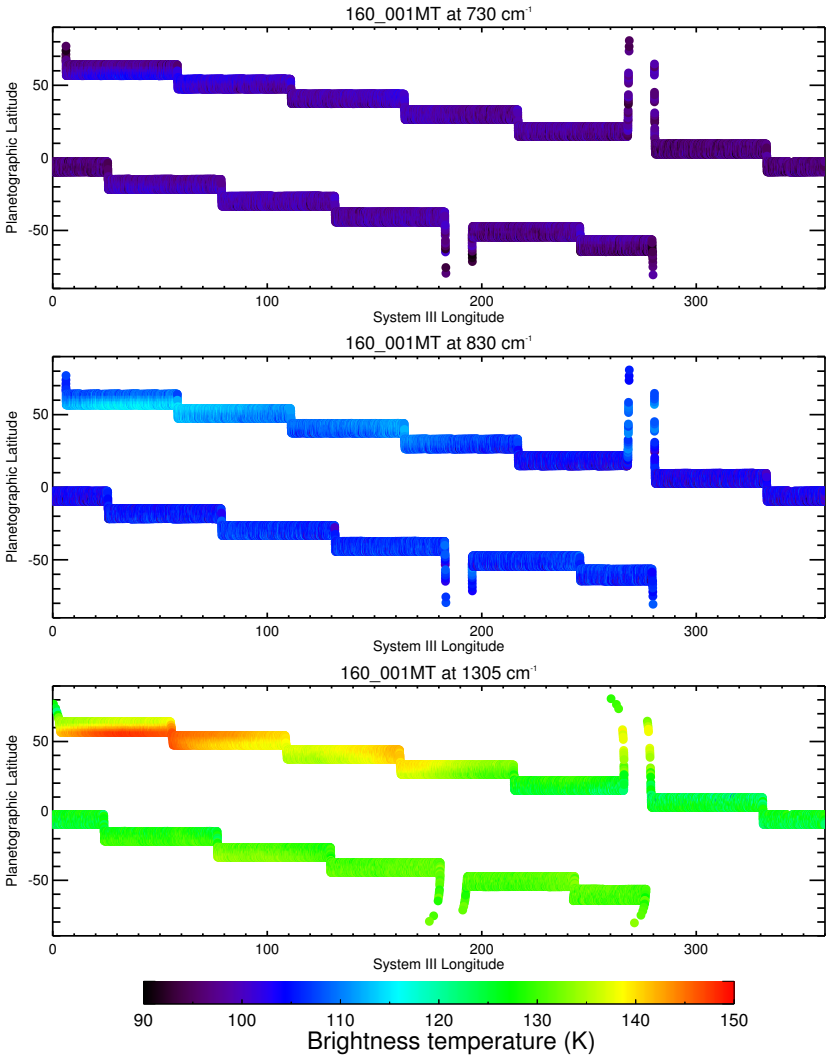

Figure 8.2: Brightness temperature maps of the 163_001MT observation (2012/04/01) at 720 cm^{-1} (the C_2H_2 band), 830 cm^{-1} (the C_2H_6) band and 1305 cm^{-1} (the CH_4 band).

Celeste spectra. Thus, individual spectra of the 120_001F FIRMAP observation were sorted into 4° planetographic latitude bins (with a 2° Nyquist overlap) in accordance with the latitudinal binning procedure applied to IRTF-Celeste observations and re-analysed in this Chapter. These observations are henceforth described as the $F09_{all}$ observations (the 'F' denotes FIRMAP, '09' denotes the year 2009 and 'all' denotes that individual spectra

of all available longitudes were coadded).

8.1.1.2 2012

To determine the temperature field in 2012, the 160_001F FIRMAP (January 2012) and 163_001MT MIRTMAP (April 2012) observations were chosen. The former observation was acquired two months before the Celeste data in 2012 but is advantageous in that it provided an almost global coverage of the planet in latitude and longitude. The latter CIRS observation was acquired during the 2012 IRTF-Celeste observing run and therefore best sampled the atmospheric conditions when IRTF-Celeste observations were acquired. Figures 8.1 and 8.2 show brightness temperature maps of these two observations in the C_2H_2, C_2H_6 and CH_4 bands.

As shown in both Figures, there were significant longitudinal variations in brightness temperature in all three emission bands, in particular from approximately 30°N to 60°N which represents the latitude range affected by the beacon. In Chapters 4, 5 and 6, all available observations in a latitude bin were averaged together since it is assumed that there are little or no variations in atmospheric properties with longitude. However, coadding CIRS observations in 2012 with such an assumption and using these results to model IRTF-Celeste spectra could induce significant sources of error. Therefore, where possible, CIRS observations in 2012 were coadded over the same longitude ranges sampled by IRTF-Celeste observations, as described below.

Using the 163_001MT observation: In this observation, CIRS mapped one latitude band before scanning to an adjacent latitude band. Thus, if individidual observations only of a certain longitude range were to be selected for coaddition, this would similarly involve restricting the available observations in latitude. For example, IRTF-Celeste data on 31/03/12 (in the 822 cm^{-1} band) sampled the planet from longitudes of approximately 130° to 240°. In the northern hemisphere, the 163_001MT observation only sampled this

longitude range from latitudes of approximately 10°N to 35°N. In order to avoid restricting the latitude ranges which could be analysed, all individual spectra from the 163_001MT observation of the v4.2 calibration were coadded into 4° planetographic latitude bins and stepped in 2° latitude increments in accordance with the latitudinal binning procedure applied to IRTF-Celeste observations. These observations are henceforth named the $MT12_{all}$ observations (where the 'MT' denotes MIRTMAP, '12' denotes the year 2012 and 'all' denotes that individual spectra of all available longitudes were coadded). Only coadds in the northern hemisphere were further analysed

Using the 160_001F observation: The 160_001F observation, though observing the planet two months prior to the Celeste data, provides almost global coverage of the planet which allowed the desired longitude and latitude ranges to be selected easily. However, even if it is assumed that general seasonal changes in temperature and composition were negligible between the 160_001F observation and IRTF-Celeste observing run, the atmospheric conditions from approximately 20°N to 55°N at a given longitude will have varied signficantly due to the longitudinal movement of the beacon. Assuming a longitudinal movement of 2.7° per day, as determined by Fletcher et al. [2012], the beacon on 31/03/12 would have moved approximately 2.7°/day x 64 days = 173° in longitude since the 160_001F observation acquired on 27/01/12. Thus, in order to best sample the atmospheric conditions sampled by IRTF-Celeste spectra on 31/03/12, individual spectra from the 160_001F observation from longitudes of 130° - 173° ≈ 320° to 240° - 173° ≈ 70° were required. Similarly, the beacon on 01/04/12 moved approximately 2.7°/day x 65 days = 176° in longitude since 27/01/12. Thus, individual spectra of the 160_001F observation from longitudes of 90° - 176° ≈ 275° to 340° - 176° ≈ 165° were selected. This selection of different longitudinal ranges for consistency in the longitudinal ranges sampled by Celeste assumes that atmospheric conditions within the beacon have not evolved and the northern hemisphere has generally not evolved seasonally over the course of two (Earth) months. While this latter assumption may be approximately true, Fletcher et al. [2012] derived a cool-

Coadd name	$\Delta\tilde{\nu}$ (cm^{-1})	Date (yyyy/mm/dd)	Latitude range	Longitude range
$F09_{all}$	15.5	2009/11/04	0° - 86°N	all available
$F12_{all}$	15.5	2012/01/27	0° - 84°N	all available
$F12_{320:70}$	15.5	2012/01/27	0° - 84°N	320° - 70°
$F12_{275:165}$	15.5	2012/01/27	0° - 84°N	275° - 165°
$MT12_{all}$	2.5	2012/04/01	0° - 66°N	all available

Table 8.1: A summary of all coadded Cassini-CIRS observations in 2009 and 2012 which were analysed.

ing rate of the beacon of 0.1 ± 0.05 K/day and thus the former assumption may not be valid.

Initially, individual 160_001F spectra at all available longitudes (approximately 30° to 360°) were sorted into 4° planetographic latitude bins that were stepped in 2° increments and coadded. These are henceforth described as the $F12_{all}$ observations using the same nomenclature as detailed for 2009 FIRMAP and 2012 MIRTMAP observations. Subsequently, the same latitudinal binning procedure was applied to individual 160_001F spectra observed at longitudes from 320° to 70° and from 275° to 165°. These two sets of observations are henceforth described as the $F12_{320:70}$ and $F12_{275:165}$ observations. Table 8.1 summarises all CIRS observations analysed in this Chapter.

8.1.2 Analysis

Using the retrieval procedure outlined in Section 4.2, the vertical temperature profile and the stratospheric concentrations of acetylene and ethane were retrieved from the $F09_{all}$, $F12_{all}$, $F12_{320:70}$, $F12_{275:165}$ and $MT12_{all}$ coadded observations.

The vertical contribution functions of the $\Delta\tilde{\nu}$ = 15.5 cm^{-1} FIRMAP observations have already been presented in Chapter 4. Figure 8.3 compares these contribution functions with those of the $\Delta\tilde{\nu}$ = 2.5 cm^{-1} MIRTMAP observations. As shown, at both spectral resolutions, the collision-induced spectrum provides greatest sensitivity to the ∼200 mbar

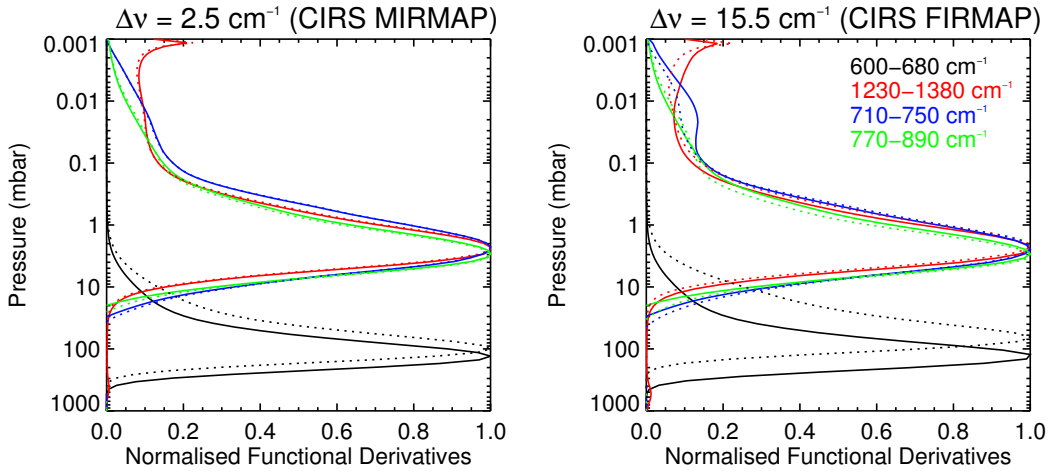

Figure 8.3: A comparison of the vertical functional derivatives between $\Delta\tilde{\nu} = 2.5$ cm^{-1} and $\Delta\tilde{\nu} = 15.5$ cm^{-1} observations averaged over the collision-induced spectrum (600 - 680 cm^{-1}, the sensor of tropospheric temperature, black), the CH_4 ν_4 band (1230 - 1380 cm^{-1}, the sensor of stratospheric temperature, red) and the C_2H_2 ν_5 (710 - 750 cm^{-1}, blue) and C_2H_6 ν_9 (770 - 890 cm^{-1}, green) bands used as sensors of the concentrations of these species. Solid and dashed profiles show contribution functions corresponding to low emission angle (<15°) and high emission angle (>60°) observations respectively.

level with more sensitivity to a slightly higher altitude when high emission angle observations were used. The weighting function of the CH_4 band peaks at the 1-2 mbar level at a spectral resolution of $\Delta\tilde{\nu} = 15.5$ cm^{-1}. However, at $\Delta\tilde{\nu} = 2.5$ cm^{-1}, the weighting function peaks at a slightly higher pressure (approximately 3 - 4 mbar) and also shows some sensitivity to the 0.01 mbar level. Thus, differences in the vertical information content of stratospheric temperature between the two spectral resolutions cannot be ruled out. However, as we will see in 8.1.3, the consistency in stratospheric temperatures at 2.1 mbar retrieved from $\Delta\tilde{\nu} = 2.5$ cm^{-1} and $\Delta\tilde{\nu} = 15.5$ cm^{-1} demonstrates that both spectral resolutions provide similar sensitivity to this pressure level. At both spectral resolutions, the C_2H_2 and C_2H_6 bands also peak in sensitivity at the 1-2 mbar level and thus temperature and the abundances of these two hydrocarbons can be disentangled. Stratospheric temperatures and the concentrations of acetylene and ethane are presented at the 2.1 mbar level in the next section, in accordance with previous Chapters.

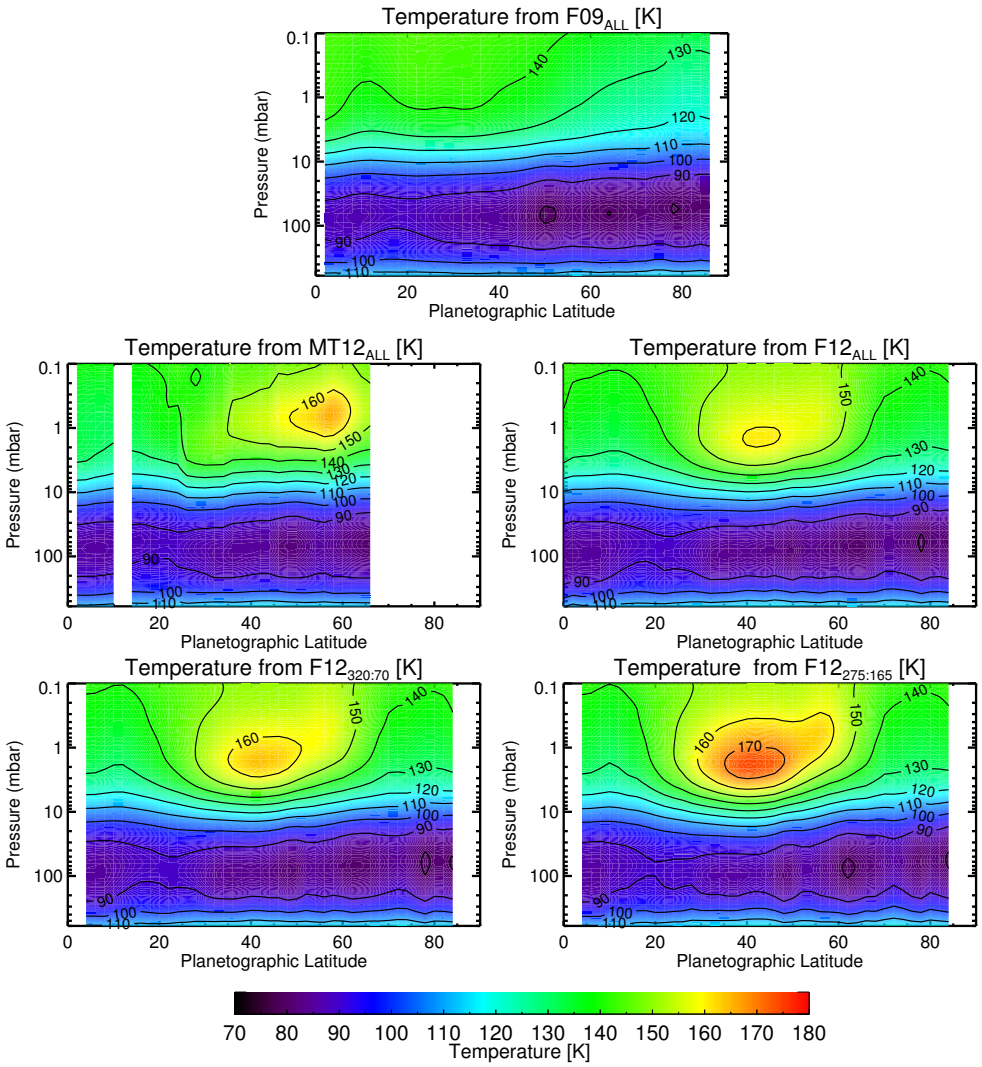

Figure 8.4: The retrieved latitudinal-vertical distributions of temperature from $F09_{all}$ (top), $MT12_{all}$ (middle left), $F12_{320:70}$ (middle right), $F12_{320:70}$ (bottom left) and $F12_{275:165}$ (bottom right).

8.1.3 Results

Figure 8.4 shows the retrieved distributions of temperature from the $F09_{all}$, $F12_{all}$, $F12_{320:70}$, $F12_{275:165}$ and $MT12_{all}$ observations detailed in Section 8.1.1. From the same observations, Figure 8.5 shows the retrieved results of stratospheric temperature and the concentrations

of acetylene and ethane at the 2.1 mbar level. There were generally negligible differences in retrieved results depending on whether observations of the v3.2, v4.2 or v4.3 calibrations were used. Figure 8.5 shows results retrieved from v4.2 observations but error bars reflect any differences in the results when v3.2 or v4.3 observations were used instead.

8.1.3.1 Low latitudes

At latitudes lower than 15°N, the temperature at 2.1 mbar exhibits a decrease from 2009 to 2012. In this latter year, the temperature at this level exhibits little variation with the ranges of longitude sampled in the observations. This indicates little or negligible zonal variation in stratospheric temperature at these latitudes in comparison to higher latitudes affected by the beacon. While a radiative climate model predicts a decrease in temperature of only 2-3 K at latitudes lower than 10°N (Figure 1.3), the temperature at 2°N, for example, decreases from 140.5 ± 0.5 K to 132.6 ± 0.7 K. Thus, a radiative explanation is ruled out and instead, the cooling trend is attributed to the evolution of the SSAO. The interannual differences in stratospheric temperature at the equator in Chapter 6 were attributed to either a recent deviation of the SSAO from its expected behaviour or more dramatically, the *death* of the SSAO. The fact that the SSAO continues to modulate stratospheric temperatures at equatorial latitudes from 2009 to 2012 suggests that the latter explanation can be ruled out.

While acetylene exhibits little evolution from 2009 to 2012 at low latitudes, ethane's concentration shows a significant decrease at latitudes lower than 30°N. This is demonstrated in Figure 8.6 which shows retrievals from $F09_{all}$ and $F12_{all}$ observations at 24°N. From 2009 to 2012, radiances in the C_2H_2 and CH_4 bands remained approximately constant while the radiance C_2H_6 band decreased. This corresponds to a decrease in ethane's concentration from 5.61 ± 0.14 ppmv to 3.52 ± 0.13 ppmv from 2009 to 2012 while acetylene's concentration is constant within error bars (172.73 ± 10.62 ppbv and 183.19 ± 8.72

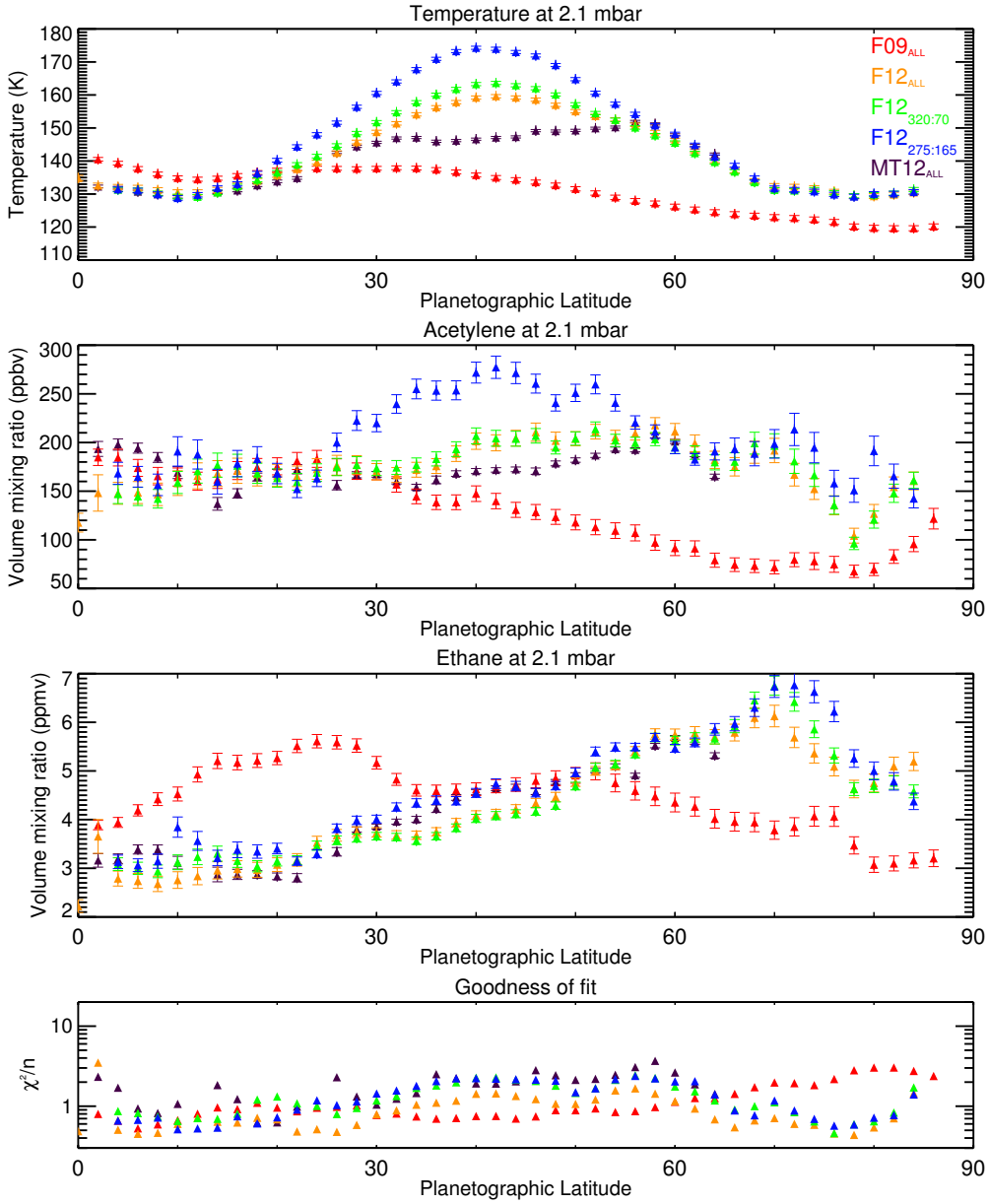

Figure 8.5: Retrieved temperatures and the concentrations of acetylene and ethane at 2.1 mbar from $F09_{all}$ (red), $F12_{all}$ (orange), $F12_{320:70}$ (green), $F12_{275:165}$ (blue) and $MT12_{all}$ (purple) observations. Results and uncertainties retrieved from v4.2 observations are shown. However, error bars on these values have been increased to include the value retrieved from v3.2 and v4.3 observations if these values differed by greater than 1σ.

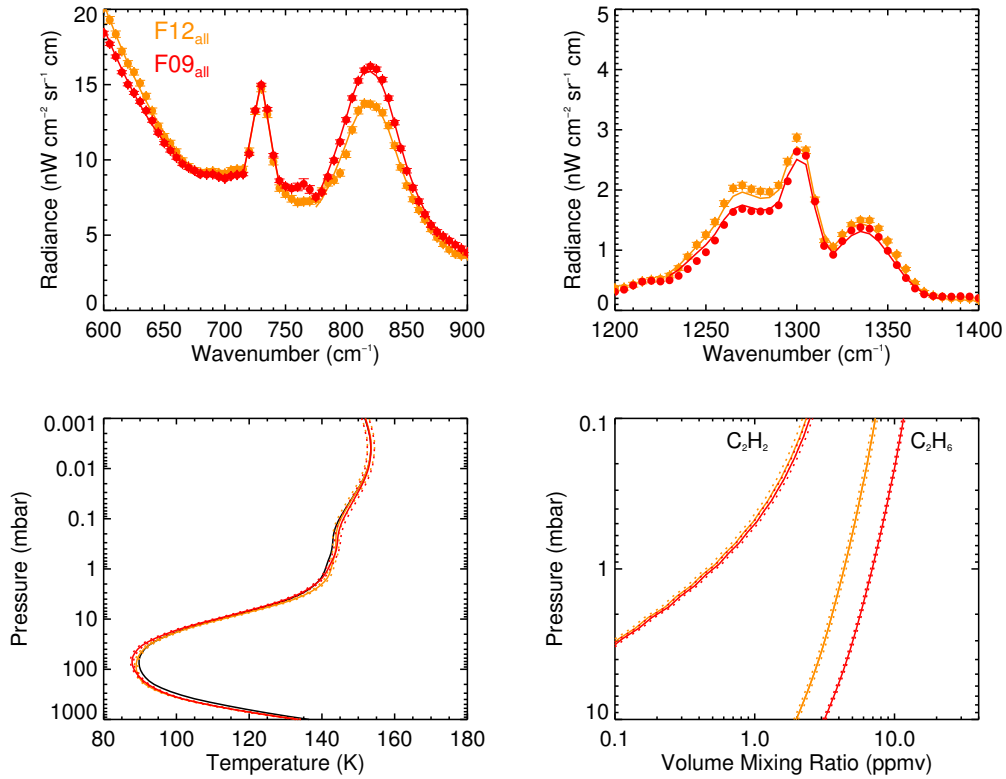

Figure 8.6: Observation-model comparisons and the corresponding retrievals of temperature, acetylene and ethane at 24°N from $F09_{all}$ (red), $F12_{all}$ (orange) observations. Black profiles indicate the *a priori* profile, coloured solid profiles show retrieved profiles and dotted profiles indicate the uncertainty on these retrievals.

ppbv respectively). The decrease in ethane's concentration with time would nominally imply the presence of upwelling which advects hydrocarbon-depleted air from lower in the stratosphere. However, as detailed in Chapter 5, ethane's concentration increased at 25°N from 2005 to 2009, which was attributed to downwelling associated with Hadley circulation. Thus, the most recent changes in ethane's concentration and the implied upwelling represent a significant change of the vertical motion compared to 2005 and 2009.

According to the global circulation model (Figure 1.8, Friedson and Moses [2012]), the downwelling at 25°N will weaken as northern summer approaches and the Hadley circulation undergoes a direction reversal. At this point, upwelling instead occurs at approxi-

mately 10°N while downwelling occurs at 25°S. Thus, uprising vertical motion is expected but only from approximately 5°N to 15°N and not the much larger range in latitude where ethane's concentration shows a decrease. Thus, the exact cause of ethane's decrease at lower latitudes remains uncertain.

8.1.4 The beacon

In all longitude ranges, there is good agreement in retrieved temperatures at the 2.1 mbar level south of 20°N and north of 55°N in 2012. However, between these two latitudes in this year, there is significant variation in retrieved temperatures depending on the longitude range that is sampled in the coaddition procedure. This represents the latitude range occupied by Saturn's beacon. The apparent difference in latitudinal position of the beacon in the $MT12_{all}$ observations (approximately 55°N) in comparison to other 2012 observations (approximately 40°N) was noted and was attributed to differences in the spatial sampling. While the FIRMAP observation provides full coverage of the beacon feature (Figure 8.1), the MIRTMAP observation (Figure 8.2) did not map the warm temperatures associated with beacon in the latitude band centred on 40°N but sampled the warmer temperatures at higher latitudes.

Figure 8.7 compares retrieved temperatures and hydrocarbon concentrations at 40°N from $F09_{all}$ (before the emergence of the beacon in 2010) and $F12_{320:70}$ and $F12_{275:165}$ observations. Between the two longitudinal averages in 2012, the temperature at the 2.1 mbar level increases by 11.0 ± 0.7 K, the acetylene concentration increases by 65.0 ± 13.5 ppbv and the ethane concentration by 0.53 ± 0.12 ppmv. These thermal and chemical enhancements were produced by downwelling within the vortex, which advects hydrocarbon-richer air from higher in the stratosphere and adiabatically heated the region. In reality, the thermal and chemical contrasts are likely to be larger since the observations, including the beacon region (that is approximately 80° of longitude in size), are also averaged over longitudes

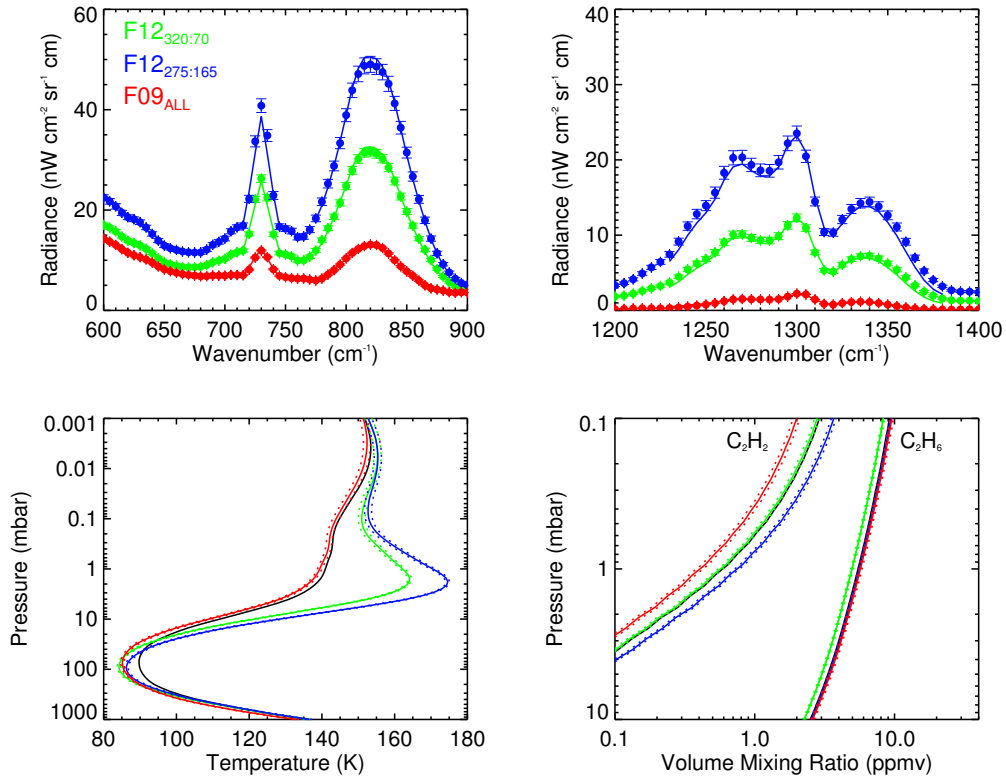

Figure 8.7: Observation-model comparisons and the corresponding retrievals of temperature, acetylene and ethane at 40°N from 2009 (red), 310 - 70° (green) and 260 - 160° (blue). Black profiles indicate the *a priori* profile, coloured solid profiles show retrieved profiles and dotted profiles indicate the uncertainty on these retrievals.

with lesser thermal and chemical enhancements.

Whilst acetylene exhibits a strong enrichment inside the beacon with respect to other longitudes in the same latitude band, ethane's enrichment (though significant with respect to error bars) appears less pronounced. In fact, there is very little departure of ethane from the overall trend of increasing concentration with latitude that is discussed further in Section 8.1.5. This is also in agreement Fletcher et al. [2012] who also determined a larger enrichment of acetylene compared to ethane within and outside the beacon region. This could be attributed to acetylene's stronger vertical gradient and thus increased sensitivity to downwelling within the vortex compared to ethane. However, Fletcher et al. [2012]

also suggest some sensitivity of the C_2H_2 emission to significantly warmer temperatures at μbar pressures at which the CH_4 band observed by CIRS has no sensitivity. The increased concentrations of C_2H_2 could, in part, be the attempt of the retrieval to reproduce the observed C_2H_2 radiances, which are due to increased temperatures at μbar levels rather than an actual increase in acetylene's abundance.

8.1.5 High latitude enrichment of hydrocarbons

The meridional profiles of both acetylene and ethane at high latitude in 2012 have undergone significant changes since 2009. Acetylene's enrichment from 2009 to 2012 at latitudes from 25°N to 55°N has been attributed to the downwelling within the beacon vortex (Section 8.1.4). Similarly, ethane's concentration does vary depending on the longitude range sampled in this latitude range. However, north of 55°N in 2012, temperatures at the 2.1 mbar level are consistent irrespective of the longitude range sampled in the observations. Thus, 55°N appears to mark the northern boundary of the beacon vortex. North of this boundary, both hydrocarbons exhibit a significant increase in concentration. For example, at 70°N, acetylene increases in concentration from 71.9 ± 6.9 ppbv ($F09_{all}$) to 191.8 ± 12.5 ppbv ($F12_{all}$) and ethane increases from 3.53 ± 0.13 ppmv to 5.61 ± 0.14 ppmv using the same observations.

An overall increase in ethane's concentration with latitude in the southern hemisphere was observed in 2005 (Chapter 4). The overall increase in ethane's concentration with latitude in the northern hemisphere in 2012 therefore mimicks similar behaviour observed of this molecule in the southern hemisphere (Chapter 4). This confirms the conclusions of Chapter 5 which attributed the enrichment of ethane's concentration at high-northern latitudes in 2009 with respect to 2005 to be the beginning of an emergence of such a meridional enrichment. The fact that this feature has emerged only 7 years since 2005 indicates that the mechanism producing this meridional enrichment of ethane acts on a

timescale comparable with, or less than, half a Saturn year. As suggested in Chapter 5, the Hadley circulation might extend to higher latitudes and enrich hydrocarbon concentrations in regions of downwelling or there might an overall hemisphere-to-hemisphere circulation. The enrichment of acetylene from 2009 to 2012 from 55°N to 75°N is also suggestive of downwelling in this latitude range.

Both hydrocarbons exhibit a maximum in concentration at approximately 70°N and subsequently decrease towards the north pole. Temperatures at the 2.1 mbar level north of 70°N appear approximately constant with latitude. Thus, in 2012, the emergence of thermal and chemical enrichments indicative of the onset of a northern polar vortex are yet to observed.

8.2 C_2H_2 & C_2H_6 in 2012 from IRTF-Celeste

8.2.1 Radiative transfer modelling of IRTF-Celeste spectra

8.2.1.1 Determining the FWHM and instrument line function

It was important to first the determine the FWHM and instrument line function with which to convolve line data such that the observed IRTF-Celeste spectra could be modelled. The reference Saturnian atmsphere (Section 3.1.4) was adopted as the atmospheric model and Nemesis, in line-by-line mode, was used to forward model several spectra of different line functions and different widths.

In the 743 cm^{-1} band, forward model spectra were computed using triangular and Hamming line functions ranging in width from FWHM = 0.08 cm^{-1} to 0.12 cm^{-1}. Similarly, in the 822 cm^{-1} band, forward model spectra were computed using the same line functions but with FWHMs ranging from 0.15 cm^{-1} to 0.19 cm^{-1}. The FWHM and line function

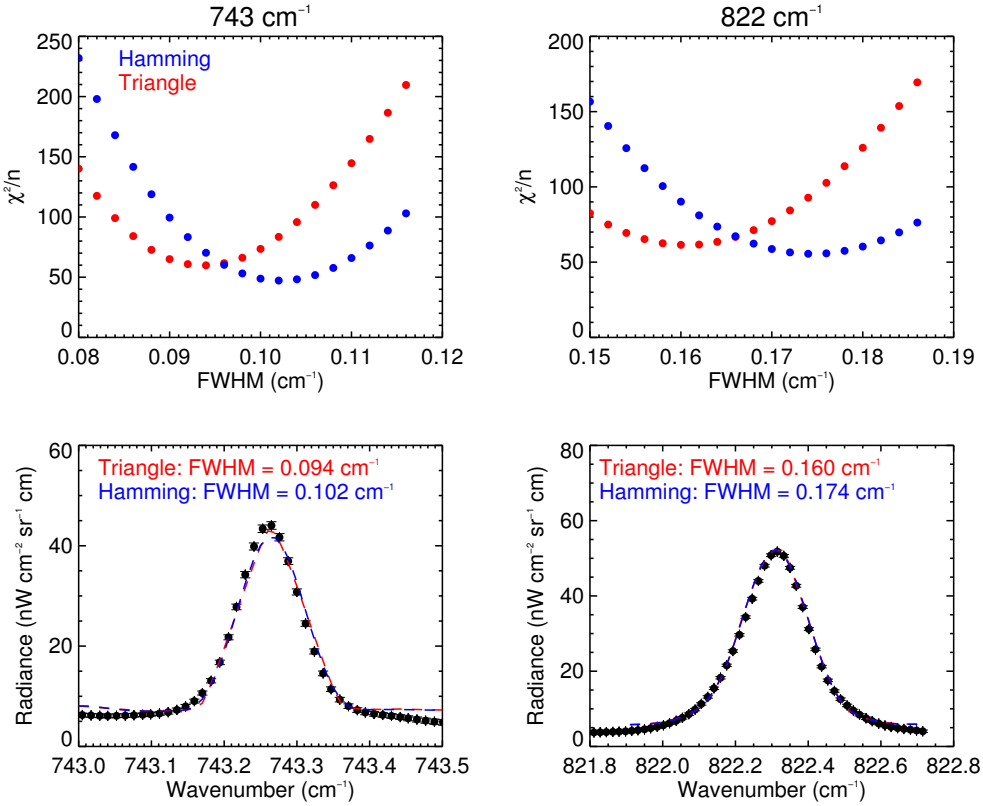

Figure 8.8: Values of χ^2 (Equation 8.1 using Hamming (blue) and triangular (red) line functions of different FWHMs. The best FWHMs of each line function are also shown for comparison.

that minimised χ^2 as shown in Equation 8.1, were considered those as best fit.

$$\chi^2 = \sum_{\tilde{\nu}} \left(\frac{R_{\text{obs}}(\tilde{\nu}) - aR_{\text{FM}}(\tilde{\nu}, \text{FWHM}, S)}{\sigma_{\text{obs}}(\tilde{\nu})} \right)^2 \tag{8.1}$$

Here, $R_{\text{obs}}(\tilde{\nu})$ and $\sigma_{\text{obs}}(\tilde{\nu})$ are the radiance and noise of an observed IRTF-Celeste spectrum and $R_{\text{FM}}(\tilde{\nu}, \text{FWHM}, S)$ is the forward modelled spectrum using a line function, S of FWHM. a is a scaling factor such that the forward modelled and observed spectrum match in radiance. Figure 8.8 shows the results of χ^2 using these different line functions and FWHMs. As shown, a triangular line function of width, FWHM = 0.094 cm^{-1} and a Hamming line function of width, FWHM = 0.102 cm^{-1} minimise χ^2 for 743 cm^{-1} data

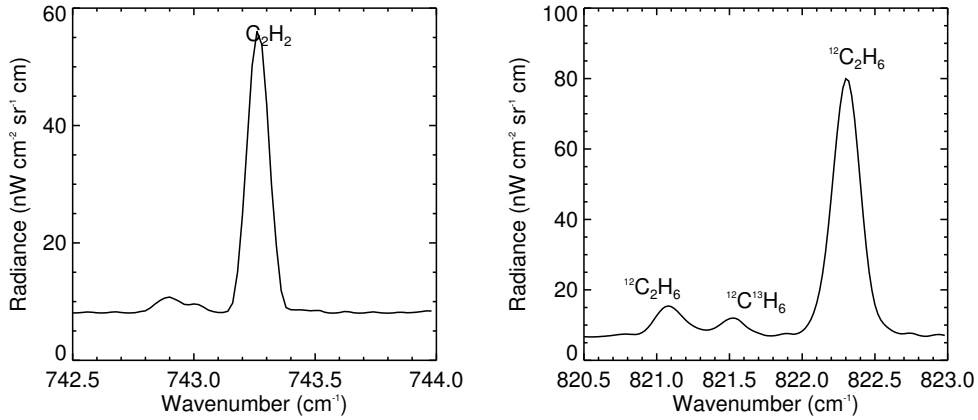

Figure 8.9: Forward modelled IRTF-Celeste spectra at 743 cm^{-1} (left) and 822 cm^{-1} (right).

though the Hamming function produces a marginally better fit. For 822 cm^{-1} data, a triangular line function of width FWHM = 0.160 cm^{-1} and Hamming function of width FWHM = 0.174 cm^{-1} produce the best fit but again with a slightly improved fit exhibited by the Hamming function. Thus, Hamming line functions of width FWHM = 0.102 cm^{-1} and FWHM = 0.174 cm^{-1} were used to convolve line data in order to model the IRTF-Celeste spectra in the 743 cm^{-1} and 822 cm^{-1} bands respectively.

8.2.1.2 Generating k-distributions

Nemesis can forward model spectra and conduct retrievals in either line-by-line mode or using the correlated-k method. At the spectral resolutions achieved by IRTF-Celeste, individual molecular lines are resolved and so modelling spectra using the former treatment would be nominally considered the most sensible approach. However, production of several subsequent forward modelled spectra as NEMESIS seeks an optimal solution was very time consuming due to the computational expense of this treatment of line data. Instead, retrievals were conducted using the correlated-k method. As detailed later in this Section, there is little confidence in the meridional trends of C_2H_2 and C_2H_6 derived

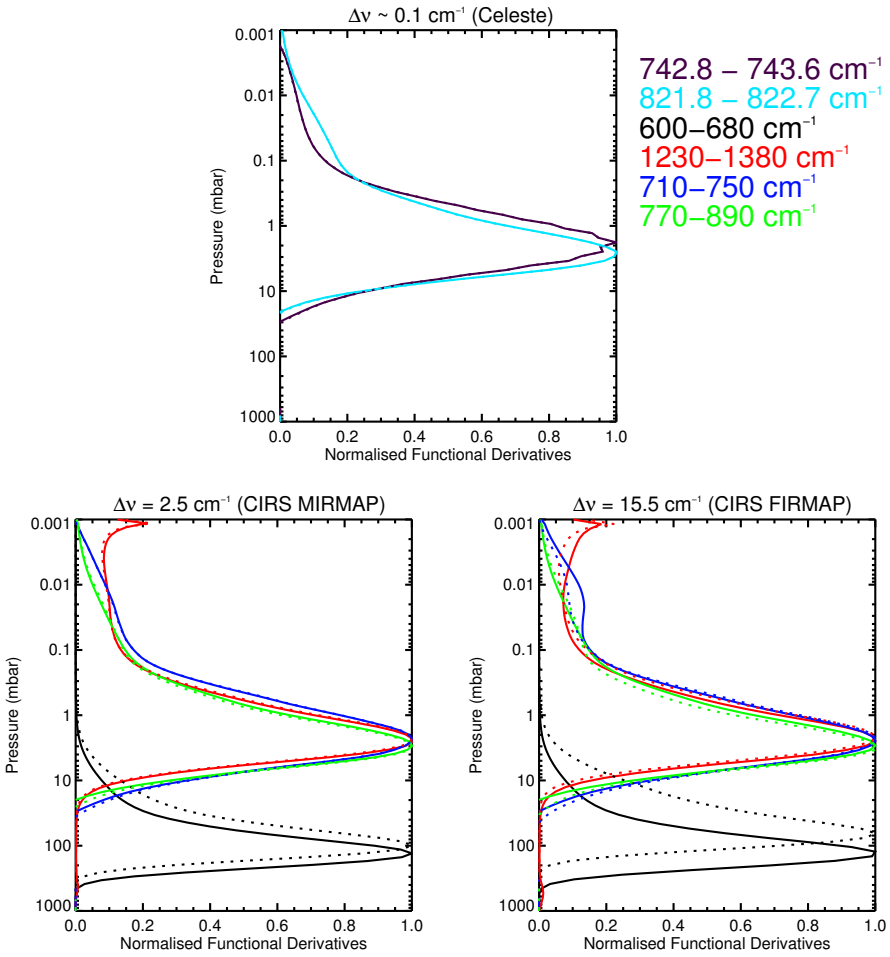

Figure 8.10: Vertical contribution functions of IRTF-Celeste spectra (top) from 743.0 - 743.5 cm^{-1} at a FWHM = 0.102 cm−1 (purple) and from 821.8 cm^{-1} to 822.7 cm^{-1} at a FWHM = 0.174 cm^{-1} (cyan). Vertical contribution functions from CIRS observations at a FWHM = 2.5 cm^{-1} and 15.5 cm^{-1} over the spectral regions used to retrieve stratospheric temperature, acetylene and ethane are also shown for comparison.

from IRTF-Celeste spectra due to calibration uncertainties and so additional uncertainties introduced by using the correlated-k method instead of the line-by-line method were considered irrelevant in this Section.

Two sets of k-distributions for CH_4, C_2H_2, $^{13}C^{12}CH_6$, $^{12}C_2H_6$, PH_3 and NH_3 were generated using the line data detailed in Table 3.1: the first set using a Hamming line function of

width FWHM = 0.102 cm^{-1} for modelling 743 cm^{-1} data, the second set using a Hamming line function of width FWHM = 0.174 cm^{-1} for modelling the 822 cm^{-1} data. Figure 8.9 shows forward-modelled IRTF-Celeste spectra at 743 cm^{-1} and 822 cm^{-1} using the reference Saturnian atmosphere detailed in Section 3.1.4. In the latter observation, the telluric $^{12}C/^{13}C$ ratio has been assumed to set the reference $^{13}C^{12}CH_6$ vertical profile.

8.2.1.3 Vertical information content

Figure 8.10 compares the vertical contribution functions of these features in the IRTF-Celeste observations with those from Cassini-CIRS. Although retrievals of acetylene and ethane from IRTF-Celeste use only a single line spanning less than 1 cm^{-1} in size while retrievals from Cassini-CIRS observations use several lines spanning greater than 20 cm^{-1}, the vertical information content at the two spectral resolutions appears very similar. All three pectral resolutoins, there is peak sensitivity to stratospheric temperature and the concentrations of acetylene and ethane at the 1-2 mbar level. Thus, results from IRTF-Celeste observations will be presented at the 2.1 mbar level in accordance with the CIRS results presented earlier in this Chapter.

8.2.2 IRTF-Celeste observations

IRTF-Celeste spectra of C_2H_6 emission at 822 cm^{-1} on 31/03/12 and 02/04/12 and C_2H_2 emission at 743 cm^{-1} on 01/04/12 were analysed. These spectra were averaged together into 4° planetographic latitude bins stepped in increments of 2° as detailed in Chapter 7.

8.2.3 A review of the radiometric calibration

It seemed logical to initially assess the success of the calibration of IRTF-Celeste spectra using the calibration methods described in Section 7.4 of the previous chapter. IRTF-Celeste spectra were therefore compared with the results of Cassini-CIRS observations acquired at very similar times. The Celeste and CIRS spectra have different emission angles and highly different spectral resolutions. Therefore, a direct comparison of radiances between the two datasets was avoided. Instead, synthetic IRTF-Celeste spectra were computed using atmospheric temperatures and C_2H_2/C_2H_6 results retrieved from the Cassini-CIRS observations.

In the 743 cm^{-1} band, two sets of synthetic Celeste spectra were computed using the results retrieved from the $MT12_{all}$ and $F12_{275:165}$ observations. This latter set of observations were considered to best sample the longitude ranges covered by IRTF-Celeste observations in this band. In the 822 cm^{-1} band, two sets of spectra were computed using the $MT12_{all}$ and $F12_{320:70}$ observations. This latter set were similarly considered to best sample the longitude ranges observed by IRTF-Celeste in the 822 cm^{-1} band. At each latitude, the vertical temperature profile and concentrations of acetylene and ethane retrieved from the CIRS observations were adopted in the atmospheric model and synthetic IRTF-Celeste spectra were computed at the emission angle at which Celeste viewed that latitude.

Figure 8.11 compares the radiances of these synthetic spectra with those from IRTF-Celeste spectra calibrated using the forward model of Mars. As demonstrated in Table 7.3, calibration using the Martian forward model derived the lowest calibration scaling factor of all the methods attempted in Section 7.4 and thus yielded the lowest radiances in both bands. Yet, as shown in Figure 8.11, these radiances were considerably higher than those of the synthetic forward models irrespective of the CIRS observations and longitude ranges sampled. At 743.25 cm^{-1} (the peak of the C_2H_2 line feature), calibrated spectra

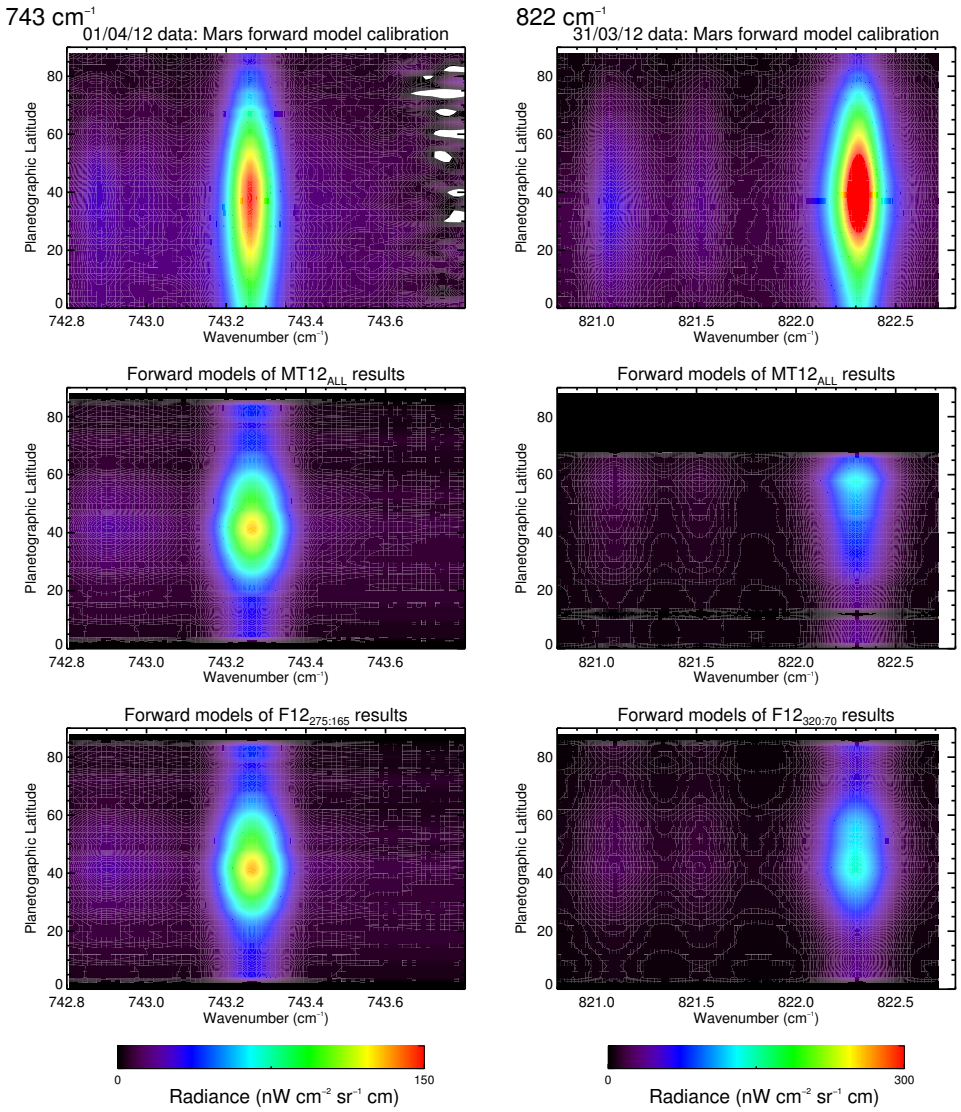

Figure 8.11: A comparison of radiances of IRTF-Celeste spectra of Saturn calibrated using a forward model of Mars (top left and top right) with those of synthetic IRTF-Celeste spectra forward modelled using the $MT12_{all}$ results (middle left and right), $F12_{275:165}$ (bottom left) and $F12_{320:70}$ (bottom right) results.

were approximately 1.18 and 1.16 more radiant than those forward modelled from the $MT12_{all}$ and $F12_{275:165}$ observations respectively. At 822.3 cm^{-1} (the peak of the C_2H_6 feature), calibrated spectra are over 4 times more radiant than both sets of synthetic spectra.

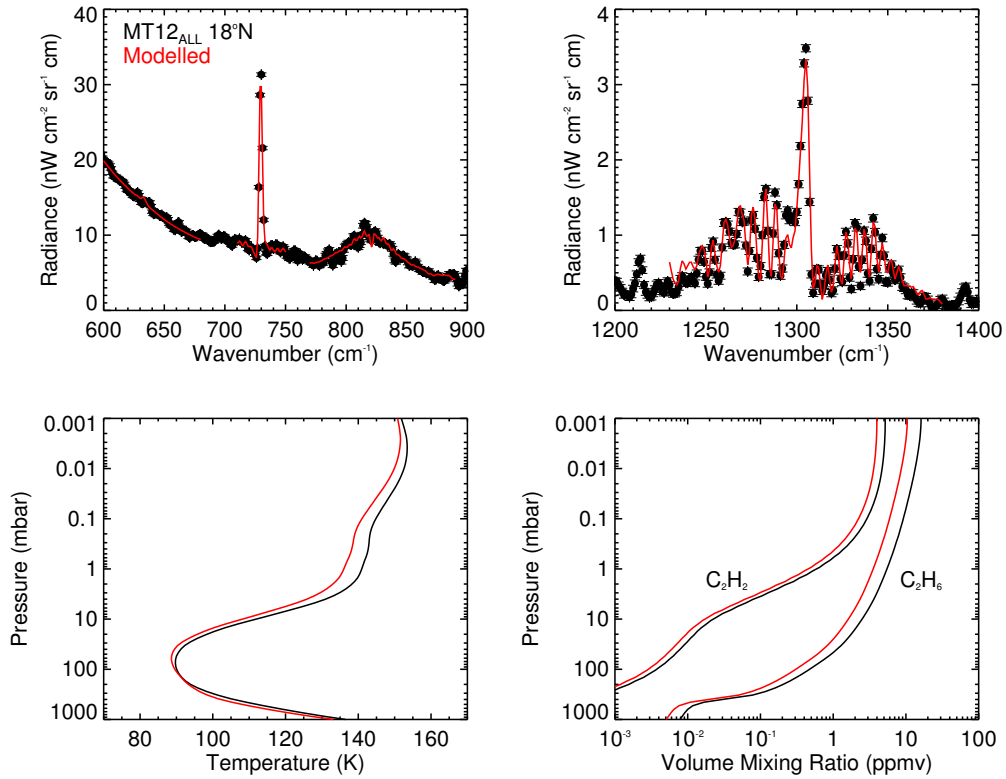

Figure 8.12: Retrieval of temperature and the concentrations of acetylene and ethane at 18°N from the $MT12_{all}$ observations acquired on 2012/04/01. The top plot shows the observed spectra and corresponding noise (black points with error bars) and the modelled spectra (solid red). The bottom plots show the retrieved vertical profiles of temperature and the volume mixing ratios of acetylene and ethane (red) with respect to the *a priori* profiles (black).

As discussed in Section 8.2.1.3, CIRS and Celeste provide sensitivity to C_2H_2 and C_2H_6 at very similar altitudes. Thus, the disrepancy in calibrated and forward modelled radiances cannot be attributed to differences in the vertical information content. A discussion of possible sources of error in using either observed or modelled spectra of Venus and Mars as calibration standards has already been presented in Section 7.4.3. These likely account for the discrepancies in radiances shown here.

8.2.4 Alternative calibration

Instead of using Venus and Mars as calibration standards, IRTF-Celeste spectra were alternatively calibrated by using the synthetic IRTF-Celeste spectra computed in the previous section. Figure 8.12 shows the vertical temperature profile and concentrations of acetylene and ethane retrieved at 18°N from $MT12_{all}$ observations. This latitude has been selected to conduct the calibration since 1) it represents the sub-observer latitude at the time IRTF-Celeste spectra were acquired and thus observations at this latitude are zero in emission angle and 2) temperatures and concentrations retrieved at this latitude exhibit little variation depending on the longitudes sampled in the coaddition (Figure 8.5).

Three synthetic spectra at zero emission were computed in each band adopting 1) $T(p)$, $C_2H_2(p)$, $C_2H_6(p)$, 2) $T(p) + \sigma_T(p)$, $C_2H_2(p) + \sigma_{C_2H_2}(p)$, $C_2H_6(p) + \sigma_{C_2H_6}(p)$ and 3) $T(p) - \sigma_T(p)$, $C_2H_2(p) - \sigma_{C_2H_2}(p)$, $C_2H_6(p) - \sigma_{C_2H_6}(p)$ in the atmospheric model, where $T(p) \pm \sigma_T(p)$, $C_2H_2(p) \pm \sigma_{C_2H_2}(p)$ and $C_2H_6(p) \pm \sigma_{C_2H_6}(p)$ are the retrieved temperature profile and concentrations of acetylene and ethane and their associated uncertainties. The radiances in these latter two spectra were adopted as the radiances at the $\pm 1\sigma$ level in order to represent the uncertainty in the CIRS retrieval as uncertainty on the synthetic radiances. The IRTF-Celeste observations were then scaled to fit these synthetic spectra as shown in Figure 8.13.

As shown, the calibration scale factor in the 743 cm^{-1} band has only been calculated using the spectrum from 742.9 cm^{-1} to 743.4 cm^{-1} since radiances are noisier at higher wavenumbers due to telluric absorption (Figure 7.4). In 822 cm^{-1} data, the scale factor is only calculated using the spectrum from 821.7 cm^{-1} to 822.6 cm^{-1}: the feature at 821.5 cm^{-1} is due to $^{13}C^{12}H_6$ and the forward model assumes the $^{13}C/^{12}C$ ratio derived from CH_4 measurements [Fletcher et al., 2009] although the ratio from C_2H_6 may be different. Table 8.2 shows the calibration scale factors derived from this procedure. These scaling

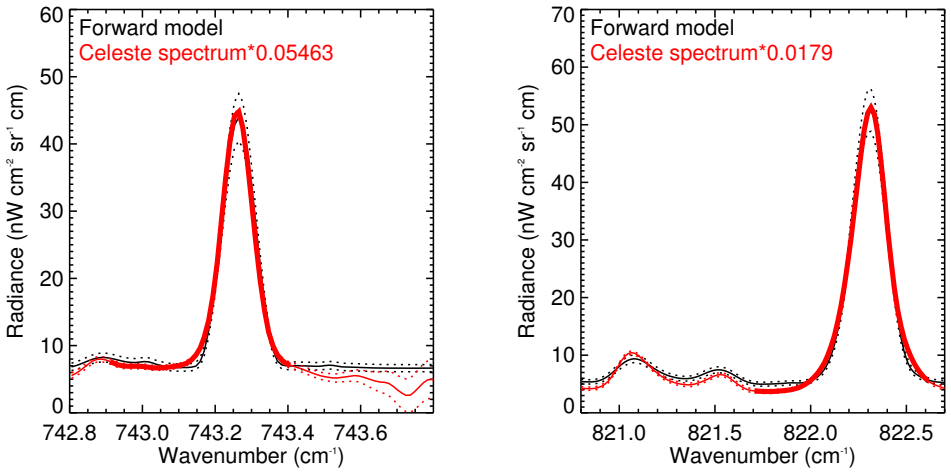

Figure 8.13: Calibration using a forward model of MIRTMAP results: the synthetic Celeste observations using temperatures and concentrations of acetylene and ethane retrieved from a MIRTMAP spectrum at 18°N (black) and the scaled Celeste observations at the same latitude (red) for calibration at 743 cm^{-1} (left) and 822 cm^{-1} (right). Spectral regions with thicker lines in both spectra indicate the wavenumber ranges used to calculate the calibration scaling factor.

Date (yyyy/mm/dd)	Band (cm^{-1})	Calibration scaling factors x 10^2
31/03/12	822	1.79 ± 0.03
01/04/12	743	5.46 ± 0.08

Table 8.2: The calibration scale factors (for radiances in units of nW cm^{-2} sr^{-1} cm) derived by scaling the observed Celeste spectra to the forward model

factors were then applied to all IRTF-Celeste spectra in the 743 cm^{-1} and 822 cm^{-1} bands.

8.2.5 Retrieval of C_2H_2 and C_2H_6

The 822 cm^{-1} band includes features both from $^{12}C_2H_6$ (821.05 cm^{-1} and 822.3 cm^{-1}) and $^{13}C^{12}CH_6$ (821.55 cm^{-1}). In this thesis, the focus was simply to retrieve the concentration of $^{12}C_2H_6$. Ethane is therefore retrieved from 821.8 cm^{-1} to 822.7 cm^{-1} since this feature

corresponds to $^{12}C_2H_6$ and is most sensitive to the 1-2 mbar level in accordance with a similar sensitivity in CIRS measurements. However, the $^{12}C/^{13}C$ ratio of C_2H_6 could readily be retrieved from the 822 cm^{-1} band. This is suggested as future work in Chapter 9. The concentration of C_2H_2 was retrieved from 742.8 cm^{-1} to 743.5 cm^{-1} avoiding the noisy continuum at higher wavenumbers.

C_2H_2: At each latitude, the vertical temperature profile $T(p)$ retrieved from the $MT12_{all}$ observation was adopted as the model temperature profile and the concentration (scaling factor applied to the reference vertical profile of C_2H_2) was adopted as the *a priori* concentration. The concentration of C_2H_2 was then allowed to vary while temperature was held constant. Two further retrievals were performed where instead $T(p) + \sigma_{T(p)}$ and $T(p) - \sigma_{T(p)}$ were adopted as the model temperature profile. This serves to test the sensitivity of the retrieved concentration of C_2H_2 on the uncertainties associated with the CIRS temperature retrieval. In the Results section (Section 8.2.6), the uncertainty on the retrieved concentration of C_2H_2 is set to be the largest of either the uncertainty in C_2H_2 from the retrieval using $T(p)$ as the temperature profile or half the range in concentration of C_2H_2 when $T(p) + \sigma_T(p)$ and $T(p) - \sigma_T(p)$ were instead adopted. All retrievals as detailed were then repeated using the temperature profiles retrieved from the $F12_{all}$ and $F12_{275:165}$ observations.

C_2H_6: The retrieval of C_2H_6 was performed using a very similar method as described above for C_2H_2, except the CIRS-retrieved concentration of C_2H_6 was adopted as the *a priori* concentration and allowed to vary. In addition, retrievals were conducted adopting the $MT12_{all}$, $F12_{all}$ and $F12_{320:70}$ observations (instead of the $F12_{275:165}$ observations).

8.2.6 Results

Figures 8.14 and 8.15 show the retrieved temperatures from CIRS and the concentrations of acetylene and ethane at 2.1 mbar retrieved from CIRS and Celeste. In general, concen-

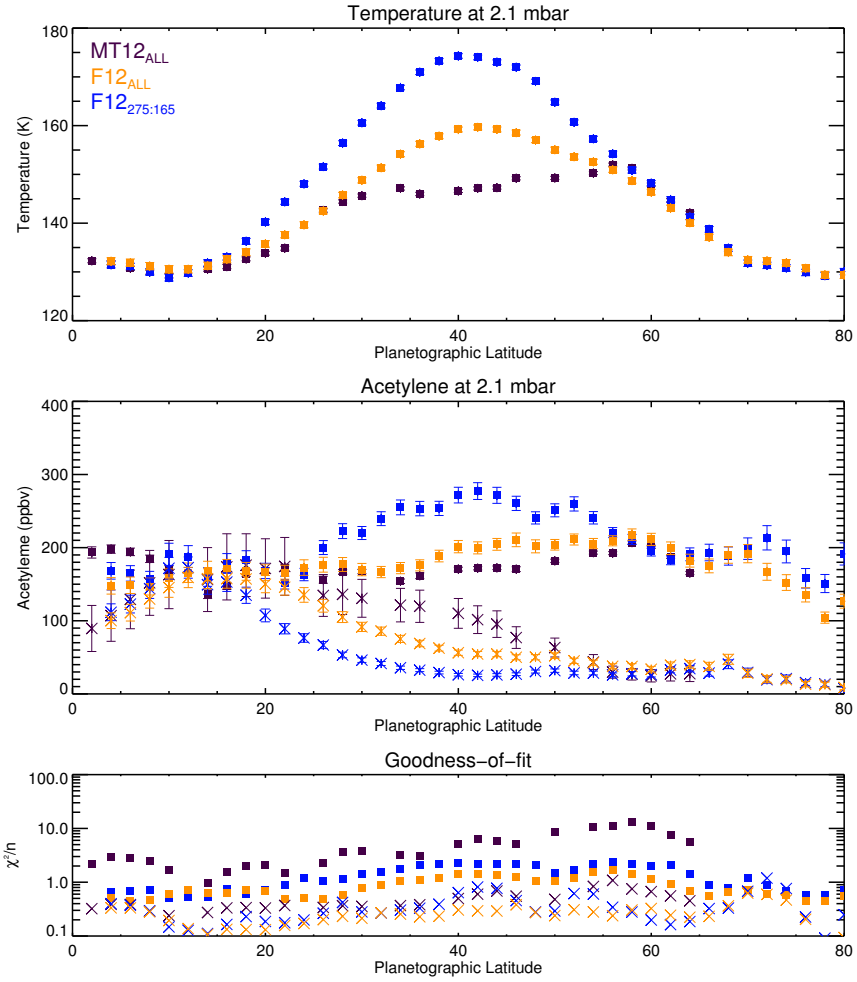

Figure 8.14: The retrieved temperatures (top) and concentrations of acetylene at 2.1 mbar (middle) from Cassini-CIRS observations (points) and IRTF-Celeste spectra (crosses). Red, green and purple results indicate retrievals conducted respectively using the 163_001MT observations at all available longitude, the 160_001F observation from 260° - 160° and the same observation at all longitudes.

trations of both species from CIRS and Celeste agree within error bars from approximately 10°N to 20°N. Figure 8.16 compares observed and modelled spectra at 18°N (the latitude used to conduct the radiometric calibration). Using the different vertical temperature profiles from CIRS, all modelled spectra exhibit a good fit to both C_2H_2 and C_2H_6 features and retrieved concentrations are consistent irrespective of the temperature profile used and

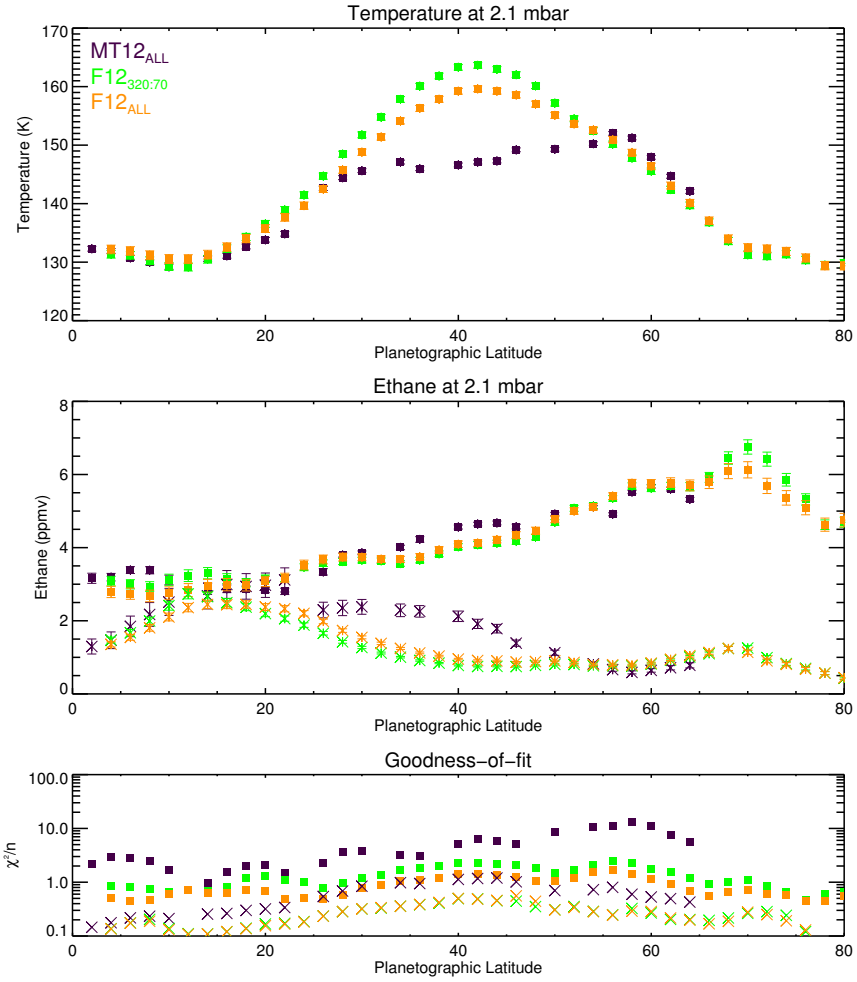

Figure 8.15: The retrieved temperatures (top) and concentrations of ethane at 2.1 mbar (middle) from Cassini-CIRS observations (points) and IRTF-Celeste spectra (crosses). Red, blue and purple results indicate retrievals conducted respectively using the 163_001MT observations at all available longitude, the 160_001F observation from 310° - 70° and the same observation at all longitudes.

show agreement with CIRS results. However, at higher latitudes, the meridional profiles retrieved from CIRS and Celeste deviate significantly with lower concentrations retrieved in the latter dataset. Figure 8.17 compares observed and modelled spectra and the corresponding temperature, acetylene and ethane profiles at 40°N. This latitudes marks the warmest temperatures and concentrations associated with the beacon and exemplifies a

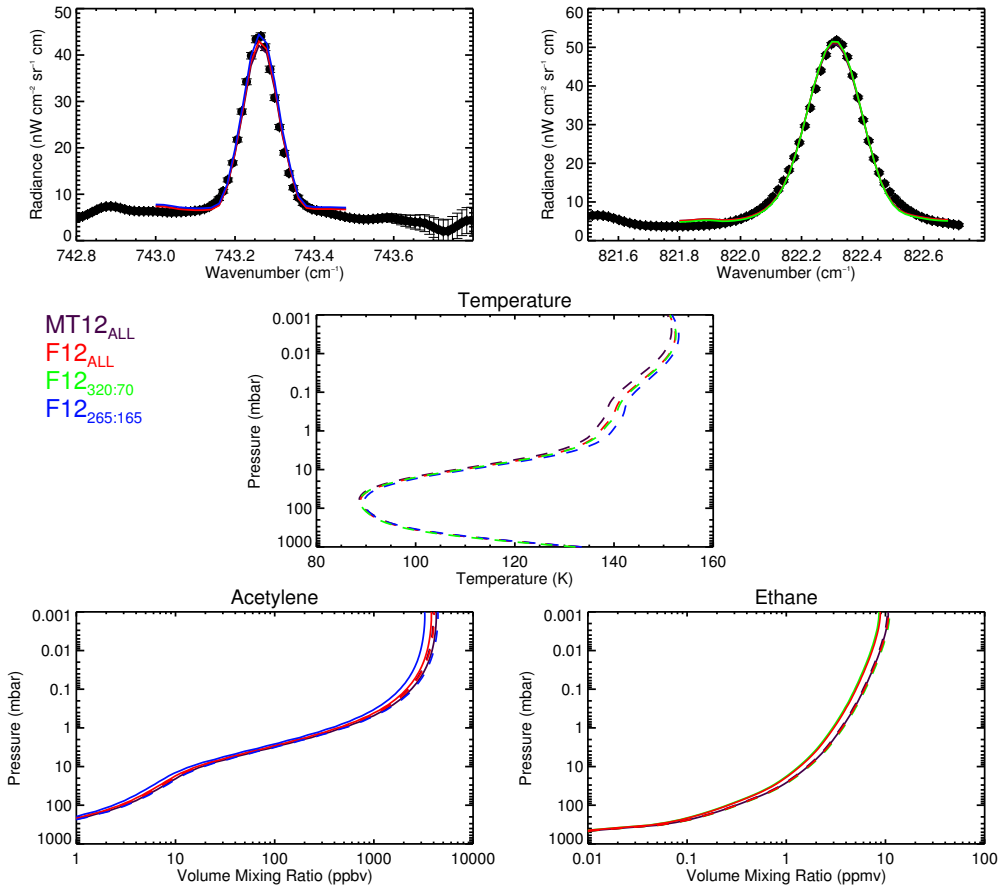

Figure 8.16: Observed IRTF-Celeste spectra in the 743 cm^{-1} and 822 cm^{-1} bands (black points with error bars) at 18°N. Modelled IRTF-Celeste spectra and the associated vertical profiles of acetylene and ethane using temperatures retrieved from $MT12_{all}$ (purple), $F12_{all}$ (red), $F12_{320:70}$ (green) and $F12_{265:165}$ (blue) are shown as solid, coloured lines. Dashed, coloured profiles show the vertical temperature profiles retrieved from CIRS using the same colours.

latitude where there is significant disagreement between CIRS and Celeste concentrations despite all modelled spectra exhibiting a good fit to the observations.

A physical interpretation of CIRS results has already been presented in Section 8.1.3. However, further interpretation of the properties of Saturn's northern hemisphere are not presented due to the disagreement between CIRS and Celeste results. A discussion of the possible sources of disagreement between CIRS and Celeste results is presented in the next

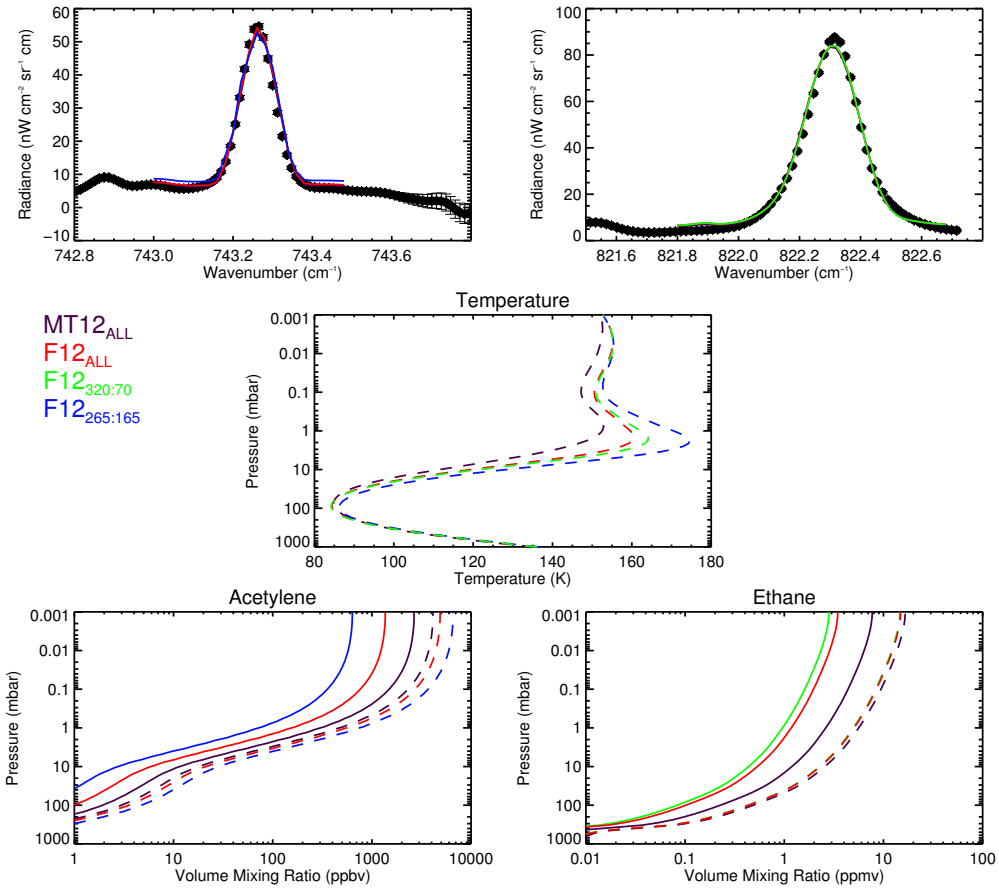

Figure 8.17: Observed IRTF-Celeste spectra in the 743 cm^{-1} and 822 cm^{-1} bands (black points with error bars) at 40°N. Modelled IRTF-Celeste spectra and the associated vertical profiles of acetylene and ethane using temperatures retrieved from $MT12_{all}$ (purple), $F12_{all}$ (red), $F12_{320:70}$ (green) and $F12_{265:165}$ (blue) are shown as solid, coloured lines. Dashed, coloured profiles show the vertical temperature profiles retrieved from CIRS using the same colours.

section.

8.3 Sources of disagreement between CIRS and Celeste

8.3.1 Is the disagreement a calibration artefact?

The agreement in concentrations retrieved from CIRS and Celeste from approximately 10°N to 20°N was expected given the results of Cassini-CIRS observations at 18°N were used to calibrate the IRTF-Celeste data. The disagreement at higher latitudes could indicate that the calibration scale factor applied to IRTF-Celeste spectra (Table 8.2) is not valid in these regions. Figure 8.18 compares IRTF-Celeste spectra at 40°N with forward modelled spectra using the retrieved temperature, acetylene and ethane concentrations from the $MT12_{all}$ observations. As shown, applying a factor of 1.28 and 1.41 to the observed 743 cm^{-1} and 822 cm^{-1} spectra yields radiances which exhibit a good correspondence to the forward model. This essentially demonstrates that if the observed 743 cm^{-1} and 822 cm^{-1} spectra were respectively 1.28 and 1.41 times more radiant than those of the current calibration, concentrations of acetylene and ethane comparable with those from Cassini-CIRS would be retrieved. However, if these scale factors were to be applied to all the 743 cm^{-1} and 822 cm^{-1} observations, concentrations retrieved from CIRS and Celeste might agree at 40°N but there would then be disagreement at 18°N. It should also be noted that even if factors of 1.28 and 1.41 were applied to the calibration scale factors shown in Table 8.2, the calibration scale factors derived from observations/model spectra of Venus and Mars (Table 7.3) are still too large.

As is generally true of ground-based observing in the thermal infrared, the radiometric calibration represents a sizeable source of uncertainty. However, it does not appear that a single calibration scale factor would yield spectra from which concentrations of acetylene and ethane comparable with CIRS would be retrieved. Thus, possible sources of error in the calibration of IRTF-Celeste spectra alone cannot explain the observed disagreement in the concentrations retrieved from CIRS and Celeste.

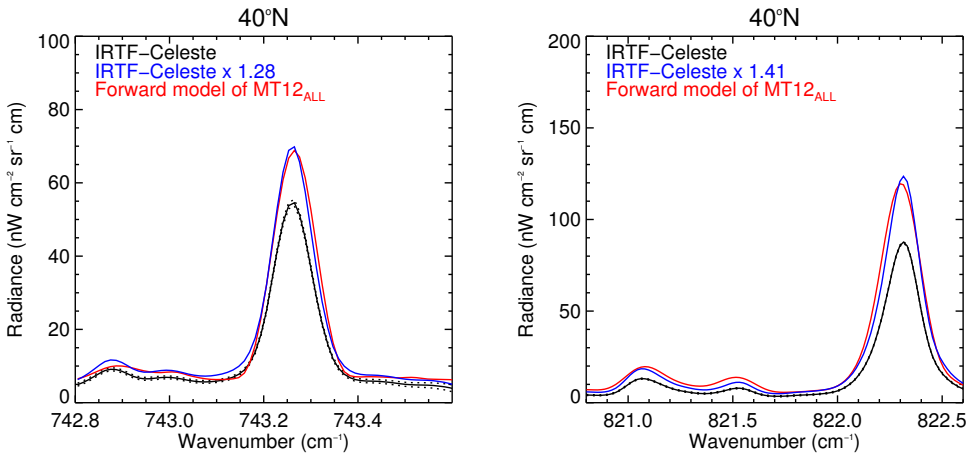

Figure 8.18: IRTF-Celeste observations (black) of 40°N in the 743 cm^{-1} (left) and 822 cm^{-1} band and forward modelled spectra (red) using retrieved temperatures and C_2H_2/C_2H_6 concentrations derived from $MT12_{all}$ observations. The blue spectra show forward models in the 743 cm^{-1} and 822 cm^{-1} bands respectively scaled by factors of 1.28 and 1.41 in order to match the observed spectra.

8.3.2 Is the disagreement a result of zonal variations in temperature?

The agreement in concentrations between CIRS and Celeste from 10°N to 20°N may in part be due to the fact that observations at 18°N were used to calibrate the data. However, this latitude range also represents a region of the planet where there appears to be little zonal variation in atmospheric temperatures and concentrations. As shown in Figures 8.1 and 8.2, there were little or negligible zonal variations in C_2H_2, C_2H_6 and CH_4 emission from the equator to 20°N. However, the beacon introduced significant zonal variations in brightness and thus temperature/concentration at higher latitudes. The fact that zonal variations are minimal from the equator to 20°N is also demonstrated in Figure 8.5, where retrieved stratospheric temperatures and the concentrations of acetylene and ethane exhibit agreement, irrespective of the longitude range sampled in the coaddition of observations. Thus, the disagreement in concentrations retrieved from CIRS and Celeste at latitudes higher than 25°N may also be explained in part by zonal variations in temperature hindering a correct characterisation of the temperature field. For example, the coaddition

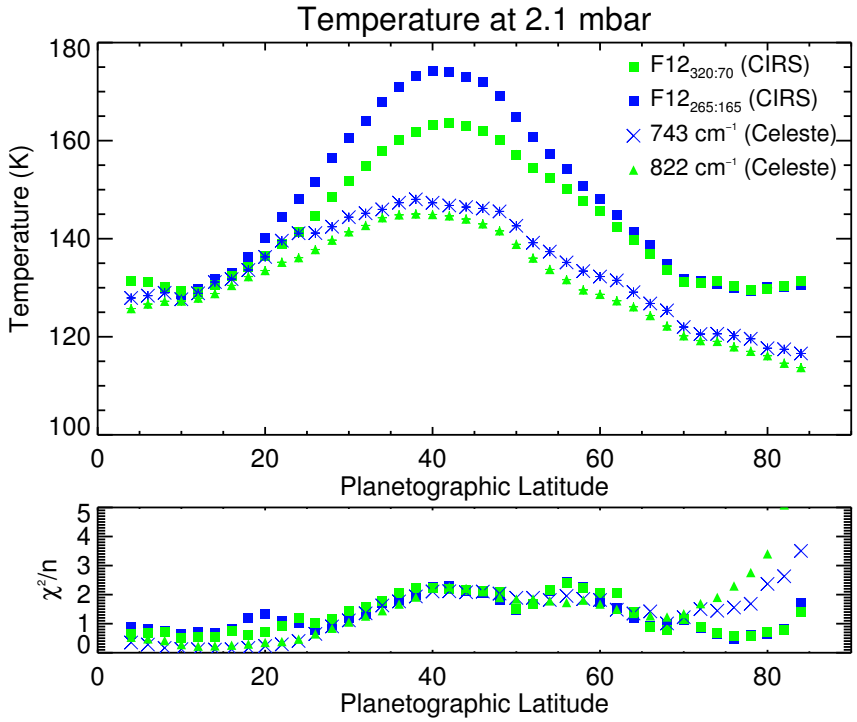

Figure 8.19: A comparison of temperatures retrieved from the $F12_{265:165}$ (blue squares)) $F12_{320:70}$ observations (green squares) and those retrieved from IRTF-Celeste spectra in the 743 cm^{-1} (blue crosses) and 822 cm^{-1} (green triangles) where hydrocarbon concentrations are held fixed. The goodness-of-fit values are also shown for comparison.

of CIRS observations in a latitude band may sample a warmer region of the zone which was not sampled in the averaging of IRTF-Celeste spectra. In using a warmer temperature profile to model the IRTF-Celeste spectra, a smaller concentration of acetylene or ethane is retrieved in order to fit the observed radiances. The differences in spatial resolution on Saturn between CIRS and Celeste may also introduce a similar effect. The high spatial resolution provided by CIRS allows smaller-scale variations in atmospheric conditions with latitude or longitude to be resolved. However, the same variations may be blurred together/not observed when viewed by an instrument from Earth which achieves a lower spatial resolution.

In order to demonstrate whether corrections to the CIRS-retrieved temperatures could rec-

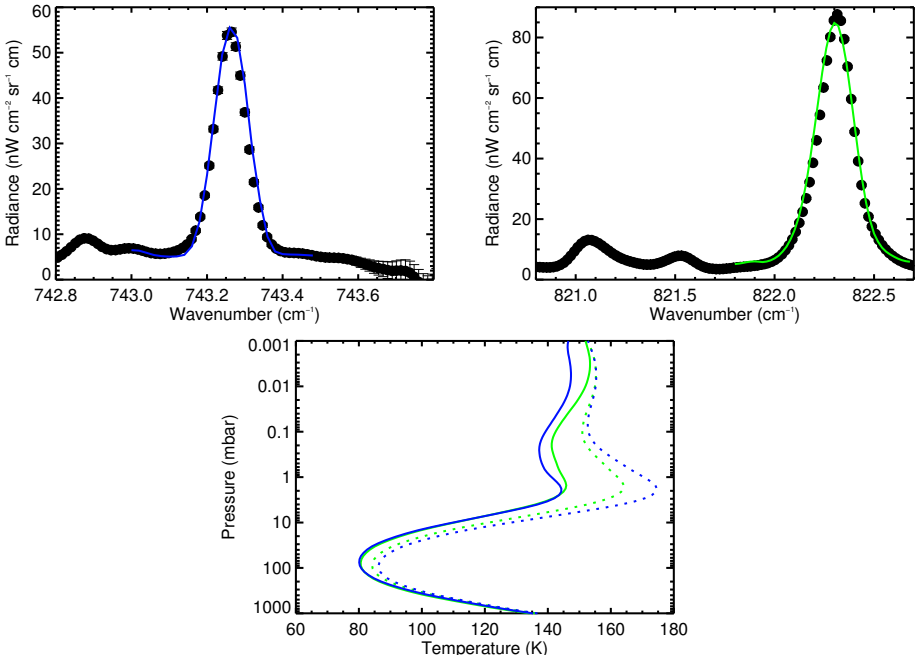

Figure 8.20: Retrieval of temperature from IRTF-Celeste spectra (black points with error bars) at 40°N in the 743 cm^{-1} (left) and 822 cm^{-1} (right) bands. Solid spectra in blue and green show the modelled spectra corresponding to the retrieved temperature profiles in the bottom plot (solid) which have been allowed to vary from *a priori* profiles retrieved from CIRS (dashed).

oncile the discrepancy between CIRS and Celeste concentrations of acetylene and ethane, a further sets of retrievals have been performed. In modelling the same spectral regions of the 743 cm^{-1} band as detailed in Section 8.2.5, the vertical temperature profile $T(p)$ retrieved from the $F12_{265:165}$ (CIRS) observations (that were considered to best sample the longitude range observed by IRTF-Celeste) at each latitude was adopted as the *a priori* temperature profile and allow to vary. The retrieved concentrations of C_2H_2 and C_2H_6 from the same set of results were then adopted in the atmospheric model but not allowed to vary. Thus, these retrievals aim to the fit the C_2H_2 feature by deviating the temperature profile determined from CIRS. A similar set of retrievals was then performed using instead the 822 cm^{-1} data and the results from $F12_{320:70}$ observations. Figure 8.19 compares the results of these temperature retrievals with those from CIRS.

As shown, the temperatures at 2.1 mbar retrieved from $F12_{320:70}$ and $F12_{265:165}$ (CIRS) observations exhibit good agreement with those retrieved from IRTF-Celeste spectra in both bands at latitudes equatorward of 20°N. This demonstrates that a negligible correction in temperature is required in order to fit both the 743 cm^{-1} and 822 cm^{-1} features where the CIRS-retrieved concentrations of acetylene and ethane were held fixed. This is likely to be because the 18°N results from CIRS were used to calibrate the Celeste data and also the fact that zonal variations in temperature and composition are minimal in this latitude range. At higher latitudes, the temperatures retrieved by these two methods deviate significantly with temperatures retrieved from IRTF-Celeste spectra cooler by up to 20 K at 40°N. Figure 8.20 compares observed and modelled spectra at 40°N in retrieving temperature from IRTF-Celeste. As shown, using CIRS-retrieved concentrations of C_2H_2 and C_2H_6, it is possible to fit the emission features of these two hydrocarbons by modifying the temperature profile retrieved from CIRS alone. In addition, it is comforting that the temperature retrieved from the 743 cm^{-1} and 822 cm^{-1} bands (acquired on two different nights of observing) match at 1 - 2 mbar level where there is greatest sensitivity in the observations. However, for concentrations of acetylene and ethane retrieved from CIRS and Celeste to match, these retrievals imply that the zonal mean temperature at 2.1 mbar derived from CIRS observations is too warm by up to 20 K. Variations in temperature of this magnitude were observed at beacon latitudes from CIRS depending on the longitude range sampled in the coaddition (Figure 8.5). However, given the $F12_{265:165}$ and $F12_{320:70}$ CIRS observations were coadded over the longitude ranges sampled by IRTF-Celeste in the 743 cm^{-1} and 822 cm^{-1} bands, such large temperature disagreements are less believable. A cooling of the beacon between late January and late March would be expected but at the cooling rate derived by Fletcher et al. [2012] of 0.1 ± 0.01 K/day, differences of temperature only up to 7 K would be expected over the 65 days elapsed between the two datasets.

Thus, corrections to the temperature profile derived from CIRS can reconcile the con-

centrations of acetylene and ethane retrieved from these two datasets. However, considerably large temperature corrections of up to 20 K were required which might suggest that poorly characterising the vertical temperature profile alone cannot account entirely for the discrepancy in the concentrations retrieved from Celeste and CIRS. It is likely that the discrepancy in concentrations retrieved from CIRS and Celeste are partly due to sources of error associated with the radiometric calibration and sources of error in using CIRS-retrieved temperatures in modelling the IRTF-Celeste spectra.

8.4 Summary

An analysis of Cassini-CIRS and IRTF-Celeste observations of Saturn's northern hemisphere has been conducted. Results from CIRS observations indicated large variations in temperature and the concentration of acetylene at the 2.1 mbar level from 25°N to 55°N depending on the longitude range used in the coaddition of observations. This indicates large zonal variations in these properties due to the beacon vortex that covers this latitude range.

While this beacon dominates the northern stratosphere in 2012, large changes in the general shapes of the meridional profiles of acetylene and ethane in comparison to 2009 results indicate significant seasonal change over these three years. In particular, the meridional profile of ethane's concentration in 2012 at the 2.1 mbar level exhibits an overall increase in concentration with latitude thus mimicking similar behaviour observed of this molecule in the southern hemisphere. The emergence of this feature in only 7 (Earth) years confirms that the physical processes shaping ethane's meridional profile act on a timescale of less than half a Saturn year. Meridional transport of ethane to high-northern latitudes by either Hadley circulation or a general hemisphere-to-hemisphere circulation which reverses direction every half year has been suggested in previous Chapters.

Chapter 9

Conclusions & Future Work

9.1 Conclusions

Saturn's seasonal variability from 2005 to 2012 has been investigated in this thesis. Even over the 7 years of Cassini-CIRS observations analysed in Chapters 4, 5 and 6, Saturn's stratosphere was revealed to be highly dynamic. In addition, a comparison of results derived from Voyager-IRIS observations in 1980 and Cassini-CIRS observations in 2009 and 2010 was used to assess the extent of interannual variability. A summary of the results highlighted by these analyses is presented below.

Hadley circulation: Cross-equatorial Hadley circulation was revealed at low latitudes in the results of Chapter 5 and a GCM indicates that this circulation is seasonally-reversing. This circulation contrasts stratospheric circulations observed on our own planet. On Earth, both Hadley circulation in the troposphere and Brewer-Dobson circulation in the stratosphere are generally of the form of upwelling at equatorial latitudes, where the most solar heat is deposited annually, and downwelling at high latitudes. On Saturn, the circulation however flows from the summer hemisphere to winter hemisphere. These differences demonstrate the impact that the physical properties of the planet such as the length of *day* and *year* can have on the atmospheric circulation.

Polar Hotspots Saturn's polar regions were revealed to be host to dynamical and perhaps auroral phenomena. A dissipation of zonal winds in Saturn's south polar vortex was observed from 2005 to 2010 corresponding to the onset of Autumn (Chapter 5). Results in 2012 (Chapter 8) do not indicate the enhanced temperatures and hydrocarbon concentration at high-northern latitudes that would indicate the emergence of a similar vortex

at Saturn's northern pole, however, this is expected to emerge at a later date. Both polar regions were found to be warmer and richer in hydrocarbon concentration in 1980 during solar maximum compared to 2009/2010 during solar minimum (Chapter 6). While this result could be an artefact of the poorer signal-to-noise ratio of observations in the former year, this difference could be a result of stronger auroral processes during solar maximum driving heating and heightened hydrocarbon production.

The equatorial oscillation: Changes in temperature at equatorial latitudes (Chapter 5) show an evolution of Saturn's equatorial oscillation that is consistent with previous studies [Guerlet et al., 2011; Schinder et al., 2011] once differences in the vertical information content of the observations were considered. However, equatorial temperatures in 1980 and 2009/2010 reveal considerable interannual differences in this oscillation, indicating that its period is more quasi-semiannual (Chapter 6). This is possibly due to a beating of this oscillation in the stratosphere with a tropospheric quasi-biennial oscillation with a period of two Saturn years. The period of Earth's stratospheric oscillation ranges from 6.2±0.8 to 6.8 ±0.6 months, as determined from limb-sounding satellite and LIDAR (light detecting and ranging) observations [Guharay et al., 2009] and is therefore also not exactly semiannual in period.

9.2 Future Work

9.2.1 Further investigation of seasonal changes from Cassini-CIRS

The evolution of Saturn's stratosphere has only been investigated from 2005 to 2012 in this thesis. Though a wealth of variable features have been revealed in this time, this time period represents less than a quarter of a Saturn year. A larger time range of observations should be analysed in order to further investigate the variability of the stratosphere highlighted by this work. Cassini-CIRS observations acquired up to the end of the mission in

2017, that will cover Saturn's northern summer solstice, may be used to investigate the following:

- Reversal of Hadley circulation: the low latitude Hadley circulation is predicted to reverse in direction as northern summer approaches with upwelling at 15°N, cross-equatorial flow and downwelling at 25°S. Cassini-CIRS spectra may be used to monitor hydrocarbon abundances at these latitudes in order to capture this circulation reversal as it takes place.
- Monitoring of Saturn's north pole: the emergence of a northern polar vortex is predicted as northern summer solstice approaches. Regularly monitoring of temperatures and composition at northern polar regions will provide insight into how, and over what timescales, these polar vortex features form.
- The period of Saturn's equatorial oscillation: tracking the evolution of the equatorial oscillation over the entire Cassini mission (2004 to 2017) will allow a much larger proportion of the oscillation's period to be captured by a single dataset. This will better indicate how semiannual or quasi-semiannual the stratospheric oscillation is in period and whether there is an influence or *beating* with oscillations in other altitude ranges in Saturn's atmosphere.

9.2.2 Future observations using the Celeste spectrograph

Although an extensive and regular dataset, the limited spectral resolution of Cassini-CIRS observations when viewing the planet in the nadir only sounds a single pressure level in the stratosphere. However, the variability of Saturn's stratosphere extends above and below this level and processes at different altitudes are likely to be coupled. Thus, in addition to the investigation from CIRS observations described in the previous Section, Saturn's seasonal variability should also be investigated using high spectral resolution observations

such as those from the Celeste instrument or other thermal infrared instruments with a high resolving power. By viewing different emission lines which are sensitive to different pressure levels, a much larger altitude range of Saturn's stratosphere may be probed by this instrument. Given the challenges faced in calibrating and modelling Celeste observations in Chapter 8, the following improvements are suggested in future observing runs of the Celeste instrument.

9.2.2.1 Possible improvements to calibration

As concluded in Chapter 7, Venus and Mars are not considered suitable calibration standards. An attempt at calibrating Celeste data using point-source calibration standards such as stars or asteroids has proven problematic in previous Celeste observing runs since these objects illuminate the slit of the instrument differently from a planet like Saturn (private communication with the Celeste team). Although Celeste data was calibrated with Cassini-CIRS data in this thesis (though with a high uncertainty due to differences in the spatial and temporal sampling), this should be avoided in future. A means of calibrating Celeste data independently of Cassini-CIRS should be sought such that the two datasets truly complement each other. The Cassini mission will end in 2017 and so an independent method of calibrating Celeste data is required such that Saturn may continue to be studied in the thermal infrared after this year.

Exposure of the instrument detector on dark, matt cards mounted on the telescope, which serve as a blackbody, could be considered. This method has proven a successful means of intensity calibration for the TEXES instrument [Lacy et al., 2002] which operates from 5μm to 25μm (Leigh Fletcher, private communication). The IRTF also monitors the temperature of the dome to high precision - an exposure on the inside of the dome could also be considered as a means of calibration. These methods should be tested in future Celeste observing runs while there are Cassini-CIRS observations with which to compare

calibrated radiances.

9.2.2.2 Possible improvements to data acquisition

Without Celeste observations of CH_4 emission, there was no choice but to use Cassini-CIRS temperature results to model IRTF-Celeste spectra of C_2H_2 and C_2H_6 emission (Chapter 8). With the storm beacon inducing significant zonal variations in temperature and composition, selecting Cassini-CIRS spectra that sampled the same regions on the planet was a challenge. Thus, acquisition of CH_4 spectra from IRTF-Celeste in addition to other molecule species is suggested in future observing runs.

In previous Celeste runs, the grating setting were set to observe the spectral features from only one molecular species at one time. In future runs, perhaps the grating settings could be continuously alternated between observing, for example, CH_4, C_2H_2 and C_2H_6 emission. This ensures that spectra used to determine temperature and chemical abundance sample similar longitudes at similar times. Thus, variations in Earth's atmospheric conditions and the sensitivity of the instrument can be considered negligible.

Figure 9.1 shows a possible wavenumber region of CH_4 emission that could be observed in future in Celeste observing runs. These CH_4 lines have been observed by the TEXES instrument and successfully used to determine the vertical temperature profile [Greathouse et al., 2005]. As demonstrated, this 3 cm^{-1} band sounds the Saturnian atmosphere from pressures of 10 mbar to 0.001 mbar and thus could be used to retrieve the vertical temperature profile across this pressure range. This signifies the advantage in using high spectral resolution observation from ground-based instruments such as Celeste. However, Saturn must be observed at a radial velocity of greater than 20 km/s (in either direction) in order for CH_4 emission from the planet to be doppler shifted out of telluric CH_4 absorption lines, as demonstrated in Figure 9.1. Requiring Saturn at high doppler shifts would limit the date ranges for which telescope time could be applied. At these doppler shifts, the

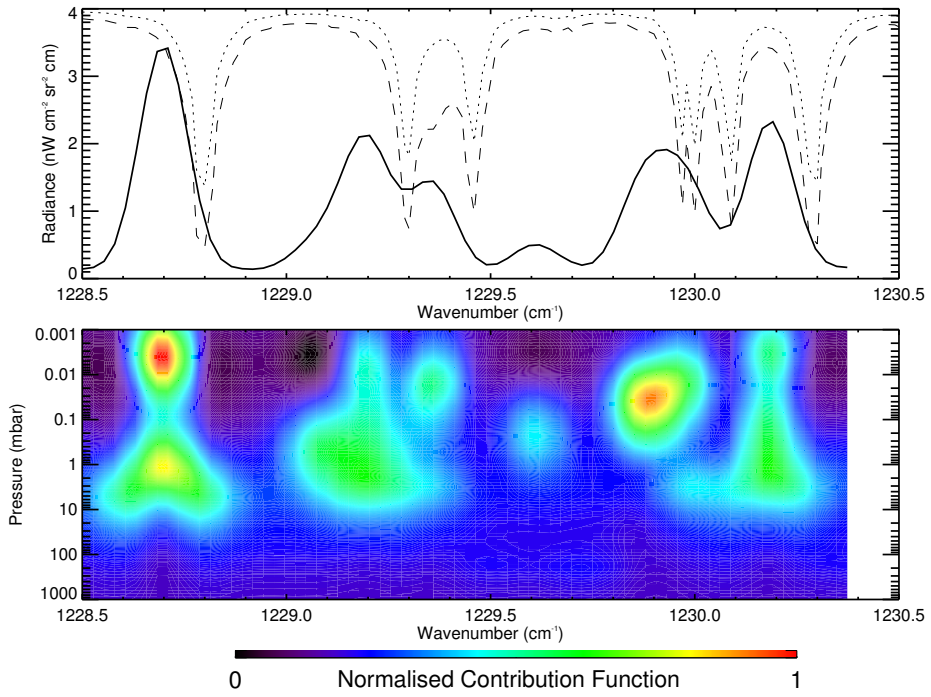

Figure 9.1: A synthetic spectrum (top) of CH_4 emission (solid) at IRTF-Celeste spectral resolution (FWHM = 0.105 cm^{-1}) doppler shifted by 25 km/s. The dotted and dashed lines show transmission spectra through the Earth at an airmass of 1.0 and PWV = 1.0 mm and airmass of 2.0 and PWV = 4.0 mm respectively, multiplied by a factor of 4. The contour plots shows the normalised vertical contribution function of this spectrum.

planet is observable at low airmass for fewer hours than when the planet is at opposition, for example. This would represent a sacrifice in the total integration time that the planet could be observed in a particular band.

9.2.3 Development of further models

The evolution of Saturn's stratosphere is a result of coupling of radiative, photochemical and dynamical processes. Current models of Saturn's stratosphere have coupled at most two of these processes [Friedson and Moses, 2012; Moses and Greathouse, 2005]. A model encompassing all three of these processes, though computationally expensive, would be

invaluable in interpreting observed changes in Saturn's stratosphere.

In addition, the introduction of auroral-induced chemistry into current photochemical schemes and whether this could have any observable effect on the abundances of C_2H_2 and C_2H_6 at polar regions should be considered in the development of future models. This would confirm whether the increased abundances of these hydrocarbons observed in 1980 were due to solar maximum.

Appendix A

Appendix A: Tables of Cassini-CIRS observations

Table A.1: **COMPSIT** observations: Details of the 0.5 cm^{-1} observations from Cassini-CIRS from 2005 to 2013. The long-format name of the observations have the form CIRS_aaaSA_COMPSIT_bbb, which has been shortened to aaa_bbbC in this table. The numbers of spectra listed are for FP4 observations (with those for FP3 being very similar). All latitudes are planetographic.

Observation Name	Date (dd/mm/yyyy)	Solar Longitude	Number of target spectra	Number of deep-space spectra	Southern Latitude	Northern Latitude	Minimum emission angle	Maximum emission angle
00A_B013C	19/10/2004	301	2782	339	-80	-71	59	74
00A_A012C	8/11/2004	302	6783	2183	-76	-59	47	66
00A_B012C	9/11/2004	302	4160	2184	-76	-59	48	67
00B_A011C	3/12/2004	303	729	1183	-54	-43	34	45
00B_A012C	4/12/2004	303	4230	683	-53	-38	55	75
00B_B011C	7/12/2004	303	1912	314	-54	-45	39	49
00B_C011C	8/12/2004	303	5461	184	-55	-45	40	51
003_A014C	1/2/2005	305	2074	296	-65	-12	29	74
003_B014C	2/2/2005	305	2185	296	-38	-12	29	43
003_C014C	3/2/2005	305	2952	296	-35	-10	58	73
020_001C	28/1/2006	317	3293	2081	-56	6	38	76
020_002C	29/1/2006	317	3399	2073	-55	6	37	72
020_003C	30/1/2006	317	3149	2078	-34	6	60	79
021_001C	12/2/2006	317	3298	378	11	55	37	71
021_002C	13/2/2006	317	3625	379	11	52	38	68
021_003C	14/2/2006	317	3409	376	11	25	58	64
022_A003C	1/4/2006	319	6638	1994	44	72	44	78
022_B003C	2/4/2006	319	3890	1994	44	66	50	78
023_A004C	18/4/2006	320	4363	2121	58	75	55	76
023_B004C	19/4/2006	320	4617	2121	58	77	55	79
023_C004C	20/4/2006	320	3697	712	58	74	55	74
024_A005C	30/5/2006	321	4775	2041	30	66	28	63
024_B005C	31/5/2006	321	4674	2041	30	41	54	64
024_C005C	1/6/2006	321	4760	2041	30	41	55	65
025_A006C	18/6/2006	322	4654	1784	-76	-29	29	78
025_B006C	19/6/2006	322	4081	1684	-49	-30	56	77
025_C006C	20/6/2006	322	3953	1684	-49	-30	56	76
049_008C	16/8/2007	336	2155	706	-57	-44	44	57
049_B008C	17/8/2007	336	5424	606	-57	-44	58	76
063_001C	3/4/2008	343	2419	3171	-67	-63	66	78
076_001C	15/7/2008	347	2191	2012	-89	-84	68	83
082_001C	24/8/2008	348	1670	58	58	59	56	62
084_002C	12/9/2008	349	450	58	-84	-81	62	66
086_001C	22/9/2008	349	2842	1960	84	86	55	63
093_001C	14/11/2008	351	3345	2355	67	78	28	71
094_001C	21/11/2008	351	504	2355	22	84	2	76
094_002C	27/11/2008	351	2868	1955	-58	-48	63	84
097_001C	13/12/2008	352	1000	1828	-77	2	6	83
097_002C	13/12/2008	353	1975	2230	-44	-10	4	29
098_002C	30/12/2008	353	1975	2230	-44	-10	4	29
099_001C	6/1/2009	353	3920	1730	-66	-64	3	15
099_003C	7/1/2009	353	2670	1730	-81	-80	56	66
099_002C	8/1/2009	353	2585	1730	-24	-18	60	62
102_001C	29/1/2009	354	2060	1230	10	87	4	82
103_004C	18/2/2009	354	3985	566	-69	-63	60	76
106_001C	19/3/2009	355	3505	66	87	88	29	41
106_002C	24/3/2009	355	3530	66	-47	-45	6	17
107_001C	28/3/2009	356	3485	66	4	53	22	64
108_002C	7/4/2009	356	80	1888	-60	-54	6	15

Table A.1 continued...

Observation Name	Date (dd/mm/yyyy)	Solar Longitude	Number of target spectra	Number of deep-space spectra	Southern Latitude	Northern Latitude	Minimum emission angle	Maximum emission angle
108_005C	15/4/2009	356	3470	1888	80	83	18	22
109_004C	28/4/2009	357	2840	1493	43	55	0	11
109_005C	30/4/2009	357	2780	1493	71	74	10	14
110_004C	11/5/2009	357	3205	1493	-46	-34	63	78
110_005C	15/5/2009	357	2745	1493	63	66	5	6
111_003C	24/5/2009	357	2300	362	-79	-77	17	21
112_002C	13/6/2009	358	3505	430	54	58	6	9
119_001C	2/10/2009	2	7504	74	40	49	56	66
119_002C	10/10/2009	2	1558	74	10	33	69	77
119_004C	20/10/2009	2	2040	1095	20	50	48	75
119_005C	23/10/2009	3	2110	1156	20	52	49	80
120_001C	28/10/2009	3	1690	656	-79	-68	66	81
120_003C	5/11/2009	3	1315	656	-80	-68	66	82
121_002C	25/11/2009	4	1445	413	-35	-34	66	81
121_003C	26/11/2009	4	1052	96	-36	-35	66	77
121_004C	27/11/2009	4	2	128	1	1	54	54
122_003C	1/12/2009	4	2705	85	23	24	52	69
122_004C	4/12/2009	4	2201	126	-36	-35	66	81
123_003C	30/12/2009	5	2653	3232	-49	-11	49	81
126_004C	5/2/2010	6	4995	4000	-60	-51	54	64
126_001C	11/2/2010	6	278	3946	48	53	57	63
126_002C	15/2/2010	6	915	3946	-66	-38	36	68
126_003C	15/2/2010	6	367	3946	53	58	60	66
127_001C	22/2/2010	7	6520	3922	60	71	64	81
127_002C	28/2/2010	7	4508	3925	48	65	56	81
128_001C	12/3/2010	7	3880	3163	-65	-55	64	80
128_002C	16/3/2010	7	6430	2963	-21	-14	67	72
128_003C	25/3/2010	8	2932	3478	-64	-42	51	80
128_004C	26/3/2010	8	2798	3463	-28	-2	67	82
129_001C	30/3/2010	8	3290	4000	14	22	68	73
129_003C	13/4/2010	8	7579	3034	57	77	54	79
130_001C	19/4/2010	8	7483	2434	47	56	64	79
130_003C	1/5/2010	9	3385	2405	15	36	53	67
130_004C	7/5/2010	9	8015	1881	51	61	63	78
131_001C	9/5/2010	9	6946	1381	41	66	48	78
131_002C	14/5/2010	9	3470	1081	15	38	53	69
132_001C	26/5/2010	10	2435	1042	2	21	64	79
133_001C	14/6/2010	10	2680	881	-70	-61	60	71
133_002C	17/6/2010	10	506	672	-9	58	18	67
134_001C	28/6/2010	11	48	498	-6	-2	52	53
134_002C	11/7/2010	11	1912	509	-27	-6	65	81
134_003C	12/7/2010	11	1860	382	-15	-6	65	69
134_004C	13/7/2010	11	1883	203	-32	-1	50	58
134_005C	13/7/2010	11	918	209	-15	-1	4	70
134_006C	14/7/2010	11	6803	209	25	53	49	80
135_001C	16/7/2010	11	4330	208	27	36	64	72
135_002C	18/7/2010	11	3000	207	-31	-2	51	58
136_001C	16/8/2010	12	4591	1849	6	27	55	80
137_001C	7/9/2010	13	531	1531	-62	-42	53	81
137_002C	9/9/2010	13	967	333	20	51	48	81
137_003C	10/9/2010	13	970	333	-27	-18	65	72
137_004C	11/9/2010	13	4479	1003	38	51	62	78
138_001C	13/9/2010	13	1657	333	-15	-6	67	71
138_002C	15/9/2010	13	1396	1365	-26	-18	65	72

Table A.1 continued...

Observation Name	Date (dd/mm/yyyy)	Solar Longitude	Number of target spectra	Number of deep-space spectra	Southern Latitude	Northern Latitude	Minimum emission angle	Maximum emission angle
138_003C	18/9/2010	14	2972	1364	-33	-9	52	61
139_001C	5/10/2010	14	8550	1065	26	42	62	77
143_001C	2/1/2011	17	4013	2478	51	72	52	78
144_001C	27/1/2011	18	2793	1948	1	21	57	62
145_001C	24/2/2011	19	1975	1592	-69	-60	60	70
145_002C	24/2/2011	19	1975	1592	-69	-60	59	70
145_003C	25/2/2011	19	1959	1592	9	31	65	81
145_004C	26/2/2011	19	536	1593	8	30	66	81
145_005C	26/2/2011	19	1975	1592	8	17	66	70
145_006C	28/2/2011	19	1948	1592	-55	-41	60	80
145_007C	3/3/2011	19	3510	865	30	41	60	71
145_008C	6/3/2011	19	965	865	-5	30	5	68
146_001C	9/3/2011	19	975	865	-5	30	5	67
146_002C	10/3/2011	19	580	865	-5	30	5	66
146_003C	12/3/2011	19	975	865	-5	46	4	56
146_004C	13/3/2011	19	973	865	-4	45	4	56
146_005C	14/3/2011	19	972	865	-4	45	4	56
146_006C	18/3/2011	20	1784	365	53	58	61	68
146_007C	19/3/2011	20	980	365	-75	-64	66	77
148_001C	7/5/2011	21	4040	104	-48	-37	52	64
149_001C	15/6/2011	23	4055	156	-43	-32	53	63
150_001C	7/7/2011	23	4049	949	43	75	39	74
150_002C	11/7/2011	23	3955	948	-14	39	13	83
151_001C	28/7/2011	24	4002	948	-78	-43	39	79
151_002C	5/8/2011	24	1505	278	-33	-26	54	59
151_003C	7/8/2011	24	1250	278	-50	-41	51	59
151_004C	8/8/2011	24	303	278	-12	-3	67	70
151_005C	10/8/2011	24	965	278	-34	-25	63	70
152_001C	13/8/2011	25	1880	1087	-35	-25	63	71
152_003C	15/8/2011	25	1434	278	2	11	67	69
152_004C	17/8/2011	25	1145	278	-49	-41	51	60
152_005C	17/8/2011	25	1145	278	-33	-26	50	55
153_001C	10/9/2011	26	4050	483	38	75	33	74
154_002C	4/10/2011	26	4035	483	10	36	55	72
156_002C	4/11/2011	27	4055	613	-58	-47	61	78
158_002C	9/12/2011	29	4038	1187	-67	-55	61	80
159_001C	31/12/2011	29	3611	187	-36	-14	52	64
159_002C	10/1/2012	30	965	291	-39	-31	61	68
159_003C	10/1/2012	30	965	291	-39	-31	62	69
159_004C	13/1/2012	30	1735	291	42	52	59	71
159_005C	14/1/2012	30	1760	291	31	41	60	70
160_002C	17/1/2012	30	1505	291	-56	-46	41	51
160_003C	18/1/2012	30	1810	291	-55	-46	55	67
160_004C	19/1/2012	30	965	291	41	51	39	49
160_005C	19/1/2012	30	965	291	41	51	39	49
161_001C	16/2/2012	31	4046	2934	37	50	63	80
162_001C	11/3/2012	32	4055	2434	49	61	60	78
164_002C	16/4/2012	33	4040	3131	43	48	67	75
167_003C	9/6/2012	35	4060	194	-40	-7	47	52
170_001C	19/8/2012	37	1075	185	-54	-20	5	33
170_002C	20/8/2012	37	930	183	-39	-32	11	17
170_003C	21/8/2012	37	1410	183	-33	-25	44	46
170_004C	23/8/2012	37	965	183	-34	-27	46	49
171_001C	23/8/2012	37	1808	183	-84	-42	15	75
171_002C	26/8/2012	37	410	183	-38	-36	60	68

Table A.1 continued...

Observation Name	Date (dd/mm/yyyy)	Solar Longitude	Number of target spectra	Number of deep-space spectra	Southern Latitude	Northern Latitude	Minimum emission angle	Maximum emission angle
171_003C	26/8/2012	37	1855	183	-57	-6	50	56
171_004C	27/8/2012	37	1505	183	-75	-72	53	60
171_005C	30/8/2012	37	425	182	-3	-1	67	68
171_006C	31/8/2012	37	1440	183	-80	-76	42	47
172_002C	21/9/2012	38	2210	183	-87	-83	52	58
173_002C	14/10/2012	39	2175	101	-20	-7	55	58
173_003C	14/10/2012	39	2175	101	-20	-7	55	58
174_003C	15/11/2012	40	910	20	-15	-10	6	9
174_004C	17/11/2012	40	1505	20	-76	-72	52	57
174_005C	18/11/2012	40	1530	398	-53	-49	11	17
175_001C	21/11/2012	40	940	2047	-64	-60	16	21
175_003C	24/11/2012	40	965	2047	-80	-75	58	64
175_004C	2/12/2012	41	1970	755	-44	-42	66	73
177_001C	25/12/2012	41	2700	755	-24	6	60	68
178_004C	5/1/2013	42	1345	1140	42	43	52	67
179_003C	25/1/2013	42	3735	979	-40	-15	57	78
182_003C	25/2/2013	43	535	1481	43	44	63	70
182_002C	3/3/2013	44	2265	981	-89	-83	58	70
186_001C	14/4/2013	45	3993	1141	1	9	69	70
188_001C	1/5/2013	46	635	981	42	43	59	71
189_002C	15/5/2013	46	3775	641	-27	-23	68	72
176_003C	9/12/2012	41	535	755	42	43	66	78

Table A.2: **MIRMAP** observations: Details of the 2.5 cm^{-1} observations from Cassini-CIRS from 2005 to 2013. The long-format name of the observations have the form CIRS_aaaSA_MIRMAP_bbb, which has been shortened to aaa_bbbM in this table. The numbers of spectra listed are for FP4 observations (with those for FP3 being very similar). All latitudes are planetographic.

Observation Name	Date (dd/mm/yyyy)	Solar Longitude	Number of target spectra	Number of deep-space spectra	Southern Latitude	Northern Latitude	Minimum emission angle	Maximum emission angle
003_001AM	22/2/2005	305	27583	1771	-80	-50	46	80
003_003AM	23/2/2005	305	15122	1771	-77	-41	36	76
003_003BM	24/2/2005	306	14801	1371	-77	-41	36	76
004_039AM	1/3/2005	306	15298	1371	-80	-59	54	79
004_039BM	2/3/2005	306	15332	1371	-81	-59	55	81
006_004AM	23/4/2005	307	14863	2027	-87	-75	61	78
007_004BM	24/4/2005	307	6802	444	-87	-75	61	80
008_006AM	26/5/2005	309	16260	4000	-88	-69	58	81
008_006BM	27/5/2005	309	14568	4000	-87	-69	57	80
009_007AM	13/6/2005	309	16085	4000	-77	-32	20	67
009_007BM	13/6/2005	309	15490	4000	-77	-32	18	66
010_008AM	2/7/2005	310	7282	2471	-61	-20	7	51
010_008BM	3/7/2005	310	5955	2471	-51	-20	7	36
011_009AM	18/7/2005	310	15398	3233	-85	-9	3	81
011_009BM	19/7/2005	310	14588	2933	-78	-9	2	70
012_002AM	8/8/2005	311	14922	982	-80	-2	2	80
012_002BM	8/8/2005	311	15415	645	-84	-2	2	75
026_014M	8/8/2005	323	15950	4000	61	86	44	75
026_013M	8/8/2005	322	28623	4000	43	79	37	78
025_012AM	8/8/2005	322	15356	4000	31	79	26	78
025_012BM	8/8/2005	322	15414	4000	31	81	27	81
023_011M	8/8/2005	320	28742	4000	21	70	18	79
023_010AM	8/8/2005	320	15307	4000	7	59	6	55
023_010BM	8/8/2005	320	16249	4000	7	78	6	76
030_036M	8/8/2005	326	29371	1230	3	82	4	78
028_015M	8/8/2005	324	16276	2664	52	84	43	81
046_024M	18/6/2007	334	21151	4000	-76	-20	18	78
047_024BM	18/6/2007	334	14940	4000	-74	-8	8	76
048_025M	9/7/2007	334	28627	4000	-79	-41	36	78
048_026M	25/7/2007	335	30685	4000	-81	-51	46	81
049_027M	4/9/2007	336	16096	355	-79	-60	52	75
050_037M	23/9/2007	337	30471	1751	-85	-68	59	79
050_028M	4/10/2007	337	14940	204	-77	-32	29	77
050_028BM	4/10/2007	337	15463	204	-74	-31	29	74
051_029M	30/10/2007	338	15822	254	-76	28	3	77
054_031M	11/12/2007	340	22563	4000	32	88	13	80
054_038M	14/12/2007	340	19263	4000	44	89	19	82
054_038BM	14/12/2007	340	18540	4000	54	89	28	83
054_032AM	14/12/2007	340	14939	4000	9	89	1	79
054_032BM	14/12/2007	340	14984	4000	9	89	1	78
055_041AM	14/12/2007	340	14962	4000	63	89	30	82
055_041BM	14/12/2007	340	14939	4000	63	87	28	79
055_033M	9/1/2008	341	17362	4000	71	89	47	82
061_043M	17/3/2008	343	28735	3889	81	90	59	81
112_001M	4/6/2009	358	23164	108	42	89	19	78
118_001M	27/9/2009	2	26464	3581	-73	-42	47	81
122_001M	3/12/2009	4	12563	4000	-77	4	2	76
122_002M	5/12/2009	4	20665	4000	-68	-15	13	66
123_001M	21/12/2009	4	30569	3997	-82	-32	25	79

Table A.2 continued...

Observation Name	Date (dd/mm/yyyy)	Solar Longitude	Number of target spectra	Number of deep-space spectra	Southern Latitude	Northern Latitude	Minimum emission angle	Maximum emission angle
125_001M	22/1/2010	6	23970	4000	32	76	31	78
126_001M	19/2/2010	7	28718	4000	-79	-47	42	78
129_001M	31/3/2010	8	32166	4000	14	78	12	77
130_001M	5/5/2010	9	28159	4000	52	81	47	81
132_001M	10/6/2010	10	31534	1120	-81	-52	46	81
134_001M	10/7/2010	11	17355	1062	16	79	15	80
135_001M	19/7/2010	12	45146	562	31	76	30	77
137_001M	28/8/2010	13	45884	3366	42	79	40	82
137_002M	6/9/2010	13	7139	3066	-80	-16	13	79
138_001M	16/9/2010	13	18510	1868	-76	-12	7	71
138_002M	19/9/2010	14	18280	1671	-65	-31	22	58
143_001M	3/1/2011	17	30835	2309	63	81	59	80
145_001M	1/3/2011	19	21174	4000	-81	-62	59	80
146_001M	12/3/2011	19	7645	3066	55	76	50	74
146_002M	14/3/2011	19	7645	2566	-74	-56	51	73
146_003M	15/3/2011	20	29654	4000	47	82	42	82
148_001M	4/5/2011	21	26277	4000	38	77	33	76
149_001M	13/6/2011	23	30328	1258	-78	-37	33	78
151_001M	26/7/2011	24	25252	4000	31	81	27	80
152_001M	16/8/2011	25	3055	1084	20	60	16	56
152_003M	20/8/2011	25	10570	603	10	70	8	68
158_001M	3/12/2011	28	30498	620	37	78	32	77
159_001M	26/12/2011	29	29963	1146	-82	-36	31	81
160_001M	23/1/2012	30	29474	279	14	79	14	80
162_001M	14/3/2012	32	27920	4000	42	82	37	82
167_001M	15/6/2012	35	31057	386	-83	-20	23	77
170_001M	17/8/2012	37	25715	417	-83	-3	2	72
172_001M	2/10/2012	39	30892	217	-89	-71	50	80
177_001M	17/12/2012	41	7419	4000	-89	-2	2	79
180_001M	6/2/2013	43	20326	3268	-89	-67	36	83
187_001M	17/4/2013	45	32811	1289	-89	-54	22	83

Table A.3: **MIRTMAP** observations: Details of the 2.5 cm^{-1} sit-and-stare observations from Cassini-CIRS from 2005 to 2013. The long-format name of the observations have the form CIRS_aaaSA_MIRTMAP_bbb, which has been shortened to aaa_bbbMT. The numbers of spectra listed are for FP4 observations (with those for FP3 being very similar). All latitudes are planetographic.

Observation Name	Date (dd/mm/yyyy)	Solar Longitude	Number of target spectra	Number of deep-space spectra	Southern Latitude	Northern Latitude	Minimum emission angle	Maximum emission angle
118_001MT	29/9/2009	2	13233	4000	-73	84	3	80
119_001MT	21/10/2009	2	18221	4000	-71	81	2	80
123_001MT	31/12/2009	5	31202	4000	-89	72	1	82
126_001MT	18/2/2010	6	12682	4000	-4	80	3	79
127_001MT	24/2/2010	7	19562	4000	-81	4	3	81
131_001MT	11/5/2010	9	18540	4000	-4	82	2	82
139_001MT	22/10/2010	15	5979	680	47	81	43	82
143_001MT	19/1/2011	18	28067	4000	-63	78	2	77
145_001MT	23/2/2011	19	18488	4000	-82	-15	13	83
147_001MT	25/4/2011	21	30348	4000	-80	80	3	80
150_001MT	6/7/2011	23	31968	4000	-79	81	2	80
151_001MT	30/7/2011	24	23059	4000	4	83	3	84
151_002MT	4/8/2011	24	18432	3103	-82	-9	8	82
155_001MT	22/10/2011	27	31918	2343	-82	81	2	82
159_001MT	8/1/2012	30	30366	1450	-80	78	2	79
163_001MT	1/4/2012	32	26900	4000	-81	81	2	81
183_001MT	15/3/2013	44	18499	106	-89	-10	1	83

Table A.4: **FIRMAP** observations: Details of the 15.5 cm^{-1} observations from Cassini-CIRS from 2005 to 2013. The long-format name of the observations have the form CIRS_aaaSA_FIRMAP_bbb, which has been shortened to aaa_bbbF in this table. The numbers of spectra listed are for FP4 observations (with those for FP3 being very similar). All latitudes are planetographic.

Observation Name	Date (dd/mm/yyyy)	Solar Longitude	Number of target spectra	Number of deep-space spectra	Southern Latitude	Northern Latitude	Minimum emission angle	Maximum emission angle
00A_001F	30/10/2004	302	20443	900	-89	-14	1	85
004_004F	10/3/2005	306	54854	1707	-10	84	0	86
006_005AF	8/4/2005	307	22832	3551	-86	12	0	83
006_005BF	9/4/2005	307	21335	1518	-86	-15	9	83
008_007F	22/5/2005	308	53333	2626	-14	86	0	86
012_009F	30/7/2005	311	41444	4000	-90	-31	6	86
012_008F	3/8/2005	311	45579	2970	-85	2	1	86
017_010F	30/10/2005	314	37707	4000	-7	84	0	86
018_011F	25/11/2005	315	29490	4000	-9	84	0	86
022_014BF	23/3/2006	319	21876	4000	-13	85	0	85
022_014AF	22/3/2006	319	26572	4000	-10	85	0	86
027_015F	13/8/2006	323	24682	4000	-9	85	1	84
040_018F	2/3/2007	330	38883	1165	34	90	0	85
049_020F	1/9/2007	336	17381	4000	-83	-4	4	83
055_030F	1/1/2008	340	39014	4000	2	90	0	78
060_A027F	5/3/2008	343	23566	4000	5	90	0	85
060_B027F	6/3/2008	343	30950	4000	7	90	0	85
068_A024F	20/5/2008	345	12217	1780	-11	86	0	86
068_B024F	21/5/2008	345	13112	696	3	90	0	86
075_A002F	10/7/2008	347	23360	3996	-8	89	0	86
076_A001F	16/7/2008	347	33211	4000	-87	-8	3	85
076_B002F	11/7/2008	347	27220	2678	7	90	0	86
076_C002F	12/7/2008	347	30174	898	23	90	0	86
076_B001F	17/7/2008	347	25577	4000	-84	9	0	86
082_001F	23/8/2008	348	31823	773	10	90	0	86
095_001F	28/11/2008	351	34918	4000	8	90	0	86
097_002F	19/12/2008	352	76074	4000	-88	0	0	70
098_001F	29/12/2008	353	62674	4000	-90	0	0	78
120_001F	4/11/2009	3	39795	1456	-52	85	0	85
139_002F	18/10/2010	15	25735	3867	-85	7	0	85
152_001F	21/8/2011	25	43246	193	0	85	0	86
160_001F	27/1/2012	30	27502	520	-3	84	0	86
170_001F	15/8/2012	37	19018	888	-12	82	0	86
171_001F	1/9/2012	37	37471	2155	-89	0	0	82

Appendix B

Appendix B: Radiative transfer models of Earth, Venus and Mars

B.1 Earth

Radiative transfer modelling of Earth's atmosphere was necessary in order to model transmission spectra at infrared wavelengths for reference in reduction and calibration of IRTF-Celeste observations (see Chapter 7).

B.1.1 Reference atmosphere

The reference atmospheric profile for Earth is based on the *US standard* profile [Sissenwine et al., 1962] which is most representative of mid-latitude regions. The atmosphere has been defined on 50 atmospheric layers from surface level to 120 km. Figure B.1 shows the vertical profiles of temperature and the volume mixing ratios of different gases.

It was necessary to model the transmission spectra of Earth using different values for the precipitable water vapour (or PWV) in mm. This quantity serves as a measure of atmospheric water content if all water vapour in a vertical column condensed onto the surface as a liquid layer. Equation B.1 describes the calculation of the PWV from the vertical profile of the volume mixing ratio of H_2O.

$$\text{PWV (mm)} = \frac{1}{\rho_{H_2O(l)} R_{H_2O(g)}} \int_{z_0}^{z_{\max}} \frac{X_{H_2O}(z) p(z)}{T(z)} dz \tag{B.1}$$

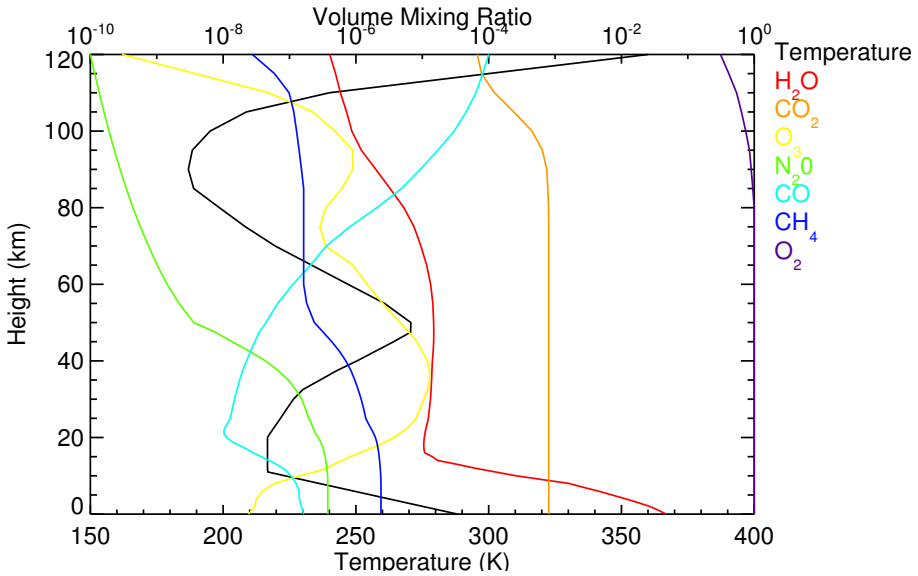

Figure B.1: The *US standard* reference profile of Earth: the vertical profiles of temperature (black), H_2O (red), CO_2 (orange), O_3 (yellow), N_2O (green), CO (cyan), CH_4 (blue) and O_2 (purple) with height in km.

Here, $X_{H_2O}(z)$ is the volume mixing ratio of water vapour, $p(z)$ is pressure, $T(z)$ is the temperature at height, z, where z_0 is the surface height. $\rho_{H_2O(l)}$ and $R_{H_2O(g)}$ are the density of liquid water and the gas constant of water vapour respectively. Whilst the concentrations of all other gases were kept constant, the vertical profile of H_2O vapour was scaled by a factor in order to model the transmission through the Earth's atmosphere for a chosen PWV. Table B.1 summarises the scaling factors applied to the H_2O vertical profile in the *US standard* atmosphere to yield PWVs ranging from 1mm to 4mm at a base height, $z_0 = 4.2$ km (the altitude of the Mauna Kea Observatory).

B.1.2 Modelling of transmission spectra

Radtrans was used to simulate a grid of transmission spectra of Earth. Line data from the HITRAN 2008 database [Rothman et al., 2009] was used. In addition, the forward model includes optical depths appropriate for Rayleigh scattering of an N_2-O_2 dominated atmo-

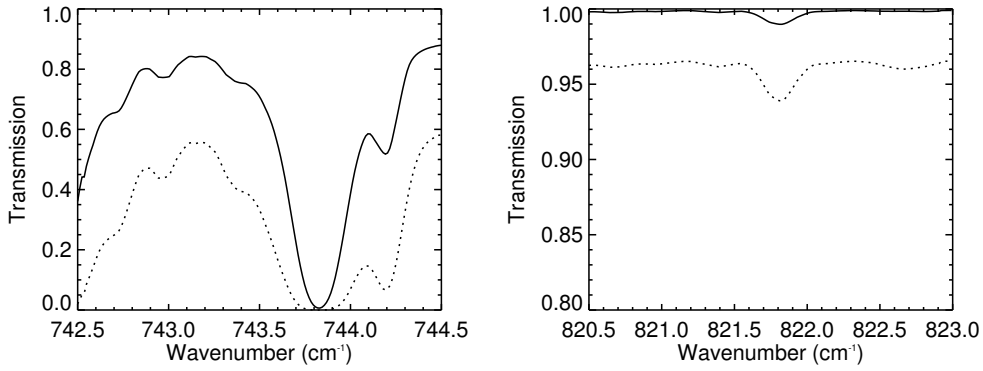

Figure B.2: Example transmission spectra in the 743 cm^{-1} (left) and 822 cm^{-1} bands (right). Solid spectra correspond to a PWV of 1 mm at an airmass of 1, dotted spectra are those at PWV of 4mm and an airmass of 3.

sphere (though this has negligible effect on the radiances at thermal infrared wavenumbers) and the continua of H_2O. Two sets of spectra were modelled: one set from 742.5 cm^{-1} to 744.5 cm^{-1} at a FWHM = 0.102 cm^{-1} and the second from 820.4 cm^{-1} to 823.0 cm^{-1} at a FWHM = 0.174 cm^{-1}. The base height was set to 4.2 km to simulate the transmission down to the altitude of the Mauna Kea observatory. PWVs ranging from 1.0 mm to 4.0 mm were generated since this represents the range in water vapour content experienced during the data acquisition of Celeste observations. Transmission spectra for airmass factors ranging from 1.0 to 3.0 were generated by setting the emission angle from 0° to 70.5° respectively. Figure B.2 shows examples of the modelled transmission spectra in the 743 cm^{-1} and 822 cm^{-1} bands.

PWV (mm)	Scale Factor
1.0	0.42
1.5	0.63
2.0	0.84
2.5	1.06
3.0	1.28
3.5	1.48
4.0	1.7

Table B.1: The scale factors applied to the H_2O vertical mixing ratio profile of H_2O in the *US standard* profile to produce a PWV of the values shown at $z_0 = 4.2$ km.

B.2 Venus

Modelling of thermal infrared spectra of Venus at high spectral resolution was attempted in order to conduct the radiometric calibration of the IRTF-Celeste observations (see Chapter 7).

B.2.1 Reference atmosphere and cloud model

The reference atmosphere and cloud profiles of Venus were acquired from Jo Barstow who has used them extensively in modelling of VIRTIS observations from Venus express [Barstow et al., 2012]. The profile is defined on 111 atmospheric layers from the surface up to 150 km. Figure B.3 shows the vertical profiles of temperature and the volume mixing ratios of gases.

The temperature profile incorporates data from the Venera and Pioneer venus probes

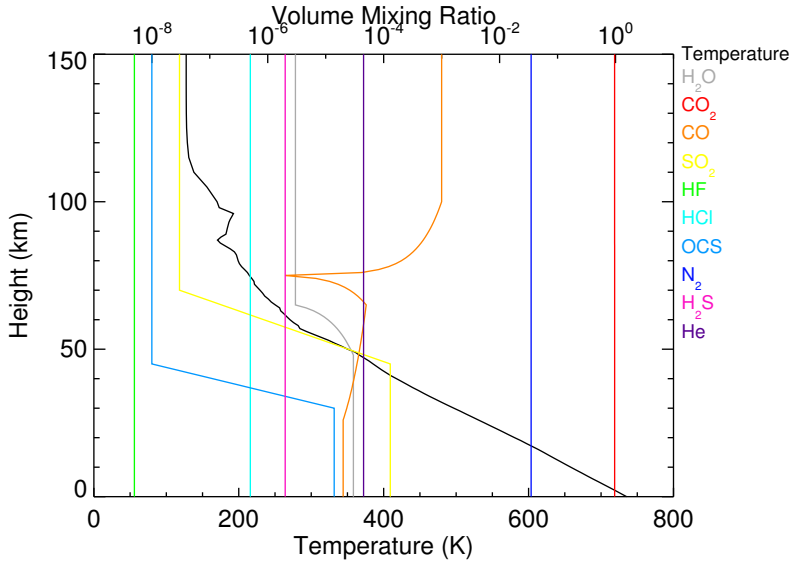

Figure B.3: The reference atmosphere of Venus: the vertical profiles of temperature (black), H_2O (grey), CO_2 (red), CO (orange), SO_2 (yellow), HF (green), HCl (cyan), OCS (light blue), N_2 (dark blue), H_2S (pink) and He (purple).

[Seiff et al., 1985] at altitudes below 45 km (where the temperature is not expected to vary meridionally) while using VeRa (radio occultation) data [Tellmann et al., 2009] were used for altitudes above 45 km. In the latter, a temperature profile of the equator was chosen for consistency with the Celeste observations of Venus which were selected in close proximity to the equator. The vertical profiles of gases in the Venuatian atmosphere are based on those of Tsang et al. [2008] with exception of the CO and H_2O vertical profiles which have been updated using recent remote sensing measurements as described by Barstow et al. [2012].

The *nominal cloud model*, as described by Barstow et al. [2012] was initially been adopted as the cloud model. This model comprises 4 types of H_2SO_4 particles: mode 1, mode 2, mode 2' and mode 3 which range from 0.3 μm to 3.65 μm in size. Figure B.4 shows the vertical distribution of these 4 cloud particles in Venus' atmosphere. Optical constants of sulphuric acid from 600 cm^{-1} to 900 cm^{-1} at a concentration of 84.5% were taken from Table II of Palmer and Williams [1975]: the chosen concentration is in accordance with retrieved values of the acid concentration at equatorial latitudes [Barstow et al., 2012]. Using these optical constants, the extinction cross-sections and single-scattering albedos were computed assuming Mie scattering with a Log-normal distribution.

B.2.2 Modelling dayside thermal infrared spectra of Venus

Thermal infrared spectra of Venus were forward modelled using Nemesis with sunlight switched on to model the dayside of Venus. Again, line data from the HITRAN 2008 database was used [Rothman et al., 2009]. In addition, optical depths of the H_2O continuum and for Rayleigh scattering of a CO_2 dominated atmosphere have been included in the forward model though this latter source of opacity is negligible at thermal infrared wavelengths. Optical depths of the CO_2-CO_2 collision-induced absorption or CIA have also been omitted since such absorption is negligible over the spectral range modelled.

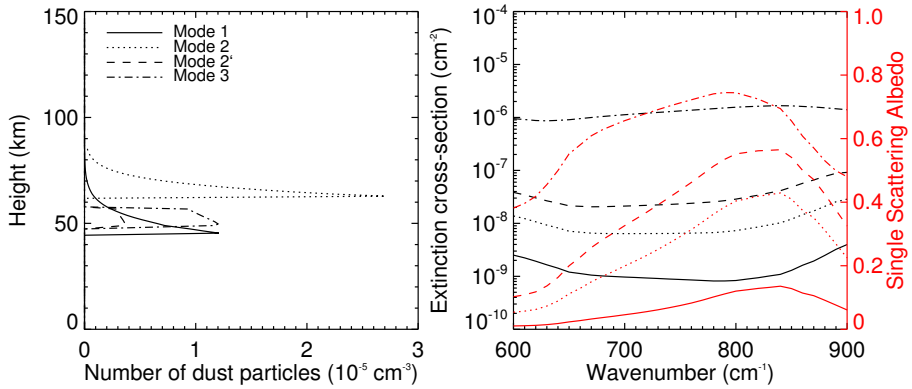

Figure B.4: The vertical distribution of mode 1 (solid), mode 2 (dotted), mode 2' (dashed) and mode 3 (dot-dashed) particles with height in the Venutian atmosphere (left) and their extinction cross-sections (black) and single-scattering albedos (red) as a function of wavenumber (right).

The surface emissivity of Venus has been set to be unity in order the model the surface as a blackbody. However, this is irrelevant at 822 cm^{-1} which does not provide sensitivity to Venus' surface (Figure B.6).

Celeste spectra of Venus in the 743 cm^{-1} were acquired at too high a terrestrial airmass for their use as calibration spectra to be viable. Thus, I have only computed forward models of Venus in the 822 cm^{-1} band. The spectral range was set from 820.5 cm^{-1} to 823 cm^{-1} at a FWHM of 0.174 cm^{-1} in accordance with the Celeste observations described in Chapter 7. A nominal spectrum of Venus was produced using an emission angle of 30° and at a solar angle of 60° in order to model the spectra obtained of the equator from IRTF-Celeste. Using the aerosol particle size and vertical distributions provided by Jo Barstow, this nominal spectrum represented a very low ($<10^{-5}$) cloud opacity at 822 cm^{-1}.

Figure B.5 compares the spectrum of this nominal model with that of a scaled (uncalibrated) Celeste spectrum and the Venera 15 spectrum for comparison. As shown, the forward modelled spectrum yields radiances almost a factor of 2 higher than that observed by Venera 15. In addition, the shape of the modelled spectrum in this spectral

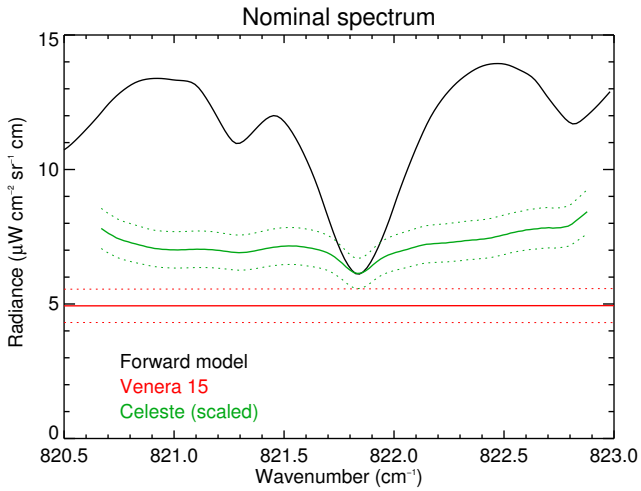

Figure B.5: The *nominal* forward model of Venus' spectrum in the 822 cm^{-1} band (black solid) and a scaled (uncalibrated) observation from IRTF-Celeste of the equator of Venus (green). Venera 15 radiances are shown for comparison (red).

range does not match that of Celeste. It was concluded that the low cloud opacity was the cause of the discrepancy in radiances and that increasing the optical depth of cloud particles might yield radiances more comparable with Venera 15 and spectral features more comparable with that of IRTF-Celeste.

Figure B.6 shows contribution functions of the 822 cm^{-1} band in the Venusian atmosphere: this spectral region is most sensitive to the lower cloud deck where mode 1, 2 and 3 particles dominate the cloud composition. However, mode 3 particles are largest in size (3.65 μm) and thus changes in their concentration alone would yield the largest change in radiances in the spectral range that is being modelled. Thus, the physical and optical properties of the mode 3 particles were varied.

The mode 3 cloud particles were parameterised using a variable cloud base height, optical depth and fractional scale height. The cloud base height, z_{base}, was initially set to 45 km (in accordance with the nominal cloud model (Figure B.4), the fractional scale height, H, to 10 km and the optical depth, τ_3 of mode 3 particles was varied. A very large optical depth (τ >5) was required in order for forward modelled radiances to be comparable with

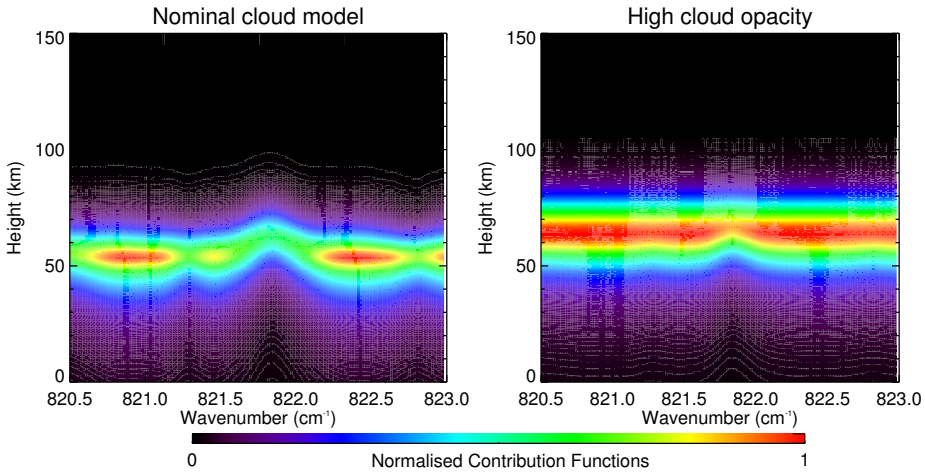

Figure B.6: The normalised, absolute contribution functions in the 822 cm^{-1} band in the Venusian atmosphere using the *nominal cloud model* (left) and the *high cloud opacity model*, as described in the text.

that of Venera 15 and for the modelled spectrum to exhibit a similar shape to that of Celeste. The parameter space of all three variables was searched and the χ^2 parameter (Equation B.2) computed in order to find the cloud parameters which provided the best fit to the observations.

$$\chi^2 = \sum_{\tilde{\nu}} \left(\frac{\gamma S(\tilde{\nu}) - R_{\mathrm{FM}}(z_{\mathrm{base}}, \tau_3, H, \tilde{\nu})}{\gamma \sigma_S(\tilde{\nu})} \right)^2 \tag{B.2}$$

$S(\tilde{\nu})$ and $\sigma_S(\tilde{\nu})$ is the (uncalibrated) spectrum and associated noise from the IRTF-Celeste observation of Venus, $\mathrm{R}_{\mathrm{FM}}(z_{\mathrm{base}}, \tau_3, H, \tilde{\nu})$ is the forward-modelled spectrum and $\gamma = R_{\mathrm{FM}}(z_{\mathrm{base}}, \tau_3, H, 821.85\ \mathrm{cm}^{-1})/S(821.85\ \mathrm{cm}^{-1})$ is a scaling factor such that uncalibrated Celeste spectrum and the forward-modelled spectrum match in radiance at the CO_2 feature centred at 821.85 cm^{-1}. Figure B.7 shows χ^2 maps of all three cloud variables. Although a forward model using a cloud base height of 45.5 km, an optical depth of 20.5 and a scale height of 27.5 km is found to minimise χ^2, there is a significant degeneracy in the parameter space which provides a good fit to the uncalibrated Celeste spectrum of Venus.

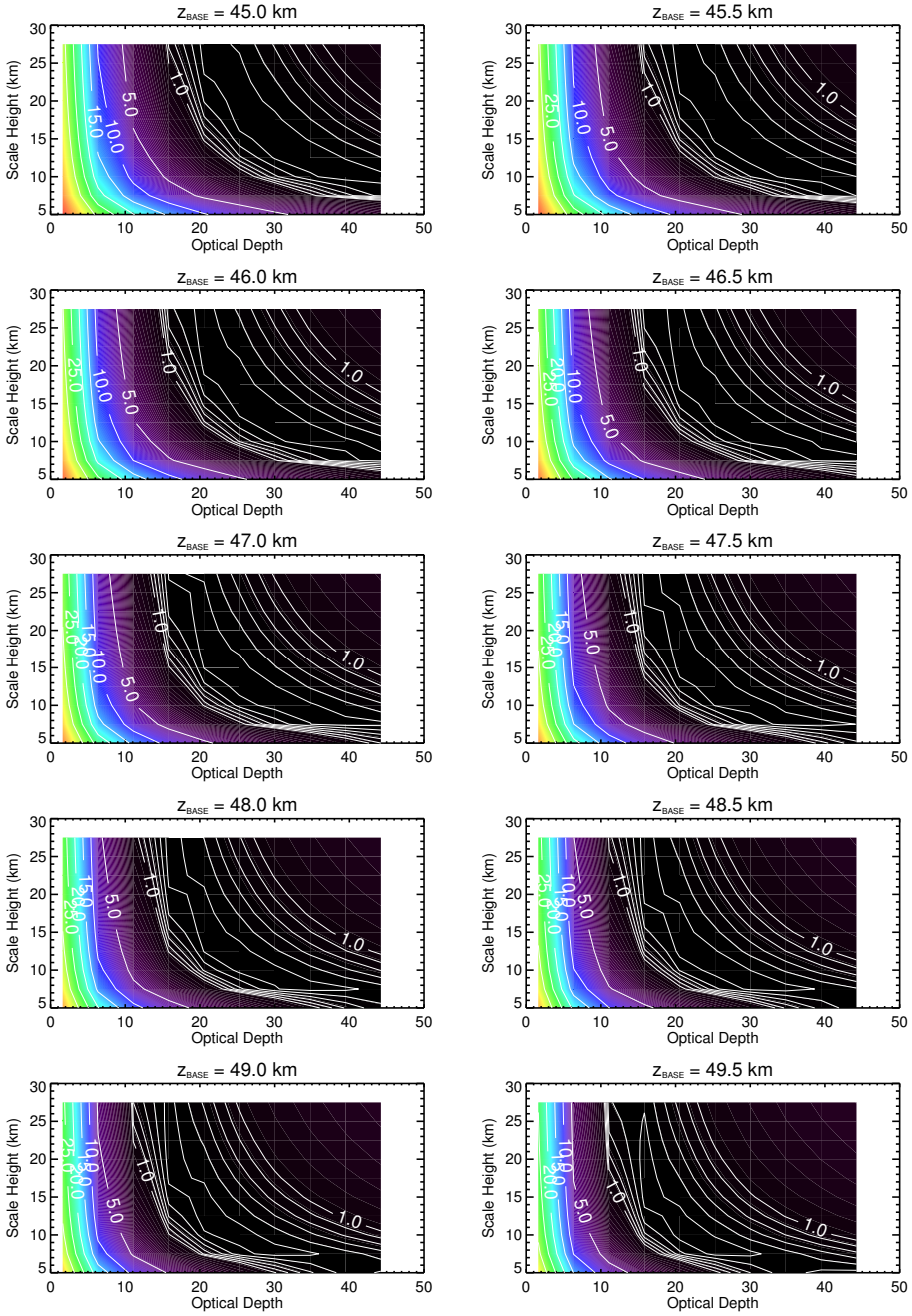

Figure B.7: χ^2 maps of optical depth of mode 3 particles at 822 cm^{-1} with scale height (km). Each plot shows the χ^2 values for a different cloud base height as indicated.

The forward model corresponding to the cloud parameters listed above is adopted as the *high cloud opacity* model, which is used as the calibration standard in Chapter 7. In

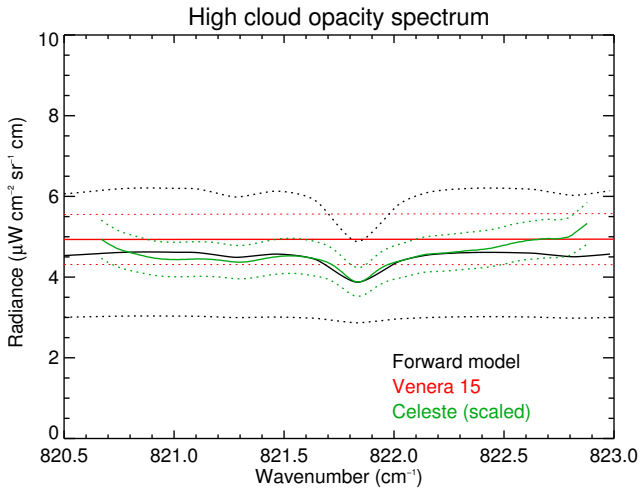

Figure B.8: The *high cloud opacity* forward model of Venus' spectrum in the 822 cm^{-1} band (black solid) and the scaled (uncalibrated) observation of Venus from IRTF-Celeste on 2012/03/31. Venera 15 radiances (red) are shown for comparison. Solid lines indicate spectra while dotted lines show the corresponding uncertainty/noise.

order to represent the uncertainty on the radiances of this forward model (accounting for the degeneracy in parameter space), all forward models with $\chi^2 < 1$ were searched and the most radiant and least radiant forward model at 821.85 cm^{-1} were adopted as the radiances at the $+1\sigma$ and -1σ levels respectively. Figure B.8 shows the forward model of Venus corresponding to the *high cloud opacity* model.

B.3 Mars

Modelling of thermal infrared spectra of Mars was also necessary for use in the radiometric calibration of IRTF-Celeste observations (see Chapter 7).

B.3.1 Reference atmosphere and dust model

Figure B.9 shows the reference Martian atmosphere which has been defined on 55 atmospheric layers from the surface to 100 km. The temperature profile is taken from Seiff [1982] and the vertical profiles of volume mixing ratios of gases are taken from Owen [1982], both of which have used data from the Viking lander and Mars 6 probe in proximity to northern summer solstice on Mars. The vertical distribution of dust and the extinction cross-sections and single-scattering albedos of Martian dust (Figure B.10) have been provided by Ramin Lolachi who uses these profiles/optical properties in modelling MCS (Mars Climate Sounder) data. The vertical distribution of dust is dependent on the vertical mixing and dust settling rates: the distribution shown in Figure B.10 is based on a modelled vertical profile from Wolff et al. [2006] assuming a scale height of H = 10 km and a parameter, $\nu = 0.1$, defined in their paper, which serves as a measure of diffusion and settling times. The extinction cross-sections and single-scattering albedos have been produced using optical constants also from Wolff et al. [2006] and assuming a modified gamma distribution using a mean particle size of 1.06 μm and variance of 3.0 μm.

The reference temperature profile is consistent with data obtained in approximately northern summer solstice, a similar season at the time observations of Mars were obtained with Celeste (Table 7.1). However, the surface temperature of Mars is highly variable with latitude, solar time and season. Using the Mars climate database[1], the surface temperatures at the sub-observer latitude (22°N) and longitudes representing the sub-observer

[1] http://www-mars.lmd.jussieu.fr/mcd_python/

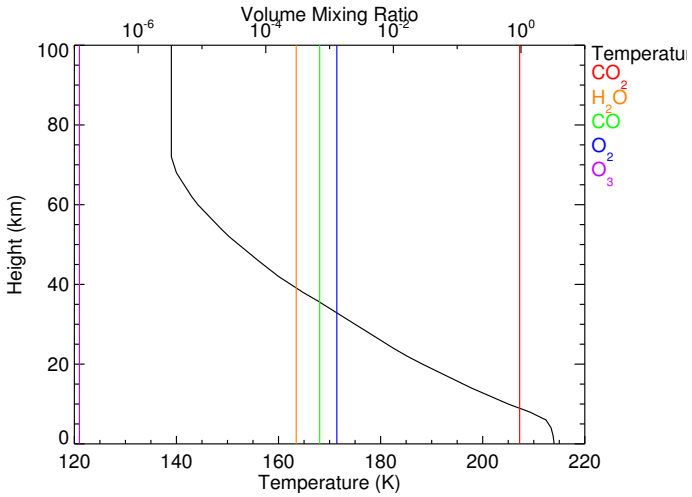

Figure B.9: The reference atmosphere of Mars: the vertical profiles of temperature (black), CO_2 (red), H_2O (orange), CO (green), O_2 (blue) and O_3 (purple).

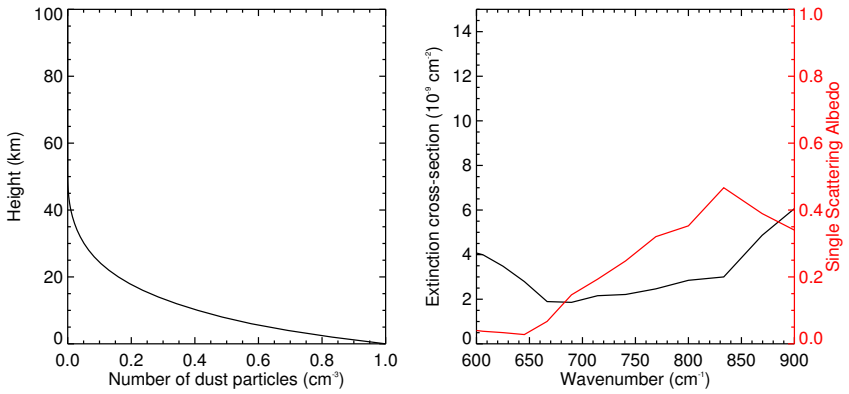

Figure B.10: The vertical distribution of aerosols (left) and their extinction cross-sections (black) and single-scattering albedos (red) as a function of wavenumber (right).

meridian at the time Celeste observations of Mars in 2012 were acquired (Table 7.1), were determined. These are shown in Table B.2.

B.3.2 Modelling dayside thermal infrared spectra of Mars

Thermal infrared spectra of Mars were forward modelled using Nemesis with sunlight switched on to simulate the dayside of the planet. Again, line data from the HITRAN 2008

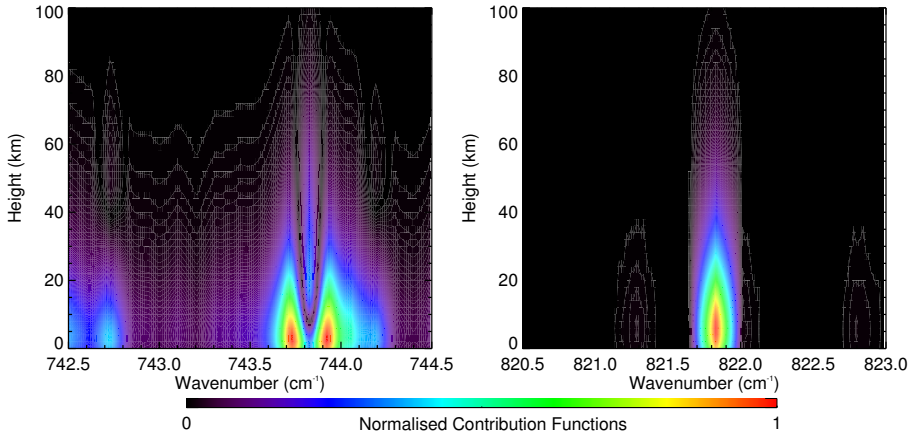

Figure B.11: The normalised, absolute contribution functions in the 743 cm^{-1} (left) and 822 cm^{-1} (right) bands in the Martian atmosphere.

database was used. In addition, optical depths of the H_2O and for Rayleigh scattering of a CO_2 dominated atmosphere have been included in the forward model though the latter have negligible effect at thermal infrared wavelengths. Optical depths of the CO_2-CO_2 collision-induced absorption or CIA have been omitted since, in the spectral range modelled (700 cm^{-1} to 800 cm^{-1}), such absorption is considered negligible.

Two sets of spectra were modelled: one set from 742.5 cm^{-1} to 744.5 cm^{-1} at a FWHM = 0.102 cm^{-1} and the second from 820.4 cm^{-1} to 823.0 cm^{-1} at a FWHM = 0.174 cm^{-1} respectively. In accordance with the Celeste spectra of Mars at the sub-observer latitude (22°N), spectra in both the 743 cm^{-1} and 822 cm^{-1} bands were forward modelled at

Date (yy-mm-dd)	Time (UTC)	Latitude	Longitude	Surface Temperature (K)
01-04-12	05:20	22°N	78°	$209.6^{+6.0}_{-8.1}$
01-04-12	06:20	22°N	90°	$198.2^{+6.3}_{-0.2}$

Table B.2: The surface temperatures of Mars at the latitudes/longitudes viewed by Celeste that represent the times that 822 cm^{-1} and 743 cm−1 observations were obtained respectively. The uncertainties on the temperatures represent the differences in temperature between longitudes 10° east and west of the longitude given.

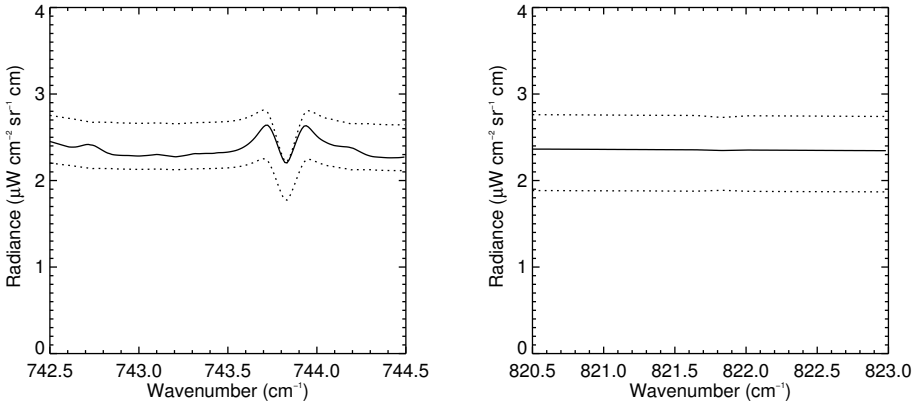

Figure B.12: Forward models of Mars (black, solid) in the 743 cm^{-1} (left) and 822 cm^{-1} bands (right) with dotted lines showing the uncertainty on the radiances (as described in the text).

zero emission angle. Figure B.11 shows the contribution functions of these spectral regions in the Martian atmosphere: for a low dust opacity, in both bands, these spectral regions are most sensitive to the surface of Mars. Thus, the surface temperature at the latitude/longitude corresponding to the observations likely represents the largest uncertainty in the radiances of the forward model. In addition to forward models at the surface temperatures given in Table B.2, forward models have also been computed at the surface temperatures corresponding at the $\pm 1\sigma$ level. These radiances were then adopted as the radiances at the $\pm 1\sigma$ level.

Figure B.12 shows the forward models of Mars in the 743 cm^{-1} and 822 cm^{-1} bands. In the 822 cm^{-1} band, the spectrum is approximately constant in radiance with wavenumber. In contrast, the spectrum in the 743 cm^{-1} band features a CO_2 absorption feature at $\sim$743.8 cm^{-1}.

References

D.G. Andrews. *An Introduction to Atmospheric Physics*. Cambridge University Press, 2000. 5

M. P. Baldwin, L. J. Gray, T. J. Dunkerton, K. Hamilton, P. H. Haynes, W. J. Randel, J. R. Holton, M. J. Alexander, I. Hirota, T. Horinouchi, D. B. A. Jones, J. S. Kinnersley, C. Marquardt, K. Sato, and M. Takahashi. The quasi-biennial oscillation. *Reviews of Geophysics*, 39(2):179–229, 2001. doi: 10.1029/1999RG000073. 16, 89

J. K. Barstow, C. C. C. Tsang, C. F. Wilson, P. G. J. Irwin, F. W. Taylor, K. McGouldrick, P. Drossart, G. Piccioni, and S. Tellmann. Models of the global cloud structure on Venus derived from Venus Express observations. *Icarus*, 217:542–560, feb 2012. doi: 10.1016/j.icarus.2011.05.018. 221, 222

B. Bezard. Detection of New Hydrocarbons on the Giant Planets. In *AAS/Division for Planetary Sciences Meeting Abstracts #30*, volume 30 of *Bulletin of the American Astronomical Society*, page 1059, September 1998. 7

B. Bézard and D. Gautier. A seasonal climate model of the atmospheres of the giant planets at the Voyager encounter time. I - Saturn's stratosphere. *Icarus*, 61:296–310, February 1985. doi: 10.1016/0019-1035(85)90110-1. 9

B. Bézard, J. I. Moses, J. Lacy, T. Greathouse, M. Richter, and C. Griffith. Detection of Ethylene (C_2H_4) on Jupiter and Saturn in Non–Auroral Regions. In *AAS/Division for Planetary Sciences Meeting Abstracts #33*, volume 33 of *Bulletin of the American Astronomical Society*, page 1079, November 2001. 7

W. E. Blass, G. W. Halsey, and D. E. Jennings. Self- and foreign-gas broadening of ethane lines determined from diode laser measurements at 12 microns. *Journal of Quantitative Spectroscopy and Radiative Transfer*, 38:183, September 1987. doi: 10.1016/0022-4073(87)90083-5. 58

A. Borysow and L. Frommhold. Theoretical collision-induced rototranslational absorption spectra for the outer planets - H2-CH4 pairs. *The Astrophysical Journal*, 304:849–865, May 1986. doi: 10.1086/164221. 58

A. Borysow and L. Frommhold. Collision-induced rototranslational absorption spectra of CH_4-CH_4 pairs at temperatures from 50 to 300 K. *The Astrophysical Journal*, 318:940–943, July 1987. doi: 10.1086/165426. 58

J. Borysow, L. Trafton, L. Frommhold, and G. Birnbaum. Modeling of pressure-induced far-infrared absorption spectra Molecular hydrogen pairs. *The Astrophysical Journal*, 296:644–654, September 1985. doi: 10.1086/163482. 60

J. Borysow, L. Frommhold, and G. Birnbaum. Collison-induced rototranslational absorption spectra of h_2-he pairs at temperatures from 40 to 3000 k. *The Astrophysical Journal*, 326:509–515, March 1988. doi: 10.1086/166112. 58

A. P. Boss. Giant planet formation by gravitational instability. *Science*, 276:1836–1839, 1997. doi: 10.1126/science.276.5320.1836. 2

J. Bouanich, J. Salem, H. Aroui, J. Walrand, and G. Blanquet. H_2-broadening coefficients in the ν_2 and ν_4 bands of PH_3. *Journal of Quantitative Spectroscopy and Radiative Transfer*, 84(2): 195 – 205, 2004. doi: http://dx.doi.org/10.1016/S0022-4073(03)00143-2. 58

L. R. Brown and D. B. Peterson. An Empirical Expression for Linewidths of Ammonia from Far-Infrared Measurements. *Journal of Molecular Spectroscopy*, 168:593–606, December 1994. doi: 10.1006/jmsp.1994.1305. 58

L. R. Brown, D. Chris Benner, J. P. Champion, V. M. Devi, L. Fejard, R. R. Gamache, T. Gabard, J. C. Hilico, B. Lavorel, M. Loete, G. Ch. Mellau, A. Nikitin, A. S. Pine, A. Predoi-Cross, C. P. Rinsland, O. Robert, R. L. Sams, M. A. H. Smith, S. A. Tashkun, and Vl. G. Tyuterev. Methane line parameters in hitran. *Journal of Quantitative Spectroscopy and Radiative Transfer*, 82(1-4): 219 – 238, 2003. ISSN 0022-4073. doi: DOI:10.1016/S0022-4073(03)00155-9. The HITRAN Molecular Spectroscopic Database: Edition of 2000 Including Updates of 2001. 58

L. F. Burlaga, N. F. Ness, D. A. Gurnett, and W. S. Kurth. Evidence for a Shock in Interstellar Plasma: Voyager 1. *The Astrophysical Journal Letter*, 778:L3, November 2013. doi: 10.1088/2041-8205/778/1/L3. 24

S. Calcutt, F. Taylor, P. Ade, V. Kunde, and D. Jennings. The Composite Infrared Spectrometer. *Journal of the British Interplanetary Society*, 45:381–386, September 1992. 37

B. E. Carlson, J. Caldwell, and R. D. Cess. A model of Saturn's seasonal stratosphere at the time of the Voyager encounters. *Journal of Atmospheric Sciences*, 37:1883–1885, August 1980. doi: 10.1175/1520-0469(1980)037⟨1883:AMOSSS⟩2.0.CO;2. 9

R. D. Cess and J. Caldwell. A Saturnian stratospheric seasonal climate model. *Icarus*, 38:349–357, June 1979. doi: 10.1016/0019-1035(79)90191-X. 9

D. Charbonneau, T. M. Brown, D. W. Latham, and M. Mayor. Detection of Planetary Transits Across a Sun-like Star. *The Astrophysical Journal Letters*, 529:L45–L48, January 2000. doi: 10.1086/312457. 2

B. J. Conrath and D. Gautier. Saturn helium abundance: A reanalysis of voyager measurements. *Icarus*, 144:124–134, March 2000. doi: 10.1006/icar.1999.6265. 59

R. Courtin, D. Gautier, A. Marten, B. Bézard, and R. Hanel. The composition of saturn's atmosphere at northern temperate latitudes from voyager iris spectra - NH_3, PH_3, C_2H_2, C_2H_6, CH_3D, CH_4, and the saturnian d/h isotopic ratio. *The Astrophysical Journal*, 287:899–916, dec 1984. doi: 10.1086/162748. 7, 8

T. de Graauw, L. N. Haser, D. A. Beintema, P. R. Roelfsema, H. van Agthoven, L. Barl, O. H. Bauer, H. E. G. Bekenkamp, A.-J. Boonstra, D. R. Boxhoorn, J. Cote, P. de Groene, C. van Dijkhuizen, S. Drapatz, J. Evers, H. Feuchtgruber, M. Frericks, R. Genzel, G. Haerendel, A. M. Heras, K. A. van der Hucht, T. van der Hulst, R. Huygen, H. Jacobs, G. Jakob, T. Kamperman, R. O. Katterloher, D. J. M. Kester, D. Kunze, D. Kussendrager, F. Lahuis, H. J. G. L. M. Lamers, K. Leech, S. van der Lei, R. van der Linden, W. Luinge, D. Lutz, F. Melzner, P. W. Morris, D. van Nguyen, G. Ploeger, S. Price, A. Salama, S. G. Schaeidt, N. Sijm, C. Smoorenburg, J. Spakman, H. Spoon, M. Steinmayer, J. Stoecker, E. A. Valentijn, B. Vandenbussche, H. Visser, C. Waelkens, L. B. F. M. Waters, J. Wensink, P. R. Wesselius, E. Wiezorrek, E. Wieprecht, J. J. Wijnbergen, K. J. Wildeman, and E. Young. Observing with the ISO Short-Wavelength Spectrometer. *Astronomy & Astrophysics*, 315:L49–L54, November 1996. 7

T. de Graauw, H. Feuchtgruber, B. Bézard, P. Drossart, T. Encrenaz, D. A. Beintema, M. Griffin, A. Heras, M. Kessler, K. Leech, E. Lellouch, P. Morris, P. R. Roelfsema, M. Roos-Serote, A. Salama, B. Vandenbussche, E. A. Valentijn, G. R. Davis, and D. A. Naylor. First results

of ISO-SWS observations of saturn: detection of CO_2, CH_3C_2H, C_4H_2 and tropospheric H_2O. *Astronomy & Astrophysics*, 321:L13–L16, May 1997. 60

T. Encrenaz, M. Combes, Y. Zeau, L. Vapillon, and J. Berezne. A tentative identification of C_2H_4 in the spectrum of Saturn. *Astronomy & Astrophysics*, 42:355, September 1975. 7

L. Esposito and S.M. Krimigis. *Saturn from Cassini-Huygens*. SpringerLink: Springer e-Books. Springer, 2009. ISBN 9781402092176. URL `http://books.google.co.uk/books?id=M56CHHxVMP4C`. 8

G. Fischer, W. S. Kurth, D. A. Gurnett, P. Zarka, U. A. Dyudina, A. P. Ingersoll, S. P. Ewald, C. C. Porco, A. Wesley, C. Go, and M. Delcroix. A giant thunderstorm on saturn. *Nature*, 475: 75–77, July 2011. doi: 10.1038/nature10205. 17

F M Flasar, V G Kunde, M M Abbas, R K Achterberg, P Ade, A Barucci, B Bézard, G L Bjoraker, J C Brasunas, and S Calcutt. Exploring the saturn system in the thermal infrared: The composite infrared spectrometer. *Space Science Reviews*, 115(1-4):169–297, 2004. i, 37

L. N. Fletcher, P. G. J. Irwin, N. A. Teanby, G. S. Orton, P. D. Parrish, R. de Kok, C. Howett, S. B. Calcutt, N. Bowles, and F. W. Taylor. Characterising saturn's vertical temperature structure from Cassini/CIRS. *Icarus*, 189:457–478, August 2007. 11, 64, 69

L. N. Fletcher, P. G. J. Irwin, G. S. Orton, N. A. Teanby, R. K. Achterberg, G. L. Bjoraker, P. L. Read, A. A. Simon-Miller, C. Howett, R. de Kok, N. Bowles, S. B. Calcutt, B. Hesman, and F. M. Flasar. Temperature and composition of saturn's polar hot spots and hexagon. *Science*, 319:79–81, January 2008. doi: 10.1126/science.1149514. i, 14, 15, 76, 92

L. N. Fletcher, G. S. Orton, N. A. Teanby, P. G. J. Irwin, and G. L. Bjoraker. Methane and its isotopologues on Saturn from Cassini/CIRS observations. *Icarus*, 199:351–367, February 2009. doi: 10.1016/j.icarus.2008.09.019. 60, 189

L. N. Fletcher, R. K. Achterberg, T. K. Greathouse, G. S. Orton, B. J. Conrath, A. A. Simon-Miller, N. Teanby, S. Guerlet, P. G. J. Irwin, and F. M. Flasar. Seasonal change on Saturn from Cassini/CIRS observations, 2004-2009. *Icarus*, 208:337–352, July 2010. doi: 10.1016/j.icarus.2010.01.022. 9, 11, 59, 77, 85, 113

L. N. Fletcher, B. E. Hesman, P. G. J. Irwin, K. H. Baines, T. W. Momary, A. Sanchez-Lavega, F. M. Flasar, P. L. Read, G. S. Orton, A. Simon-Miller, R. Hueso, G. L. Bjoraker, A. Mamoutkine, T. del Rio-Gaztelurrutia, J. M. Gomez, B. Buratti, R. N. Clark, P. D. Nicholson, and C. Sotin. Thermal structure and dynamics of saturn's northern springtime disturbance. *Science*, 332:1413–1417, June 2011. doi: 10.1126/science.1204774. 17, 166

L. N. Fletcher, B. E. Hesman, R. K. Achterberg, P. G. J. Irwin, G. Bjoraker, N. Gorius, J. Hurley, J. Sinclair, G. S. Orton, J. Legarreta, E. García-Melendo, A. Sánchez-Lavega, P. L. Read, A. A. Simon-Miller, and F. M. Flasar. The origin and evolution of saturn's 2011-2012 stratospheric vortex. *Icarus*, 221:560–586, November 2012. doi: 10.1016/j.icarus.2012.08.024. 18, 156, 166, 171, 179, 200

T. Fouchet, S. Guerlet, D. F. Strobel, A. A. Simon-Miller, B. Bézard, and F. M. Flasar. An equatorial oscillation in saturn's middle atmosphere. *Nature*, 453:200–202, may 2008. i, 16, 72, 73, 74, 75, 100, 101, 128

A. J. Friedson and J. I. Moses. General circulation and transport in saturn's upper troposphere and stratosphere. *Icarus*, 218:861–875, April 2012. doi: 10.1016/j.icarus.2012.02.004. i, 18, 20, 21, 101, 104, 106, 177, 207

A. J. Friedson, R. A. West, A. K. Hronek, N. A. Larsen, and N. Dalal. Transport and Mixing in Jupiter's Stratosphere Inferred from Comet S-L9 Dust Migration. *Icarus*, 138:141–156, March 1999. doi: 10.1006/icar.1998.6063. 20

A. J. Friedson, R. A. West, E. H. Wilson, F. Oyafuso, and G. S. Orton. A global climate model of titan's atmosphere and surface. *Planetary & Space Science*, 57:1931–1949, December 2009. doi: 10.1016/j.pss.2009.05.006. 20

F. C. Gillett and W. J. Forrest. The 7.5 to 13.5 micron spectrum of saturn. *The Astrophysical Journal Letters*, 187:L37–L39, January 1974. doi: 10.1086/181387. 4

T. K. Greathouse, J. H. Lacy, B. Bézard, J. I. Moses, C. A. Griffith, and M. J. Richter. Meridional variations of temperature, C_2H_2 and C_2H_6 abundances in Saturn's stratosphere at southern summer solstice. *Icarus*, 177:18–31, September 2005. doi: 10.1016/j.icarus.2005.02.016. 10, 19, 65, 71, 77, 104, 206

T. K. Greathouse, J. H. Lacy, B. Bézard, J. I. Moses, M. J. Richter, and C. Knez. The first detection of propane on Saturn. *Icarus*, 181:266–271, March 2006. doi: 10.1016/j.icarus.2005.09.016. 7

A. W. Grossman, D. O. Muhleman, and G. L. Berge. High-resolution microwave images of Saturn. *Science*, 245:1211–1215, September 1989. doi: 10.1126/science.245.4923.1211. 60

S. Guerlet, T. Fouchet, B. Bézard, A. A. Simon-Miller, and F. Michael Flasar. Vertical and meridional distribution of ethane, acetylene and propane in Saturn's stratosphere from CIRS/Cassini limb observations. *Icarus*, 203:214–232, September 2009. doi: 10.1016/j.icarus.2009.04.002. 10, 11, 16, 19, 21, 59, 60, 64, 65, 69, 70, 71, 75, 77, 105, 113

S. Guerlet, T. Fouchet, B. Bézard, J. I. Moses, L. N. Fletcher, A. A. Simon-Miller, and F. Michael Flasar. Meridional distribution of CH_3C_2H and C_4H_2 in saturn's stratosphere from CIRS/cassini limb and nadir observations. *Icarus*, 209:682–695, October 2010. doi: 10.1016/j.icarus.2010.03.033. 94, 138

S. Guerlet, T. Fouchet, B. Bézard, F. M. Flasar, and A. A. Simon-Miller. Evolution of the equatorial oscillation in saturn's stratosphere between 2005 and 2010 from Cassini/CIRS limb data analysis. *Geophysical Research Letters*, 38:09201, May 2011. 15, 16, 85, 86, 87, 100, 101, 107, 129, 130, 203

A. Guharay, D. Nath, P. Pant, B. Pande, J. M. Russell III, and K. Pandey. Observation of semi-annual and annual oscillation in equatorial middle atmospheric long term temperature pattern. *Annales Geophysicae*, 27(11):4273–4280, 2009. doi: 10.5194/angeo-27-4273-2009. 203

G. W. Halsey, J. J. Hillman, S. Nadler, and D. E. Jennings. Temperature dependence of the hydrogen-broadening coefficient for the ν_9 fundamental of ethane. *Journal of Quantitative Spectroscopy and Radiative Transfer*, 39:429–434, June 1988. doi: 10.1016/0022-4073(88)90087-8. 58

R. Hanel, B. Schlachman, E. Breihan, R. Bywaters, F. Chapman, M. Rhodes, D. Rodgers, and D. Vanous. Mariner 9 Michelson interferometer. *Applied Optics*, 11:2625, Nov 1972. doi: 10.1364/AO.11.002625. 160

R. Hanel, D. Crosby, L. Herath, D. Vanous, D. Collins, H. Creswick, C. Harris, and M. Rhodes. Infrared spectrometer for voyager. *Applied Optics*, 19:1391–1400, May 1980. doi: 10.1364/AO.19.001391. i, 26

R. Hanel, B. Conrath, F. M. Flasar, V. Kunde, W. Maguire, J. C. Pearl, J. Pirraglia, R. Samuelson, D. P. Cruikshank, D. Gautier, P. J. Gierasch, L. Horn, and C. Ponnamperuma. Infrared observations of the saturnian system from Voyager 2. *Science*, 215:544–548, January 1982. doi: 10.1126/science.215.4532.544. 28

G. Hébrard and A. Lecavelier Des Etangs. A posteriori detection of the planetary transit of HD 189733 b in the Hipparcos photometry. *Astronomy & Astrophysics*, 445:341–346, January 2006. doi: 10.1051/0004-6361:20054308. 2

W. Herbst and G. E. Assousa. Observational evidence for supernova-induced star formation - Canis Major R1. *The Astrophysical Journal*, 217:473–475, October 1977. doi: 10.1086/155596. 1

B. E. Hesman, D. E. Jennings, P. V. Sada, G. L. Bjoraker, R. K. Achterberg, A. A. Simon-Miller, C. M. Anderson, R. J. Boyle, C. A. Nixon, L. N. Fletcher, and G. H. McCabe. Saturn's latitudinal C_2H_2 and C_2H_6 abundance profiles from Cassini/CIRS and ground-based observations. *Icarus*, 202:249–259, July 2009. doi: 10.1016/j.icarus.2009.02.013. 19, 64, 65, 71, 77, 149

B. E. Hesman, L. Fletcher, G. L. Bjoraker, P. V. Sada, R. K. Achterberg, D. E. Jennings, A. W. Lunsford, R. J. Boyle, T. Kerr, P. N. Romani, A. A. Simon-Miller, C. A. Nixon, G. R. Davis, and P. G. Irwin. The evolution of trace species and temperature in saturn's northern storm region. *AGU Fall Meeting Abstracts*, page H4, dec 2011. 166

B. E. Hesman, G. L. Bjoraker, P. V. Sada, R. K. Achterberg, D. E. Jennings, P. N. Romani, A. W. Lunsford, L. N. Fletcher, R. J. Boyle, A. A. Simon-Miller, C. A. Nixon, and P. G. J. Irwin. Elusive ethylene detected in saturn's northern storm region. *The Astrophysical Journal*, 760:24–31, November 2012. doi: 10.1088/0004-637X/760/1/24. 7, 18

C. J. A. Howett, P. G. J. Irwin, N. A. Teanby, A. Simon-Miller, S. B. Calcutt, L. N. Fletcher, and R. de Kok. Meridional variations in stratospheric acetylene and ethane in the southern hemisphere of the saturnian atmosphere as determined from Cassini/CIRS measurements. *Icarus*, 190:556–572, October 2007. 19, 64, 65, 77

J. Hurley, P.G.J. Irwin, L.N. Fletcher, J.I. Moses, B. Hesman, J. Sinclair, and C. Merlet. Observations of upper tropospheric acetylene on saturn: No apparent correlation with 2000 km-sized thunderstorms. *Planetary and Space Science*, 2012. doi: 10.1016/j.pss.2011.12.026. 41

J. W. Hurrell, J. J. Hack, A. S. Phillips, J. Caron, and J. Yin. The Dynamical Simulation of the Community Atmosphere Model Version 3 (CAM3). *Journal of Climate*, 19:21622183, 2006. doi: 10.1175/JCLI3762.1. 20

P. G. J. Irwin, N. A. Teanby, R. de Kok, L. N. Fletcher, C. J. A. Howett, C. C. C. Tsang, C. F. Wilson, S. B. Calcutt, C. A. Nixon, and P. D. Parrish. The NEMESIS planetary atmosphere radiative transfer and retrieval tool. *Journal of Quantitative Spectroscopy and Radiative Transfer*, 109:1136–1150, April 2008. 60

N. Jacquinet-Husson, N.A. Scott, A. Chédin, K. Garceran, R. Armante, A.A. Chursin, A. Barbe, M. Birk, L.R. Brown, C. Camy-Peyret, C. Claveau, C. Clerbaux, P.F. Coheur, V. Dana, L. Daumont, M.R. Debacker-Barilly, J.M. Flaud, A. Goldman, A. Hamdouni, M. Hess, D. Jacquemart,

P. Kpke, J.Y. Mandin, S. Massie, S. Mikhailenko, V. Nemtchinov, A. Nikitin, D. Newnham, A. Perrin, V.I. Perevalov, L. Régalia-Jarlot, A. Rublev, F. Schreier, I. Schult, K.M. Smith, S.A. Tashkun, J.L. Teffo, R.A. Toth, Vl.G. Tyuterev, J. Vander Auwera, P. Varanasi, and G. Wagner. The 2003 edition of the GEISA/IASI spectroscopic database. *Journal of Quantitative Spectroscopy and Radiative Transfer*, 95(4):429 – 467, 2005. doi: 10.1016/j.jqsrt.2004.12.004. 53, 58

D. E. Jennings, P. N. Romani, G. L. Bjoraker, P. V. Sada, C. A. Nixon, A. W. Lunsford, R. J. Boyle, B. E. Hesman, and G. H. McCabe. 12C/13C ratio in ethane on titan and implications for methane's replenishment. *The Journal of Physical Chemistry A*, 113(42):11101–11106, 2009. doi: 10.1021/jp903637d. 7, 142

E. Karkoschka and M. Tomasko. Saturn's vertical and latitudinal cloud structure 1991-2004 from hst imaging in 30 filters. *Icarus*, 179(1):195–221, 2005. doi: 10.1016/j.icarus.2005.05.016. 21

S. J. Kim, J. Caldwell, A. R. Rivolo, R. Wagener, and G. S. Orton. Infrared polar brightening on Jupiter. III - Spectrometry from the Voyager 1 IRIS experiment. *Icarus*, 64:233–248, November 1985. doi: 10.1016/0019-1035(85)90088-0. 94, 138

I. Kleiner, G. Tarrago, C. Cottaz, L. Sagui, L.R. Brown, R.L. Poynter, H.M. Pickett, P. Chen, J.C. Pearson, R.L. Sams, G.A. Blake, S. Matsuura, V. Nemtchinov, P. Varanasi, L. Fusina, and G. Di Lonardo. NH_3 and PH_3 line parameters: the 2000 HITRAN update and new results. *Journal of Quantitative Spectroscopy and Radiative Transfer*, 82:293 – 312, 2003. doi: http://dx.doi.org/10.1016/S0022-4073(03)00159-6. 58

V. G. Kunde, P. A. Ade, R. D. Barney, D. Bergman, J.-F. Bonnal, R. Borelli, D. Boyd, J. C. Brasunas, G. Brown, S. B. Calcutt, F. Carroll, R. Courtin, J. Cretolle, J. A. Crooke, M. A. Davis, S. Edberg, R. Fettig, M. Flasar, D. A. Glenar, S. Graham, J. G. Hagopian, C. F. Hakun, P. A. Hayes, L. Herath, L. Horn, D. E. Jennings, G. Karpati, C. Kellebenz, B. Lakew, J. Lindsay, J. Lohr, J. J. Lyons, R. J. Martineau, A. J. Martino, M. Matsumura, J. McCloskey, T. Melak, G. Michel, A. Morell, C. Mosier, L. Pack, M. Plants, D. Robinson, L. Rodriguez, P. Romani, W. J. Schaefer, S. Schmidt, C. Trujillo, T. Vellacott, K. Wagner, and D. Yun. Cassini infrared Fourier spectroscopic investigation. In L. Horn, editor, *Society of Photo-Optical Instrumentation Engineers (SPIE) Conference Series*, volume 2803 of *Society of Photo-Optical Instrumentation Engineers (SPIE) Conference Series*, pages 162–177, October 1996. 37

J. H. Lacy, M. J. Richter, T. K. Greathouse, D. T. Jaffe, and Q. Zhu. Texes: A sensitive high-resolution grating spectrograph for the mid-infrared. *Publications of the Astronomical Society of the Pacific*, 114:153–168, February 2002. doi: 10.1086/338730. 7, 205

M. Lecar, M. Podolak, D. Sasselov, and E. Chiang. On the Location of the Snow Line in a Protoplanetary Disk. *The Astrophysical Journal*, 640:1115–1118, April 2006. doi: 10.1086/500287. 1

J.-M. Lee, L. N. Fletcher, and P. G. J. Irwin. Optimal estimation retrievals of the atmospheric structure and composition of HD 189733b from secondary eclipse spectroscopy. *MNRAS*, 420:170–182, feb 2012. doi: 10.1111/j.1365-2966.2011.20013.x. 60

A. Levy, N. Lacome, and G. Tarrago. Hydrogen and Helium Broadening of Phosphine Lines. *Journal of Molecular Spectroscopy*, 157:172–181, January 1993. doi: 10.1006/jmsp.1993.1014. 58

L. Li, R. K. Achterberg, B. J. Conrath, P. J. Gierasch, M. A. Smith, A. A. Simon-Miller, C. A. Nixon, G. S. Orton, F. M. Flasar, X. Jiang, K. H. Baines, R. Morales-Juberias, A. P. Ingersoll, A. R. Vasavada, A. D. Del Genio, R. A. West, and S. P. Ewald. Strong temporal variation over one saturnian year: From voyager to cassini. *Scientific Reports*, 3, August 2013. doi: http://dx.doi.org/10.1038/srep02410. 132

M.-C. Liang, R.-L. Shia, A. Y.-T. Lee, M. Allen, A. J. Friedson, and Y. L. Yung. Meridional Transport in the Stratosphere of Jupiter. *The Astrophysical Journal*, 635:L177–L180, December 2005. doi: 10.1086/499624. 20

J. S. Margolis. Measurement of hydrogen-broadened methane lines in the ν_4 band at 296 and 200K. *Journal of Quantitative Spectroscopy and Radiative Transfer*, 50:431–441, oct 1993. doi: 10.1016/0022-4073(93)90073-Q. 58

H. W. Moos and J. T. Clarke. Detection of acetylene in the Saturnian atmosphere, using the IUE satellite. *The Astrophysical Journal Letters*, 229:L107–L108, April 1979. doi: 10.1086/182939. 6

T. G. Moran, D. E. Jennings, L. D. Deming, G. H. McCabe, P. V. Sada, and R. J. Boyle. Solar Magnetograms at 12 μm Using the Celeste Spectrograph. *Solar Physics*, 241:213–222, April 2007. doi: 10.1007/s11207-007-0271-1. i, 7, 141

J. I. Moses and T. K. Greathouse. Latitudinal and seasonal models of stratospheric photochemistry on saturn: Comparison with infrared data from IRTF/TEXES. *Journal of Geophysical Research (Planets)*, 110:E09007, June 2005. doi: 10.1029/2005JE002450. 12, 13, 66, 71, 95, 105, 207

J. I. Moses, B. Bézard, E. Lellouch, G. R. Gladstone, H. Feuchtgruber, and M. Allen. Photochemistry of Saturn's Atmosphere. I. Hydrocarbon Chemistry and Comparisons with ISO Observations. *Icarus*, 143:244–298, February 2000. doi: 10.1006/icar.1999.6270. 6, 7, 8, 11, 60, 97, 105

J. I. Moses, M.-C. Liang, Y. L. Yung, and R.-L. Shia. Meridional Distribution of Hydrocarbons on Saturn: Implications for Stratospheric Transport. In *Planetary Atmospheres*, pages 85–86, 2007. 20

O. Muñoz, F. Moreno, A. Molina, D. Grodent, J. C. Gérard, and V. Dols. Study of the vertical structure of saturn's atmosphere using HST/WFPC2 images. *Icarus*, 169:413–428, June 2004. doi: 10.1016/j.icarus.2003.12.018. 56

K. S. Noll, R. F. Knacke, A. T. Tokunaga, J. H. Lacy, S. Beck, and E. Serabyn. The abundances of ethane and acetylene in the atmospheres of Jupiter and Saturn. *Icarus*, 65:257–263, March 1986. doi: 10.1016/0019-1035(86)90138-7. 7

G. S. Orton, E. Serabyn, and Y. T. Lee. Vertical distribution of PH_3 in saturn from observations of its 1-0 and 3-2 rotational lines. *Icarus*, 146:48–59, July 2000. doi: 10.1006/icar.2000.6390. 60

G. S. Orton, M. Gustafsson, M. Burgdorf, and V. Meadows. Revised ab initio models for H_2-H_2 collision-induced absorption at low temperatures. *Icarus*, 189:544–549, August 2007. doi: 10.1016/j.icarus.2007.02.003. 58

Glenn S. Orton, Padma A. Yanamandra-Fisher, Brendan M. Fisher, A. James Friedson, Paul D. Parrish, Jesse F. Nelson, Amber Swenson Bauermeister, Leigh Fletcher, Daniel Y. Gezari, Frank

Varosi, Alan T. Tokunaga, John Caldwell, Kevin H. Baines, Joseph L. Hora, Michael E. Ressler, Takuya Fujiyoshi, Tetsuharu Fuse, Hagop Hagopian, Terry Z. Martin, Jay T. Bergstralh, Carly Howett, William F. Hoffmann, Lynne K. Deutsch, Jeffrey E. van Cleve, Eldar Noe, Joseph D. Adams, Marc Kassis, and Eric Tollestrup. Semi-annual oscillations in saturn's low-latitude stratospheric temperatures. *Nature*, 453:196–199, May 2008. i, 16, 17, 128, 129

T. Owen. The composition of the Martian atmosphere. *Advances in Space Research*, 2:75–80, 1982. doi: 10.1016/0273-1177(82)90107-7. 228

K. F. Palmer and D. Williams. Optical constants of sulfuric acid - Application to the clouds of Venus. *Applied Optics*, 14:208–219, January 1975. 222

R. A. Plumb and J. D. Mahlman. The zonally averaged transport characteristics of the gfdl general circulation/transport model. *Journal of Atmospheric Sciences*, 44:298–327, January 1987. doi: 10.1175/1520-0469(1987)044⟨0298:TZATCO⟩2.0.CO;2. 20

J. B. Pollack, O. Hubickyj, P. Bodenheimer, J. J. Lissauer, M. Podolak, and Y. Greenzweig. Formation of the Giant Planets by Concurrent Accretion of Solids and Gas. *Icarus*, 124:62–85, November 1996. doi: 10.1006/icar.1996.0190. 1

C. C. Porco, E. Baker, J. Barbara, K. Beurle, A. Brahic, J. A. Burns, S. Charnoz, N. Cooper, D. D. Dawson, A. D. Del Genio, T. Denk, L. Dones, U. Dyudina, M. W. Evans, B. Giese, K. Grazier, P. Helfenstein, A. P. Ingersoll, R. A. Jacobson, T. V. Johnson, A. McEwen, C. D. Murray, G. Neukum, W. M. Owen, J. Perry, T. Roatsch, J. Spitale, S. Squyres, P. Thomas, M. Tiscareno, E. Turtle, A. R. Vasavada, J. Veverka, R. Wagner, and R. West. Cassini imaging science: Initial results on saturn's atmosphere. *Science*, 307:1243–1247, February 2005. doi: 10.1126/science.1107691. 132

K. A. Rages and E. L. Barth. Saturn Limb Hazes as Seen from Cassini. In *AAS/Division for Planetary Sciences Meeting Abstracts*, volume 44 of *AAS/Division for Planetary Sciences Meeting Abstracts*, page 500.05, oct 2012. 56

L.S. Rothman, I.E. Gordon, A. Barbe, D.Chris Benner, P.F. Bernath, M. Birk, V. Boudon, L.R. Brown, A. Campargue, J.-P. Champion, K. Chance, L.H. Coudert, V. Dana, V.M. Devi, S. Fally, J.-M. Flaud, R.R. Gamache, A. Goldman, D. Jacquemart, I. Kleiner, N. Lacome, W.J. Lafferty, J.-Y. Mandin, S.T. Massie, S.N. Mikhailenko, C.E. Miller, N. Moazzen-Ahmadi, O.V. Naumenko, A.V. Nikitin, J. Orphal, V.I. Perevalov, A. Perrin, A. Predoi-Cross, C.P. Rinsland, M. Rotger, M. Simeckov, M.A.H. Smith, K. Sung, S.A. Tashkun, J. Tennyson, R.A. Toth, A.C. Vandaele, and J. Vander Auwera. The HITRAN 2008 molecular spectroscopic database. *Journal of Quantitative Spectroscopy and Radiative Transfer*, 110(9-10):533 – 572, 2009. ISSN 0022-4073. doi: DOI:10.1016/j.jqsrt.2009.02.013. HITRAN. 19, 53, 219, 222

P. V. Sada, G. H. McCabe, G. L. Bjoraker, D. E. Jennings, and D. C. Reuter. 13C-ethane in the atmospheres of jupiter and saturn. *The Astrophysical Journal*, 472:903, dec 1996. doi: 10.1086/178120. 58

J. Salem, J. Bouanich, J. Walrand, H. Aroui, and G. Blanquet. Hydrogen line broadening in the ν_2 and ν_4 bands of phosphine at low temperature. *Journal of Molecular Spectroscopy*, 228(1):23 – 30, 2004. doi: http://dx.doi.org/10.1016/j.jms.2004.06.015. 58

A. Sanchez-Lavega, F. Colas, J. Lecacheux, P. Laques, D. Parker, and I. Miyazaki. The Great White SPOT and disturbances in Saturn's equatorial atmosphere during 1990. *Nature*, 353: 397–401, October 1991. doi: 10.1038/353397a0. 133

A. Sánchez-Lavega, T. del Río-Gaztelurrutia, R. Hueso, J. M. Gómez-Forrellad, J. F. Sanz-Requena, J. Legarreta, E. García-Melendo, F. Colas, J. Lecacheux, L. N. Fletcher, D. Barrado y Navascués, D. Parker, International Outer Planet Watch Team, T. Akutsu, T. Barry, J. Beltran, S. Buda, B. Combs, F. Carvalho, P. Casquinha, M. Delcroix, S. Ghomizadeh, C. Go, J. Hotershall, T. Ikemura, G. Jolly, A. Kazemoto, T. Kumamori, M. Lecompte, P. Maxson, F. J. Melillo, D. P. Milika, E. Morales, D. Peach, J. Phillips, J. J. Poupeau, J. Sussenbach, G. Walker, S. Walker, T. Tranter, A. Wesley, T. Wilson, and K. Yunoki. Deep winds beneath saturn's upper clouds from a seasonal long-lived planetary-scale storm. *Nature*, 475:71–74, July 2011. doi: 10.1038/nature10203. 17

P. J. Schinder, F. M. Flasar, E. A. Marouf, R. G. French, C. A. McGhee, A. J. Kliore, N. J. Rappaport, E. Barbinis, D. Fleischman, and A. Anabtawi. Saturn's equatorial oscillation: Evidence of descending thermal structure from cassini radio occultations. *Geophysical Research Letters*, 38:08205, April 2011. 85, 86, 87, 107, 203

A. Seiff. Post-Viking models for the structure of the summer atmosphere of Mars. *Advances in Space Research*, 2:3–17, 1982. doi: 10.1016/0273-1177(82)90172-7. 228

A. Seiff, J. T. Schofield, A. J. Kliore, F. W. Taylor, and S. S. Limaye. Models of the structure of the atmosphere of Venus from the surface to 100 kilometers altitude. *Advances in Space Research*, 5:3–58, 1985. doi: 10.1016/0273-1177(85)90197-8. 222

J. A. Sinclair, P. G. J. Irwin, L. N. Fletcher, J. I. Moses, T. K. Greathouse, A. J. Friedson, B. Hesman, J. Hurley, and C. Merlet. Seasonal variations of temperature, acetylene and ethane in saturn's atmosphere from 2005 to 2010, as observed by Cassini-CIRS. *Icarus*, 225:257–271, 2013. 64, 65, 79

J. A. Sinclair, P. G. J. Irwin, L. N. Fletcher, T. Greathouse, S. Guerlet, J. Hurley, and C. Merlet. From Voyager-IRIS to Cassini-CIRS: Interannual variability in Saturn's stratosphere? *Icarus*, 233:281–292, May 2014. 109

N. Sissenwine, M. Dubin, and H. Wexler. The u.s. standard atmosphere, 1962. *Journal of Geophysical Research*, 67(9):3627–3630, 1962. ISSN 2156-2202. doi: 10.1029/JZ067i009p03627. 218

G. R. Smith, D. E. Shemansky, J. B. Holberg, A. L. Broadfoot, B. R. Sandel, and J. C. McConnell. Saturn's upper atmosphere from the voyager 2 EUV solar and stellar occultations. *Journal of Geophysical Research*, 88:8667–8678, November 1983. doi: 10.1029/JA088iA11p08667. 8

S. Tellmann, M. Pätzold, B. Häusler, M. K. Bird, and G. L. Tyler. Structure of the Venus neutral atmosphere as observed by the Radio Science experiment VeRa on Venus Express. *Journal of Geophysical Research (Planets)*, 114:E00B36, April 2009. doi: 10.1029/2008JE003204. 222

A. Tokunaga, R. F. Knacke, and T. Owen. The detection of ethane on Saturn. *The Astrophysical Journal Letters*, 197:L77–L78, April 1975. doi: 10.1086/181782. 5, 6

C. C. C. Tsang, P. G. J. Irwin, F. W. Taylor, and C. F. Wilson. A correlated-k model of radiative transfer in the near-infrared windows of Venus. *Journal of Quantitative Spectroscopy & Radiative Transfer*, 109:1118–1135, April 2008. doi: 10.1016/j.jqsrt.2007.12.008. 222

J. Vander-Auwera, N. Moazzen-Ahmadi, and J.-M. Flaud. Toward an accurate database for the 12 μm region of the ethane spectrum. *The Astrophysical Journal*, 662:750–757, June 2007. 19, 58, 77

P. Varanasi. Intensity and linewidth measurements in the 13.7-micron fundamental bands of $^{12}C_2H_2$ and $^{12}C^{13}CH_2$ at planetary atmospheric temperatures. *Journal of Quantitative Spectroscopy and Radiative Transfer*, 47:263–274, April 1992. doi: 10.1016/0022-4073(92)90145-T. 58

P. Winkelstein, J. Caldwell, S. J. Kim, M. Combes, G. E. Hunt, and V. Moore. A determination of the composition of the Saturnian stratosphere using the IUE. *Icarus*, 54:309–318, May 1983. doi: 10.1016/0019-1035(83)90200-2. 7

M. J. Wolff, M. D. Smith, R. T. Clancy, N. Spanovich, B. A. Whitney, M. T. Lemmon, J. L. Bandfield, D. Banfield, A. Ghosh, G. Landis, P. R. Christensen, J. F. Bell, and S. W. Squyres. Constraints on dust aerosols from the Mars Exploration Rovers using MGS overflights and Mini-TES. *Journal of Geophysical Research (Planets)*, 111:12, December 2006. 228

R. V. Yelle, C. A. Griffith, and L. A. Young. Structure of the jovian stratosphere at the galileo probe entry site. *Icarus*, 152:331–346, August 2001. doi: 10.1006/icar.2001.6640. 6

L.V. Zasova, V.I. Moroz, V. Formisano, N.I. Ignatiev, and I.V. Khatuntsev. Exploration of venus with the venera-15 ir fourier spectrometer and the venus express planetary fourier spectrometer. *Cosmic Research*, 44(4):349–363, 2006. doi: 10.1134/S0010952506040083. 159